

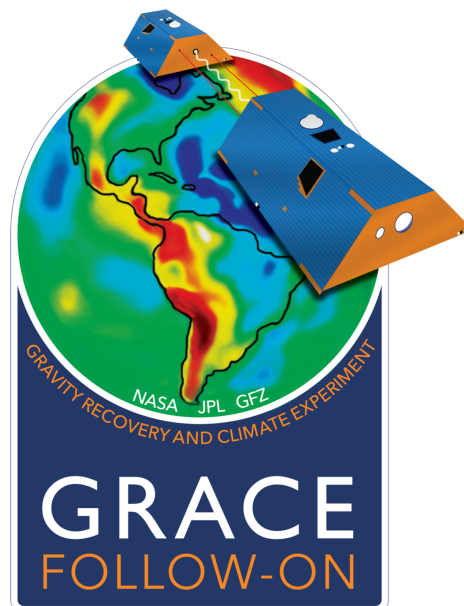
MAX-PLANCK-INSTITUTE FOR GRAVITATIONAL PHYSICS
(ALBERT EINSTEIN INSTITUTE)
LEIBNIZ UNIVERSITÄT HANNOVER

MASTER THESIS

BY

LAURA MÜLLER

**Generation of Level 1 Data Products and Validating the
Correctness of Currently Available Release 04 Data for
the GRACE Follow-On Laser Ranging Interferometer**



1st EXAMINER: PROF. DR. GERHARD HEINZEL

2nd EXAMINER: PROF. DR.-ING. HABIL. JÜRGEN MÜLLER

SUPERVISORS: VITALI MÜLLER, MALTE MATTHIAS MISFELDT

OCTOBER 22, 2021

With minor adjustments from February 01, 2022.

Kurzzusammenfassung

Die Gravity Recovery and Climate Experiment (GRACE) Follow-On Mission umkreist die Erde, während Abstandsänderungen zwischen dem Satellitenpaar mit einer noch nie dagewesenen Genauigkeit vermessen werden. Dies wird mit dem ersten Laser Ranging Interferometer (LRI, zu deutsch *Laser Distanz Interferometer*), welches zwischen den entfernten Satelliten operiert, erreicht. Die Mission basiert auf einer amerikanisch-deutschen Zusammenarbeit zur Untersuchung des Erdgravitationsfeldes und dessen zeitlichen Variationen. Speziell das LRI, welches nun seit ca. 3 Jahren zuverlässig arbeitet, wurde mitunter vom Albert Einstein Institut (AEI) entwickelt.

Das AEI ist daran interessiert die LRI Level 1 Datenprodukte zu verifizieren und zu validieren um sicherzustellen, dass die offiziell bereitgestellten LRI Daten (Release 04 oder v04) korrekt und für die Schwerefeldbestimmung nützlich sind. Damit wird der Titel dieser Arbeit, welcher zu deutsch *Generierung von Level 1 Datenprodukten und Validierung der Korrektheit von aktuell zugänglichen Release 04 Daten für das GRACE Follow-On Laser Ranging Interferometer* ist, verständlich. Level 1 Daten resultieren aus der Rohtelemetrie der Satelliten und dienen als Zwischenschritt, bevor die eigentlichen Schwerefeldlösungen erstellt werden können. Darüber hinaus werden die Level 1 Daten in Level 1A und Level 1B Produkte unterteilt, wobei Level 1B aus der Weiterverarbeitung von Level 1A hervorgeht.

Die Autorin dieser Arbeit hat im bestehenden System für Datenverarbeitung und Datenanalyse am AEI eine Verarbeitungskette implementiert, die alternative Datenprodukte des LRI Level 1A und insbesondere das LRI1B generiert. Sie werden v50 Daten genannt. Datensätze von v04 und v50 wurden verglichen, um Diskrepanzen zwischen beiden Versionen zu identifizieren. Es stellte sich heraus, dass die LRI Level 1A v04 Datenprodukte einige kleinere Fehler aufweisen, wie z. B. fehlende Datenpakete, falsche Einheiten oder Zeitrahmenkennungen, die nicht mit der Dokumentation der Produkte übereinstimmen. Die LRI Phasenmessungen werden jedoch korrekt im LRI1A Produkt bereitgestellt, was die wichtigsten Daten für die Herleitung des LRI1B Produkts und die anschließende Bestimmung des Schwerefelds sind. Im Fall von LRI1B zeigt die Entfernungsmessung in v50 an einzelnen Tagen ein geringeres Rauschen als v04. Dies kann mit Instrumenten Neustarts, Problemen in den Zeit-Produkten und Sprüngen in der Phasenmessung zusammenhängen, die z. B. durch Aktivierung der Satelliten Schubdüsen ausgelöst werden und nicht vollständig in den v04 Daten beseitigt wurden.

Zusammenfassend behandelt diese Arbeit einige theoretische Grundlagen zur Laserinterferometrie und zu relativistischen Effekten im Weltraum. Anschließend wird die GRACE Follow-On Mission und die Funktionsweise des LRI ausführlich vorgestellt. Darüber hinaus werden die verschiedenen Levels der Datenverarbeitung besprochen und die Prozessschritte der LRI Level 1A und LRI1B Generierung erläutert. Schließlich werden die Unterschiede von v04 und v50 und deren Ursprünge verdeutlicht.

Schlagnworte: Laser Interferometrie, GRACE-Follow-On, Laser Ranging Interferometer

Abstract

The satellite pair of the Gravity Recovery and Climate Experiment (GRACE) Follow-On orbits the Earth, while their inter-satellite distance changes are measured with an accuracy never reached before. This is achieved with the first Laser Ranging Interferometer (LRI) that operates between two distant spacecraft. The mission is based on a US-German collaboration for investigating Earth's gravitational field and its temporal variations. The LRI was developed with the involvement of the Albert Einstein Institute (AEI) and the instrument has been running reliably for about 3 years now.

The AEI has an interest in verifying and validating the LRI Level 1 data products, to ensure that the officially provided LRI data (Release 04 or v04) is correct and useful for gravity field determination. Level 1 data results from the raw telemetry of the spacecraft and serves as an intermediate step before the actual gravity field solutions can be created. Furthermore, the Level 1 data is divided into Level 1A and Level 1B products, where Level 1B is the result of further processing of Level 1A.

The author of this thesis has implemented a processing chain in the existing framework of data processing and data analysis at AEI. The new processing chain generates alternative LRI Level 1A data products and especially the LRI1B product. They are referred to as v50 data. The data sets of v04 and v50 were compared in order to identify discrepancies between both versions. It turns out that the LRI Level 1A v04 products show some minor imperfections like a few missing packets of the data, incorrect units or time frame identifiers which do not match with the product description. However, the LRI phase measurements within the LRI1A product are provided correctly, which is the most important data for deriving a correct LRI1B product and the subsequent gravity field solutions. In the case of LRI1B, the range measurement in v50 shows a lower noise level on some individual days than v04. This might be related to instrument reboots, incorrect clock data, and to jumps in the phase measurement, which result for example from thruster activation, but were probably not completely removed from v04 data.

In summary, this thesis will introduce some theoretical basics on laser interferometry and occurring effects of relativity in space. Afterwards, the GRACE Follow-On mission and the functionality of the LRI are presented in detail. Furthermore, the different levels of data processing are discussed and the LRI Level 1A and LRI1B processing steps are explained. Finally, the differences of v04 and v50, and their origins will be clarified.

Keywords: Laser Interferometry, GRACE Follow-On, Laser Ranging Interferometer

Table of Contents

Kurzzusammenfassung	i
Abstract	iii
Table of Contents	v
List of Acronyms	ix
List of Figures	xi
List of Tables	xiii
1 Introduction	1
2 Laser Interferometry and Relativistic Effects	3
2.1 Heterodyne Photocurrent and Phase Readout	3
2.2 Effects of Relativity	6
2.2.1 General Aspects of Relativity	6
2.2.2 Effects on Clocks in Low Earth Orbiters	7
2.2.3 Light Travel Time	9
3 GRACE Follow-On Satellites	11
3.1 Mission Overview	11
3.2 Science Data System	13
3.2.1 Levels of Data Processing	13
3.3 Time Frames and Processing Units	14
3.3.1 Global Positioning System (GPS)	14
3.3.2 Ultra Stable Oscillator	15
3.3.3 Instrument Processing Unit	15
3.3.4 On-Board Computer	15
3.3.5 Laser Ranging Processor	17
3.3.6 General Time Conversion	18
4 Laser Ranging Interferometer (LRI)	21
4.1 LRI Instrument Setup	21
4.1.1 Laser and Cavity	22
4.1.2 Fast Steering Mirror	22

4.1.3	Triple Mirror Assembly	22
4.2	Lightpath of the LRI	23
4.3	Relation of Phase Measurement and Instantaneous Range	25
4.4	Carrier to Noise Ratio	29
5	Raw Data Flow in GRACE Follow-On and AEI	31
5.1	Data Generation on Spacecraft Level	31
5.2	Preparation of Level 0 Data at AEI	32
6	Generation of AEI LRI1B v50 Product	37
6.1	Preparation of Raw Phase Data	38
6.2	Deglitching	39
6.3	First Phase Smoothing Step for φ_M and φ_T	41
6.4	Smooth LRI Time to GPS Time Conversion	42
6.5	Phase Difference Transponder - Master	45
6.5.1	Effects of Relativity in Time-tags	48
6.5.2	Alternative Methods to Remove the Phase Ramp	50
6.6	Second Smoothing Step for φ_{LRI}	53
6.7	Visualisation of All Phase Jump Removal Steps	53
6.8	Latest Adjustments of First and Second Smoothing Step	56
6.9	Converting Phase to Distance Measurement	57
6.9.1	Cross-Calibration LRI and KBR	57
6.9.2	Calibrated Frequency Model	60
6.10	CRN Filter	60
6.11	Preparation of Different Data Streams for LRI1B	63
6.12	Time Derivatives and Removal of Instabilities	64
6.13	Post-Processing Steps for Quality Flag of LRI1B	65
6.14	Summary of the Generated LRI1B v50 Product	66
7	Verifying the Official LRI Level 1B Product	71
7.1	Comparison of Scale Factor and Time Shift	71
7.2	Comparison of Biased Range for January 2019	75
7.3	Comparison of Biased Range September 2020	78
7.4	Comparison of Light Time Correction	83
7.5	Time Derivatives of Biased Range and Light Time Correction	85
7.6	Conclusion of Verification	89
8	Summary and Outlook	91
A	Theoretical Basics	93
A.1	Spectral Analysis of Signals	93
A.1.1	Discrete Fourier Transformation	93
A.1.2	Window Functions	95
A.1.3	Spectra and Spectral Densities	98
A.2	Central 5-Point Numerical Differentiation Method	99

A.3	Scale Factor and Time Shift between Two Similar Time Series	103
B	The LRI Level 1A v50 Processing at AEI	107
B.1	LRI Data Product - LRI1A	107
B.2	LRI Steering Mirror Data Product - LSM1A	109
B.3	LRI Housekeeping Data Product - LHK1A	110
B.4	LRI Log Messages - LLG1A	114
B.5	LRI Light Time Product - LLT1A	115
B.6	Summary of Time-tags and Sorting for Level 1A Products	117
C	Validation of SDS LRI Level 1A v04 data	119
C.1	Comparison of LRI1A v04 and v50	119
C.2	Comparison of LSM1A v04 and v50	120
C.3	Comparison of LHK1A v04 and v50	121
C.4	Comparison of LLG1A v04 and v50	124
	Bibliography	127

List of Acronyms

Acronym		Acronym	
ACC	Accelerometer	GF1	GRACE C
AEI	Albert Einstein Institute	GF2	GRACE D
AS	Amplitude Spectrum	GFO	GRACE Follow-On
ASD	Amplitude Spectral Density	GFZ	Geoforschungszentrum Potsdam
CC	cross-calibration	GPS	Global Positioning System
CCS	Channel Cycle Slip	GRACE	Gravity Recovery and Climate Experiment
CNR	Carrier to Noise Ratio	GrGPS	GRACE GPS time
COM	Center of Mass	time	
CRN	N Convolutions of a Rectangle	IAU	International Astronomical Union
DFT	Discrete Fourier Transformation	ID	Identifier
DLR	Deutsches Zentrum für Luft- und Raumfahrt	IPU	Instrument Processing Unit
doy	Day of Year	JPL	Jet Propulsion Laboratory
DTR	Datation Report	KBR	K-Band Ranging
DWS	Differential Wavefront Sensing	LHK1A	LRI Housekeeping Product of Level 1A
ECI	Earth-centered inertial	LISA	Laser Interferometer Space Antenna
ENBW	Equivalent Noise Bandwidth	LLG1A	LRI Log Message Product of Level 1A
ESA	European Space Agency	LLT1A	LRI Light Time Product of Level 1A
FLL	Frequency-Locked Loop	LO	Local Oscillator
FPGA	Field Programmable Gate Array	LOS	Line of Sight
FreqModel	calibrated frequency model	LRI	Laser Ranging Interferometer
FSM	Fast Steering Mirror	LRI1A	LRI Product of Level 1A
GCRS	Geocentric Celestial Reference System	LRI1B	LRI Product of Level 1B
GEP	Gaussian error propagation	LRP	Laser Ranging Processor
		LSM1A	LRI Steering Mirror Product of Level 1A

Acronym		Acronym	
LTC	Light Time Correction	RX	Received
MATLAB	MATrix LABoratory, software package by Mathworks, Inc	S/C	Spacecraft
MJ	Mega Phase Jump	SDS	Science Data System
MWI	Microwave Instrument	SLDR	Sidelobe Drop Rate
		SST	Satellite-Satellite Tracking
NASA	National Aeronautics and Space Administration	TAI	International Atomic Time
NAVS	Number of Averages	TCG	Geocentric Coordinate Time
Nd:YAG	Neodymium doped Yttrium Aluminium Garnet	Tlm	Telemetry
NENBW	Normalized Equivalent Noise Bandwidth	TMA	Triple Mirror Assembly
NGGM	Next Generation Gravity Missions	TT	Terrestrial Time
		TTL	Tilt-To-Length
OBC	On-Board Computer	TWR	Two-Way Ranging
OCXO	Oven Controlled Quartz Oscillator	TX	Transmitted
		USO	Ultra Stable Oscillator
PD	Photodiode	UTC	Coordinated Universal Time
PJ	Phase Jump	UTCSR	University of Texas, Center for Space Research
PS	Power Spectrum		
PSD	Power Spectral Density	VC2	Housekeeping Telemetry
PSLL	Peak Sidelobe Level	VC4	Science Telemetry
PUS	Packet Utilisation Standard	VP	Vertex Point
PusTime	Pus-Packet-Time	YAML	YAML Ain't Markup Language
QPD	Quadrant Photodiode		
rcv time	Receiver time		
RDC	Raw Data Center		
rev	time of orbit revolution		
rms	Root Mean Square		

List of Figures

Title Page	GRACE Follow-On Logo [JPL].	0
2.1	Setup of a simplified homodyne and heterodyne interferometer.	4
2.2	Principle of gravitational red-shift.	7
3.1	Map of gravity anomalies.	12
3.2	Sketch of time frames and time conversions for GRACE Follow-On.	16
3.3	Example for time offset between LRP rcv time and OBC time.	19
3.4	Example for time offset between OBC time and IPU rcv time.	19
3.5	Example for time offset between IPU rcv time and GPS time.	19
4.1	Laser Ranging Interferometer setup.	23
4.2	Lightpath and frequencies in the Laser Ranging Interferometer.	25
4.3	Applying the absolute laser frequency on phase or phase rate to derive the biased range.	27
4.4	Minkowski diagram for light time correction principal.	29
5.1	Flow of LRI/LRP raw telemetry on spacecraft level.	33
5.2	Sketch of <code>gislparsed</code> time-tag assignments for different LRI data streams.	34
6.1	Principle of LRI phase wrapping.	38
6.2	Example for a phase jump and mega phase jump event.	40
6.3	Offset rate of raw and smoothed time correction.	43
6.4	Amplitude spectral density of raw and smoothed time correction.	44
6.5	Modelled clock rates for GRACE Follow-On due to relativistic effects.	48
6.6	Comparison of modelled relativistic effect and inverse master time-tags.	49
6.7	Amplitude spectrum of finite differences of master time-tags and effects from GPS satellites and Earth's rotation.	50
6.8	ASD of transponder phase ramp in the ranging (master) phase.	52
6.9	Analysis of first and second phase smoothing step for removing glitches.	54
6.10	Phase jump size and pre-fit rms for glitch events on master.	56
6.11	Improvements due to new adjustments for first and second smoothing step.	57
6.12	CRN-filter: impulse response of filter coefficients.	62
6.13	CRN-filter: impulse response in frequency domain.	62
6.14	CRN-filter: phase delay.	62
6.15	Effect of CRN Filter on LRI biased range.	63
6.16	Example for unstable behaviour in derivatives of biased range.	64
6.17	Overview of AEI processing steps for the LRI1B v50 product.	68
6.18	Availability of LRI1B v50 ranging data and quality flag events for 2018-2021.	69
7.1	Comparison of scale factors in January 2019 for v04 and v50 models.	72

7.2	Long-term observation of absolute laser frequency of v04 and v50 for 2019 to July 2021.	73
7.3	Long-term observation of estimated time shift of v04 and v50 for 2019 to July 2021.	73
7.4	Time series of biased range of v04 and v50 in January 2019.	76
7.5	ASD of biased range of v04 and v50 for January 2019.	77
7.6	Quality Flag of LRI1B v50 in September 2020.	79
7.7	ASD of biased range of v04 and v50 for time spans in September 2020.	80
7.8	ASD of biased range of v04 and v50 for September 5th, 8th and 19th in 2020.	81
7.9	ASD biased range and LTC for January 1st, 2019 and August 27th, 2020.	83
7.10	Comparison of light time correction for v04 and v50 in January 2019.	84
7.11	Derivative of LRI biased range with numdiff and CRN-filter.	85
7.12	Comparison of numdiff and CRN-filter derivative with analytical solution.	86
7.13	Biased range and light time correction of v04 and v50 for July 2020.	88
7.14	Range rate and light time rate of v04 and v50 for July 2020.	88
7.15	Range acceleration and light time acceleration of v04 and v50 for July 2020.	88
A.1	Visualisation of spectral leakage for a sinusoidal signal.	94
A.2	Nuttall4a transfer function.	96
A.3	LRI biased range spectrum and leakage models for different window functions.	97
A.4	Sketch of a 5-point-stencil in one dimension.	99
A.5	Comparison of analytical and numerical derivative for 3- and 5-point method.	101
A.6	Comparison of analytical and central 5-point numerical differentiation method in time domain.	102
B.1	Flow chart of Level 1A time-tag assignments.	117
C.1	LSM1A time-tag difference for v04 and v50 data.	120
C.2	LHK1A example for wrong assigned VC2 data.	122
C.3	LHK1A example for wrong sorting in v04.	123
C.4	LHK1A example for unusual LRP state.	124
C.5	LRI1A cut-out for comparison of v04 and v50.	125
C.6	LLG1A example for a bug in the telemetry of BootMessages.	125

Data analysis and its visualisation was done with:
 MATLAB version R2020b © 1994-2021 The MathWorks, Inc.
Flow charts and diagrams were created with:
 draw.io/diagrams.net © 2005-2021 JGraph Ltd

List of Tables

6.1	Description of glitch types and deglitching strategy.	41
6.2	Parameters for CRN-filter.	60
6.3	Description of LRI1B format.	66
7.1	Time spans with issues in CLK1B v04 data.	75
7.2	Quality reducing observations per day, for data segments in September 2020.	82
7.3	Increased ASD level for v04 ranging data in 2020.	82
7.4	Light time correction jumps in v04 from 2018 to July 2021.	84
A.1	Properties of different window functions.	96
A.2	Definition of two signals for testing the cross-correlation method.	104
B.1	Description of LRI1A format.	108
B.2	Description of LSM1A format.	110
B.3	Description of LHK1A format.	111
B.4	Connections of strings and numbers for different instrument states in LHK1A.	112
B.5	Types of LHK1A sensor measurements.	113
B.6	Description of LLG1A format.	114
B.7	Description of LLT1A format.	116
C.1	Missing <code>HealthMonitor</code> data in LRI1A v04.	120
C.2	Wrong assigned data in LHK1A v04.	122
C.3	Missing <code>LriHealthMonitor</code> and <code>LriHousekeepingTlm</code> data in LHK1A v04. . .	122
C.4	Missing <code>ADCSamples</code> and <code>LaserTlm</code> in LHK1A v04.	122
C.5	Other packets missing in v04.	123
C.6	Unusual state of LRP.	123
C.7	Issues in v04 due to a faulty <code>BootMessage</code>	124

1

Introduction

The Gravity Recovery and Climate Experiment (GRACE) consisted of two identical satellites, which were in orbit from 2002 to 2017 for measuring inter-satellite distance changes with a Microwave Instrument (MWI). This US-German collaboration gave the opportunity for investigating the static and time variable part of the gravitational field, that results e.g. from changes in the groundwater storage [Frappart and Ramillien, 2018] or from ice mass changes [Chen et al., 2006]. It was also shown that global gravity models of the Earth have been improved by the GRACE data [Tapley et al., 2004a].

In order to continue the determination of the temporal variations in Earth's local mass changes, a GRACE Follow-On mission was launched on May 22, 2018. The satellite pair of GRACE Follow-On is a rebuild of their predecessors with updated versions of the original instruments. In addition, they feature a new Laser Ranging Interferometer (LRI) for measuring the same inter-satellite distance variations like the Microwave Instrument (MWI). The LRI range measurements perform with a noise level well below its requirement of $80 \text{ nm}/\sqrt{\text{Hz}}$ for Fourier frequencies above 30 mHz [Abich et al., 2019], while the MWI noise is at approximately $1 \mu\text{m}/\sqrt{\text{Hz}}$ [Müller, 2017]. The LRI still delivers reliable low-noise data after more than 900 days of operation, which highlights the success of the first laser interferometer between distant spacecraft [AEI, 2021]. The LRI demonstrated the feasibility of ranging measurements with laser interferometers for next generation gravity missions. Additionally, the LRI acts as a technology demonstrator for the Laser Interferometer Space Antenna (LISA), which is a planned mission for detecting gravitational waves by using laser links between three satellites in a triangular configuration with arm lengths of 2.5 million kilometers [Wanner, 2019].

The Albert Einstein Institute (AEI) was involved in designing and testing the LRI [Müller, 2013] and contributes to the operation and the data analysis. For that reason, it is in the AEI teams interest that the LRI data products are correct and useful for gravity field recovery. Therefore, the author's main focus included the verification and validation of the publicly available LRI Level 1 data products, which are available in release 04 or version 04 (v04) by the time of the writing. The Level 1 data is generated from the raw telemetry of the satellites and is divided into two minor steps of Level 1A and Level 1B. They are intermediate processing steps, before the derivation of the actual gravity field solutions take place [Wen, 2019]. There are some LRI related Level 1A data products, where different LRI data streams are included.

However, the most important one is the LRI1A with the raw phase measurements of the LRI. Its further processing yields the LRI1B, which contains the important ranging information for gravity field recovery.

Already existing processing chains allowed to generate independent LRI Level 1 data products at AEI and compare them with the official v04 data of the Science Data System (SDS). The AEI data products can be identified by the name v50.

Furthermore, alternative algorithms which might improve the data quality of LRI1B are investigated at the AEI. This includes for example the deglitching, which removes phase jumps from the LRI phase measurement [Misfeldt, 2019]. In addition, a new model for the absolute laser frequency is being investigated [Misfeldt et al., 2020]. Thus, some processing steps of LRI1B v50 differ from the v04 processing, which makes it reasonable to compare their data quality and find out if an improvement can be achieved.

The comparison of Level 1A data products can be done in a text editor, while the differences of LRI1B v04 and v50 are visualised with different plots. Within this thesis, the obtained results from that comparison, and all necessary processing steps for the generation of Level 1A and the LRI1B are shown.

The basics of laser interferometry and some relativistic effects in space are explained in chapter 2. Afterwards, the GRACE Follow-On mission will be presented in chapter 3. In chapter 4 the architecture of the LRI and its operation principle are shown. The LRI raw data generation on the spacecraft level and its processing to LRI Level 1B is discussed in chapter 5 and chapter 6, while the comparison between AEI and SDS LRI1B is done in chapter 7. Finally, chapter 8 summarises this thesis and gives an outlook for future investigations. The interested reader can find the data processing for LRI Level 1A data products and their comparison to v04 in appendix B and appendix C.

2

Laser Interferometry and Relativistic Effects

This chapter introduces some theoretical basics and derivations for supporting the content in later chapters. The measurement principles of homodyne and heterodyne interferometry for a simplified interferometer setup are explained in section 2.1. Furthermore, the heterodyne photocurrent is derived to highlight the phase information, which is needed to compute the inter-satellite distance changes in GRACE Follow-On. Relativistic effects arising on the light travel path of a photon and orbiting clocks are emphasized in section 2.2.

2.1 Heterodyne Photocurrent and Phase Readout

The Mach-Zehnder-Interferometer is a common experimental setup for measuring distance changes in the arm-length of an interferometer. There exist the two different measurement principles: homodyne and heterodyne interferometry. The homodyne measurement principle (fig. 2.1 a)) operates with a single laser, whose beam is divided at a beamsplitter, and where interfering beams have the same frequency. One of the two resulting beams serves as a reference beam, while the other one travels through an optical system, where it experiences an additional change in phase. Finally another beamsplitter recombines the two beams and leads them to a photodiode (PD).

In contrast to that, heterodyne interferometry works with different frequencies for the interfering laser beams. Figure 2.1 (b) displays a simplified sketch of such an interferometer setup, where two lasers generate the laser beams with frequencies ω_1 and ω_2 and with amplitudes A_1 and A_2 . Due to the different beam paths there also occurs a relative phase change between the beams. We will denote their phases with φ_1 and φ_2 in the following. Finally, a sinusoidal signal at $\omega_1 - \omega_2$, also called beat note frequency, is produced at the output of the recombination beamsplitter, which is a specific peculiarity for heterodyne interferometry [Schwarze, 2018].

The two arriving beams on the photodiodes of fig. 2.1 (b) can be expressed by the light fields E_1 and E_2 . These incident light fields generate a photocurrent on the photoreceivers PD1 and PD2, caused by the photoelectric effect. In the following we compute this photocurrent I_c for

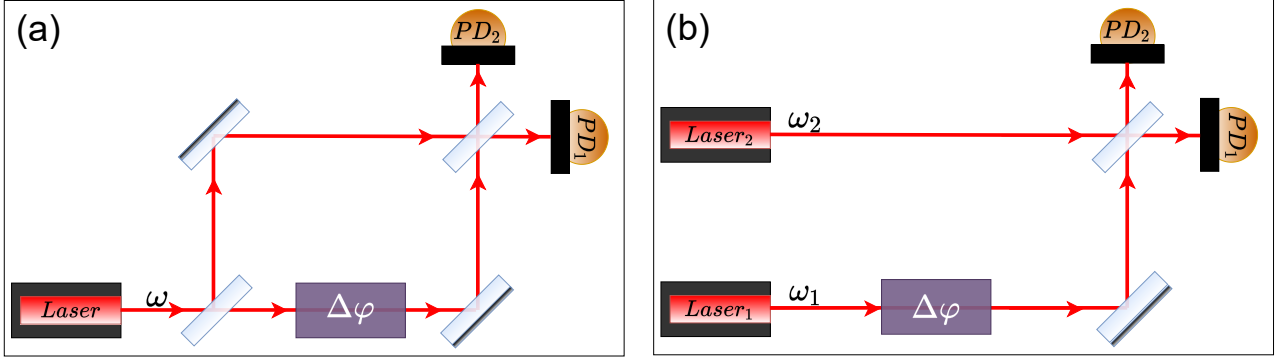


Figure 2.1: Simplified interferometer setup for **(a)** homodyne and **(b)** heterodyne interferometry. In **(a)** the reference beam and the beam affected by an optical system, have the same frequency at the recombination, while in **(b)** two different frequencies are generated and the resulting interference signal on the photodiodes is a beat note signal. Sketches based on [Schwarze \[2018\]](#).

the photodiodes PD1 and PD2 with responsivity κ , i.e.

$$I_c = \kappa \int_{\text{PD}} |E_1 + E_2|^2 dx dy. \quad (2.1)$$

The laser beams are split by the beamsplitter into reflected and transmitted parts. For example, a 50:50 beamsplitter reflects a beam with $R=0.5$ and transmits with $T=0.5$ by assuming no losses at this process. Therefore, one can define the amplitude coefficients of a beamsplitter with [\[Freise and Strain, 2010\]](#)

$$\rho = \sqrt{R}, \quad \tau = \sqrt{T} \quad (2.2)$$

$$\rho^2 + \tau^2 = 1. \quad (2.3)$$

Due to energy conversion, the outputs of a recombination beamsplitter have a phase-shift of 90 degree ($\pi/2$), commonly described by a factor i (imaginary number). The output amplitudes can be expressed in one of the possible conventions by the matrix relation [\[Freise and Strain, 2010\]](#)

$$\begin{pmatrix} B_1 \\ B_2 \end{pmatrix} = \begin{pmatrix} \rho & i\tau \\ i\tau & \rho \end{pmatrix} \cdot \begin{pmatrix} A_1 \\ A_2 \end{pmatrix}, \quad (2.4)$$

such that the electric fields on PD1 and PD2 can be expressed as

$$E_{1,\text{PD1}} = \rho \cdot A_1 \exp(i\omega_1 t + i\varphi_1) \quad E_{1,\text{PD2}} = i\tau \cdot A_1 \exp(i\omega_1 t + i\varphi_1) \quad (2.5)$$

$$E_{2,\text{PD1}} = i\tau \cdot A_2 \exp(i\omega_2 t + i\varphi_2) \quad E_{2,\text{PD2}} = \rho \cdot A_2 \exp(i\omega_2 t + i\varphi_2), \quad (2.6)$$

where the real valued amplitudes A_1 and A_2 and the phases φ_1 and φ_2 are in general spatial dependent [\[Müller, 2013\]](#).

Inserting these light fields into eq. (2.1) for the photocurrent yields

$$I_{c,\text{PD1}} = \kappa \left(\int_{\text{PD1}} \rho^2 \cdot |A_1|^2 dx dy + \int_{\text{PD1}} \tau^2 \cdot |A_2|^2 dx dy + 2\text{Re} \left[\int_{\text{PD1}} E_{1,\text{PD1}} \cdot E_{2,\text{PD1}}^* dx dy \right] \right) \quad (2.7)$$

$$I_{c,\text{PD2}} = \kappa \left(\int_{\text{PD2}} \tau^2 \cdot |A_1|^2 dx dy + \int_{\text{PD2}} \rho^2 \cdot |A_2|^2 dx dy + 2\text{Re} \left[\int_{\text{PD2}} E_{1,\text{PD2}} \cdot E_{2,\text{PD2}}^* dx dy \right] \right), \quad (2.8)$$

where E_2^* is the complex conjugated light field of E_2 and $\text{Re}(x)$ the real part of x [Mahrdt, 2014]. One can show that the third term in eq. (2.7) can be converted to a spatial independent function and a normalized overlap integral by expanding with $\sqrt{P_{1,\text{PD1}} \cdot P_{2,\text{PD1}}}/\sqrt{P_{1,\text{PD1}} \cdot P_{2,\text{PD1}}}$, where $P_{1,\text{PD1}}$ and $P_{2,\text{PD1}}$ are the powers of the beams on PD1, so that [Mahrdt, 2014]

$$\int_{\text{PD1}} E_{1,\text{PD1}} \cdot E_{2,\text{PD1}}^* \, dx dy = \int_{\text{PD1}} -i\rho\tau \cdot A_1 A_2 \cdot \exp\left(i(\omega_1 - \omega_2)t + i(\varphi_1 - \varphi_2)\right) \, dx dy \quad (2.9)$$

$$= \exp\left(i(\omega_1 - \omega_2)t\right) \cdot \sqrt{P_{1,\text{PD1}} \cdot P_{2,\text{PD1}}} \cdot \dots$$

$$\int_{\text{PD1}} \underbrace{\frac{i\rho\tau \cdot A_1 A_2}{\sqrt{P_{1,\text{PD1}} \cdot P_{2,\text{PD1}}}} \cdot \exp\left(i(\varphi_1 - \varphi_2 + \pi)\right)}_{:= \Gamma(t) \text{ normalised overlap integral on PD1}} \, dx dy \cdot \quad (2.10)$$

The additional phase term in the argument of the overlap integral results from the relation $\exp(i\pi) = -1$. The third term in eq. (2.8) is computed in the same way. However, the argument of the overlap integral $\Gamma(t)$ differs in a phase shift of 180 degree (π), i.e.

$$\int_{\text{PD2}} E_{1,\text{PD2}} \cdot E_{2,\text{PD2}}^* \, dx dy = \int_{\text{PD2}} i\rho\tau \cdot A_1 A_2 \cdot \exp\left(i(\omega_1 - \omega_2)t + i(\varphi_1 - \varphi_2)\right) \, dx dy \quad (2.11)$$

$$= \exp\left(i(\omega_1 - \omega_2)t\right) \cdot \sqrt{P_{1,\text{PD2}} \cdot P_{2,\text{PD2}}} \cdot \dots$$

$$\int_{\text{PD2}} \underbrace{\frac{i\rho\tau \cdot A_1 A_2}{\sqrt{P_{1,\text{PD2}} \cdot P_{2,\text{PD2}}}} \cdot \exp\left(i(\varphi_1 - \varphi_2)\right)}_{:= \Gamma(t) \text{ normalised overlap integral on PD2}} \, dx dy \cdot \quad (2.12)$$

Moreover, the overlap integral allows to define the heterodyne efficiency η and the phase ϕ , i.e.

$$\eta = |\Gamma(t)|^2$$

$$\phi = \arg(\Gamma(t)) \quad (2.13)$$

which can be used in a complex notation for rewriting the overlap integral Γ as [Mahrdt, 2014]

$$\Gamma = |\Gamma(t)| \exp\left(i \arg(\Gamma(t))\right) = \sqrt{\eta} \exp\left(i\phi\right) \cdot \quad (2.14)$$

Inserting this expression in eq. (2.10) and eq. (2.12), simplifies the third term of eq. (2.7) and eq. (2.8) to

$$2\text{Re} \left[\int_{\text{PD}} E_1 E_2^* \, dx dy \right] = 2\text{Re} \left[\exp\left(i(\omega_1 - \omega_2)t\right) \cdot \sqrt{P_1 \cdot P_2 \cdot \eta} \cdot \exp\left(i\phi\right) \right]. \quad (2.15)$$

For a complex number z , the relation $\text{Re}(z) = 1/2(z + z^*)$ holds. Therefore, we obtain

$$2\text{Re} \left[\int_{\text{PD}} E_1 E_2^* \, dx dy \right] = \sqrt{P_1 \cdot P_2 \cdot \eta} \cdot \exp\left(i(\omega_1 - \omega_2)t + i\phi\right) +$$

$$\sqrt{P_1 \cdot P_2 \cdot \eta} \cdot \exp\left(-i(\omega_1 - \omega_2)t - i\phi\right) \quad (2.16)$$

$$= 2 \cdot \sqrt{P_1 \cdot P_2 \cdot \eta} \cdot \cos\left((\omega_1 - \omega_2)t + \phi\right) \cdot \quad (2.17)$$

Now it is possible to solve the initial eq. (2.7) and eq. (2.8). The integral over $\rho^2 \cdot |A_1|^2$ and $\tau^2 \cdot |A_2|^2$ describes a constant (DC) power on the photodiode PD1, which can be expressed as

$P_{\text{DC,PD1}} = P_{1,\text{PD1}} + P_{2,\text{PD1}}$. In the same way one can compute the DC power on PD2. This DC power indicates the average power delivered by the laser beams on the corresponding PD. Accordingly, an oscillating (AC) power P_{AC} is given by the previously solved term and contains the phase information in the argument of the cosine [Müller, 2013]. The photocurrents become

$$I_{c,\text{PD1}} = \kappa \left(\underbrace{P_{1,\text{PD1}} + P_{2,\text{PD1}}}_{P_{\text{DC,PD1}}} - \underbrace{2\sqrt{\eta_{\text{PD1}} \cdot P_{1,\text{PD1}} \cdot P_{2,\text{PD1}} \cos((\omega_1 - \omega_2)t + (\varphi_1 - \varphi_2))}}_{P_{\text{AC,PD1}}} \right), \quad (2.18)$$

$$I_{c,\text{PD2}} = \kappa \left(\underbrace{P_{1,\text{PD2}} + P_{2,\text{PD2}}}_{P_{\text{DC,PD2}}} + \underbrace{2\sqrt{\eta_{\text{PD2}} \cdot P_{1,\text{PD2}} \cdot P_{2,\text{PD2}} \cos((\omega_1 - \omega_2)t + (\varphi_1 - \varphi_2))}}_{P_{\text{AC,PD2}}} \right). \quad (2.19)$$

In summary the entire photocurrent is made up of an AC and a DC part. In section 4.3 will be discussed how to extract the phase information ϕ from the photocurrent for the Gravity Recovery and Climate Experiment Follow On mission.

2.2 Effects of Relativity

The signals mentioned in the previous section are recorded as a time series. On-board clocks of current space missions allow to time-tag data very precisely. These clocks in space are measurably affected by relativistic effects. For comparing data between different spacecraft or with time-scales on Earth, it is necessary to take these effects into account.

2.2.1 General Aspects of Relativity

Albert Einstein postulated the constancy of the speed of light c already in 1905, which means that all information propagates only with a finite speed. In special relativity this results in the phenomenon of time dilation. It can be shown that a clock with time t' of a moving observer runs slower relative to a clock with time t in a stationary system, i.e. [Einstein, 1905]

$$\Delta t' = \Delta t \cdot \sqrt{1 - \left(\frac{v}{c}\right)^2}, \quad v < c. \quad (2.20)$$

Another effect, called gravitational red-shift, causes a frequency shift for clocks in a gravitational potential. Figure 2.2 illustrates the idea of gravitational red-shift: a photon with the wavelength λ propagates upwards from the gravitational potential at Earth's surface Φ_0 to the potential Φ_{rec} . Its wavelength becomes shifted to the longer (red) part of the spectrum, when it travels away from a gravitational source. Conversely, the wavelength is shifted into the blue part, when it moves towards a gravitating mass. It is emitted with a frequency of ν_0 and is detected at Φ_{rec} with a frequency of ν_{rec} . The formula for the Doppler effect, which describes the observed frequency, is [Maloney, 2017]

$$\nu_{\text{rec}} = \nu_0 \left(1 - \frac{\Delta\Phi}{c^2} \right) \quad (2.21)$$

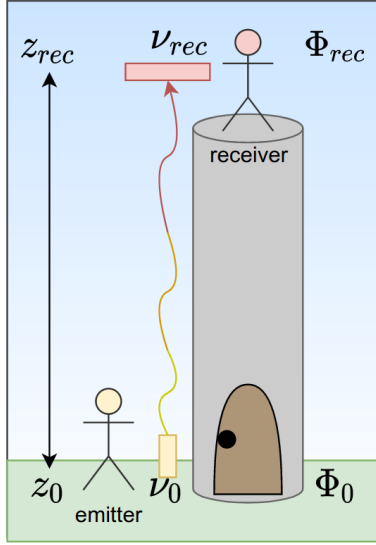


Figure 2.2: Principle of gravitational red-shift for a photon emitted on the Earth surface and detected at a higher gravitational potential.

with

$$\Delta\Phi > 0, \text{ for gravitational redshift}$$

$$\Delta\Phi < 0, \text{ for gravitational blueshift.}$$

Here, the difference of the potential is $\Delta\Phi = \Phi_{\text{rec}} - \Phi_0$. This frequency shift is inversely equal to a shifted clock rate. Consequently, the elapsed time intervals of a clock at the emitter position with time t , compared with a clock at the receiver with time t' can be written as

$$\Delta t' = \Delta t \frac{1}{\left(1 - \frac{\Delta\Phi}{c^2}\right)}. \quad (2.22)$$

This relation indicates that a clock on Earth ticks slower than an equal one in space. In fact, we can rewrite eq. (2.20) and eq. (2.22) and apply a Taylor expansion to get

$$\left(\frac{\Delta t'}{\Delta t}\right)_{\text{time dilation}} = \sqrt{1 - \left(\frac{v}{c}\right)^2} \approx 1 - \frac{v^2}{2c^2} \quad (2.23)$$

$$\left(\frac{\Delta t'}{\Delta t}\right)_{\text{redshift}} = \frac{1}{\left(1 - \frac{\Delta\Phi}{c^2}\right)} \approx 1 + \frac{\Delta\Phi}{c^2}. \quad (2.24)$$

Combining these effects allows to obtain the time-varying part of the total relativistic effect on clocks as

$$\frac{\Delta t'}{\Delta t} - 1 = \frac{\Delta\Phi}{c^2} - \frac{v^2}{2c^2}. \quad (2.25)$$

In this section, the special relativistic framework was used. In the next section the same effect is derived for general relativity.

2.2.2 Effects on Clocks in Low Earth Orbiters

Now we want to consider a four dimensional space-time for the Earth, i.e. considering general relativity. The Geocentric Celestial Reference System (GCRS) is a non-rotating coordinate system with its origin located in the Earth's geocenter. The GCRS is known as an Earth-centered inertial (ECI)¹ frame. The International Astronomical Union (IAU) recommendations ([IAU, 2000, Resolution B1.3]) define the GCRS with the elements of the metric tensor $g_{\mu\nu}$, with $\mu, \nu = 0, 1, 2, 3$ as

$$g_{00} = -1 + h_{00} = -1 + \frac{2V}{c^2} - \frac{2V^2}{c^4} + \mathcal{O}(c^{-6}) \quad (2.26)$$

$$g_{a0} = g_{0a} = h_{0a} = -\frac{4U^a}{c^3} + \mathcal{O}(c^{-5}) \quad (2.27)$$

$$g_{aa} = 1 + h_{aa} = 1 + \frac{2V}{c^2} + \mathcal{O}(c^{-4}), \quad (2.28)$$

where the index 0 denotes the time coordinate and $a = 1, 2, 3$ the spatial coordinates. This approach is also used by Yan et al. [2021]. $g_{\mu\nu}$ is the result of the Minkowski metric with

¹The GCRS is only a quasi-inertial frame due to the geodetic precession from Earth's rotation around the sun. The predicted effect is about 2 arcseconds per century. [Müller et al., 2008]

diag(-1,1,1,1) and a small perturbation $h_{\mu\nu}$ of the space-time, due to gravitation [Müller, 2017, Appendix B]. $V = V(t, \vec{x})$ denotes the scalar gravitational potential of the Earth at coordinates (t, \vec{x}) with the Geocentric Coordinate Time (TCG) and U^a is a vector potential. The common convention of geodesy is used, where the potential gets a positive sign ($V = -\Phi \approx GM/r$) [Moyer, 1979].

For further calculations only terms up to order c^{-2} will be kept. This approximation allows to compute the square of the line element ds as

$$ds^2 = \left(-1 + \frac{2V}{c^2}\right)(cdt)^2 + \left(1 + \frac{2V}{c^2}\right)(dx^2 + dy^2 + dz^2) . \quad (2.29)$$

This yields the increment $d\tau$ as [IAU, 1991, Recommendation I]

$$d\tau^2 = \frac{-ds^2}{c^2} \quad (2.30)$$

for the elapsed proper time of a clock. Dividing eq. (2.29) by $(cdt)^2$ and rewriting eq. (2.30) results in

$$\frac{d\tau^2}{dt^2} = - \left[\left(-1 + \frac{2V}{c^2}\right) + \left(1 + \frac{2V}{c^2}\right) \frac{(dx^2 + dy^2 + dz^2)}{(cdt)^2} \right] . \quad (2.31)$$

It was shown by Moyer [1979] that the last term can be expressed with the velocity $v^2 = (dx^2 + dy^2 + dz^2)/dt^2$. The resulting term of $2Vv^2/c^4$ is dropped and the square-root is computed with a Taylor expansion, to derive

$$\frac{d\tau}{dt_{\text{TCG}}} = \sqrt{1 - \frac{2V}{c^2} - \frac{v^2}{c^2}} \approx 1 - \frac{V}{c^2} - \frac{v^2}{2c^2} . \quad (2.32)$$

As it was mentioned in the beginning, the corresponding coordinate time is given by the TCG, which provides the proper time of a clock in absence of any gravity potential ($V = 0$) [Puetzfeld and Lämmerzahl, 2019]. In this thesis, the measurements are usually in the Global Positioning System (GPS) time, so we have to adjust the theoretical calculation from eq. (2.32) by another coordinate time. The GPS time and the Coordinated Universal Time (UTC) as well, are defined by the International Atomic Time (TAI), i.e. [ESA, 2011]

$$\text{TAI} = \text{GPS time} + 19 \text{ seconds} = \text{UTC} + \text{leap seconds} . \quad (2.33)$$

Another related time frame is the Terrestrial Time (TT) [ESA, 2011]

$$\text{TT} = \text{TAI} + 32.184 \text{ seconds} \quad (2.34)$$

which gives the time in SI seconds on Earth's geoid. Obviously it is necessary to scale the current coordinate time from TCG into TT, because TCG does not consider the Earth's gravitational potential. Thus, it ticks faster than a comparable clock on the geoid. The relation between TT and TCG is given by the gravitational potential (Φ_0) on Earth's geoid and was defined by the IAU as [IAU, 2000, Resolution B1.9]

$$\frac{dt_{\text{TT}}}{dt_{\text{TCG}}} = 1 + \frac{\Phi_0}{c^2} = 1 - 6.969290134 \cdot 10^{-10} . \quad (2.35)$$

Since, GPS time and the coordinate time in TT are referring both to Earth's geoid, the ratio $d\tau/dt_{\text{TT}}$ has to be closer to 1 than $d\tau/dt_{\text{TCG}}$. Consequently, we add the term $-\Phi_0/c^2$, which yields [Ashby, 2003]

$$\frac{d\tau}{dt_{\text{TT}}} = 1 + \frac{\Phi(\vec{r}) - \Phi_0}{c^2} - \frac{v^2}{2c^2} . \quad (2.36)$$

The second term considers the difference between the gravitational potential at a satellite's position \vec{r} and a reference clock resting on the geoid. This effect was introduced as gravitational red-shift in section 2.2.1. The third term results from a second order Doppler effect, due to the relative velocity of the moving clock in the satellite and the resting one at Earth. It is equivalent to the effect of time-dilatation presented in eq. (2.20) [Larson et al., 2007]. As expected, eq. (2.36) is consistent with the result from eq. (2.25).

Further calculations use an approximation for the gravitational potential [Ashby, 2003]

$$\Phi(\vec{r}) = -\frac{GM}{r} \left[1 - J_2 \left(\frac{a_e}{r} \right)^2 \cdot \left(\frac{3z^2}{2r^2} - \frac{1}{2} \right) \right], \quad (2.37)$$

where the first term gives the potential of the central field at $r = \sqrt{x^2 + y^2 + z^2}$ based on satellite coordinates in an ECI frame. The second term considers the effect of a flattened Earth by the J_2 coefficient. The product GM are the gravitational constant and the mass of the Earth. The radius of the Earth is denoted by a_e and the third component of the position vector is described with z .

We estimate the magnitude for the drift of the proper time of the satellite w.r.t. GPS time using eq. (2.36). The speed of light in vacuum is denoted with c , $GM = 3.986 \cdot 10^{14} \text{ m}^3/\text{s}^2$, $a_e = 6371 \text{ km}$, $J_2 = 1.08 \cdot 10^{-3}$, $v = 7600 \text{ m/s}$, $r = 6371 + 490 \text{ km}$ and assuming a value for $z = z_{\max} \approx r$, i.e.

$$\frac{d\tau}{dt_{TT}} - 1 = - \underbrace{\frac{GM}{rc^2}}_{6.5 \cdot 10^{-10}} + \underbrace{\frac{GM}{rc^2} \cdot J_2 \left(\frac{a_e}{r} \right)^2 \cdot \frac{3z^2 - r^2}{2r^2}}_{6 \cdot 10^{-13}} - \underbrace{\frac{v^2}{2c^2}}_{3.21 \cdot 10^{-10}} - \underbrace{\frac{\Phi_0}{c^2}}_{-7 \cdot 10^{-10}} \approx -0.27 \cdot 10^{-9}. \quad (2.38)$$

As a consequence, the proper time of such a satellite clock in a LEO and with the time coordinate in terrestrial time is approx. 9 ms behind an equal clock at Earth's geoid after one year. Obviously this effect is small, but section 6.5 will show that it is relevant.

2.2.3 Light Travel Time

A laser interferometer in space, where satellites exchange the light between each other, requires consideration of relativistic effects for the flight time of a photon. The photons are traveling through the same space-time, as it was introduced with eq. (2.26) to eq. (2.28). Thus, their paths are also affected by time-dilation and gravity. Yan et al. [2021] derive the relation between the line element ds and the infinitesimal propagation time dt as

$$dt = \frac{n}{c_n} ds = \frac{1 + 2 \cdot V/c_0^2 - 4 \cdot \vec{U} \cdot \vec{d}_0/c_0^3}{c_0} \cdot n \cdot ds + \mathcal{O}(c^{-5}) \quad (2.39)$$

with the normalized vector \vec{d}_0 for the propagation direction, n the refractive index and c_n denotes the coordinate speed of light in GCRS frame. Integrating along the photon's path \mathcal{P} yields the light propagation time \mathcal{L} , i.e. [Yan et al., 2021]

$$\mathcal{L} \approx \int_{\mathcal{P}} \frac{ds}{c_n(t, \vec{r})} + \frac{1}{c_0} \int_{\mathcal{P}} (n - 1) ds = \mathcal{L}_{\text{rel}} + \mathcal{L}_{\text{media}}. \quad (2.40)$$

The propagation time of a photon, which is going through the medium of the neutral atmosphere and the ionosphere of the Earth, is described with the second term $\mathcal{L}_{\text{media}}$. In the low

Earth orbit of approx. 500 km altitude the refractive index of neutral atmosphere is similar to that of vacuum, hence it is negligible [Yan et al., 2021]. However, the ionosphere, which is a specific layer in the atmosphere, contains free electrons. Thus, the refractive index has to be considered. Due to the frequency dependency of the refractive index, the result depends on the wavelength of the photon. Nonetheless, this correction is not necessary for laser interferometry at a wavelength of $\lambda = 1064$ nm, but the effect has to be taken into account for microwaves [Müller, 2017].

The term of \mathcal{L}_{rel} in eq. (2.40) is caused by relativistic effects using contributions of special relativity (SR) and general relativity (GR), such that the light travel time can be written as

$$\mathcal{L}_{\text{rel}} = \Delta\tau_{\text{SR}} + \Delta\tau_{\text{GR}} . \quad (2.41)$$

The term of general relativistic effects is defined as

$$\Delta\tau_{\text{GR}} = \Delta t_{\text{PM}} + \Delta t_{\text{HM}} + \Delta t_{\text{SM}} , \quad (2.42)$$

where Δt_{PM} is the effect caused by Earth's central field, Δt_{HM} considers the higher moments of the gravitational potential, and Δt_{SM} embodies the time-delay due to the spin moment of the Earth [Müller, 2017].

The term for special relativity can be divided into a time delay Δt_{inst} , which results from the instantaneous range between two satellites T and M, at the time of photon reception t_r and an additional correction term, such that [Yan et al., 2021]

$$\Delta\tau_{\text{SR}} = \frac{|\vec{r}_T(t_r) - \vec{r}_M(t_r)|}{c_0} + \Delta t_{\text{SR}} = \Delta t_{\text{inst}} + \Delta t_{\text{SR}} , \quad (2.43)$$

where Δt_{SR} denotes the travel time of the photon in a flat space-time without gravity. Inserting eq. (2.42) and eq. (2.43) into eq. (2.41) yields the light travel time

$$\mathcal{L}_{\text{rel}} = \Delta t_{\text{inst}} + \Delta t_{\text{SR}} + \Delta t_{\text{PM}} + \Delta t_{\text{HM}} + \Delta t_{\text{SM}} \quad (2.44)$$

$$\mathcal{L} \stackrel{\text{eq. (2.40)}}{\approx} \mathcal{L}_{\text{rel}} = \Delta t_{\text{inst}} + \mathcal{T} , \quad (2.45)$$

where all correction terms from special and general relativity are summarised in \mathcal{T} , which is the so-called Light Time Correction (LTC). The formulas for computing the individual parts of the LTC are presented in detail by Yan et al. [2021] in section 3.

The Laser Ranging Interferometer of GRACE Follow-On operates between two distant spacecraft, called master and transponder (cf. chapter 4). In section 4.3, it will be shown that the ranging information can be extracted by using the phase measurement from both satellites. A signal emitted on the transponder satellite, propagates to the master. The measurement which is taken at the emitting event at transponder, has to be compared with the arriving event of the signal at the master. That means

$$\varphi_{\text{LRI}} = \varphi_T(t_M - \mathcal{L}_{\text{TM}}) - \varphi_M(t_M) , \quad (2.46)$$

where the timing information of the transponder is adjusted to the master, by considering the light propagation time (eq. (2.45)) for the path of transponder \rightarrow master (TM). These relations are also introduced by the LRI light time product in appendix B.5. Additionally, the light time correction $c_0\mathcal{T}_{\text{TWR}}$ for the two-way ranging principle of the LRI will be discussed in section 4.3, which corrects for the ranging error also caused by the effect of the light travel time.

3

GRACE Follow-On Satellites

This chapter presents the two satellite missions Gravity Recovery and Climate Experiment (GRACE) and GRACE Follow-On (GFO). General properties and working principles are discussed in section 3.1. Additionally, there is included an explanation for the gravity anomaly maps, which are the final results from GRACE and GFO data processing. Furthermore, a few on-board instruments of GFO are introduced. Section 3.2 discusses the institutions which are responsible for the official data processing and how the data is divided into different main “Levels”. Afterwards in section 3.3, follows the description for the processing units and how to convert between their different time information in general.

3.1 Mission Overview

The pair of identical satellites of the GRACE mission was operating from 2002 until 2017. They were orbiting on a nearly polar orbit in an altitude of approximately 500 km. The GRACE A and GRACE B spacecraft (S/C) were flying behind each other in a separation of 220 km. This mission collected data for the gravity field determination, by measuring the inter-satellite distance changes with a Microwave-Instrument [Tapley et al., 2004b].

The distance variations are converted to maps of gravity anomalies by using several processing steps (cf. section 3.2.1). These maps show the differences between a theoretical ellipsoidal model for Earth’s gravity and the actual gravity field. These differences are given in the units of mGal. 100 mGal are equal to 1 mm/s^2 [Müller, 2017].

Figure 3.1 illustrates some features of the Earth, where the yellow and red areas indicate locations with a stronger field than average. Noticeable heights at the Earth’s surface are for example the Himalaya mountains close to India (cf. left globe fig. 3.1) or the Andean mountains in South-America (cf. right globe fig. 3.1). Here, the gravity anomaly shows values up to +50 mGal. The other extreme can be found in the Indian Ocean, which is sketched in a dark blue valley. Blue and green areas represent the places, where gravity is weaker than average. In these cases the gravity anomalies reach minimal values of -50 mGal .

Those maps are created from data of approx. 30 days, which is the usual update rate for the maps, because the satellites need to sample the complete world fine enough. Many researches

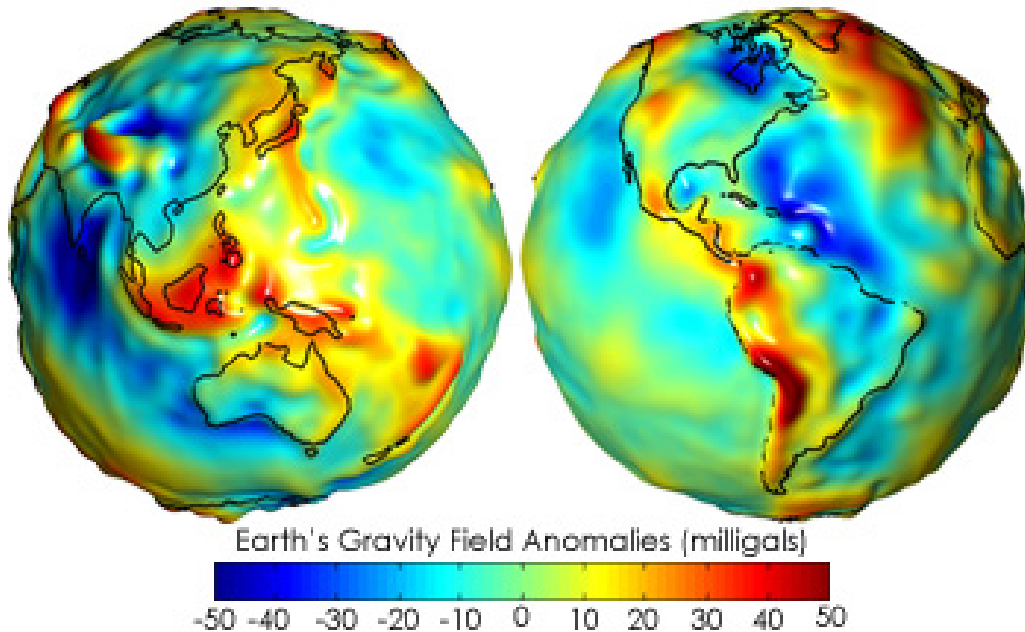


Figure 3.1: Gravity anomaly maps from GRACE and GRACE-FO data processing show the difference of a simplified model of Earth's gravity field and the actual one. Especially noticeable are features like the Himalaya mountains (+50 mGal) or the region at the Indian Ocean (-50 mGal). Picture from [NASA \[2004\]](#).

used the GRACE data for generating similar maps, to investigate parts of the time variable gravity field i.e. changes in sea level and groundwater storage, glacier and ice melting at the polar caps [[NASA, 2004](#)].

For continuing this useful data recording, the GRACE Follow-On (GFO) mission was launched on May 22, 2018. The new satellites GRACE C and GRACE D, also called GF1 and GF2, are very similar to their predecessors. They also use a nearly polar orbit with an inclination of 89° and an altitude of 500 ± 10 km (in 2020). GF1 and GF2 are following each other with a separation of 220 ± 50 km and are orbiting the Earth in approximately 94.6 minutes (January 2019). This constellation allows to retrieve monthly gravity solutions for the whole globe. GFO hosts updated versions of the original instruments from GRACE and also a new technology demonstrator, the Laser Ranging Interferometer (LRI). It measures the inter-satellite distance variations, just like the MWI, but with a lower noise [[Abich et al., 2019](#)]. The LRI will be presented in more detail in chapter 4.

The distance variations between the moving S/C arise from non-gravitational and gravitational forces. The latter one are the desired quantity and will be measured by the satellites as follows. When the satellite pair fly over a region with a higher mass, just like the Himalaya region, it causes first a higher acceleration of the leading S/C 1 and the distance increases. When the leading S/C crossed that area and leaves the mountain behind, it is slowing down. At the same time, the second S/C is accelerated due to the mass concentration at the Earth below, and the inter-satellite distance decreases. After both have passed this region the distance will increase again, because the second one is also slowing down due to the higher attraction backwards [[Misfeldt, 2019](#)].

Accelerometer The non-gravitational forces include for example, atmospheric drag, solar radiation pressure, thruster activations and more [Müller, 2017]. To remove the non-gravitational effects from the ranging measurements, it is necessary to measure them using accelerometers, these are located at the center of mass at each S/C. In principle, they observe linear and angular accelerations, caused by the undesired disturbances. Over the mission time the center of mass shifts slightly, for example by using the propellant of the satellites. Therefore, it is necessary to adjust it occasionally to the reference points of the accelerometers by moving trim masses [Misfeldt, 2019].

Star Camera Assembly One method to determine the orientation of the satellites in an inertial frame is to use star cameras. These instruments take digital images from the sky and compare them with a star catalogue in order to identify the camera head orientation. After the internal processing they can provide the attitude angles as a set of quaternions [Frommknecht, 2007].

The star tracker of GRACE Follow-On have (in comparison to GRACE) three camera heads to avoid blinding of all heads from moon and sun at the same time [Müller, 2017].

Microwave Instrument (MWI) The Microwave Instrument (MWI) is the primary science instrument on GRACE-Follow-On and measures the inter-satellite distance via dual one-way ranging (DOWR) [Wen, 2019], where each spacecraft sends two signals in the frequency range of microwaves to the other one. They operate with the 24 GHz K-band and with the 32 GHz Ka-band for estimating the refraction effect of the ionosphere of the Earth [ESA eoPortal]. This K-Band Ranging (KBR) concept achieves a noise level of approximately 1 to $2\ \mu\text{m}/\sqrt{\text{Hz}}$ [Müller, 2017] for Fourier frequencies larger than $0.176\ \text{mHz}$ ($= 1/(94.6\ \text{min})$), which correspond to the orbital frequency in January 2019.

3.2 Science Data Sytsem

The Science Data System (SDS) consists of various organizations, namely Jet Propulsion Laboratory (JPL), University of Texas, Center for Space Research (UTCSR) and Geoforschungszentrum Potsdam (GFZ). Several responsibilities are distributed among them, which include the processing, archiving, verifying and providing the GRACE Follow-On data to the public [Wen, 2019].

3.2.1 Levels of Data Processing

SDS divides the data processing in four major levels, which are explained in the text below.

Level 0: Level 0 is the raw telemetry of the satellites and forms the base. This data includes measurements or sensor values in a binary format. Additionally, Level 0 includes internal instrument data, however, this is omitted in the subsequent levels. The raw telemetry is assigned to two different categories, they are called science (VC4) and housekeeping (VC2) data [Wen, 2019].

Level 1: Level 1 is the first generated data product by processing the Level 0 data. The processing of Level 1 is divided into Level 1A and Level 1B. Level 1A is obtained from a 'non-destructive' process, because it is possible to go back to Level 0 by applying an inverse data processing. Only some internal instrument data cannot be reconstructed, because it is only

used in Level 0 and not available for the higher levels of processing. For Level 1A the data is reformatted from binary to ascii files and the measurements are converted to engineering units. The high data rate of Level 1A is downsampled and filters are applied for Level 1B. Furthermore, the data is re-tagged to GPS time and calculations for variables of interest are performed here, for example the biased range and CNR [Wen, 2019].

The currently available data products for Level 1 by SDS are named release 04 (RL04) or version 04 (v04).

Level 2: Monthly solutions of Level 1B data are used for estimating spherical harmonic coefficients of the Earth’s gravitational potential [GFZ, 2018]. This Level 2 includes precise orbit solutions [Wen, 2019] and shows monthly gravity field anomalies. For example maps like shown in fig. 3.1 can be generated.

Level 3: In this step Level 2 is converted to surface mass anomalies and geographical corrections and processing filters are utilised [Wen, 2019]. The data is mapped on a geographical grid and shows for instance hydrology maps.

3.3 Time Frames and Processing Units

On board each satellite are build in different processing units, i.e. the Instrument Processing Unit (IPU), the On-Board Computer (OBC), and the Laser Ranging Processor (LRP). All of them have their own clock, which are referring to an Ultra Stable Oscillator (USO) or to a quartz oscillator. At certain time intervals the different clocks are synchronised with each other. These clocks are different realizations of the GPS time, and their time information can be converted into one of the other as it is shown in fig. 3.2. The next subsections will present the units in more detail and explain the illustrated paths of time-conversion.

3.3.1 Global Positioning System

The satellites of GFO are equipped with antennas for GPS. The GPS receivers allow to track the positions, velocities and times of the satellites in their orbit around the Earth with respect to the Earth surface [JPL, 2018]. This concept is called High-Low Satellite-Satellite Tracking (SST), where a satellite in a lower Earth orbit is tracked from the GPS satellites in a much higher orbit. Together with the measurements of the inter-satellite distance from MWI or LRI, which is known as Low-Low-SST, it is possible to determine effects of gravity on the two S/C [Misfeldt, 2019].

GPS time → GrGPS time The GPS time is illustrated in the lower left part of fig. 3.2, which serves as the time frame to time-tag all measurements and telemetry. The GPS time refers to the epoch of January 6th, 1980, 00:00:00, while the so-called GRACE GPS time (GrGPS time) counts seconds past January 1st, 2000, 12:00:00. The difference between GPS and GrGPS time is a constant number, i.e.

$$\text{GrGPS time_tag} = \text{GPS time_tag} - 630\,763\,200\text{s} \quad (3.1)$$

can be used for converting GPS to GrGPS time information [Wen, 2019]. In chapter 6 and appendix B will be shown that the GrGPS time is the preferred reference epoch to depict the processed data of GRACE Follow-On measurements.

3.3.2 Ultra Stable Oscillator

One USO within each spacecraft, is used to drive clocks in LRP and IPU. This relation is shown by the green timing arrows between the boxes of USO, LRP and IPU in fig. 3.2. The frequencies of these Oven Controlled Quartz Oscillators (OCXOs) are [Misfeldt, 2019]

$$f_{\text{OCXO,GF1}} = 4832000\text{Hz} \quad (3.2)$$

$$f_{\text{OCXO,GF2}} = 4832099\text{Hz} . \quad (3.3)$$

By using an electrical frequency multiplication these values are increased to the USO frequencies of [Misfeldt, 2019]

$$f_{\text{USO,GF1}} = 8 \cdot f_{\text{OCXO,GF1}} = 38\,656\,000\text{Hz} \quad (3.4)$$

$$f_{\text{USO,GF2}} = 8 \cdot f_{\text{OCXO,GF2}} = 38\,656\,792\text{Hz} . \quad (3.5)$$

These are the internal clock rates and are used for sampling KBR, LRI and GPS phase measurements [Wen, 2019]. In this thesis they are also notated with `clock_rate`.

3.3.3 Instrument Processing Unit

The Instrument Processing Unit (IPU) is responsible for processing GPS and KBR measurements as well as for the star camera attitude quaternions [ESA eoPortal].

IPU receiver time → GPS time As shown in fig. 3.2 the IPU receiver (`rcv`) time is synchronised with the GPS time after every IPU reboot (green arrow), to compensate for drifts by the USOs w.r.t. GPS time. Moreover, the resulting offset between GPS and IPU time is recorded in the CLK1B data product as `eps_time` and can be used to convert measurements from the IPU into GPS time (blue arrow) [Wen, 2019].

The CLK1B of v04 data is reported every 10 seconds and is derived from precise orbit determination using GPS. Together with the included IPU `rcv` time-tags in GrGPS seconds, one can derive

$$\text{GPS time} = \text{IPU rcv time} + \text{CLK1B}_{\text{eps_time}} . \quad (3.6)$$

In general, `eps_time` shows a drift between IPU and GPS, however, by detrending this result one can archive a plot as shown in fig. 3.5. On February 1st in 2021, we can observe 1/rev and 2/rev oscillations, and an additional 2/day oscillation, which will be discussed in section 6.5.1.

3.3.4 On-Board Computer

The On-Board Computer (OBC) handles the onboard data and storage, and e.g. it is responsible for the attitude and orbit control system, for the thermal control system and as well as for the downlink of the data [Kornfeld et al., 2019]. The OBC also adds the timing information to the measurements, which do not belong to the GPS, KBR [Wen, 2019] or LRI.

OBC time → IPU rcv time From fig. 3.2 one can see that the OBC time uses an independent quartz oscillator, in order to have a time reference, even when the other units e.g. IPU or LRP are switched off. However, this quartz oscillator is less accurate in comparison to the USO [Misfeldt, 2019]. For longer time spans that would lead to a drift in the OBC time w.r.t. to GPS or IPU `rcv` time.

The OBC measures the difference between its internal clock and the IPU `rcv` time (USO clock)

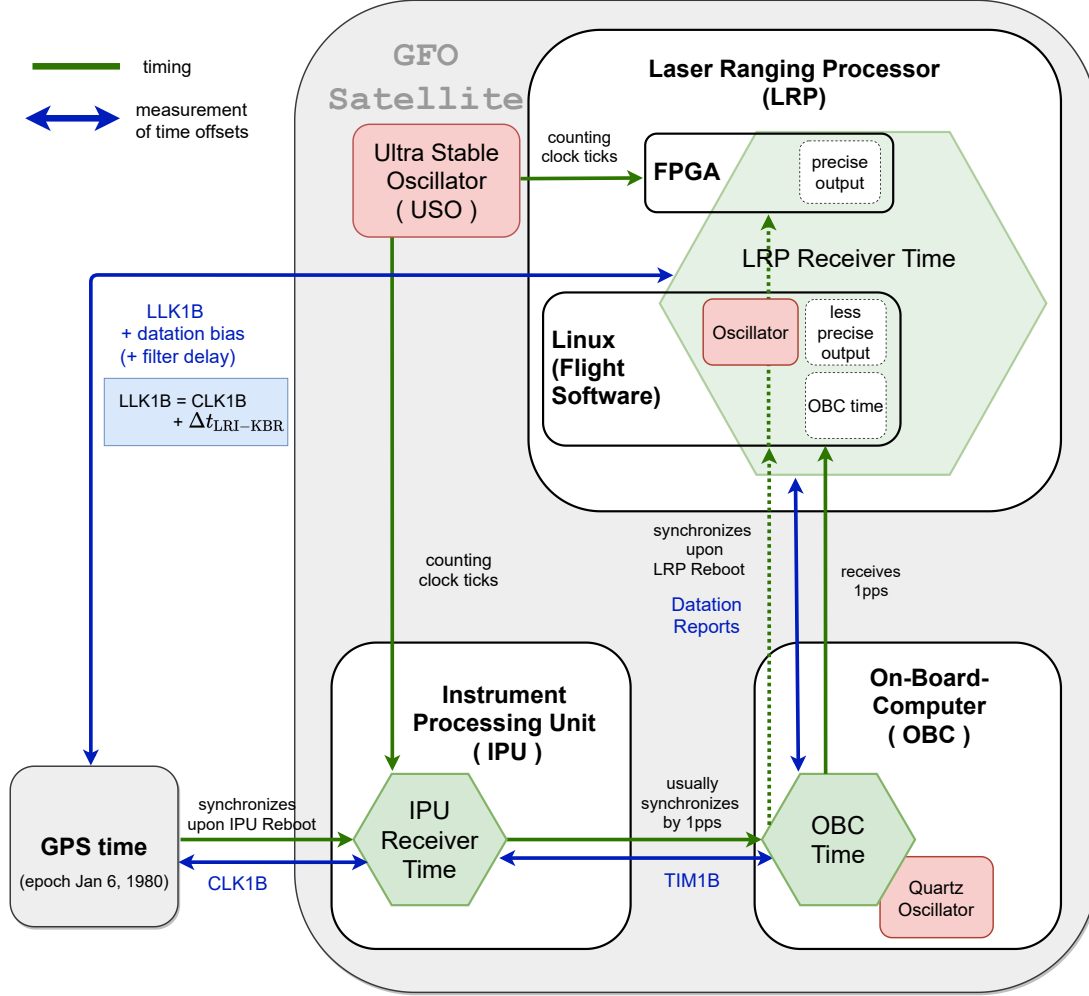


Figure 3.2: Visualisation of different time frames and time conversions on the satellites. The white boxes are representing the different units and the green hexagons the corresponding clocks. They are running with different oscillators, which are shown in red. For converting between the time frames, the data products shown by the blue arrows has to be applied to the measurements to be converted.

by 1-per-second pulses (1pps), which is shown by the green arrow in fig. 3.2. The TIM1B v04 data product gives this mapping between IPU rcv time and OBC time every 8 seconds [Wen, 2019], but most of the time this offset is close to zero, because the OBC oscillator is steered towards the IPU rcv time. However, the derived offset from TIM1B ($TIM1B_{offset}$) shows a quantization noise of a few hundred nanoseconds. This is illustrated in fig. 3.4 for February 1st, 2021.

If TIM1B is not available, the $TIM1B_{offset}$ can usually be set to zero, i.e. the column for the OBC time in GrGPS seconds will be used as the IPU rcv time. The IPU rcv time in TIM1B contains a fractional part in nanoseconds, which needs to be converted to seconds for further calculations. Deriving the clock offset between IPU rcv time and OBC time can be performed as follows:

$$TIM1B_{offset} = IPU \text{ rcv time} - OBC \text{ time} . \quad (3.7)$$

3.3.5 Laser Ranging Processor

The Laser Ranging Processor (LRP) is the main computing engine of the LRI and handles all the data streams, which will be discussed in detail in section 5.1. We assume that the LRP is divided into two systems, i.e. the LRP processor, which executes a linux operating system, and the LRP FPGA. FPGA means field-programmable gate array, and it is optimised for recording the LRI phase measurements with high precision.

Figure 3.2 shows that the LRP receiver time has two different outputs for a precise and less precise time-tagging. The reason for that is, the USO drives the clock of the FPGA, which allows a precise time-tagging e.g. for the LRI phase measurements. Additionally, there are some less time-critical data streams, i.e. where microsecond or millisecond accuracy is sufficient. They receive their time-tags from the operating system (JPL calls it Flight Software).

LRP receiver time → OBC time One can see from fig. 3.2 that the LRP internal clocks are synchronised with the OBC time after every LRP reboot. After the reboot the FPGA is only synchronised once, while the operating system will still receive a 1pps signal from the OBC. With this signal the LRP is able to calculate the OBC time itself (priv. comm. C. Woodruff, JPL, Aug 2021). This time information with integer second accuracy is also used for time-tagging data (cf. section 5.1).

Every LRP reboot leads to a change in the offset between OBC and LRP time, which is reported in the Datation Reports (DTRs). This offset is also called datation bias and it remains constant until the next LRP or IPU restart up to some hundred nanosecond readout uncertainty (e.g. on February 1st, 2021 it is approximately $0.3\mu\text{s}$, cf. fig. 3.3). In general, the DTR offset is smaller than $\pm 1.5\text{ s}$ [Wen, 2019].

For getting the offset between LRP and OBC time, one has to extract the Datation Reports (DTR) from the `gis1` files (cf. section 5.2), or use the ‘Iridatation’ event from the SOE (Sequence of Events) file of SDS. DTRs are reported irregularly up to a few times per day, i.e. two times per day for 2018 until 2020-12-14 and afterwards ≈ 25 times per day.

The DTRs contain an integer part for the OBC time given as the days passed since 1980-01-06 00:00:00 (start of GPS epoch). This value is multiplied by 86400 seconds, to convert the day into GPS seconds and it is combined with the reported millisecond value on that day to obtain the total OBC time in GPS format.

The corresponding LRP time-tags, reported in that packets as well, are also divided into an integer and fractional part. The latter one is given in clock ticks, which needs to be divided by the `clock_rate` to obtain seconds. Now the offset between OBC time and LRP rcv time can be computed as

$$\text{DTR}_{\text{offset}} = \text{OBC time} - \text{LRP rcv time} . \quad (3.8)$$

Finally, it should be noted that some special cases such as LRP and IPU reboots have to be considered. At these reboots the $\text{DTR}_{\text{offset}}$ is changed, due to the synchronisation of the different clocks (cf. fig. 3.2). Additionally, one has to pay attention if a DTR was recorded immediately after the IPU reboot, because the OBC time may not have adjusted to the new IPU rcv time in that moment. This would lead to a wrong DTR offset.

3.3.6 General Time Conversion

A conversion of a given LRI time-tag in LRP rcv time is possible by using the presented products as follows:

$$\text{GPS time_tag} = \text{LRI time_tag} + \text{DTR}_{\text{offset}} + \text{TIM1B}_{\text{offset}} + \text{CLK1B}_{\text{offset}} (+\Delta t_{\text{filter}}) . \quad (3.9)$$

The filter delay

$$\Delta t_{\text{filter,phase}} [s] = 28802038 \text{ clock ticks}/\text{clock_rate} \quad (3.10)$$

has to be considered in case of LRI phase measurements and

$$\Delta t_{\text{filter,I\&Q}} [s] = 3999960 \text{ clock ticks}/\text{clock_rate} \quad (3.11)$$

for I&Q values [Wen, 2019]. This option of time-tag correction is shown by the blue path at the bottom of fig. 3.2.

The second possibility, illustrated by the upper left path in fig. 3.2, uses the LLK1B data product. It includes the time offsets from CLK1B and an additional estimated time offset $\Delta t_{\text{LRI-KBR}}$ per day. $\Delta t_{\text{LRI-KBR}}$ is derived from a cross-calibration with KBR and LRI data, so that the difference between the two data sets is minimized [Wen, 2019]. Deriving such a time shift will be explained in more detail in section 6.9. This option of time-tag correction requires also the knowledge of the datation bias, such that

$$\text{GPS time_tag} = \text{LRI time_tag} + \text{LLK1B} + \text{datation_bias} (+\Delta t_{\text{filter}}) . \quad (3.12)$$

We will discuss the implementation of the time-tag conversion at AEI in section 6.4.

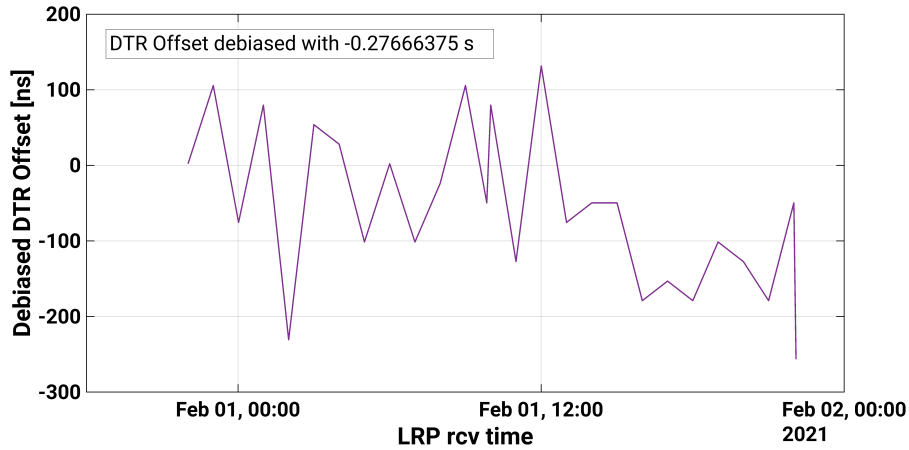


Figure 3.3: Datation Report Offset of GF1 on Feb 1st, 2021. A readout uncertainty of $\approx 0.3\mu\text{s}$ are observed.

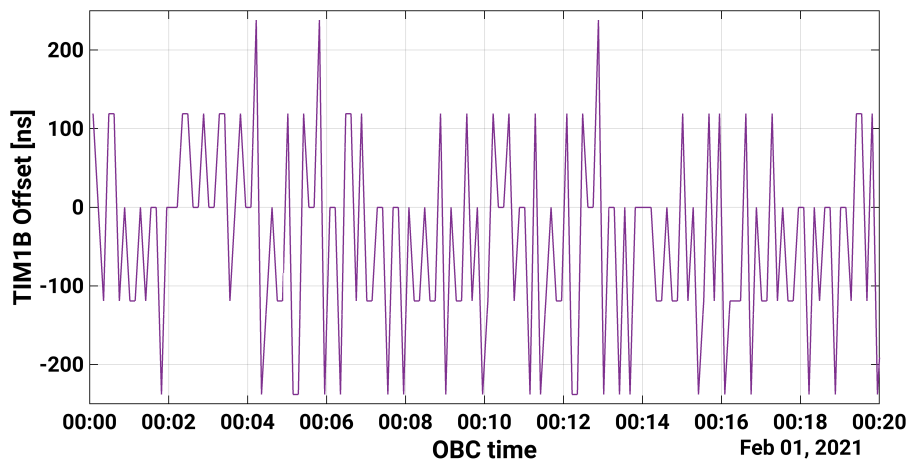


Figure 3.4: TIM1B Offset for GF1 on Feb 1st, 2021. It shows a quantization noise of a few hundred nanoseconds.

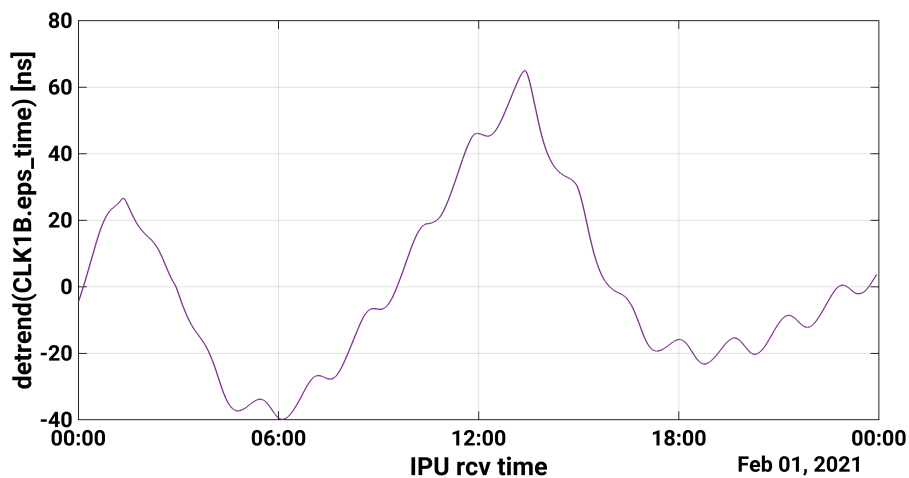


Figure 3.5: Detrended `eps_time` value for GF1 on Feb 1st, 2021. A 2/day pattern and the 1/rev and 2/rev oscillations are observed, which will be discussed in more detail in section 6.4 and section 6.5.1.

4

Laser Ranging Interferometer

The Laser Ranging Interferometer (LRI) is the first operating laser interferometer between distant satellites. It was designed as a technology demonstrator for future space-missions, e.g. for Next Generation Gravity Missions (NGGM) or the Laser Interferometer Space Antenna (LISA). [Abich et al. \[2019\]](#) have shown that the LRI noise is below its requirement of $80 \text{ nm}/\sqrt{\text{Hz}}$ for Fourier frequencies above 30 mHz. Clearly, the LRI has a lower noise level than the Microwave Instrument (MWI) (cf. section 3.1).

This chapter conveys the idea for taking measurements of the inter-satellite distance changes with this new instrument. The setup of this Laser Ranging Interferometer is explained in section 4.1. Furthermore, the different components forming an interferometer are presented. In the next section 4.2 the lightpath of the LRI and the resulting beatnote frequencies at the two spacecraft are explained. Afterwards, the resulting measurements and how the ranging information can be derived is pointed out in section 4.3. Finally the so called Carrier to Noise Ratio is introduced in section 4.4.

4.1 LRI Instrument Setup

Figure 4.1 provides an overview of the LRI setup and how it is operating. All instrument units of the LRI are integrated at both satellites, because they should be interchangeable between the role of master and transponder spacecraft (S/C). In case of fig. 4.1 the S/C 1 is in master role and S/C 2 has the transponder role. In this thesis S/C 1 and S/C 2 are also called GF1 and GF2.

Moreover, the diagram comprises the paths and directions of the laser beams, illustrated by the red lines and arrows. Especially noticeable is the “racetrack” [[Sheard et al., 2012](#)] configuration of the LRI. This racetrack was necessary because GRACE Follow-On is in principle a rebuild of the GRACE mission. The Line of Sight (LOS), which is the connecting line between the Center of Mass (COM) of the two satellites, is already occupied by the K/Ka-Band Ranging (KBR) antennas and by cold gas tanks (they are not shown in fig. 4.1). For that reason the LRI was built as an off-axis laser interferometer [[Sheard et al., 2012](#)]. The next subsections present some of the most important units and conveys the working principle of the LRI.

4.1.1 Laser and Cavity

Both S/C hosts a laser with a Nd:YAG (Neodymium doped Yttrium Aluminium Garnet) laser crystal in a non-planar ring oscillator (NPRO) configuration. These lasers were built by Tesat-Spacecom. The fibre coupled laser light has an optical power of 25mW and a wavelength of 1064nm, which is equivalent to a frequency of $\nu \approx 281$ THz. The master lasers frequency is stabilised by locking the laser to an optical cavity. Each satellite has one cavity manufactured by Ball Aerospace [Abich et al., 2019], but only the master S/C makes use of it. In fig. 4.1 at S/C 1 the laser and cavity are summarised as “stabilised master laser”. The frequency of the transponder laser is controlled by a Frequency-Locked Loop (FLL). The FLL ensures that the frequency of the transponder laser is following the received frequency from the master plus a 10 MHz offset, i.e. the transponder laser frequency is always larger than the master laser frequency ($\nu_M < \nu_T$). Using the transponder laser also ensures that the beam is enhanced in power, before sending the beam back to the master S/C (cf. section 4.2) [Misfeldt, 2019].

4.1.2 Fast Steering Mirror

For the following explanation one can have a look at the visualisation of the different beam paths in fig. 4.2.

The Fast Steering Mirror (FSM) ensures a precise pointing between the two S/C and an alignment between local oscillator (LO) beam and the received (RX) beam, which comes from the remote S/C, regardless of spacecraft attitude jitter. This jitter is $\approx 300\mu\text{rad}$ [Misfeldt, 2019]. However, the LRI only requires a coalignment error below $10\mu\text{rad}$ between the LO and RX beam [Schütze et al., 2014b], such that an active beam steering is necessary. Therefore, the FSM is rotatable around two axes. It is necessary that LO beam and RX beam are parallel, for achieving a transmitted (TX) beam, which is then anti-parallel to the RX beam, due to Triple Mirror Assembly properties (see section 4.1.3 below).

The position where the interferometric contrast is maximized and where the relative tilt between RX and LO beam becomes close to zero, are measured by the Differential Wavefront Sensing (DWS) technique [Schütze et al., 2014b]. For this measurements a multi-section photodiode (= Quadrant Photodiode (QPD)) is necessary, which is hit by two interfering beams, potentially with a relative angular tilt to each other. Due to this tilt the linear combination of the phase segments are different. The vertical and horizontal direction, i.e. the DWS signals, can be computed from [Misfeldt, 2019]

$$\text{DWS}_v = \frac{(\Phi_1 + \Phi_2) - (\Phi_3 + \Phi_4)}{2} \quad (4.1)$$

$$\text{DWS}_h = \frac{(\Phi_1 + \Phi_3) - (\Phi_2 + \Phi_4)}{2} . \quad (4.2)$$

The indices $i = 1\dots 4$ indicate the phase measurement on the four QPD segments. The exact definition of Φ_i will be introduced in section 4.3. When both DWS signals are zero, then the two beams are parallel to each other. This is the reason why the DWS signals are used by the Steering Mirror control loop, to maintain the optimal mirror position and the optimal interferometric contrast [Misfeldt, 2019].

4.1.3 Triple Mirror Assembly

An arrangement of three mirrors routes the laser beam around the components of the MWI and cold gas tanks. They are called Triple Mirror Assembly (TMA) and can be found next

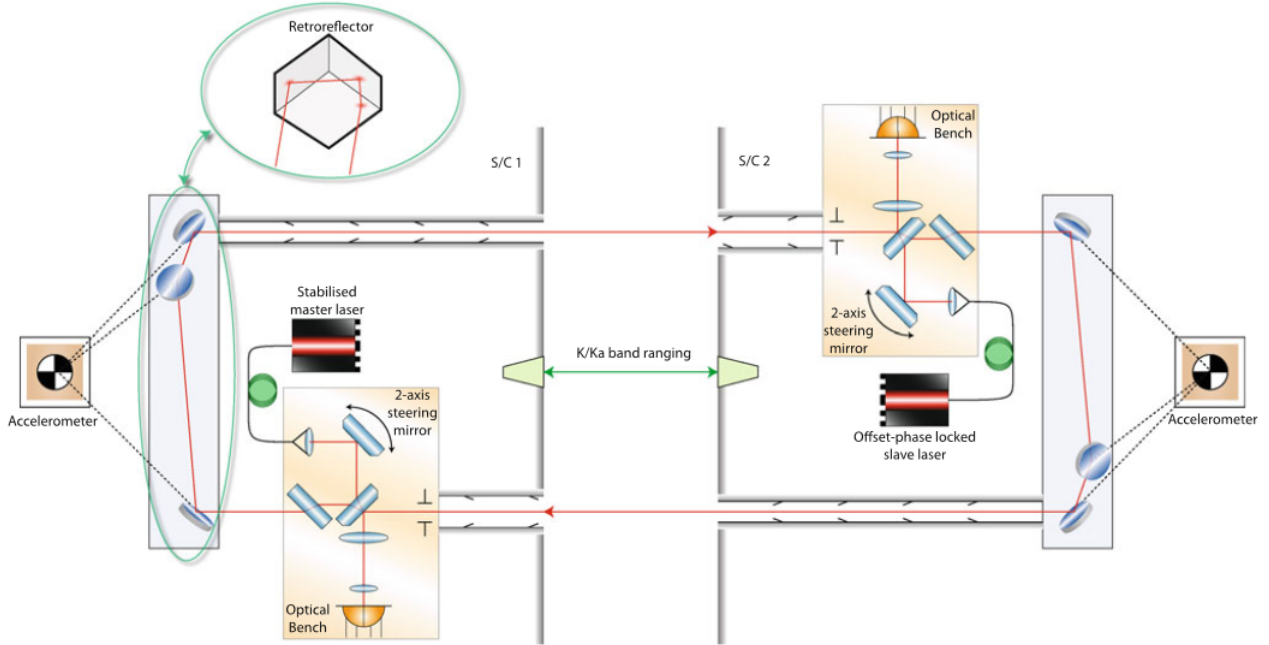


Figure 4.1: Overview of the Laser Ranging Interferometer setup. S/C 1 on the left side acts as master, while S/C 2 takes the transponder role. The Triple Mirror Assemblies route the laser beams around other components (on the LOS) to achieve this off-axis configuration. The Fast Steering Mirrors ensure a precise pointing between the locally generated laser beams and the received ones. The recombination beamsplitter deflects the beams to the corresponding QPD on each S/C, where a beatnote signal is measured. Image taken from Sheard et al. [2012, Reprinted by permission from Springer Nature Customer Service Centre GmbH].

to the accelerometers in fig. 4.1. The intersection point of these mirrors is called Vertex Point (VP) and is located in the S/C center of mass. The TMA ensures that the lateral shift between incoming and outgoing beam is always 600 mm, especially under satellite rotations. Another feature of this corner cube reflector (or retro reflector) arrangement is that the outgoing and incoming beam are anti-parallel [Schütze et al., 2014a].

The ranging measurement of the LRI refers to the distance between the locations of the vertex points. As mentioned before, they are co-aligned with the center of mass. However, the mounting into the satellite is only possible with an accuracy of $\approx 100\mu\text{m}$ [Wegener et al., 2020]. Therefore, the distance between the two S/C center of mass is slightly different to the distance between the two TMA vertex points. This difference in distance has a static offset and a dynamic effect when the satellites are rotating. The resulting offset in the ranging measurement is called Tilt-To-Length (TTL) coupling and is described by Wegener et al. [2020].

4.2 Lightpath of the LRI

The laser light traveling inside the interferometer and how the arriving signals are composed on each S/C will be explained within this section. An illustration of the emerging frequencies in the LRI lightpath are shown in fig. 4.2. The stabilised master laser generates light with the frequency ν_M^M , where the lower index denotes the origin of the emitted light and the upper index on which spacecraft it is detected. The beam of the master laser hits the beamsplitter, where it is separated into the LO beam and a TX beam (cf. fig. 4.2 lower left side). While

the LO beam goes to the QPD, the TMA shifts the TX beam by 600 mm and sends it to the transponder. On that path, the TX beam with frequency ν_M^M experiences a Doppler shift, due to the relative velocity of the satellites. The Doppler shift f_D reads

$$f_D \approx -\nu_M^M \frac{\dot{\rho}}{c_0} \quad (4.3)$$

with the relative velocity $\dot{\rho}$ (w.r.t. the LOS) and the speed of light c_0 . With a relative velocity of 1 m/s the Doppler shift has a magnitude of approx. -1 MHz [Misfeldt, 2019]. Therefore the arriving frequency at the transponder S/C is

$$\nu_M^T = \nu_M^M \left(1 - \frac{\dot{\rho}}{c_0}\right). \quad (4.4)$$

This approximation does not consider effects from transversal velocity and also the atmospheric density is assumed to be very close to zero. The LRI was designed to cope a few hundred picowatts, but because of the higher CNR, we know that at the transponder currently (2018-2021) arrives a power of ≈ 1 nW of the initial power of 25 mW [Sheard et al., 2012]. Therefore it is necessary to amplify the light power, before sending it back to the master S/C. This is achieved by the active-transponder principle, where the LO beam of the transponder has the frequency ν_T^T and interferes with the TX beam ν_M^T on the QPD. The Frequency-Locked Loop (FLL) regulates the laser frequency of the transponder, such that the frequency ν_T^T of the local oscillator is equal to the RX beam with ν_M^T up to a 10 MHz constant (f_{off}), i.e.

$$\nu_T^T = \nu_M^T + f_{\text{off}} = \nu_M^M \left(1 - \frac{\dot{\rho}}{c_0}\right) + 10 \text{ MHz} . \quad (4.5)$$

This yields the beatnote frequency (f_T) at the transponder's QPD as

$$f_T = \nu_T^T - \nu_M^M = 10 \text{ MHz} + \delta f_{\text{off}} , \quad (4.6)$$

where δf_{off} summarises all frequency noises, which results for example from imperfections and limitations of the FLL.

Next, the recombination beamsplitter (at fig. 4.2 upper right side) redirects the transponder laser beam to the TMA. The TMA inverts the beam direction and send it back to the master. This path leads to a second Doppler shift for the RX beam, which has approx. the same magnitude as the first one, because master and transponder frequency differ only in f_{off} . That means

$$-\nu_T^T \frac{\dot{\rho}}{c_0} \quad f_{\text{off}} \ll 281 \text{ THz} \quad \approx \quad -\nu_M^M \frac{\dot{\rho}}{c_0} \quad (4.7)$$

and yields an arriving optical frequency at the master S/C as

$$\nu_T^M = \nu_T^T + f_{\text{off}} + f_D . \quad (4.8)$$

The resulting beatnote f_M at the master's QPD is

$$f_M = \nu_T^M - \nu_M^M \quad (4.9)$$

$$= \nu_M^M + f_D + f_{\text{off}} + f_D - \nu_M^M \quad (4.10)$$

$$= f_{\text{off}} + 2 \cdot f_D + \delta f . \quad (4.11)$$

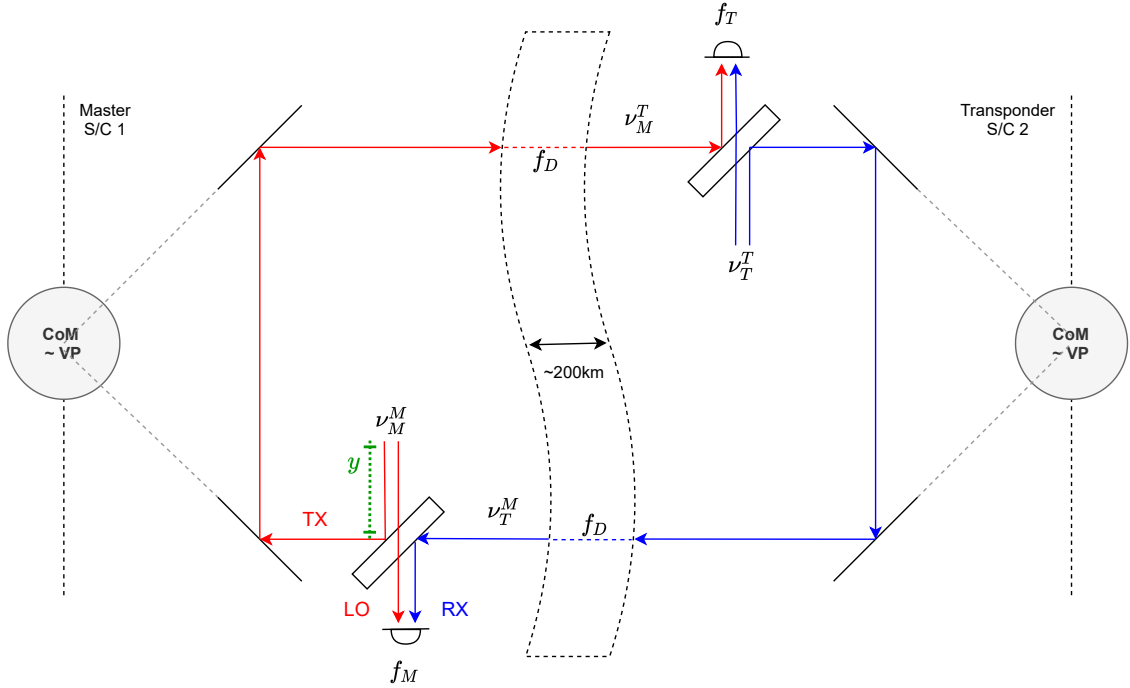


Figure 4.2: Lightpath of the LRI and emerging frequencies. The master laser's frequency ν_M^M experiences a Doppler shift f_D by traveling to the distant transponder. The transponder laser produces light with a frequency that follows the frequency of the incoming light and adds a 10 MHz offset via a Frequency-Locked Loop. The resulting beatnote frequency on the transponder is $f_T \approx 10$ MHz. The transponder laser's frequency is also Doppler shifted after traveling back to the master. The resulting beatnote frequency at the master is $f_M \approx 10 \text{ MHz} + 2f_D$.

The term $\delta f = \delta f_{\text{off}} + \delta f_{\nu_M} + \delta f_y$ represents the resulting noise from different sources. It is composed of the already mentioned FLL noise, the residual laser frequency noise of the master, and the path length changes on the optical bench which occur on the path of y in fig. 4.2. The latter one is negligible, while the laser frequency noise is one of the dominating noise sources that affects the phase measurement [Sheard et al., 2012]. Equation (4.11) shows the relation between the masters beatnote frequency and the changes in the inter-S/C distance. The frequency can be converted into a phase, which can be measured from a phase meter, by integrating the frequency in time. The next section is taking up this point.

4.3 Relation of Phase Measurement and Instantaneous Range

Equation (2.19) has shown the resulting photocurrent on a single element photodiode. Now we are able to apply it for the measurements on the satellites. The built-in photodiodes of the LRI are QPDs, which have active areas that are divided into four segments, instead of one single element. Their responsivity for a wavelength of 1064 nm is approximately $\kappa = 0.7 \text{ A/W}$ [Mahrdt, 2014].

The frequency term of $\omega_1 - \omega_2$ can be replaced by $2\pi \cdot f_b$, with the beatnote frequency f_b .

Therefore, the photocurrent for one QPD segment $i = 1, 2, 3, 4$ reads [Mahrdt, 2014]

$$I_i = \kappa \left(P_{i,LO} + P_{i,RX} + 2 \underbrace{\sqrt{\eta_i P_{i,LO} P_{i,RX}} \cos(2\pi f_b(t)t + \phi_i(t))}_{\varphi_i(t)} \right), \quad (4.12)$$

where the indices in eq. (2.19) are replaced with the notation for the LO beam and the RX beam. The phases φ_i are measured by a phasemeter and can be averaged over the four quadrants.

The transponder beatnote phase φ_T results from the optical phase $\psi_{LO,T}$ of the local oscillator beam of the transponder and from the received beam $\psi_{RX,T}$, which was sent by the master. With the light travel time of eq. (2.45) for the distance from master to transponder, the beatnote phase, which is the phase representation of the beatnote frequency in eq. (4.6), can be written as [Yan et al., 2021]

$$\varphi_T = \psi_{LO,T}(t) - \psi_M(t - \mathcal{L}_{MT}(t)) = 10\text{MHz} \cdot \tau_T^{\text{USO}}(t) + \delta\psi_{\text{off}}(t) + \text{const.} \quad (4.13)$$

where τ_T^{USO} denotes the local LRP time-tags of the transponder and $\delta\psi_{\text{off}}$ the noise of the FLL. The constant results from integrating the beatnote frequency into a phase. It embodies the unknown start value, which explains why only changes in the phase or range are observable and not the absolute distance between S/C 1 and S/C 2. When the transponder sends the light to the master S/C, the beatnote phase yields [Yan et al., 2021]

$$\varphi_M(t) = \psi_{LO,T}(t - \mathcal{L}_{TM}) - \psi_M(t) \quad (4.14)$$

$$\begin{aligned} &= \psi_M(t - \mathcal{L}_{TM} - \mathcal{L}_{MT}) - \psi_M(t) \\ &+ 10\text{MHz} \cdot \tau_T^{\text{USO}}(t - \mathcal{L}_{TM}) + \delta\psi_{\text{off}}(t - \mathcal{L}_{TM}) + \text{const.} . \end{aligned} \quad (4.15)$$

The phase subtraction in the first line of eq. (4.15) can be written as the integral of the master laser frequency for the time of emitting $t_e = t - \mathcal{L}_{TM} - \mathcal{L}_{MT}$ until time of reception $t_r = t$, i.e.

$$\psi_M(t_e) - \psi_M(t_r) = \int_{t_r}^{t_e} \nu_M dt \approx -\nu_M \cdot \int_{t_e}^{t_r} dt = -\nu_M \cdot (\mathcal{L}_{TM} + \mathcal{L}_{MT}), \quad (4.16)$$

where the frequency changes of ν_M in the period between t_e and t_r were assumed to be small, so that we can write the frequency in front of the integral. We also divide the master frequency into a constant DC part and small variations $\nu_M = \langle \nu_M \rangle + \delta\nu_M$, such that

$$\varphi_M(t) \approx -(\langle \nu_M \rangle + \delta\nu_M) \cdot (\mathcal{L}_{TM} + \mathcal{L}_{MT}) + 10\text{MHz} \cdot \tau_T^{\text{USO}}(t - \mathcal{L}_{TM}) + \delta\psi_{\text{off}}(t - \mathcal{L}_{TM}) + \text{const.} \quad (4.17)$$

shows the phase representation of the master's beatnote frequency in eq. (4.11).

One can partly remove $\delta\psi_{\text{off}}$ from the master measurement, by forming the phase difference of transponder and master phase, i.e.

$$\varphi_{\text{LRI}} = \varphi_T(t - \mathcal{L}_{TM}) - \varphi_M(t). \quad (4.18)$$

An implementation of this computation will be discussed in more detail in section 6.5. In general, this LRI phase can be converted to a one-way range by using the approach of

$$\rho_{\text{LRI}} = \frac{\lambda}{2} \varphi_{\text{LRI}} + \text{const.} . \quad (4.19)$$

The factor of $\lambda/2$ is necessary to convert the LRI phase in units of cycle into a range in meter for the half round-trip. 1 cycle is equivalent to $\approx 1 \mu\text{m}$ when using a wavelength of $\lambda = 1064 \text{ nm}$. However, at the AEI, we use a time-dependent absolute laser frequency $\nu(t) = c_0/\lambda(t)$ of the master laser to convert the phase to a range (cf. section 6.9) as

$$\rho_{\text{LRI}}(t') = \int_0^{t'-\Delta t} \frac{c_0}{2 \cdot \nu(t)} \cdot \dot{\varphi}_{\text{LRI}}(t) dt, \quad (4.20)$$

where the time delay Δt is composed of $\Delta t_{\text{LRI-KBR}} + \Delta t_{\text{CRN}}$, which will be discussed later in section 6.9 and section 6.10.

The two conversion approaches of eq. (4.19) and eq. (4.20) are visualised in fig. 4.3 when a time-dependent frequency with three levels and a constant relative velocity of 1 m/s between the satellites is assumed. The expected measured range ρ , derived from the phase, should be a smooth line that reaches 90 m after 90 s.

However, by using the simple conversion from eq. (4.19), one gets the red curve in the lower subplot. Obviously, the different laser frequency steps lead to jumps in the range. Computing the range as shown with eq. (4.20) yields the green curve without jumps. The reason for that is, the laser frequency and the phase rate show the same steps, such that they cancel each other out by an element-wise multiplication of $\dot{\varphi}(t) \cdot c_0/(2\nu(t))$. Therefore, the expected range can be achieved with the integration approach from eq. (4.20).

Furthermore, the phase meters of GRACE Follow-On derive frequencies (phase rates in the so-called phase increment register). Therefore, it seems reasonable to do this in the same way. The AEI team uses the conversion of eq. (4.20) to compute the continuous biased range in section 6.9.

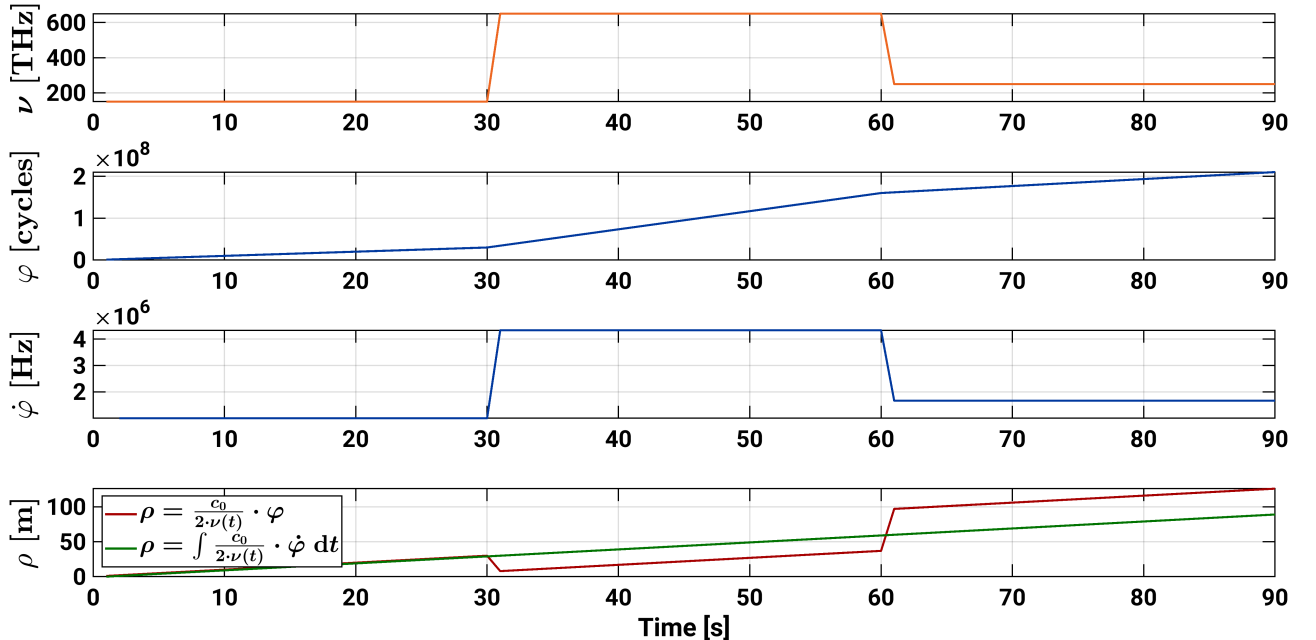


Figure 4.3: Applying the time-dependent absolute laser frequency onto the phase measurement yields a biased range (red curve) with frequency steps. This can be avoided by forming the time derivative of the phase, multiplying the resulting phase rate and conversion factor and integrating this range rate to a continuous biased range (green trace). The phase and phase rate are computed as $\varphi = \int \dot{\varphi} dt$ and $\dot{\varphi} \approx 2 \cdot \frac{\dot{\rho} \cdot \nu(t)}{c_0}$.

The resulting one-way range or also called biased range needs to be corrected by the light time correction, for getting the instantaneous range between the gravitational reference points (of the two S/C) at the same time. This distance is shown by the blue line in fig. 4.4. Assuming that the estimated absolute laser frequency ν_M^{est} is static allows to write the biased range as [Yan et al., 2021]

$$\rho_{\text{LRI}} = c_0 \int_0^t \frac{1}{2 \cdot \nu_M^{\text{est}}(t')} \cdot \frac{d}{dt'} \left(\varphi_T(t' - \mathcal{L}_{\text{TM}}) - \varphi_M(t') \right) dt' \quad (4.21)$$

$$\approx c_0 \cdot \frac{(\langle \nu_M \rangle + \delta \nu_M) \cdot (\mathcal{L}_{\text{TM}} + \mathcal{L}_{\text{MT}})}{2 \cdot \langle \nu_M^{\text{est}} \rangle} + \text{const.} \quad (4.22)$$

Additionally, we expand the first bracket in eq. (4.22) with $+\langle \nu_M^{\text{est}} \rangle - \langle \nu_M^{\text{est}} \rangle$ and replacing the light travel times with eq. (2.45), i.e.

$$\rho_{\text{LRI}} \approx c_0 \cdot \left(\frac{\langle \nu_M^{\text{est}} \rangle}{\langle \nu_M^{\text{est}} \rangle} + \frac{\langle \nu_M \rangle - \langle \nu_M^{\text{est}} \rangle}{\langle \nu_M^{\text{est}} \rangle} + \frac{\delta \nu_M}{\langle \nu_M^{\text{est}} \rangle} \right) \cdot \left(\frac{2 \cdot \Delta t_{\text{inst}} + \mathcal{T}_{\text{TM}} + \mathcal{T}_{\text{MT}}}{2} \right) + \text{const.} \quad (4.23)$$

$$= (1 + \kappa) \cdot \left(\underbrace{c_0 \cdot \Delta t_{\text{inst}}}_{\rho_{\text{inst}}} + c_0 \cdot \underbrace{\frac{\mathcal{T}_{\text{TM}} + \mathcal{T}_{\text{MT}}}{2}}_{\mathcal{T}_{\text{TWR}}} \right) + \text{const.} \quad (4.24)$$

Here, κ summarises the error terms of an incorrect estimated laser frequency and the laser frequency noise. These errors are negligible for the light time correction of this two-way ranging (TWR) principle [Yan et al., 2021]. Therefore,

$$\rho_{\text{LRI}} = \rho_{\text{inst}} + c_0 \mathcal{T}_{\text{TWR}} + \text{const.} \quad (4.25)$$

where \mathcal{T}_{TWR} denotes the light time correction for converting between biased range and instantaneous range. Rewriting eq. (4.25) yields the instantaneous range as

$$\rho_{\text{inst}} = \rho_{\text{LRI}} - c_0 \mathcal{T}_{\text{TWR}} + \text{const.} \quad (4.26)$$

For the detailed computation of \mathcal{T}_{TWR} , as it is implemented in the AEI processing, the reader is referred to Yan et al. [2021].

It should be noted that $c_0 \mathcal{T}_{\text{TWR}}$ is needed for the LRI1B product in chapter 6. This LTC will be inserted as $-c_0 \mathcal{T}_{\text{TWR}}$ to be consistent with SDS data products. Consequently, one needs to compute the instantaneous range from LRI1B data by using

$$\rho_{\text{inst}} = \rho_{\text{LRI}}^{\text{LRI1B}} + (c_0 \mathcal{T}_{\text{TWR}})^{\text{LRI1B}} + \text{const.} \quad (4.27)$$

Furthermore, the light travel times \mathcal{L}_{TM} and \mathcal{L}_{MT} for the red paths in fig. 4.4 are needed for the LLT1A data product, which is presented in appendix B.5.

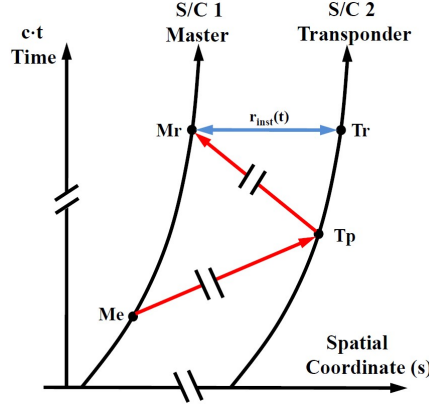


Figure 4.4: Principle of TWR measurement. Due to the finite speed of light a longer distance between the S/C is measured. The biased range is usually defined as half of the distances from Me to Tp and from Tp to Mr . To get the corrected or instantaneous range ($\rho_{inst} = r_{inst}$) it is necessary to apply the light time correction. Image from Yan et al. [2021] under Creative Commons CC BY license.

4.4 Carrier to Noise Ratio

From the QPD readout one can derive information about the quality of the signal. This Carrier to Noise Density Ratio or Carrier to Noise Ratio (CNR) can be computed from the noise power spectral density (PSD) and from the signal's Root Mean Square (rms) power at the beatnote frequency as [Müller, 2017]

$$\text{CNR} = \frac{\text{Signal RMS Power}}{\text{Noise PSD}} . \quad (4.28)$$

The CNR has units of Hz, but is usually expressed in the decibel regime (dB-Hz) [Müller, 2017]. The LRI is designed to work with a CNR above 70 dB-Hz [Abich et al., 2019]. At a lower CNR cycle slips may occur and the laser link between master and transponder may get interrupted. In order to obtain the signal power and the noise level a Fast Fourier Transform (FFT) algorithm is performed on the sum of the four QPD channels. The amplitude of the highest peak in this spectrum is stored as `fftSNR`. Furthermore, a noise estimation for the noise in the frequency bands between 8...9 MHz and 11...12 MHz is provided, which are called `noise8_9` and `noiese11_12`.

With these values we can rewrite eq. (4.28) into [Misfeldt, 2019]

$$\text{CNR} = 20\log_{10}\left(\frac{\sqrt{10^4} \cdot \text{fftSNR}}{\min(\text{noise8_9}, \text{noiese11_12})}\right) \quad (4.29)$$

as long as the noise between 8...9 MHz and 11...12 MHz is comparable to white noise. Misfeldt [2019] showed that this approach leads to non-physical drops in the CNR, whenever the beatnote frequency goes more into the frequency band of 11...12 MHz. Usually the beatnote frequency is approx. at 10 MHz, but due to the relative velocity of the two spacecraft, a related Doppler shift can cause these shifts into regions of the two noise frequency bandwidths. If the beatnote enters the upper frequency noise band, then the noise will be estimated wrong and results in a falsified CNR.

Therefore, an enhanced CNR computation was integrated into the processing at AEI, derived from diagnostic data. A beatnote frequency dependent noise model is estimated by using a linear interpolation between the two noise bands, i.e.

$$\text{noise}(f_b) = \frac{\langle \text{noise11_12} \rangle - \langle \text{noise8_9} \rangle}{11.5 \text{ MHz} - 8.5 \text{ MHz}} \cdot (f_b - 8.5 \text{ MHz}) + \langle \text{noise8_9} \rangle . \quad (4.30)$$

The values $\langle \text{noise8_9} \rangle$ and $\langle \text{noise11_12} \rangle$ represent the nominal values of the two noise bands, which are assigned to the frequencies of 8.5 MHz and 11.5 MHz for deriving the slope (fraction) in eq. (4.30). With this new noise assumption the CNR reads [Misfeldt, 2019]

$$\text{CNR} = 20 \log_{10} \left(\frac{\sqrt{10^4} \cdot \text{fftSNR}}{\text{noise}(f_b)} \right) . \quad (4.31)$$

This version of the CNR has a sampling rate of 0.1 Hz and is used in one of the LRI data products (cf. section 6.11).

5

Raw Data Flow in GRACE Follow-On and AEI

The LRI data streams and the assignments of time-tags at the flying spacecraft (S/C) are presented in section 5.1. Additionally, section 5.2 shows how the Level 0 data is used at AEI. This information is especially necessary for the processing of Level 1A in appendix B and the subsequent processing steps for generating the LRI1B product, which will be discussed in chapter 6.

5.1 Data Generation on Spacecraft Level

In this section, the LRI data generation on the spacecraft level is explained in detail. All the important information is illustrated in fig. 5.1. In the left part of this flow chart, the time-relation between each processing unit is shown, which was already introduced in section 3.3. Now this knowledge should be connected with the assignment of LRP time-tags for different LRI data streams.

The LRI data is stored in different types of so-called Pus-Packets. PUS is a Packet Utilisation Standard and was developed by the European Space Agency (ESA). PUS is a standard for satellite telemetry (Tlm) and telecommands [Kaufeler, 1994]. All recorded LRI Pus-Packets are assigned to one of two major categories, which are shown in red and orange inside the LRP box in fig. 5.1. The virtual channel VC2 includes all the housekeeping data, whereas VC4 contains all the science data [Wen, 2019].

The reader is reminded that the LRP assigns time-tags with different precision (cf. section 3.3). The LRP box in fig. 5.1 contains a list with Pus-Packets in different-colored arrows to indicate that distinctions. Pus-Packets in the green arrow provide very precise time information, as compared to the yellow ones. The time-tags, for example of each sample in the `QuadPhotoreceiverTlm` (green arrow), are separated from each other by exactly 4000000 clock ticks which corresponds to a distance in time of ≈ 0.1035 s. In contrast to that, for example the `ADCSamples`, yield a time-tag jitter of a few milliseconds. Therefore, the `ADCSamples` are assigned, among others, to the yellow arrow in fig. 5.1. Furthermore, there are several packets, which are not time-tagged from one of the two presented outputs of the LRP receiver (rcv)

time. These are considered by the pink arrow.

When storing a Pus-Packet to the internal memory, it receives additionally a so-called Pus-Packet Time (`PusTime`) from the LRP. This time information has only a resolution of integer seconds and refers to the OBC time. However, this is not applicable for `BootMessages` (and the very first `EventReport` after them, also called `defaultBootMsg`), because this messages are produced before the LRP rcv time is initialized to the correct GPS second.

In the end each Pus-Packet is sent to the On-Board Computer (OBC). At the OBC box in fig. 5.1, these Pus-Packets are all summarised as LRI data. There also exist other instrument data, e.g. Microwave Instrument data or some general S/C telemetry, which contains for example GPS orbit positions, temperatures and voltages. All of these packets are organized in three larger files. Here, the VC2 and VC4 categories appear once again and an additional third type is introduced as Offred data. The Offred data contains the general S/C telemetry. It should be noted that the VC2 and VC4 data, also known as Level 0, are stored and transmitted as binary files.

Finally, these three data streams are transmitted at ground station passes. One pass means contact between the spacecraft and the ground station antenna. The two ground stations of the Deutsches Zentrum für Luft- und Raumfahrt (DLR) are used for most of the downlinking. They are located in Weilheim and Neustritz, Germany [Misfeldt, 2019].

The files are stored at the Raw Data Center (RDC) of the DLR and from there the AEI team downloads the Offred and the Level 0 data, which includes the housekeeping (VC2) and science telemetry (VC4). This compressed LRI data uses about 70 MB per day, which includes approx. 45 files per day.

5.2 Preparation of Level 0 Data at AEI

The Level 0 data is processed by the in-house developed `LriToolbox`, which formerly was called `gisparser Toolbox` [Misfeldt, 2019]. The next part should remind of important processing steps and some details for the time-tags of LRI data will be added.

In the beginning the LRI data is identified inside the VC2 and VC4 files. This is possible by reading the headers of each Pus-Packet, which contains an instrument identifier. This step allows to extract the LRI data and Pus-Header information. The included LRI Pus-Headers are forward from our `pusreader` to the `gisparser`, which is a subroutine of the `LriToolbox` [Misfeldt, 2019]. At the same time we are able to convert the binary LRI files into ascii files, by using the binary-to-text converter, which was provided by JPL to AEI. The generated ascii files are called `gis1` files and also run through our `gisparser`.

One of the main tasks of the `gisparser` is to parse the ascii `gis1` files and store them as binary MATLAB files (*.mat), as it is shown in fig. 5.2. Inside fig. 5.2 some details on the timing information of the data and how they are processed are also illustrated. This time-tag assignments will be explained in the following text. All calculations are processed pass-wise. Afterwards, the resulting data is combined to daily, three days and eight days accumulators. For further data processing of Level 1A (cf. appendix B) and 1B, e.g. generation of monthly LRI1B data sets, more days of accumulated data are used.

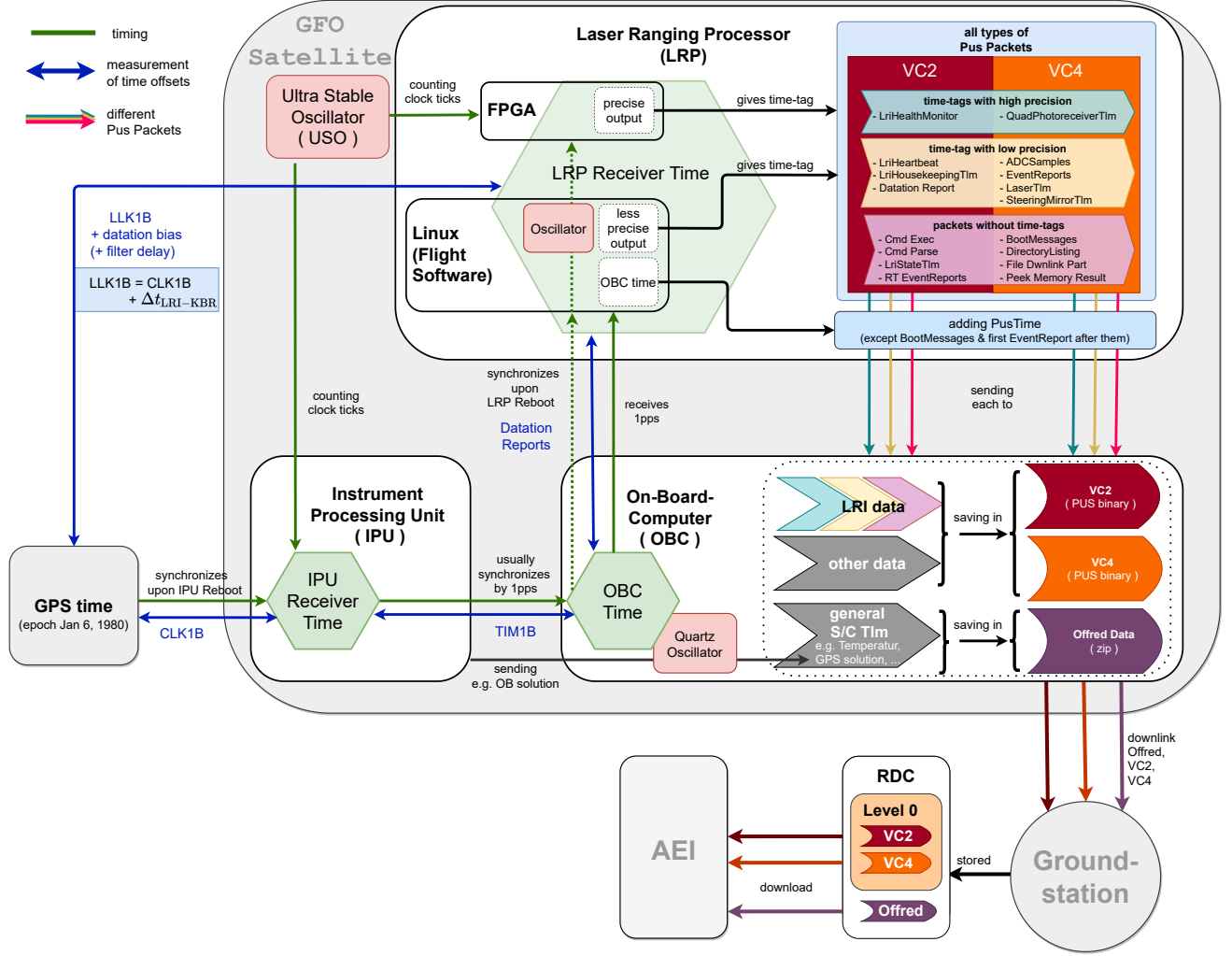


Figure 5.1: This flowchart illustrates the flow of raw telemetry on spacecraft level for LRI/LRP data. Time connections (on the left side) between different processing units were already explained in section 3.3.

Processing of LRP time-tags The green box in fig. 5.2 shows the assignment of time-tags for the different Pus-Packets, which were previously presented in the green, yellow and magenta arrow inside the LRP box, in fig. 5.1. All packets, highlighted in green and yellow (→), get an integer time-tag in GPS seconds and a fractional part in clock ticks from the LRP. These two time-tags are called TimeUp and TimeLow. Each sample of the ADCSamples, LriHousekeepingTlm, and LriHealthMonitor receive TimeUp and TimeLow information. For the LaserTlm (12 tuples per Pus-Packet) and SteeringMirrorTlm (30 tuples per Pus-Packet), only the last tuple inside one packet is time-tagged with TimeUp and TimeLow.

In these cases, the `gislparser` interpolates between the existing time-tags with the corresponding sampling frequency,

$$f_{\text{LaserTlm,GF1}} = \frac{f_{\text{USO,GF1}}}{38656000 \text{ clock ticks}} = 1 \text{ Hz} \quad (5.1)$$

$$f_{\text{LaserTlm,GF2}} = \frac{f_{\text{USO,GF2}}}{38656792 \text{ clock ticks}} = 1 \text{ Hz} \quad (5.2)$$

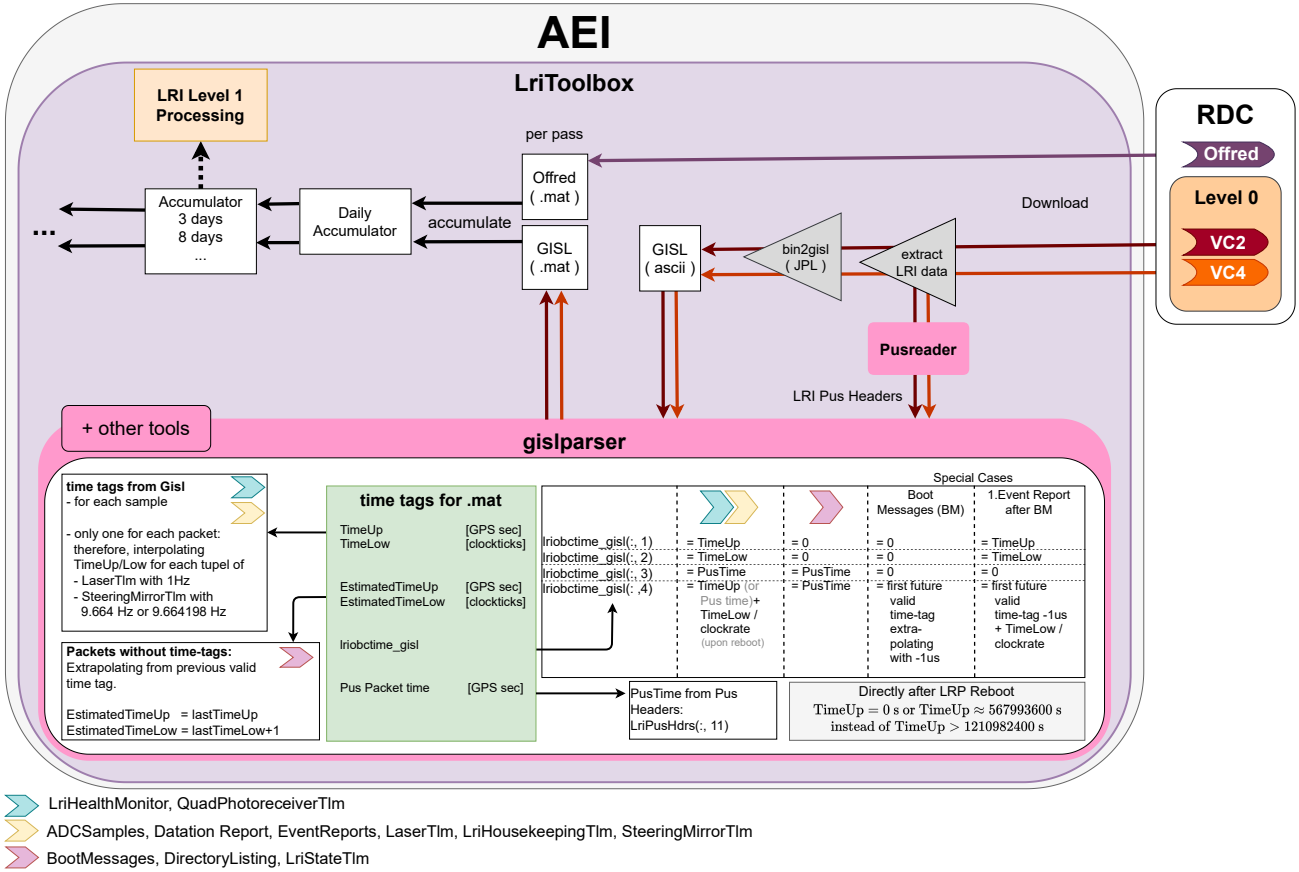


Figure 5.2: Illustration of time-tag assignment and when data is converted from so-called `gis1` files into binary files of MATLAB. The `lriobctime_gis1` variable contains different timing information from the `gis1` files, LRI Pus-Headers and a best guess time-tag for all telemetry packets. The calculation of `lriobctime_gis1` is summarised in the table on the right hand side.


$$f_{\text{FSM,GF1}} = \frac{f_{\text{USO,GF1}}}{4000000 \text{ clock ticks}} = 9.664 \text{ Hz} \quad (5.3)$$

$$f_{\text{FSM,GF2}} = \frac{f_{\text{USO,GF2}}}{4000000 \text{ clock ticks}} = 9.664198 \text{ Hz} \quad (5.4)$$

with f_{USO} from eq. (3.4) and eq. (3.5), such that each tuple inside a packet gets the timing information in form of `TimeUp` and `TimeLow`.


Magenta highlighted `gis1` packets (↗) get an `EstimatedTimeUp` and `EstimatedTimeLow` in the processing, because these ones only have the `PusTime`, but no time-tag in the `gis1` file. For the estimated time-tags the previous valid `TimeUp` and `TimeLow` are taken and incremented by 1 clock tick.

Best Guess Time-tag The green box in fig. 5.2 describes another variable inside our processing. The `lriobctime_gis1` can be interpreted as a table, where all the time-tags from `gis1` files and the `PusTime` are listed per sample, as well as an estimation for the best absolute time value is stored here. The right table in fig. 5.2 summarises the different compositions for different cases.

Computation of `lriobctime_gisl` for  Packets:

The first and second column show the original (and interpolated) `TimeUp` and `TimeLow` values. The third column contains the `PusTime`, which is in general equal to `TimeUp`. Column four contains the absolute time value for each sample. For green and yellow packets (cf. legend in fig. 5.2) it is usually the sum of `TimeUp` and `TimeLow/clock_rate`. Normal `TimeUp` values in GRACE Follow-On are larger than 1210982400 s, which corresponds to the epoch 2018-05-22 00:00:00. However, directly after a LRP reboot, `TimeUp` starts with 567993600 s and increases, because the LRP has not received a time-fix from the OBC yet. Thus, the calculation of `lriobctime_gisl` is done with the `PusTime` instead of `TimeUp` for using a correct integer time-tag. Especially for the generation of LRI Level 1A data products (cf. appendix B), this procedure ensures that the chronological order of data streams and messages maintained by sorting of `lriobctime_gisl(:,4)`. In summary we can write

$$\text{lriobctime_gisl}(\text{green_yellow_arrow}, 4) = \text{TimeUp (or PusTime)} + \text{TimeLow/clock_rate} . \quad (5.5)$$

Computation of `lriobctime_gisl` for  Packets:

The first two columns of `lriobctime_gisl` for magenta packets are zero, because they have no `TimeUp` and `TimeLow`. Therefore, column three and four are populated with the `PusTime`, i.e.

$$\text{lriobctime_gisl}(\text{magenta_arrow}, 3:4) = \text{PusTime} . \quad (5.6)$$

Special cases for `lriobctime_gisl` for some particular messages:

The affected messages in the following can be identified by their PUS type ‘19/3/1’.

BootMessages: One special case are the `BootMessages`, which occur after the LRP performs a restart. As mentioned in section 5.1 `BootMessages` have neither an integer and a fractional time stamp, nor the `PusTime`. It is necessary to estimate a time-tag first, by using a valid time-tag from the future and an extrapolation approach. If there exists N `BootMessages` their `lriobctime_gisl(i,4)`, with $i = 1 \dots N$ is computed in our processing as

$$\text{lriobctime_gisl}(i, 4) = \text{first_future_valid_time_tag} - 1\mu\text{s} \cdot (N + 1 - i) . \quad (5.7)$$

First EventReport after BootMessages: Another special case is the `defaultBootMsg` message “Rmgr::FsMgr: malloc gave:...” . It has a `TimeUp` and `TimeLow`, but `TimeUp` is not valid due to the mentioned reboot issue. This `EventReport` also does not have a `PusTime`. Therefore, `lriobctime_gisl(N + 1, 4)` uses the next valid integer time information minus $1\mu\text{s}$ and adds the original `TimeLow` information, such that

$$\begin{aligned} \text{lriobctime_gisl}(N + 1, 4) = & \text{first_future_valid_time_integer} - 1\mu\text{s} \\ & + \text{TimeLow/clock_rate} . \end{aligned} \quad (5.8)$$

6

Generation of AEI LRI1B v50 Product

The Albert-Einstein-Institut (AEI) was involved in designing and testing the Laser Ranging Interferometer of GRACE Follow-On. Moreover, the AEI team takes part in current operations and works on data analysis for this new instrument. Therefore, it is of great interest to determine new processing strategies and to improve algorithms to get the most information out of the data. In this chapter an alternative processing for the LRI Level 1B (LRI1B) product is shown. The implementation of a processing chain for this LRI1B product was one of the main tasks of the author of this thesis. This processing chain generates the data product and also compares the AEI version with the official v04 version of SDS. Additionally, all types of data gaps needed to be handled and a quality flag for special events was implemented. Besides that, some already existing tools like the `gislparsr` or the deglitching algorithm (cf. [Misfeldt, 2019]) are used inside the LRI1B processing as well. The AEI version of this data product is named v50, in order to not overlap with the SDS numbers (current release v04).

Section 6.1 presents the unwrapping and cleaning process of LRI raw phase measurements. Furthermore, different approaches for removing glitches from the LRI phase are discussed in section 6.2, section 6.3 and section 6.6, where section 6.7 visualises the results. Additionally, the implementation of converting LRP receiver time-tags into GPS time are explained in section 6.4. The computation of the LRI ranging phase from subtracting transponder and master phase is shown in section 6.5. Afterwards, the LRI biased range will be derived with the estimated absolute laser frequency from section 6.9. This data is low-pass filtered with a so-called CRN-filter (cf. section 6.10) and will be interpolated from a 10 Hz rate onto a 0.5 Hz time-grid (cf. section 6.11). Furthermore, the computation of the time derivatives of the biased range are introduced in section 6.12. The LRI1B v50 product contains a quality flag, where many events are indicated which might affect the quality of the ranging measurement. Some post-processing steps are necessary for including all of them (cf. section 6.13). Finally, section 6.14 gives a summary of all processing steps and shows the format of LRI1B v50.

6.1 Preparation of Raw Phase Data

Usually the Level 1A data is converted to Level 1B. However, in our processing it is easier to use the Level 0 data, due to already existing tools. The steps described here can also be performed with the LRI1A product. LRI1A is the main scientific Level 1A data product, because it contains the LRI phase measurements from `QuadPhotoreceiverTlm` and values for computing the CNR from `LriHealthMonitor` data. For more information about LRI1A the reader is referred to appendix B.1. Consequently, the processing for LRI1B v50 starts with the raw phase measurements from the `QuadPhotoreceiverTlm`.

Unwrapping The phase φ_M on the master satellite was given in eq. (4.15), which contains a 10 MHz phase ramp and the ranging signal. The transponder phase Φ_T in eq. (4.13), contains only the 10 MHz ramp and some other much smaller effects. Therefore, the 10 Hz phase measurement reads

$$\varphi_M(\tau_M^{\text{USO}}) \approx 10 \text{ MHz} \cdot \tau_M^{\text{USO}} + \text{ranging signal} + \text{other effects} \quad (6.1)$$

$$\varphi_T(\tau_T^{\text{USO}}) \approx 10 \text{ MHz} \cdot \tau_T^{\text{USO}} + \text{other effects} . \quad (6.2)$$

Here, the indices M and T mark to which S/C time frame the data refers. Therefore, τ_T^{USO} denotes the local LRP time-tags of the transponder satellite, which couples directly into the phase via the offset frequency of $f_{\text{off}} = 10 \text{ MHz}$.

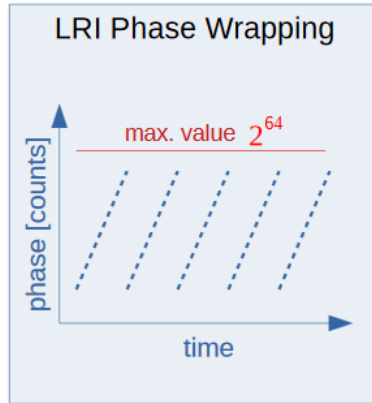


Figure 6.1: Principle of LRI Phase Wrapping.

This 10 MHz phase ramp evokes fast increasing values of phase counts. However, in order to prevent a numerical overflow of the register or variable, the Laser Ranging Processor applies a phase wrap by subtracting exactly 2^{63} counts, before the maximum of 2^{64} counts is achieved [Misfeldt, 2019]. The principle is illustrated in fig. 6.1. As a consequence, these artificially created phase reducing jumps have to be removed in the processing. This step is called unwrapping.

When unwrapping, the AEI team recommends, for maintaining numerical precision, to split the phase into a time series $\delta\varphi^{\text{ramp}}$ with a constant value for the slope ($\zeta_{T/M}$) and a time series

of smaller phase variations $\delta\varphi$ around the slope, i.e. [Müller et al., 2021]

$$\varphi(\tau_M^{\text{USO}}) = \delta\varphi(\tau_M^{\text{USO}}) + \delta\varphi^{\text{ramp}}(\tau_M^{\text{USO}}) = \delta\varphi(\tau_M^{\text{USO}}) + \zeta_M \cdot \frac{\tau_M^{\text{USO}}}{\Delta\tau_M^{\text{USO}}} \quad (6.3)$$

$$\varphi(\tau_T^{\text{USO}}) = \delta\varphi(\tau_T^{\text{USO}}) + \delta\varphi^{\text{ramp}}(\tau_T^{\text{USO}}) = \delta\varphi(\tau_T^{\text{USO}}) + \zeta_T \cdot \frac{\tau_T^{\text{USO}}}{\Delta\tau_T^{\text{USO}}}. \quad (6.4)$$

The symbol Δ is used for computing the consecutive difference, which means that $\Delta\tau_{T/M}^{\text{USO}}$ is the constant sampling time for

$$\text{GF1: } \Delta\tau_{\text{GF1}}^{\text{USO}} = \frac{4000000}{f_{\text{USO,GF1}}} \stackrel{\text{eq. (3.4)}}{=} 0.103476821192053 \text{ s} \quad (6.5)$$

$$\text{GF2: } \Delta\tau_{\text{GF2}}^{\text{USO}} = \frac{4000000}{f_{\text{USO,GF2}}} \stackrel{\text{eq. (3.5)}}{=} 0.103474701159889 \text{ s}. \quad (6.6)$$

The constant ζ describes the phase change per sample in units of cycles. Therefore, the ratio of $\zeta/\Delta\tau^{\text{USO}}$ yields the mean frequency of the phase with units of cycles/s which is equal to Hz.

Cleaning Each QPD channel of master and transponder is checked for an unstable behaviour of the phase at the beginning or end of each continuous segment. After detecting unstable behavior, which can occur for example shortly before the link is lost, a few seconds of data are cropped out.

In the end, the phase variations from the four cleaned QPD data channels are averaged to form a so-called mean clean phase. An averaged value is also computed from the four phase change per sample values $\zeta_{T/M}$. Finally, this phase data in units of counts can be converted to cycles by using the conversion factor of $0.1/2^{24}$ cycles, which is the resolution of the LRP.

Combining the mean clean phase and the value for the mean slope as shown in eq. (6.3) would yield the piston phase, an averaged phase from all four QPD segments (cf. LRI1A product in appendix B.1).

6.2 Deglitching

In the next step, the mean clean phase is passed to a deglitching algorithm for detecting and removing phase jumps. These glitches or phase jumps are unphysical steps in the phase measurement and are mainly produced by thruster activation [Abich et al., 2019]. The majority of the observed phase jumps (PJs) occur slightly time-shifted in the master and transponder measurement and are smaller than 30 cycles [Misfeldt, 2019], but sometimes also phase jumps with a magnitude of mega cycles appear (cf. section 6.7), thus they are called mega phase jumps (MJs).

One cycle corresponds to the wavelength of 1064 nm, which means a MJ of 1 mega cycle appears to be a longitudinal path-length change of 1.064 m in the full round-trip measurement. The PJ or MJ glitches are detected on the transponder phase, because it contains ideally only the phase ramp which correspond to the 10 MHz offset frequency and the PJs stand out clearly. To identify the glitches the transponder phase rate is checked for jumps larger than 0.03 Hz. The corresponding time and usually ± 10 samples around the event are stored as the assumed glitch interval. If the transponder raw phase and master raw phase show a rms

$> 10^{-3}$ cycles in these intervals, they are identified as glitches in the respective phase for the regular deglitching (cf. table 6.1). If the raw phase show a rms $< 10^{-3}$ cycles in one of these intervals, then it is not considered by the deglitching and will be marked with the glitch type “Quiet” (cf. table 6.1).

Afterwards a model is fitted to the identified glitches on the transponder phase. Then the time difference between master and transponder is roughly estimated by using the Datation Reports (DTR). The amplitudes of the transponder glitch model are used to fit the variable delay dt for the master glitch. Only in some special cases, also the glitch amplitudes A needs to be fitted separately for the master (cf. table 6.1), e.g. when a glitch occurred only in the master phase and not on the transponder. These rare events are identified by high pass filtering the master phase rate and searching for jumps larger than 0.3 Hz.

In addition, a polynomial is subtracted from the master measurement in order to remove potential ranging signal during the fit adjustment. Finally, the models are subtracted from the corresponding measurement for removing most parts of the phase jumps [Misfeldt, 2019].

In fig. 6.2 an example is shown for a PJ on the left, and for a MJ on the right hand side. The left y-axes show the jumps in the phase measurements of master and transponder and the applied glitch template, while the right y-axes giving the post-fit residual, i.e. the residual of the glitch segment after a glitch model is removed. When a glitch is fitted on the transponder, the deglitching tries to reduce the rms of the transponder post-fit residual divided by the original PJ height (rms(post-fit)/h-value), by applying different models. The models with the names `Single PJ`, `50ms PJ`, `100ms PJ` and `Variable PJ` were introduced by Misfeldt [2019]. A rms/h-value smaller than 0.002 is regarded as a successful deglitching step, and the model with the smallest value is chosen. The remaining phase disturbances do not affect the ranging measurement significantly, because the LRI noise shows rms values of approx. 0.001 cycles, when no PJ occur [Misfeldt, 2019]. The selected transponder model is also used for removing the master glitch. The remaining post-fit rms of the master is for most of the PJs smaller than 0.1 cycles (cf. section 6.7).

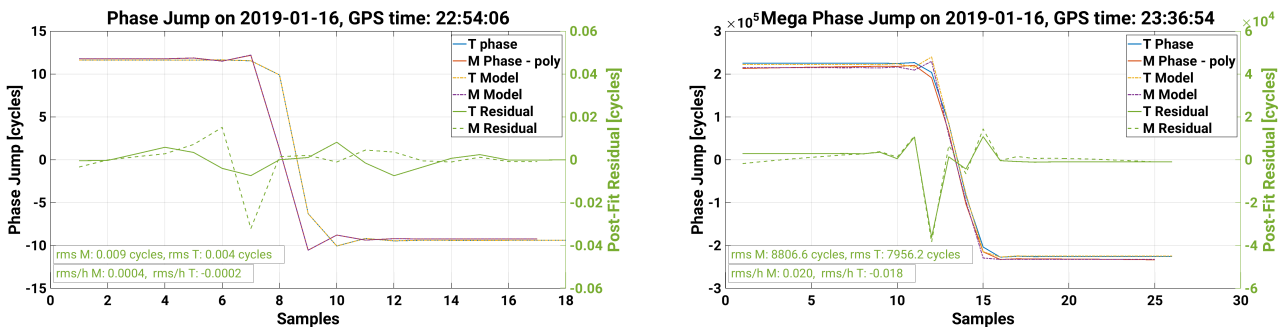


Figure 6.2: Example for a PJ on the left, and for a MJ on the right hand side (left y-axes), with their post-fit residuals (right y-axes) after the phase jump removal. The rms of the post-fit residuum in the master phase is 0.009 cycles for the PJ, and approx. 8806 cycles for the MJ. This MJ will be removed by using interpolation, because the rms of the post-fit residuum is > 0.1 cycles in the master phase. The PJ with a T.rms(post-fit)/h < 0.002 on the transponder is removed by the deglitching, such that the LRI phase is not affected significantly.

S/C	Condition for Glitch:	if pre-fit	Master			
			rms < 10 ⁻³ [cycles]	rms > 10 ⁻³ [cycles]	Step in DWS	T.rms/M.rms < 10 ⁻³
	if pre-fit	Type	Quiet	PJ	CCS	Volatile
Transponder	rms < 10 ⁻³ [cycles]	Quiet	T: no change M: no change	T: no change M: fit* ³ dt	T: no change M: fit A&dt	T: no change M: remove
	rms > 10 ⁻³ [cycles]	PJ	T: fit* ¹ M: no change	T: fit* ¹ M: fit* ³ dt	T: fit* ¹ M: fit A&dt	T: fit* ¹ M: remove
	Step in DWS	CCS	T: fit* ² M: no change	T: fit* ² M: fit A&dt	T: fit* ² M: fit A&dt	T: fit* ² M: remove
	T.rms/M.rms > 10 ³	Volatile	T: remove M: no change	T: remove M: remove	T: remove M: remove	T: remove M: remove
Remark						
T has	Try different glitch models for achieving the lowest rms(post-fit)/h value.					
PJ	First model with success criteria (T.rms(post-fit)/h ≤ 0.002) is used.					
*1:	If glitch removal is not successful (T.rms(post-fit) > 0.1 cycles) → T: remove.					
T has	Try different glitch models for achieving the lowest rms(post-fit)/h value.					
CCS	First model achieving success criteria (T.rms(post-fit)/h ≤ 0.2) is used.					
*2:	If glitch removal is not successful (T.rms(post-fit) > 0.1 cycles) → T remove.					
*3:	If glitch removal is not sufficient (M.rms(post-fit) > 0.1 cycles) → M remove → T remove.					

Table 6.1: Description of glitch types and deglitching strategy.

6.3 First Phase Smoothing Step for φ_M and φ_T

In case of larger phase jumps, like the MJ in fig. 6.2, the transponder rms(post-fit)/h threshold cannot be achieved, because the usual models are often too inexact. Here, the threshold of rms(post-fit) > 0.1 cycles is exceeded for the transponder case. The transponder phase variations are set to zero during the glitch, i.e. the raw phase is subtracted. This process is indicated with “T: remove” in table 6.1.

Additionally, a smoothing condition for the master is applied, when the post-fit rms of the master is > 0.1 cycles. Here, the phase rate is computed and a polynomial of order three is used for a smooth interpolation, before the data is integrated to the phase again. This process is indicated with “M: remove” in table 6.1.

Furthermore, so-called *volatile* events, which will be explained in the following, are also directly removed with these methods. Applying “M: remove” or “T: remove” is called first smoothing step.

Quality Flag of PJ, MJ and Other Phase Disturbances: During the process of deglitching and the first smoothing step, a time series called deglitching phase $\varphi_{\text{deglitching}}$ is generated, which includes the applied deglitching correction on the mean clean phase, such that the process of deglitching and smoothing can easily be reverted. $\varphi_{\text{deglitching}}$ is a stair case function in the time domain, where each step represents the effect of a glitch. That means, the phase jump removal was applied on that samples, where the absolute value of the difference between consecutive deglitching phase samples is larger than zero, i.e.

$$|\Delta\varphi_{\text{deglitching},T/M}| > 0. \quad (6.7)$$

To indicate the affected samples in the LRI1B v50 product they receive a particular quality flag. The quality flag contains eight bits, where bit 0 starts rightmost. All bits of the quality flag are gradually explained in this chapter, thus, a summary of all bits can be found in the end in table 6.3.

If the condition in eq. (6.7) is fulfilled for master and transponder, the samples with a difference

of < 10000 cycles will be marked by bit 2, to indicate the normal PJs. In case of MJ removals, the differences are ≥ 10000 cycles. These large jumps can extend over a few samples, which is marked with bit 3 of the quality flag. It should be noted that v04 has not such a feature.

These described PJs and MJs are indicated upon occurrence in both phases of transponder and master. However, sometimes the phase measurement on one satellite can be disturbed by other effects like sun-blindings (cf. section 6.13). These include e.g. channel cycle slips (CCS), where only one QPD channel is affected from an integer step in the phase measurement, or *volatile* segments, where one or more channels show an unusual phase oscillation rather than a typical phase jump. Sometimes, also momentum transfer events (MTE) like micro-meteorites can be observed in $\Delta\varphi_{\text{deglitching}}$. All these phase disturbances, which are only visible in one S/C measurement, are marked with bit 5.

6.4 Smooth LRI Time to GPS Time Conversion

The conversion of LRI phase time-tags from LRP receiver (rcv) time into GPS time was generally discussed in section 3.3. However, the AEI processing considers a few more points. The derivation of a total (smooth) time-tag correction is explained in detail now.

1. Compute Time Offsets First of all the AEI processing loads the DTR within a given LRI time-tag array and computes the $\text{DTR}_{\text{offset}}$ from eq. (3.8). Furthermore, the $\text{TIM1B}_{\text{offset}}$ is computed with TIM1B v04 (or Quicklook v00 data) from eq. (3.7).

2. DTR + TIM1B Smoothing Now, the derived $\text{DTR}_{\text{offset}}$ and $\text{TIM1B}_{\text{offset}}$ will be smoothed, due to their readout uncertainties of a few hundred nanoseconds. First of all, the $\text{TIM1B}_{\text{offset}}$ is interpolated (or if necessary extrapolated) with the MATLAB method ‘nearest’ onto the $\text{DTR}_{\text{offset}}$ time-tags. Afterwards, the time of occurring LRP and IPU reboots is determined. Additionally, the difference between each $\text{DTR}_{\text{offset}}$ is checked for larger jumps than the nominal noise ($\approx 0.3\ \mu\text{s}$) on Feb 1st, 2021, cf. fig. 3.3). We use a threshold of $0.85\ \mu\text{s}$. Afterwards, a mean value is computed for each DTR segment that is between these events, i.e.

$$\text{DtrTimOffsetSmoothed} = \text{mean}(\text{DTR}_{\text{offset}} + \text{TIM1B}_{\text{offset}}) , \quad (6.8)$$

which gives a smoothed offset between IPU rcv time and LRP rcv time. Because DTRs are only requested a few times per day, it is possible that sometimes no DTR between two IPU reboots is available. In these cases it is necessary to use a prediction from $\text{CLK1B}_{\text{eps.time}}$ for the DTR.

3. Interpolate Values onto LRI time-tag array To convert the time-tags of LRI phase measurements from LRP rcv time ($= \text{TimeUp} + \text{TimeLow}/\text{clock_rate}$) into IPU rcv time, it is necessary to interpolate the derived $\text{DtrTimOffsetSmoothed}$ values onto this specific LRI time-tag array. For this interpolation the method ‘previous’ of MATLAB is used. The resulting time series is called `lrp2ipu`. Adding it to the LRI time-tag array yields the same array in IPU rcv time. This allows to interpolate the CLK1B product onto the new generated IPU time-tags. These linearly interpolated $\text{CLK1B}_{\text{eps.time}}$ values contain the correction for converting the obtained IPU time-tag array to a GPS time-tag array, which is called `ipu2gps` in our processing. In general we can summarise the time correction as

$$t_{\text{corr}} = \text{lrp2ipu} + \text{ipu2gps} . \quad (6.9)$$

4. Apply Decimation Filter Delay A decimation filter introduces a delay, when the LRP records the phase measurement with a 10 Hz rate [Wen, 2019]. For removing this onboard created filter delay, presented by eq. (3.10), it is also added to the time-tag correction, i.e.

$$t_{\text{corr}} = \text{lrp2ipu} + \text{ipu2gps} + \Delta t_{\text{Filter}} . \quad (6.10)$$

5. Smoothing Total Time Correction Ideally, t_{corr} forms a smooth line and shows some 1/rev and 2/rev oscillations, due to relativistic effects on the USOs. Furthermore, a 2/day oscillation can be observed, which was previously shown with CLK1B data in fig. 3.5, and whose origin will be discussed in section 6.5.1. Therefore, a moving average of 500 seconds is used, which preserves the 1/rev and 2/rev oscillations, but suppresses the noise in higher frequencies from CLK1B data in order to not degrade the phase measurement. This will be clarified in the next paragraph. The final time series

$$t_{\text{total_corr}} = \int \text{movmean}\left(\frac{d}{dt}t_{\text{corr}}, 500\text{s}\right) dt \quad (6.11)$$

contains the entire smoothed time-tag correction, and converts the local LRP time-tags $\tau_{T/M}^{\text{USO}}$ into GPS time-tags $t_{T/M}$ as

$$t_{T/M} = \tau_{T/M}^{\text{USO}} + t_{\text{total_corr},T/M} . \quad (6.12)$$

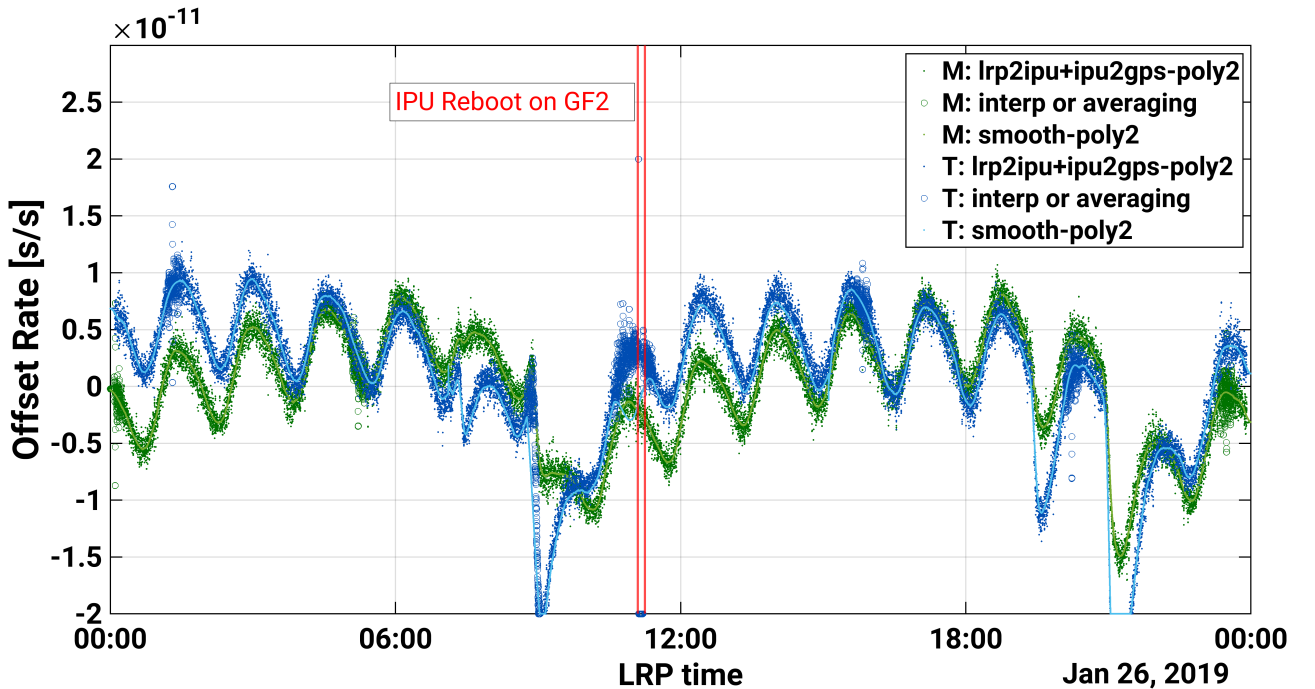


Figure 6.3: The offset rate of the raw time correction and the smooth time correction is shown for master and transponder on 2019-01-26. For example in the time period between 11:06 and 11:15 (red vertical lines), the IPU of GF2 (transponder role) performed a restart. The larger green and blue circles indicate events of interpolation and averaging for closing data gaps like these.

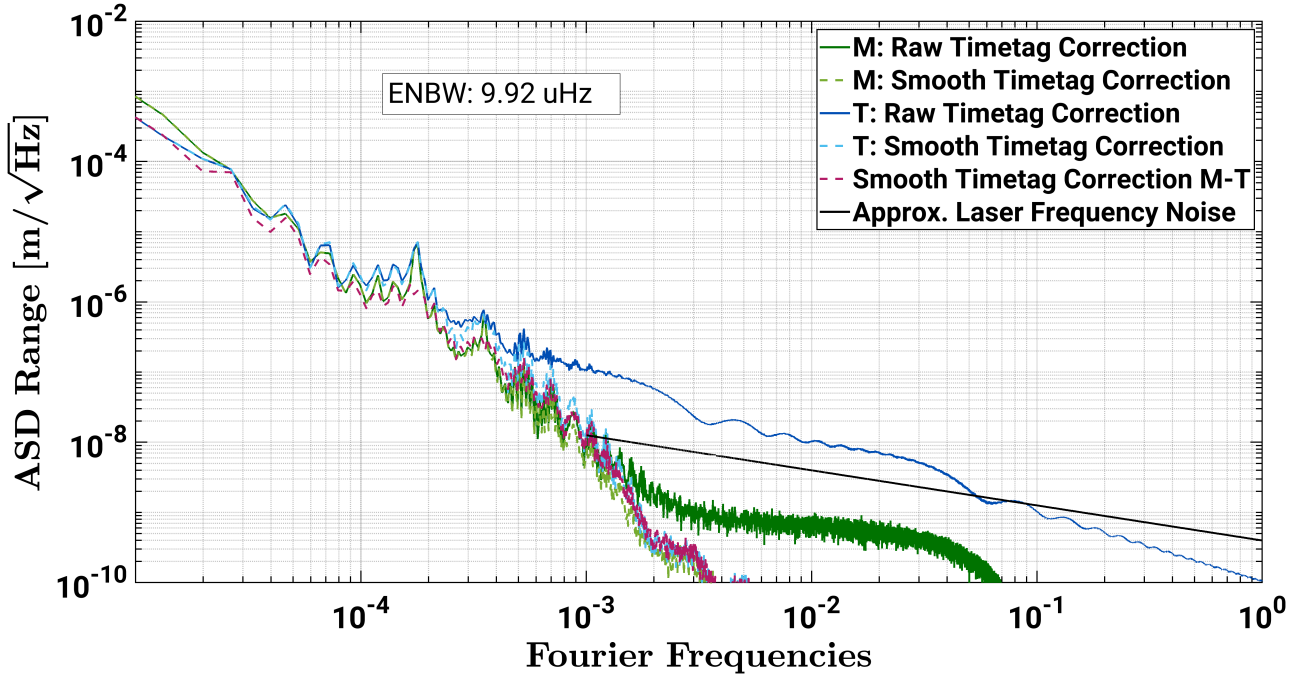


Figure 6.4: ASD of resulting ranging error for the full round-trip due to time-tag jitter. The induced ranging error from the time-tag correction at 1/rev is ≈ 25 nm (rms amplitude), for the time span of January 20th to 27th in 2019. The smoothed time correction ensures a lower noise floor for Fourier frequencies > 1 mHz in comparison to the raw time correction.

Comparison Raw and Smoothed Time Correction The derivative of the time correction (offset rate) from eq. (6.10) minus a polynomial of degree two, is shown in fig. 6.3. Little dark green dots are used for the master (M) and dark blue ones for the transponder (T). The polynomial has to be subtracted to make the variations visible.

If this correction contains a gap, an interpolation will be performed, by using polynomials and harmonic functions which also consider the orbital period. When this interpolation approach is necessary, it will be marked with dark blue or green circles in that plot. As well as when a moving average of 28800 s, instead of 500 s, was used for the last smoothing step.

The light blue curve in fig. 6.3 shows the total time correction $t_{\text{total_corr}}$ of the transponder, and the light green curve for the master. These two curves are much smoother than the raw time correction.

The corresponding LRI ranging error induced by the jitter in the raw time correction and in the smoothed time correction are illustrated with an amplitude spectral density in fig. 6.4, for a few days in January 2019. The basic principles of ASDs are discussed in appendix A.1. The black line indicates an estimation for the laser frequency noise, which is computed by [Spero, 2021]

$$\text{ASD}[\Delta\rho_{\nu_M}] = 2 \cdot \frac{10^{-15} \cdot 200 \text{ km}}{\sqrt{f_{\text{Fourier}}}}, \quad 1 \text{ mHz} < f_{\text{Fourier}} < 5 \text{ Hz}, \quad (6.13)$$

where the factor of two is used to obtain the induced ranging error $\Delta\rho_{\nu_M}$ for the full round-trip. Obviously, the raw time-tag correction $\text{ASD}[t_{\text{corr}}] \cdot 10\text{m/s}$ for the transponder (dark blue) is higher than the laser frequency noise.

In fig. 6.4, the smoothed time correction $\text{ASD}[t_{\text{total_corr}}] \cdot 10\text{m/s}$ for transponder and master is shown with the dashed lines. For the lower frequencies the smoothed and raw time correction

shows the same behaviour, because we want to preserve the actual signal at 1/rev and 2/rev. However, for higher frequencies the smoothed data is well below the laser frequency noise, and does not affect the LRI range measurement.

6.5 Phase Difference Transponder - Master

The LRI ranging phase is computed from the difference of transponder and master phase as it was described in section 4.3. Its implementation is explained here. In section 6.1 it was mentioned that the phase measurement is split into a time-series of smaller phase variations $\delta\varphi_{T/M}$ and a constant value for the phase ramp $\zeta_{T/M}$. Therefore, both parts have to be considered in forming the difference. The content within this subsection is mainly based on our technical note [Müller et al., 2021].

To subtract the phase measurements from each other they have to be in the same time reference frame, i.e. they need to have the same time-tags. Accordingly the data of one satellite must be resampled onto the other time-grid. The transponder data is resampled, because it has less dynamic range than the master phase. The resampling accounts for the time shift due to the light travel time \mathcal{L}_{TM} between the S/C (cf. section 2.2.3 and appendix B.5). The final LRI phase can be written as

$$\varphi_{LRI} = \delta\varphi_{LRI} + \delta\varphi_{LRI}^{\text{ramp}} \quad (6.14)$$

with the difference of phase variations $\delta\varphi_{LRI}$ and differences of the ramps $\delta\varphi_{LRI}^{\text{ramp}}$ like

$$\delta\varphi_{LRI}(t_M) = [\delta\varphi_T(t_M - \mathcal{L}_{TM}) - \delta\varphi_M(t_M)] \quad (6.15)$$

$$\delta\varphi_{LRI}^{\text{ramp}}(t_M) = [\delta\varphi_T^{\text{ramp}}(t_M - \mathcal{L}_{TM}) - \delta\varphi_M^{\text{ramp}}(t_M)] . \quad (6.16)$$

For maintaining the accuracy of the phase, the calculation for φ_{LRI} is split into two parts. Equation (6.15) denotes the subtraction of the phase variations of transponder and master phase in the master time frame. The transponder phase $\delta\varphi(t_T)$ with approx. 10 Hz GPS time-tags t_T is interpolated linearly with MATLAB's 'interp1' command onto the GPS time-tags $t_M - \mathcal{L}_{TM}$ in the master's frame, i.e.

$$\delta\varphi_T(t_M - \mathcal{L}_{TM}) = \text{interp1}(t_T, \delta\varphi_T(t_T), t_M - \mathcal{L}_{TM}, \text{'linear'}) . \quad (6.17)$$

In fact, we are using an own function called `interp1_highprecision`, which accepts time-tags that are represented as two doubles, i.e. an integer and a fractional part, in order to achieve sub-nanosecond resolution. Afterwards the phase variations are subtracted with full resolution of $0.1/2^{24}$ cycles as uint64.

Equation (6.16) shows the subtraction of the phase ramp time series of master and transponder. Implementing eq. (6.16) requires some precautions in order to not lose numerical precision with double precision arithmetic, since one has to subtract large numbers. Thus, to reconstruct the differential phase ramp at each sample n , the following integration approach is used

$$\delta\varphi_{LRI}^{\text{ramp}}(\tau_{M,n}^{\text{USO}}) = \frac{d}{d\tau_M^{\text{USO}}} \int_0^{\tau_{M,n}^{\text{USO}}} [\delta\varphi_T^{\text{ramp}} - \delta\varphi_M^{\text{ramp}}] d\tau_M^{\text{USO}} , \quad (6.18)$$

where the differential phase ramp time series as a function of the local LRP time-tags at the master τ_M^{USO} is computed, because this time-grid has an equidistant sampling in contrast to

the GPS time-tags. In the next step we write the derivative expression into the integral and use the constant scalar value $\Delta\tau_M^{\text{USO}}$, which represents the sampling time step of the master (cf. eq. (6.5) and eq. (6.6)), i.e.

$$\delta\varphi_{\text{LRI}}^{\text{ramp}}(\tau_{M,n}^{\text{USO}}) = \int_0^{\tau_{M,n}^{\text{USO}}} \left[\frac{d\delta\varphi_T^{\text{ramp}}(t_M - \mathcal{L}_{\text{TM}})}{d\tau_M^{\text{USO}}} - \frac{\zeta_M}{\Delta\tau_M^{\text{USO}}} \right] d\tau_M^{\text{USO}}. \quad (6.19)$$

Therefore, the term of $\zeta_M/\Delta\tau_M^{\text{USO}}$ denotes the ramp frequency, with units of cycles/s = Hz, on the master side with the constant ‘‘phase change per sample’’ value ζ_M .

Rewriting the first term in the integral of eq. (6.19) with the chain rule yields

$$\frac{d\delta\varphi_T^{\text{ramp}}}{d\tau_M^{\text{USO}}} = \frac{d\delta\varphi_T^{\text{ramp}}}{d\tau_T^{\text{USO}}} \cdot \frac{d\tau_T^{\text{USO}}}{d(t_M - \mathcal{L}_{\text{TM}})} \cdot \frac{d(t_M - \mathcal{L}_{\text{TM}})}{d\tau_M^{\text{USO}}} \quad (6.20)$$

where the first fraction is the time-derivative of the phase ramp, which is also the ramp frequency on the transponder

$$\frac{d\delta\varphi_T^{\text{ramp}}}{d\tau_T^{\text{USO}}} = \frac{\zeta_T}{\Delta\tau_T^{\text{USO}}} \quad (6.21)$$

with respect to the local LRP time-tags of the transponder. This is multiplied with the second fraction, which yields the ramp frequency in the GPS time frame of the master. By using the third part of that product, one gets the transponder ramp frequency in local LRP time-tags of the master. Based on eq. (6.20), we define a quantity r_2 , such that

$$\frac{d\delta\varphi_T^{\text{ramp}}}{d\tau_M^{\text{USO}}} = \frac{\zeta_T}{\Delta\tau_M^{\text{USO}}} \cdot r_2. \quad (6.22)$$

holds. For deriving r_2 , one can insert the left side of eq. (6.20) into eq. (6.22) and use the expression for the transponder ramp frequency of eq. (6.21), i.e.

$$\frac{\zeta_T}{\Delta\tau_T^{\text{USO}}} \cdot \frac{d\tau_T^{\text{USO}}}{d(t_M - \mathcal{L}_{\text{TM}})} \cdot \frac{d(t_M - \mathcal{L}_{\text{TM}})}{d\tau_M^{\text{USO}}} = \frac{\zeta_T}{\Delta\tau_M^{\text{USO}}} \cdot r_2. \quad (6.23)$$

The last fraction on the left side describes the time derivatives of the master GPS time-tags and the light travel time-tags w.r.t. local LRP time-tags of the master. These can be approximated by finite differences (Δ), such that

$$\frac{d(t_M - \mathcal{L}_{\text{TM}})}{d\tau_M^{\text{USO}}} = \frac{dt_M}{d\tau_M^{\text{USO}}} - \frac{d\mathcal{L}_{\text{TM}}}{d\tau_M^{\text{USO}}} \approx \frac{\Delta t_M - \Delta\mathcal{L}_{\text{TM}}}{\Delta\tau_M^{\text{USO}}}. \quad (6.24)$$

Additionally, the left side of eq. (6.23) is extended with dt_T/dt_T , i.e.

$$\frac{\zeta_T}{\Delta\tau_T^{\text{USO}}} \cdot \frac{d\tau_T^{\text{USO}}}{d(t_M - \mathcal{L}_{\text{TM}})} \cdot \frac{\Delta t_M - \Delta\mathcal{L}_{\text{TM}}}{\Delta\tau_M^{\text{USO}}} \cdot \frac{dt_T}{dt_T} = \frac{\zeta_T}{\Delta\tau_M^{\text{USO}}} \cdot r_2. \quad (6.25)$$

This can be rewritten as

$$\frac{\zeta_T}{\Delta\tau_M^{\text{USO}}} \cdot \underbrace{\left[\Delta\tau_T^{\text{USO}} \cdot \frac{dt_T}{d\tau_T^{\text{USO}}} \cdot \frac{d(t_M - \mathcal{L}_{\text{TM}})}{dt_T} \right]^{-1}}_{:=\Delta t_T(t_M - \mathcal{L}_{\text{TM}})} \cdot (\Delta t_M - \Delta\mathcal{L}_{\text{TM}}) = \frac{\zeta_T}{\Delta\tau_M^{\text{USO}}} \cdot r_2. \quad (6.26)$$

Some derivative expressions in the square brackets can also be replaced by finite differences, to simplify the new transponder GPS time-tags as

$$\Delta t_T(t_M - \mathcal{L}_{\text{TM}}) = \Delta \tau_T^{\text{USO}} \cdot \frac{\Delta t_T(t_T)}{\Delta \tau_T^{\text{USO}}} \cdot \frac{d(t_M - \mathcal{L}_{\text{TM}})}{dt_T} \quad (6.27)$$

$$= \Delta t_T(t_T) \cdot \frac{d(t_M - \mathcal{L}_{\text{TM}})}{dt_T} . \quad (6.28)$$

In our processing this $\Delta t_T(t_T)$ is resampled by means of interpolation from its GPS time-tags t_T onto the new GPS time-grid in the master frame $t_M - \mathcal{L}_{\text{TM}}$, i.e.

$$\Delta t_T(t_M - \mathcal{L}_{\text{TM}}) = \text{interp1}(t_T, \Delta t_T(t_T), t_M - \mathcal{L}_{\text{TM}}, \text{'linear'}) . \quad (6.29)$$

Finally, one can achieve the r_2 time series

$$r_2(\tau_M^{\text{USO}}) = \frac{\Delta t_M - \Delta \mathcal{L}_{\text{TM}}}{\Delta t_T(t_M - \mathcal{L}_{\text{TM}})} , \quad (6.30)$$

with eq. (6.26) and eq. (6.29), for scaling the transponder phase ramp as it appears in the master phase. The finite differences are computed with a central 3-point numerical differentiation method, which is presented in appendix A.2. Here the derivation is done with a spacing of $h = 1$ and performed separately for the integer and fractional time-tags of Δt_M and Δt_T (to preserve high numerical accuracy), before they are added and result in the finite differences in eq. (6.30).

r_2 is written as a function of τ_M^{USO} , because the GPS time-tags $t_M(\tau_M^{\text{USO}})$ and the light travel time $\mathcal{L}_{\text{TM}}(\tau_M^{\text{USO}})$ dependent on the local master time-tags. The relation between τ_M^{USO} and t_M was presented in section 6.4. Furthermore, the r_2 is basically described by two different parts:

- by the ratio $\Delta t_M / \Delta t_T(t_M - \mathcal{L}_{\text{TM}})$, which can be approximated with $1 + \Delta t_M - \Delta t_T(t_M - \mathcal{L}_{\text{TM}})$, since both quantities are ≈ 1 . That means r_2 can be interpreted as the ratio of the master's and transponder's clock rate at the same instance of time. The values of r_2 are very close to one, but even if the clocks are working exactly equal and have ideally the same clock rate, without noise and errors, r_2 would vary around one, due to relativistic effects (cf. section 2.2). Additionally, r_2 includes the information of the relation between the differential of local and GPS time-tags of master and transponder.
- by the light travel time \mathcal{L}_{TM} , which is in first order proportional to the inter-satellite distance.

In principle it is also possible to compute r_2 with a simple interpolation approach by using a vector with increasing values, e.g. $\vec{y} = [0, 1\delta y, 2\delta y, 3\delta y, \dots]$ and a constant step size like $\delta y = 1$, for calculating the consecutive difference with the MATLAB command 'diff' i.e.

$$r_2 = \frac{1}{\delta y} \cdot \text{diff}(\text{interp1}(t_T(\tau_T^{\text{USO}}), y, t_M(\tau_M^{\text{USO}}) - \mathcal{L}_{\text{TM}})) . \quad (6.31)$$

However, the numbers in the argument of $\text{diff}(\dots)$ are increasing very fast. These large values would lead to a less accurate result for the LRI phase, caused by loss of numerical precision. For that reason we use eq. (6.30).

Finally it should be noted, that the implementation of eq. (6.19) is implemented with

$$\delta\varphi_{\text{LRI}}^{\text{ramp}}(\tau_{\text{M},n}^{\text{USO}}) = \sum_{i=0}^n \underbrace{\zeta_{\text{T}} \cdot r_2(\tau_{\text{M},i}^{\text{USO}})}_{\text{T phase ramp as apparent on M}} - \underbrace{\zeta_{\text{M}}}_{\text{phase ramp on M}} \quad (6.32)$$

where the integral was replaced by the cumulative sum over the samples n .

In summary, we cannot subtract the raw phase measurements directly, because they are with respect to the corresponding time frame of the particular S/C and have a phase ramp that would cause numerical errors due to large numbers. Instead, the derivatives are subtracted from each other and integrated afterwards.

6.5.1 Effects of Relativity in Time-tags

The expression $d\tau/dt - 1$ from eq. (2.38) can be used for investigating the relativistic effects for a clock in a low Earth orbit in comparison to a resting clock at Earth's geoid.

For this calculation, the GNI1B v04 data product is used, which includes the positions and velocities of the satellites at the corresponding GPS time in a non-rotating Earth centered frame (GCRS). The result is shown in fig. 6.5. The period of first to fourth of January 2019 was chosen. The mean value of $d\tau/dt - 1$ is approximately $-2.7 \cdot 10^{-10}$ s/s, as predicted in section 2.2.

For further investigations $d\tau/dt - 1$ from eq. (2.38) is rewritten into

$$\frac{d\tau^{\text{model}}}{dt} = 1 - \frac{GM}{rc^2} + \frac{GMJ_2}{rc^2} \left(\frac{a_e}{r}\right)^2 \cdot \left(\frac{3z^2}{2r^2} - \frac{1}{2}\right) - \frac{\Phi_0}{c^2} - \frac{v^2}{2c^2}, \quad (6.33)$$

where $d\tau^{\text{model}}/dt$ denotes the derivative of the modelled proper time w.r.t. coordinate time (GPS), as derived from the orbit products.

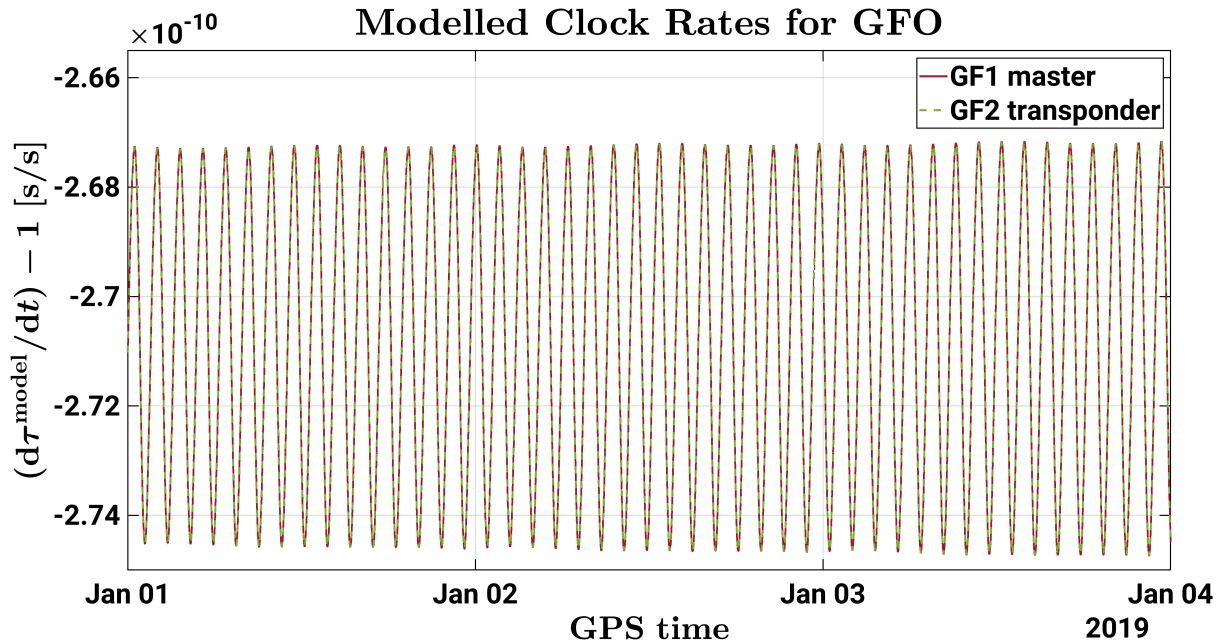


Figure 6.5: The derivatives of local LRP time $\tau_{T/M}^{\text{USO}}$ w.r.t. GPS time $t_{T/M}$, are shown. The traces are derived using eq. (2.38) and GNI1B data and represent relativistic effects in the USOs proper time w.r.t. GPS time.

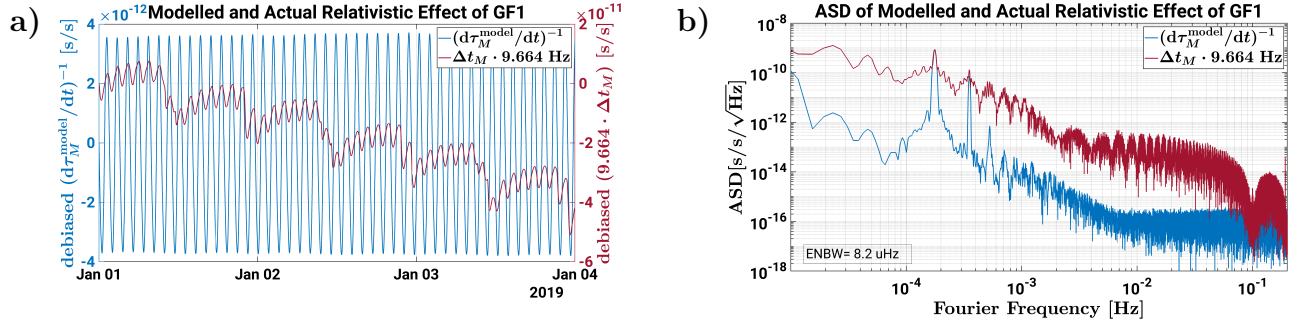


Figure 6.6: Comparison of modelled relativistic effect and the finite differences of in-flight GPS time-tags for the master GF1. **a)** shows the two time series, **b)** shows the corresponding amplitude spectral density. For both time series the amplitudes at frequencies of 1/rev and 2/rev are similar. Consequently, the GPS time-tags from LRP measurements show expected effects of relativity.

These modelled effects should be similar to the in-flight GPS time-tags, which were derived for each LRP time-tag. The derivative of the in-flight GPS time-tags t_M is rewritten with approximations of finite differences again, i.e.

$$\frac{dt_M}{d\tau_M^{\text{USO}}} = \frac{\Delta t_M}{\Delta \tau_M^{\text{USO}}} . \quad (6.34)$$

We want to check the similarity of the modeled proper time τ_M^{model} and the actual in-flight data for the master GF1, i.e.

$$\frac{\Delta t_M}{\Delta \tau_M^{\text{USO}}} = \Delta t_M \cdot 9.664 \text{ Hz} \approx \left(\frac{d\tau_M^{\text{model}}}{dt} \right)^{-1} . \quad (6.35)$$

Figure 6.6 a) compares the finite differences of in-flight GPS time-tags $\Delta t_M \cdot 9.664 \text{ Hz}$ of GF1 with the inverse model of relativistic effects $(d\tau_M^{\text{model}}/dt)^{-1}$. Both data sets are debiased for plotting. The blue curve for $(d\tau_M^{\text{model}}/dt)^{-1}$ belongs to the left y-axis and oscillates with 10^{-12} s/s . The red curve of $(\Delta t_M \cdot 9.664 \text{ Hz})$ on the right y-axis, also shows a modulation with the size of 10^{-12} s/s , and an additional 2/day pattern, which was already mentioned at the time-tag conversion in section 6.4.

The Amplitude Spectral Density (ASD) of the same data is shown in fig. 6.6 b). At frequencies of 1/rev and 2/rev, the simulated trace in blue agrees with the dark red curve from in-flight data.

In conclusion the GPS time-tags from in-flight data, which were previously converted from LRP time-tags, show similar oscillations as the modelled proper time, which was calculated from GNI1B data. Section 6.4 has explained that one GPS time-tag can be assigned to each LRP time-tag. These procedure requires the data of DTR, TIM1B and CLK1B (\approx drift of USO). That means the local LRP time-tags have an equidistant sampling, but with use of CLK1B data, the 1/rev and 2/rev oscillations from relativistic effects are introduced.

The observed 2/day oscillations in fig. 6.6 a) in the GPS time-tags are assumed to be caused by the orbit period of GPS satellites or from Earth's rotation. Therefore, an amplitude spectrum of Δt_M for a time span of 2019-01-01 to 2019-01-10 is plotted, to observe also lower frequencies such as 1/day ($\approx 11.6 \mu\text{Hz}$). Figure 6.7 shows a zoom-in for frequencies lower than 2/rev. The orbital frequencies of 1/rev (0.176 mHz) and 2/rev (0.35 mHz) of GFO are indicated with

two red circles. The orbit period of GPS satellites is 11 hours and 58 minutes [Basile et al., 2018]. The resulting n/rev for $n = 1 \dots 10$ are marked with green circles. The rotation of the Earth has a period of 23 hours and 56 minutes [Basile et al., 2018], which describes the period until the stars on the sky reach the same position as on the day before, for an observer on the Earth. The corresponding frequencies at n/rev with $n = 1 \dots 20$ are marked with blue circles.

One can see, that many n/rev frequencies of both systems are represented in the spectrum of GFO time information. But the dominating peak with the highest amplitude in fig. 6.7, is given by $1/\text{rev}$ of the GPS orbit period or by $2/\text{rev}$ of Earth's rotation period. It cannot be clearly distinguished, which of the two effects lead to the observed 2/day oscillations in the data time-tags (in section 6.4 and section 6.5.1).

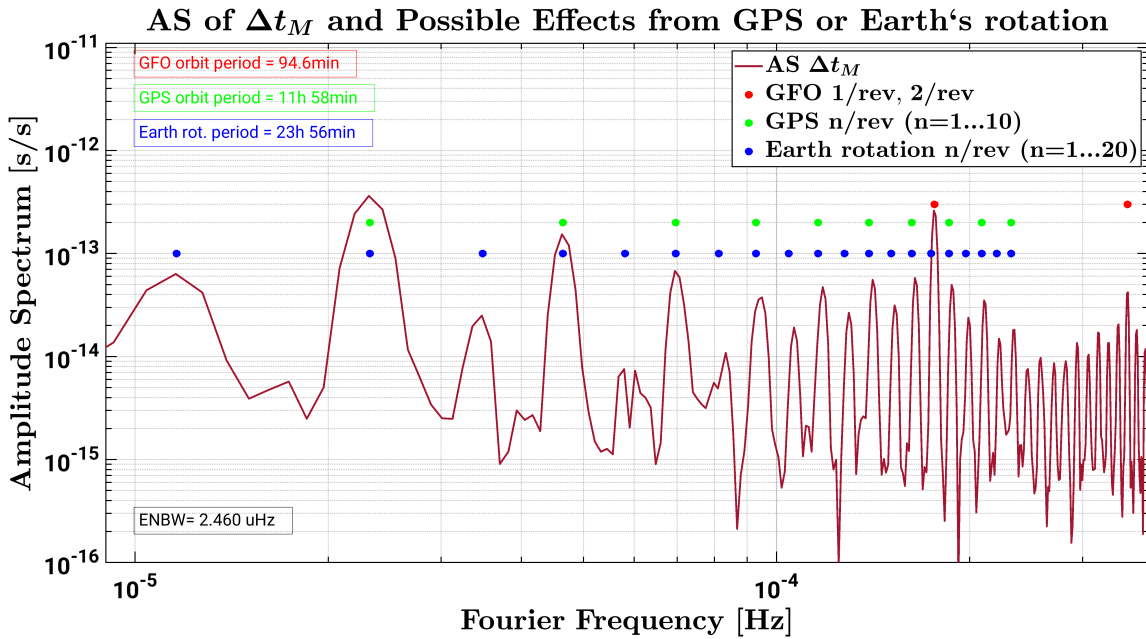


Figure 6.7: Amplitude spectrum of the finite differences of master time-tags Δt_M . Furthermore, the different n/rev frequencies of the following systems are marked: GFO, GPS satellites, and Earth's rotation. The largest peak at $23 \mu\text{Hz}$ with a rms amplitude of $\approx 3.6 \cdot 10^{-13} \text{ s/s}$ is the 2/day oscillation in the master and transponder time-tags. It could result from the GPS orbit period ($1/\text{rev}$) or from the Earth rotation period ($2/\text{rev}$) or a combination of both.

6.5.2 Alternative Methods to Remove the Phase Ramp

This section presents different methods for removing the phase ramp, when r_2 (of eq. (6.32)) cannot be calculated. The two terms in the cumulative sum of eq. (6.32) represent the phase ramp of the transponder and master in the ranging phase. The phase ramp in the master and transponder phase has a slope of $10 \text{ MHz} \hat{=} 10 \cdot 10^6 \text{ cycles/s}$, which corresponds to a range rate of 5 m/s for a wavelength of $\approx 1 \mu\text{m}$. In the time domain $\delta\varphi_{\text{LRI}}^{\text{ramp}}$ and $\zeta_T \cdot r_2$ only differ in a mean value (DC) and trend (cf. eq. (6.32)), such that the spectral content for Fourier frequencies (above DC and trend) is the same for $\delta\varphi_{\text{LRI}}^{\text{ramp}}$ and $\zeta_T \cdot r_2$, when expressed as equivalent half-roundtrip ranging error, i.e.

$$\frac{\lambda}{2} \cdot \text{ASD}[\delta\varphi_{\text{LRI}}^{\text{ramp}}](f) \approx \text{ASD}[r_2](f) \cdot \frac{5 \text{ m/s}}{2\pi f} . \quad (6.36)$$

The result of eq. (6.36) is shown as blue trace in fig. 6.8. The peaks at 1/rev and 2/rev have amplitudes of $4.38\ \mu\text{m}$ rms and $1.06\ \mu\text{m}$ rms. This is how the transponder phase ramp appears on the master satellite and how it is usually calculated for the phase ramp subtraction.

If r_2 is not used in the phase ramp subtraction, for instance, because it is unavailable or cannot be computed¹, one could try to remove just a mean trend from the master ranging phase. However, by using just a mean trend it would lead to an error shown by the blue curve in fig. 6.8.

An alternative to the removal of a mean trend/slope could be the usage of a less-accurate model of r_2 . This approach makes use of the similarity between the derived model for relativistic effects and the in-flight GPS time-tags (cf. eq. (6.35)) at 1/rev and 2/rev, which was presented in the previous section 6.5.1. The r_2 from eq. (6.30) is extended with $\Delta\tau_M^{\text{USO}}/\Delta\tau_M^{\text{USO}}$, such that

$$r_2 = \frac{(\Delta t_M/\Delta\tau_M^{\text{USO}}) - (\Delta\mathcal{L}_{\text{TM}}/\Delta\tau_M^{\text{USO}})}{\Delta t_T(t_M - \mathcal{L}_{\text{TM}})/\Delta\tau_M^{\text{USO}}} . \quad (6.37)$$

Inserting eq. (6.35) yields the model \tilde{r}_2 as

$$\tilde{r}_2 = \frac{(\text{d}\tau_M^{\text{model}}/\text{d}t)^{-1} - (\Delta\mathcal{L}_{\text{TM}}/\Delta\tau_M^{\text{USO}})}{(\text{d}\tau_T^{\text{model}}/\text{d}t)^{-1}} . \quad (6.38)$$

where $\text{d}\tau_{T/M}^{\text{model}}/\text{d}t$ is computed from eq. (6.33), and the finite differences of the light travel time $\Delta\mathcal{L}_{\text{TM}}$ are computed with a centered 3-point numerical differentiation method (cf. appendix A.2, $h = 1$), and it is linearly interpolated onto the time-tags of the used GNI1B positions and velocities. The dominating part in \tilde{r}_2 , as well as in r_2 , with a magnitude of approx. 10^{-9} , is caused by $\Delta\mathcal{L}_{\text{TM}}/\Delta\tau_M^{\text{USO}}$. The relativistic model of $\text{d}\tau_{T/M}^{\text{model}}/\text{d}t$ only contains variations of approx. 10^{-12} . Furthermore, this model does not include errors from imperfections of the USOs.

The red curve in fig. 6.8 shows the calculation from eq. (6.36) for $\text{ASD}[r_2 - \tilde{r}_2]$, where GF1 is in the master role, thus, $1/\Delta\tau_M^{\text{USO}} = 9.664\ \text{Hz}$ holds. This curve shows the resulting error, if one would use the model \tilde{r}_2 , which takes the proper time into account, for scaling the transponder phase ramp.

However, at a failure of the IPU, a precise orbit product like GNI1B is likely unavailable. To simulate a more noisy orbit product we assume uncorrelated white position noise of 10 cm for the x, y and z component and add it to the GNI1B data. This more noisy product of GNI1B is used, for computing the three different terms in eq. (6.38) again. This more noisy model is denoted as $\tilde{r}_{2,\text{noise}}$. The yellow curve in fig. 6.8 shows the calculation from eq. (6.36) for $\text{ASD}[r_2 - \tilde{r}_{2,\text{noise}}]$ for GF1 in master role. This curves gives the resulting error, if the model with noise assumption $\tilde{r}_{2,\text{noise}}$ is used for scaling the transponder phase ramp.

The green curve shows an estimate for the linear Tilt-to-Length (TTL) coupling and was computed as [Wegener et al., 2020]

$$f_{\text{Fourier}} = [10^{-4}, 0.002, 0.1]\ \text{Hz} , \quad \text{ASD}[\Delta\rho_{\text{TTL}}] = [10^{-6}, 10^{-6}, 10^{-9}]\ \text{m}/\sqrt{\text{Hz}} . \quad (6.39)$$

The red and yellow curve, which are considering the proper time, are similar for the lower frequencies. Using \tilde{r}_2 or $\tilde{r}_{2,\text{noise}}$ allows to reduce the error at 1/rev and 2/rev by approx. three

¹e.g. when the IPU on the transponder S/C fails

orders of magnitude. Consequently, the resulting error is even below the effect of TTL, hence, this calculation would be sufficient. The rms amplitudes of 3.64 nm and 0.75 nm are given in the red-yellow boxes in fig. 6.8.

For higher frequencies the yellow curve is much noisier due to the 10 cm white noise assumption. However, it was only a first estimation to get an idea of alternative methods for deriving a r_2 , when it is not possible to use IPU data. The actual orbit solution is based on reduced-dynamic orbit determination, which does not lead to such a high white noise, as it was estimated here. Depending on the precision of the used orbit product, one can expect a result between the red and yellow curve.

Additionally, the black curve is included for showing the ranging error of the laser frequency noise from cavity performance. For the half-roundtrip eq. (6.11) was divided with two.

Finally we can conclude that due to relativistic effects it is important to use r_2 to transform the transponder phase ramp to the master satellite in the phase ramp subtraction in eq. (6.32). When this data cannot be derived, the r_2 -model from orbit products could be an alternative compared to the method of removing only a mean trend/slope from the master phase.

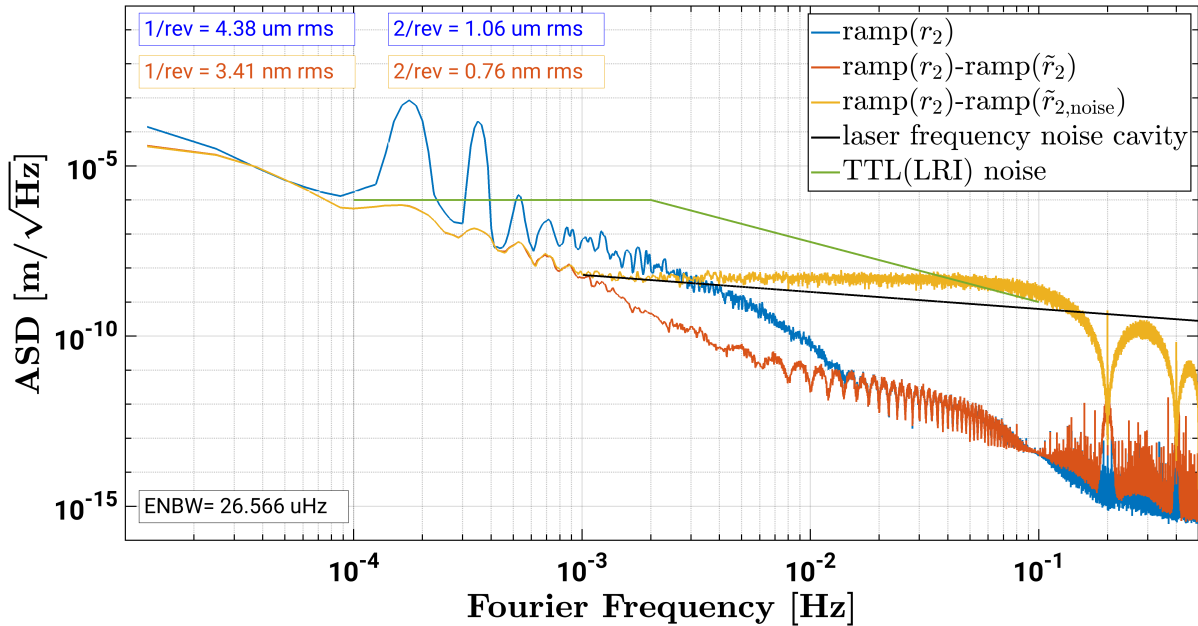


Figure 6.8: Amplitude spectral density of the transponder phase ramp in the ranging (master) phase, expressed as equivalent half-roundtrip ranging error. The blue curve results from eq. (6.36), where the clock rate ratio r_2 of GF1 and GF2 (containing CLK1B data) is used. This trace shows the error, when the master phase is only detrended instead of subtracting the transponder phase ramp, which was scaled with r_2 . The red and yellow curve include different models for r_2 , i.e. \tilde{r}_2 with GNI1B, and $\tilde{r}_{2,\text{noise}}$ with GNI1B+white noise assumption. They show the differences to the blue curve. Both models take into account the effects of relativity, which allows to reduce the resulting ranging error below the TTL coupling at 1/rev and 2/rev. The plot is based on data for the period of first to fourth January in 2019.

6.6 Second Smoothing Step for φ_{LRI}

The previous step of subtracting transponder and master phase should reduce the glitch residuals as well. However, for some events the deglitching, the first smoothing step and the phase subtraction of transponder and master are not sufficient and it is necessary to apply an additional phase smoothing step. The first smoothing step is applied on the deglitched phase of master (φ_M) and transponder (φ_T), while the second smoothing step is done for the transponder minus master combination (φ_{LRI}).

Larger glitch residuals are identified by computing the high pass filtered phase rate $|\text{hpf}(\dot{\varphi}_{\text{LRI}})|$ and finding peaks larger than 0.3 Hz. If such a jump occurs ± 5 samples around the event are used as segment to be smoothed, and a polynomial of order three is fitted onto the phase rate at the first and last two samples of this segment. Afterwards the data is integrated to obtain φ_{LRI} and the changed samples are marked with bit 1 of the quality flag (cf. table 6.3).

6.7 Visualisation of All Phase Jump Removal Steps

Figure 6.9 a) and b) give an overview about the different glitch removal approaches on the master and transponder spacecraft. The pre-fit rms, i.e. the rms value of the glitch segment before a glitch model is subtracted, is illustrated on the x-axis, while the y-axis is giving the post-fit rms, i.e. the rms value of the glitch segment after a glitch model was subtracted. It should be noted that for the pre-fits and post-fits of the master phase also a polynomial is subtracted to remove possible ranging signal for the time of deglitching (cf. section 6.2).

All glitch events are illustrated with blue circles. The majority of the assumed glitch events are identified on the transponder phase rate (cf. section 6.2). When the corresponding phase intervals show a pre-fit rms larger than 10^{-3} cycles in master or transponder phase, they are stored as glitches for the related spacecraft. This threshold is the dashed line in dark blue. That means, the glitches (blue circles) below that threshold are not processed from the deglitching for the related satellite.

In the first three years (d168 y2018 until d170 y2021) the total number of phase jump events is 119345, where 4 events occurred only on the transponder and 333 only on the master. All these glitches were processed from the deglitching and the majority was removed sufficiently. However, 224 events in the master phase and 189 events in the transponder phase needed to be removed with the first smoothing step. Furthermore, 1585 events were removed by the second smoothing step, which is applied on the transponder minus master combination.

The mega phase jumps, *volatile* and other phase jump events, where the post-fit rms after deglitching is larger than 0.1 cycle are usually removed with the first smoothing step from master and transponder phase (cf. section 6.3). This threshold is shown by the dark red dashed line in fig. 6.9 a) and b). All glitch events, which actually are removed by the first smoothing step, are indicated by dark green crosses inside the corresponding blue circles.

101 phase jump events are marked as master *volatile* in light pink filled circles and 12 *volatile* events are illustrated by the yellow circle filling for the transponder.

As shown in table 6.1, transponder *volatile* events are always removed from the master phase as well, as long as they are also identified as glitches on the master. Therefore, one can find three transponder *volatile* which are not removed from the master phase (cf. fig. 6.9 a)), because their pre-fit rms was $< 10^{-3}$ cycles so they were not processed by the regular deglitching and by the first smoothing step. Additionally, 99 *volatile* events from the master are not removed

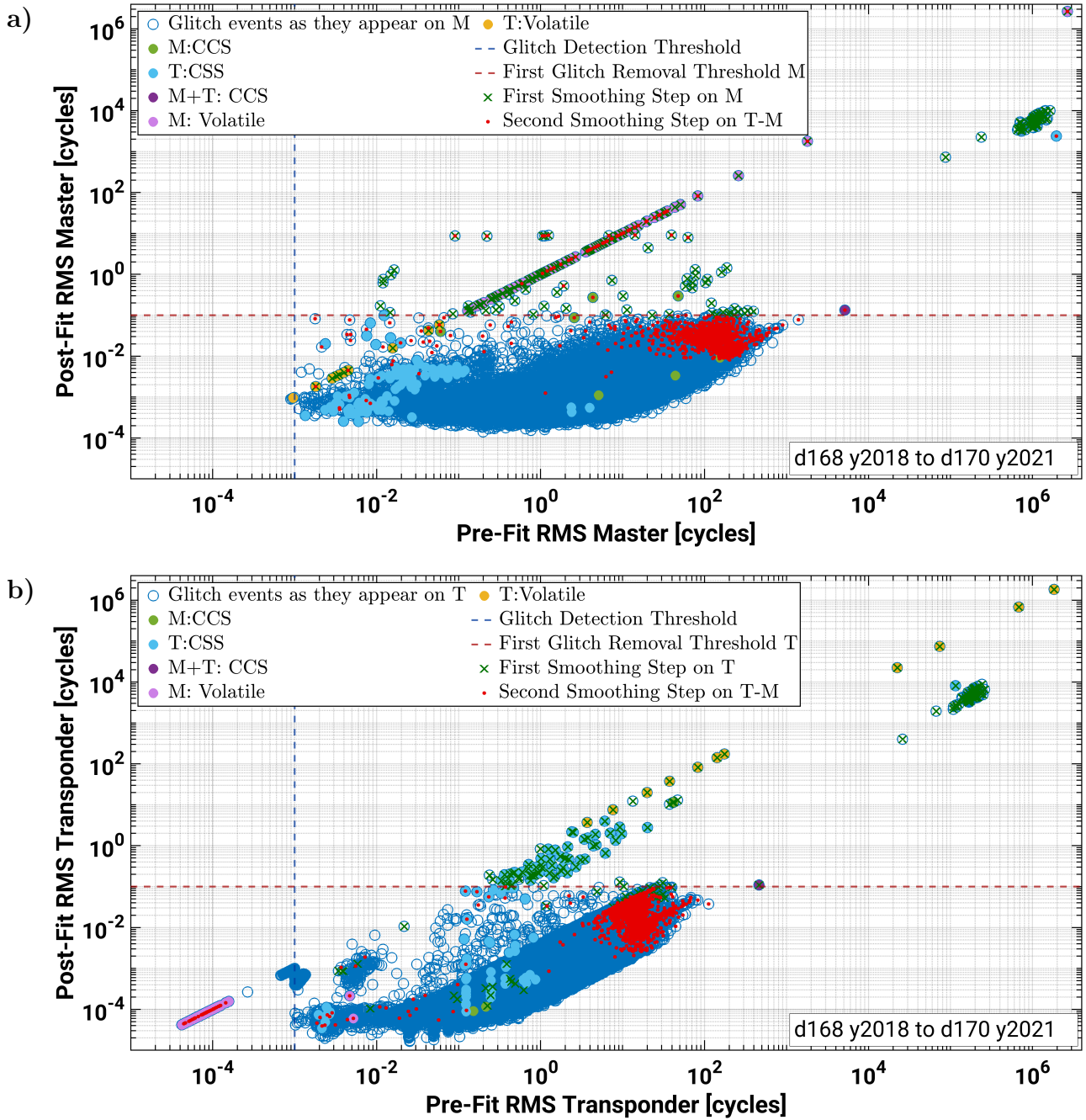


Figure 6.9: Analysis of first and second smoothing step for glitches as they appear on a) master and b) transponder. The glitch pre-fit residual is shown on the x-axis and the post-fit rms after deglitching on the y-axis. *Volatile* events or phase jumps, which were not reduced sufficiently, i.e. the rms of the post-fit residual is > 0.1 cycle, are removed from the phase data by the first smoothing step. Only some CCS of master and transponder are above this threshold for a), because the deglitching works differently for CCS than for PJ removals. However, a second smoothing step is applied on the phase data to remove such remaining glitch residuals from the LRI phase. The *volatile* events are represented by a straight line, because the pre-fit rms value was also used for the post-fit rms.

in the transponder phase, since they were not identified as transponder glitches or the usual deglitching step was sufficient.

It should be noted that the *volatile* events are represented as a straight line, because the post-fit rms would be zero after the removal and that can not be shown in the logarithmic plot. Therefore, the pre-fit rms-value was used again.

After the deglitching and first smoothing step, some data points with a master post-fit rms > 0.1 cycles still exist (cf. fig. 6.9 a)). One reason for that are Channel Cycle Slips (CCS), because the deglitching uses another threshold for removing them from master and transponder phase (cf. table 6.1). CCS in master or transponder phase are marked by a circle filling of green (7 events) and light blue (111 events), and CCS which appear in both satellites are highlighted in purple (1 event). Here, the deglitching tries to reduce the transponder post-fit rms divided by the fitted peak-to-peak phase jump size h below 0.2 with different models. The reader should be reminded that the threshold for typical PJs is $\text{rms}(\text{post-fit})/h < 0.002$. Consequently, the deglitching works not as good for CCS as for the normal phase jump removal. However, these affected data points are considered, among others, in our second smoothing step. The second smoothing step is applied on the difference of transponder and master phase. This additional glitch removal (1585 events) is represented by the light red dots.

One can also see, that many events (122) are marked with the first and second smoothing step in the master plot in fig. 6.9 a). One reason could be that the first removal was not sufficient and e.g. the *volatile* events, which were previously not removed from the transponder, due to the small pre-fit rms value, might now couple into the transponder minus master combination.

Finally, one can see for the transponder glitch events from fig. 6.9 b) that our deglitching algorithm ensures a suppression from pre-fit rms to post-fit rms by a factor of ≈ 1000 , when the pre-fit rms is between 0.1 and 100 cycles. This statement is also valid for the master glitches for pre-fit rms values between 1 and 100 cycles (cf. fig. 6.9 a)).

The same glitch events for the master are also shown in fig. 6.10. But in contrast to the other figures the pre-fit rms is illustrated on the y-axis and the x-axis shows the fitted peak-to-peak size of the phase jumps.

Obviously, the majority of the glitches, which show a magnitude of > 30 cycles are smoothed, due to the non-negligible effect onto the LRI measurement. Only a few glitches with a similar PJ height do not need the second smoothing, because sometimes the amplitudes of the residuals of the transponder minus master combination cancel out. From this plot one can also see, that ≈ 100 glitches from transponder and master phase are larger than 100 cycles and that the majority of the PJs is smaller than 30 cycles.

In summary, our deglitching ensures a suppression between pre-fit rms and post-fit rms by a factor of ≈ 1000 . All glitches with a larger size or untypical phase disturbances like *volatile* will be removed from the first smoothing step on master and transponder phase, while all events which still appear as

$$|\text{hpf}(\dot{\varphi})| > 0.3 \text{ Hz} \quad (6.40)$$

in the transponder minus master phase are going through the second smoothing step, to achieve a smooth LRI phase.

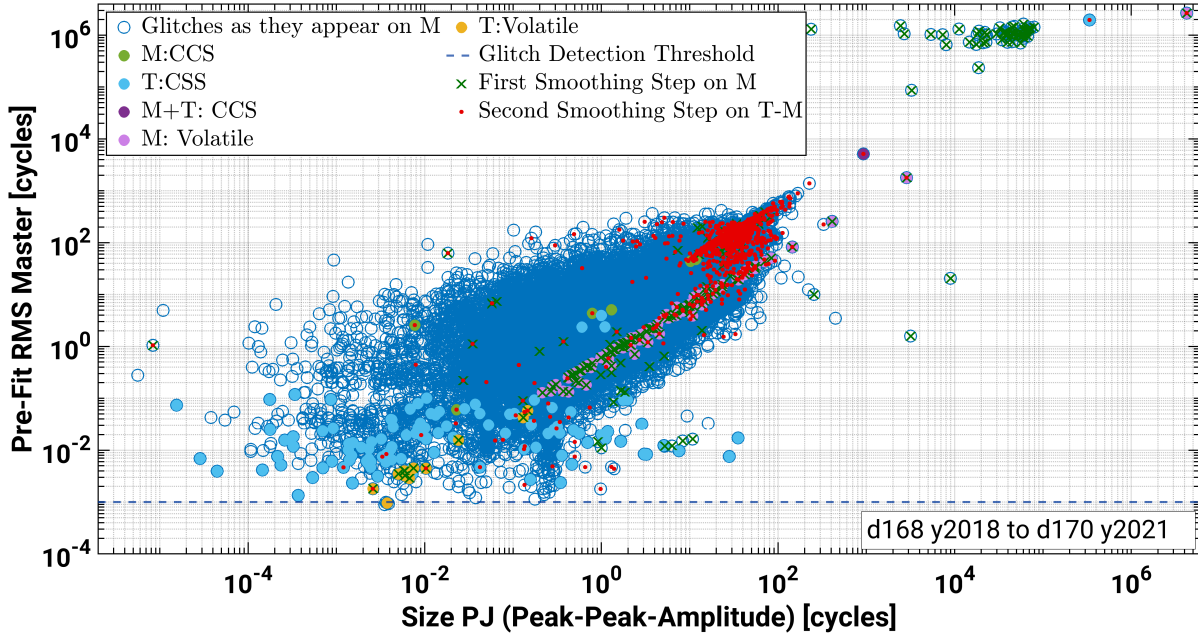


Figure 6.10: Analysis of first and second smoothing step for the PJ peak-to-peak size for the master phase. The glitch pre-fit residual is shown on the y-axis and the corresponding PJ size on the x-axis. The majority of the glitch events is smaller than 30 cycles. 87 glitch events as they appear in the master phase and 94 events as they appear in the transponder phase are larger than 100 cycles.

6.8 Latest Adjustments of First and Second Smoothing Step

In the course of this thesis, a suboptimal smoothing was observed and fixed afterwards. In the previous processing, the first smoothing step fitted a linear trend onto the first and last sample of the time derivation of the glitch segment, before it was integrated to the phase again. The same approach was used for the second smoothing step, where the selected segment consists of ± 5 samples around the event to be smoothed. An example for both cases is given in fig. 6.11. On September 5th, 2020 occurred a mega phase jump, which is removed by the first smoothing step. On September 2nd, 2020 did not occur any mega phase jumps, but some larger glitch residuals were left in the transponder minus master combination, such that the second smoothing approach is applied.

To reduce the ASD level for the orange and dark red curve in fig. 6.11, it was necessary to use a polynomial of higher order to ensure a smooth connection between the actual samples and the fitted ones. Therefore, we choose a third order polynomial which is fitted onto the first and last two samples of the corresponding phase rate segment.

By comparing the old and new smoothing steps with fig. 6.11 one can clearly observe an improvement for the data quality of φ_{LRI} .

LRI1B v50 products generated after 2021-07-27 are using the new smoothing approaches.

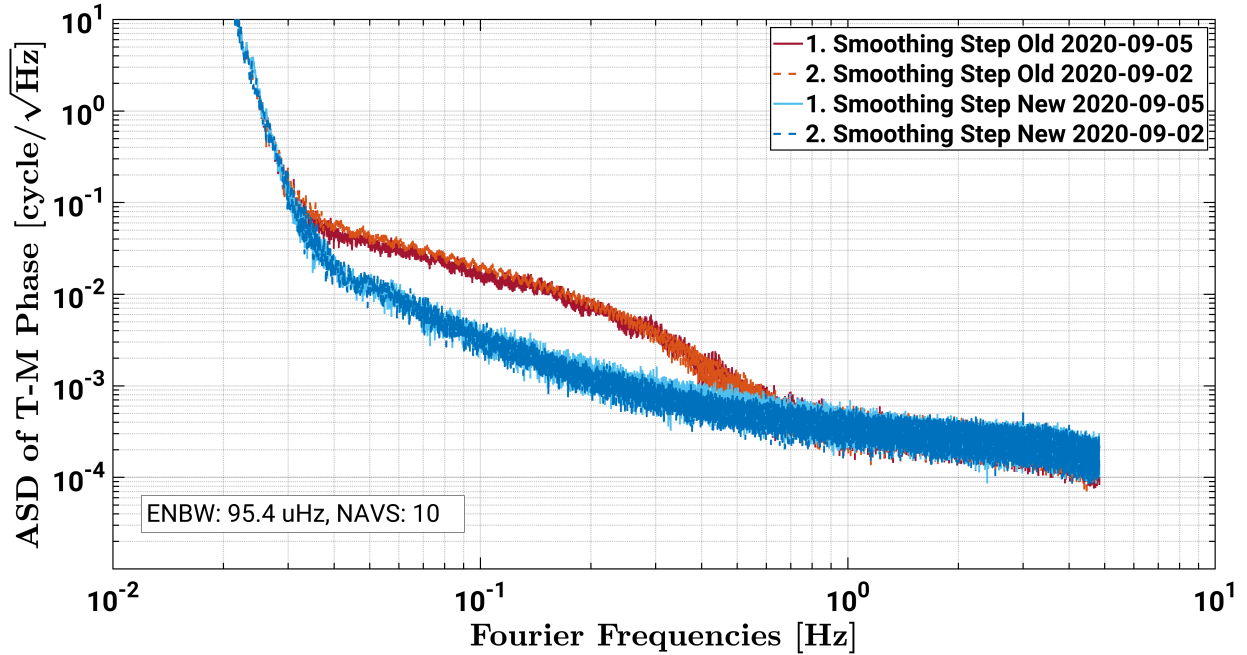


Figure 6.11: Improvement for the LRI spectrum at single days, where the first or second smoothing step needs to be applied. Instead of fitting a linear trend (old smoothing) onto the affected samples at the phase rate, a polynomial of degree three (new smoothing) is used for v50 data generation since 2021-07-27.

6.9 Converting Phase to Distance Measurement

To convert the LRI phase φ_{LRI} from cycles into a physical length in meter, it is necessary to know the absolute laser frequency ν of the master spacecraft (cf. section 4.3). This laser frequency of approx. 281 THz is stabilised by the cavity. There is no direct measurement of the frequency performed in-flight, hence, the frequency needs to be determined by other means.

In this section we want to present the implementation of two different approaches for determining the laser frequency. The first model uses a cross-calibration of LRI and KBR data (cf. section 6.9.1). The second model, which is still under investigation at AEI, is based on on-ground measurements and it is refined with in-flight data (cf. section 6.9.2). Both models yield a time dependent conversion factor $c_0/(2 \cdot \nu(t)) = \lambda(t)/2$, which is used for deriving the LRI biased range as shown in eq. (4.20).

The derived conversion factor $\lambda(t)/2$ in units of meter is reported in the fifth column of the LRI1B v50 product. Furthermore, the time shift $\Delta t_{\text{LRI-KBR}}$ between LRI and KBR data is reported in column fifteen of LRI1B v50 in units of nanosecond. The derivation of both columns is addressed in the following sections.

6.9.1 Cross-Calibration LRI and KBR

The SDS team determines the absolute laser frequency by cross-calibrating the KBR and LRI measurement on a daily basis [Wen, 2019]. This is also one of the methods at AEI that can be used to produce a LRI1B v50 set. Therefore, the LRI biased range and the KBR instantaneous range in the two-way-ranging (TWR) combination are cross-correlated with the

function `computeScaleTimeshift`, which is explained in appendix A.3 in more detail. This function determines a scale factor s and a time shift Δt between the two datasets, such that the quantity

$$\begin{aligned} & \text{rms}(\rho_{\text{LRL_TWR}}(t + \Delta t) \cdot s - \rho_{\text{KBR_TWR}}(t)) \\ & \approx \text{rms}(s \cdot \rho_{\text{LRL_TWR}}(t) + s \cdot \Delta t \cdot \dot{\rho}_{\text{LRL_TWR}}(t) - \rho_{\text{KBR_TWR}}(t)) \end{aligned} \quad (6.41)$$

is minimized. Here, $\dot{\rho}_{\text{LRL_TWR}}$ is the first derivative of the LRI biased range, the so called range rate. Besides that, the input datasets are debiased and detrended as it is explained later.

Thus, the LRI range is adjusted closer to the KBR range by using s and Δt . It should be noted that effects inside the KBR data could couple into the LRI data via the scale factor and time shift, when using this cross-calibration approach.

Preparation of KBR_TWR Range: In general LRI and KBR should measure the same instantaneous range (distance between the two S/C center of mass), such that the relation

$$\rho_{\text{KBR_inst}} = \rho_{\text{LRI_inst}} + \text{const.} \quad (6.42)$$

is valid. The instantaneous range of the KBR $\rho_{\text{KBR_inst}}$ can be derived from the KBR biased range $\rho_{\text{KBR_DOWR}}$, which is based on the so called dual-one-way-ranging (DOWR) combination, and its correction terms for the KBR antenna offset $\delta\rho_{\text{ant_corr}}$ and for a light time correction ($\mathcal{L}_{\text{DOWR}}$), such that

$$\rho_{\text{KBR_inst}} = \rho_{\text{KBR_DOWR}} + \delta\rho_{\text{ant_corr}} + \mathcal{L}_{\text{DOWR}} \cdot \quad (6.43)$$

It should be noted that the KBR biased range already contains an ionospheric correction [Wen, 2019]. For preparing the KBR data, one day of KBR1B v04 is taken and computed as shown with eq. (6.43).

The instantaneous range of the LRI could be derived from the LRI biased range $\rho_{\text{LRL_TWR}}$ and the so called LRI light time correction \mathcal{L}_{TWR} , which was presented in section 4.3 (eq. (4.27)), i.e.

$$\rho_{\text{LRI_inst}} = \rho_{\text{LRL_TWR}} + \mathcal{L}_{\text{TWR}} \cdot \quad (6.44)$$

The abbreviation TWR indicates the two-way-ranging combination of the LRI. This LRI light time correction is taken from LRI1B of v04 and is interpolated from its 0.5 Hz time-tags onto the 0.2 Hz KBR1B data. Afterwards, it is subtracted from $\rho_{\text{KBR_inst}}$ to derive an intermediate quantity that would be measured if the KBR system would be based on the two-way-ranging (TWR) principle. The expression can be derived by inserting eq. (6.44) and eq. (6.43) into eq. (6.42) and is called KBR_TWR range in the following, i.e.

$$\underbrace{\rho_{\text{KBR_DOWR}} + \delta\rho_{\text{ant_corr}} + \mathcal{L}_{\text{DOWR}} - \mathcal{L}_{\text{TWR}}}_{\rho_{\text{KBR_TWR}}} = \rho_{\text{LRL_TWR}} + \text{const.} \cdot \quad (6.45)$$

Data Preparation LRI and Correlating with KBR: In the very beginning of the LRI1B v50 generation a preliminary LRI1B product is derived using

$$\begin{aligned} \rho_{\text{LRL_TWR},0}(t + \Delta t) &= s \cdot \frac{\lambda_0}{2} \cdot \varphi_{\text{LRI}}(t + \Delta t) \\ &= s \cdot \frac{c_0}{2 \cdot \nu_0} \cdot \varphi_{\text{LRI}}(t + \Delta t) \end{aligned} \quad (6.46)$$

with $\nu_0 = 281759829\text{MHz}$, $s = 1$, $\Delta t = 0\text{s}$. As long as the scale factor s is a scalar (and not a time-dependent series), the relation in eq. (6.46) can be used. The resulting $\rho_{\text{LRI_TWR}}$ needs to be interpolated onto the 0.2 Hz KBR time-grid.

In the next step, the LRI biased range $\rho_{\text{LRI_TWR}}$ from the first estimation of the LRI1B product (iteration $i=0$) and the derived $\rho_{\text{KBR_TWR}}$ are used. First of all, the two ranges are divided into segments, when an IPU or LRP reboot occurs, or when the SNR of the Ka-Band of KBR has dropped rapidly (jumps larger than 10 dB-Hz). The latter one is a rare case and was observed e.g. on 2019-10-16 (doy 289). The following calculations only consider segments larger than 6 hours, because the correlation over shorter segments is less reliable.

The segments of 0.2 Hz LRI and KBR data are de-biased, such that the first sample starts at zero. Subsequently both data sets are detrended².

Now the LRI_TWR range and KBR_TWR range are correlated with the numdiff-method of `computeScaleTimeshift` (cf. appendix A.3), to derive a scale factor s and a time shift Δt as it was shown in eq. (6.41). The LRI1B product is calculated again by applying the derived factors as

$$\nu_i = \frac{\nu_{i-1}}{s} \quad \Rightarrow \quad \rho_{\text{LRI_TWR},i} = \frac{c_0}{2 \cdot \nu_i} \cdot \varphi_{\text{LRI},i=0} \quad (6.47)$$

$$\Delta t_i = \Delta t_{i-1} + \Delta t \quad \Rightarrow \quad t_{\text{LRI},i} = t_{\text{M}} - \Delta t_i - \Delta t_{\text{CRN}} \quad (6.48)$$

on the 10 Hz phase data. Here, t_{LRI} denotes the GPS time-tags of LRI phase or range observations, which contains the fitted offset between KBR and LRI and an offset of Δt_{CRN} , which is introduced in section 6.10. All these steps are repeated until the difference of $|\Delta t_{i-1} - \Delta t_i|$ is less than 10^{-10} s, or if six iterations ($i = 1 \dots 6$) have been completed. We rename the final time shift Δt_i to $\Delta t_{\text{LRI-KBR}}$.

The scale factor and time shift are be stored for each day. If a day contains multiple data segments, an averaged value for the whole day is computed.

Interpolating Scale and Time Shift: If a LRI1B product is computed for a period longer than one day, then the processing continues with the next days. In the end s and $\Delta t_{\text{LRI-KBR}}$ are assigned to the nearest time-tag at 12 o'clock (noon), and the first/last s and $\Delta t_{\text{LRI-KBR}}$ will be assigned to the start/end of the time series. Then the scale factor and time shift are interpolated to the 10 Hz time series (e.g. for one week or month). That is done to avoid jumps at the day bounds in the LRI biased range, when the scale factor is applied (cf. section 7.1). In this case the absolute laser frequency becomes time-dependent and must be applied as it was introduced with eq. (4.20). The final LRI biased range $\rho_{\text{LRI_TWR}}$ is renamed to ρ_{LRI} .

For future v50 releases, this processing step will be further refined. The scale factor and time shift should be weighted according to the segment length, when a day is split into segments due to instrument reboots. Additionally, we plan to investigate if the scale and time shift can be interpolated onto the 10 Hz rate in each iteration and if this alters the results. This could potentially reduce the risk that the iterations converge to their optimal states when the scale is day-wise constant, but by interpolating in the very end we compute a different state and provide that as LRI1B set.

²The range of KBR and LRI show a sinusoidal oscillation with the orbit period of GFO. Therefore, we estimate the linear trend based on points in the beginning and on points in the end, which are separated from each other by a multiple of the orbit period.

6.9.2 Calibrated Frequency Model

Presumably, in next geodesy missions a Microwave Instrument will not be present, which would not allow to perform the presented cross-calibration approach. For that reason the AEI develops an alternative method for deriving the absolute laser frequency from other LRI telemetry, like temperature values and laser set-points. These set-points are reported in the LHK1A data product, which is presented in detail in appendix B.3. The temperature of the laser is measured at the Thermal Reference Point (TRP) at the outside of the laser shielding. In 2021, this TRP measurements are not publicly available in the Level 1 data.

The alternative model uses a linear model based on measurements before the satellites were launched. Later on, the model was refined with in-flight data and is improved by further investigations. A publication on this topic is in preparation, for a few more details please refered to [Misfeldt et al., 2020].

This model yields a time dependent laser frequency $\nu(t)$. Additionally, $\nu(t)$ is smoothed by a moving mean over the orbital period, because only the long-term variations of the actual laser frequency are desired. The 1/rev oscillations from temperature variations are suppressed, because they are caused by chances of the laser temperature and not by the cavity, which defines the laser frequency. The resulting $\nu(t)$ is applied on the LRI biased range as shown in eq. (4.20). Here, the time shift $\Delta t_{\text{LRI-KBR}}$ between KBR and LRI is set to a fix value of 73 μs , because this is the mean value seen in fig. 7.3.

6.10 CRN Filter

The biased range will be filtered with a so called CRN-filter (N convolutions of a rectangle [Thomas, 2000]) to suppress high frequency noise. The approach of Wu et al. [2006] is used. The used parameters for filtering are shown in table 6.2.

Parameter	Value
Sampling rate f_s	9.664 Hz (GF1), 9.664198 Hz (GF2)
Optimal frequency f_0	0.176 mHz
Cut-off frequency f_c	0.25 Hz
Filter length in samples N_f	747
Convolution number N_c	9

Table 6.2: Parameters for the CRN-Filter.

The impulse response from the CRN filter coefficients of GF1 is computed for fig. 6.12. The impulse response is symmetric around its maximum at the 374-th filter coefficient. Therefore, the phase delay of such a Finite Impulse Response (FIR) filter can be computed by

$$\Delta t_{\text{CRN}} = \frac{(N_f - 1)}{2f_s} \approx 38.59\text{s} \quad (6.49)$$

and it has to be considered for all filtered data streams. That means the GPS time-tags, which are corrected by the $\Delta t_{\text{LRI-KBR}}$, need to be shifted by Δt_{CRN} as well, as it was shown in section 6.9.

In the next step the Discrete Fourier Transformation is computed from the filter coefficients, to show the filter response in the frequency domain. As an example, the LRI 9.664 Hz data

(GF1) for one day consists of $N = 834960$ samples. The filter coefficients were expanded with $N - N_f = 834213$ samples of zero (zero-padding), to achieve the filter response also for smaller frequencies that are relevant for the LRI. This vector $[1 \times N]$ is denoted as C_{CRN} .

Forming the DFT of a time series with real numbers yields a vector $\tilde{C}_{\text{CRN}}(f)$ of the same size, but it consists of complex numbers for negative and positive frequencies. However, the coefficients are the same for positive and negative frequencies. Thus, only the first half of the $\tilde{C}_{\text{CRN}}(f)$ is taken. Computing its absolute value results in the magnitude M of the filter response, which can be expressed in Decibel as

$$M_{\text{dB}} = 20 \cdot \log_{10}(|\tilde{C}_{\text{CRN}}(f)|) . \quad (6.50)$$

The magnitude describes the suppression of the signal at different frequencies by the filter. From fig. 6.13 can be seen, that the filter starts to affect Fourier frequencies around the cut-off frequency and suppresses the higher frequencies, which are larger than the cut-off frequency.

The phase delay for all frequencies can also be computed by

$$\psi = \arctan\left(\frac{\text{Im}(\tilde{C}_{\text{CRN}}(f))}{\text{Re}(\tilde{C}_{\text{CRN}}(f))}\right) \quad (6.51)$$

$$\Delta t_{\text{CRN}}(f) = \frac{\psi}{2\pi f} , \quad (6.52)$$

where the phase ψ in radian results from the imaginary (Im) and real (Re) part of the complex elements of $\tilde{C}_{\text{CRN}}(f)$.

In fig. 6.14 the phase delay $\Delta t_{\text{CRN}}(f)$ in the frequency domain is shown. The previously calculated value of 38.59 s (see eq. (6.49)) remains constant for Fourier frequencies < 0.33 Hz. For frequencies above this threshold the phase delay is oscillating. However, these frequencies are already suppressed by ≈ 100 dB, as it was shown with fig. 6.13. Additionally, the final data for the LRI1B product will be available in a rate of 0.5 Hz, so that the Nyquist frequency is the current cut-off frequency of $f_s/2 = 0.25$ Hz. That means the oscillating phase delay for higher frequencies does not affect the data for LRI1B at all.

Finally, it is shown how the CRN filter affects the LRI ranging data. The LRI 9.664 Hz data of GF1 from the first January 2019 is taken. The blue curve in fig. 6.15, which belongs to the left y-axis, shows the Amplitude Spectral Density of the biased range.

The dark red curve (y-axis right) denotes the absolute value $|1 - M|$, to show how the CRN filter affects data at lower frequencies like 1/rev. This is not apparent from fig. 6.13, where the suppression at higher frequencies is visible. The CRN filter was constructed to have a very small effect at the orbital frequency 0.176 mHz, which is obviously the case considering a value with $6 \cdot 10^{-16}$. For values larger than ≈ 0.16 Hz, the curve increases rapidly to 1.

This dark red curve is multiplied element-wise with the ASD of the LRI biased range, to compute the light red curve (y-axis left). This curve suggests, for example, at 1/rev only a distortion of the ranging signal at the level of $1 \cdot 10^{-13} \text{ m}/\sqrt{\text{Hz}}$. Obviously, the CRN filter does not distort the gravity signal in the ranging data significantly, which is present at frequencies below 100 mHz.

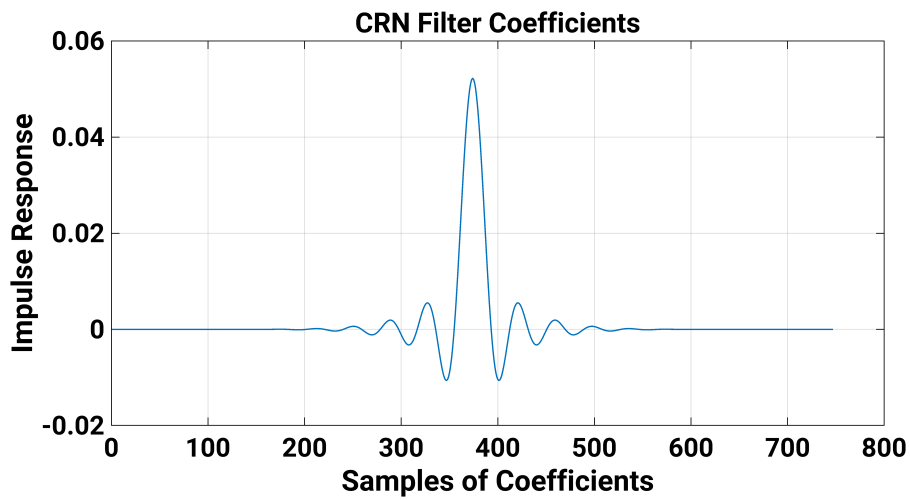


Figure 6.12: Impulse response of CRN filter coefficients. The main peak is centered around the 374 coefficient.

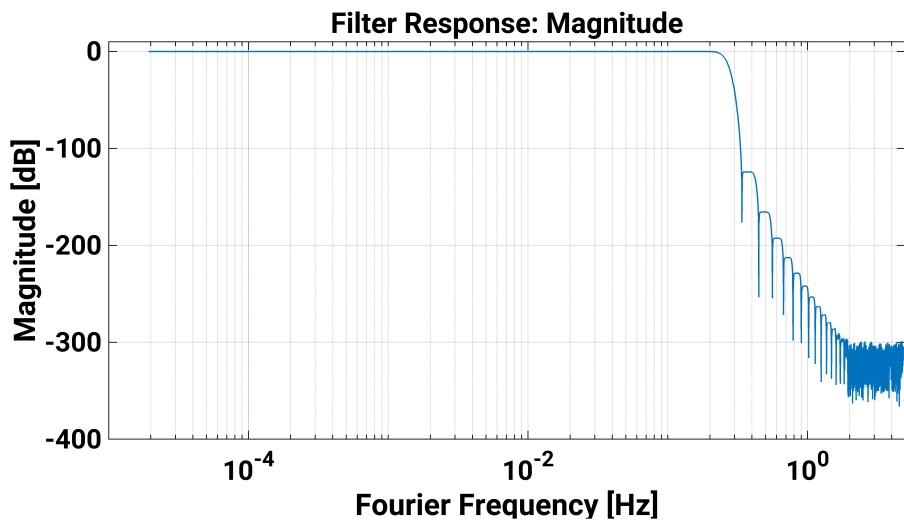


Figure 6.13: Impulse response in frequency domain.

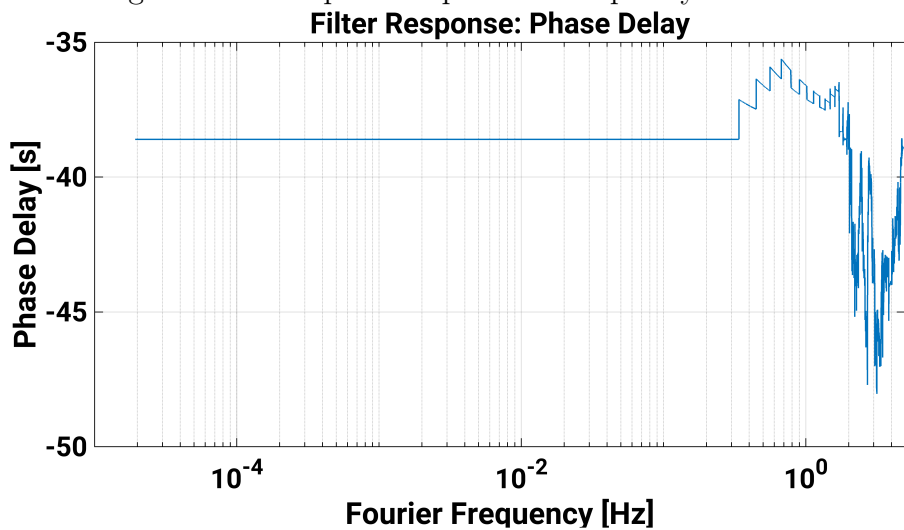


Figure 6.14: Resulting phase delay of CRN filter.

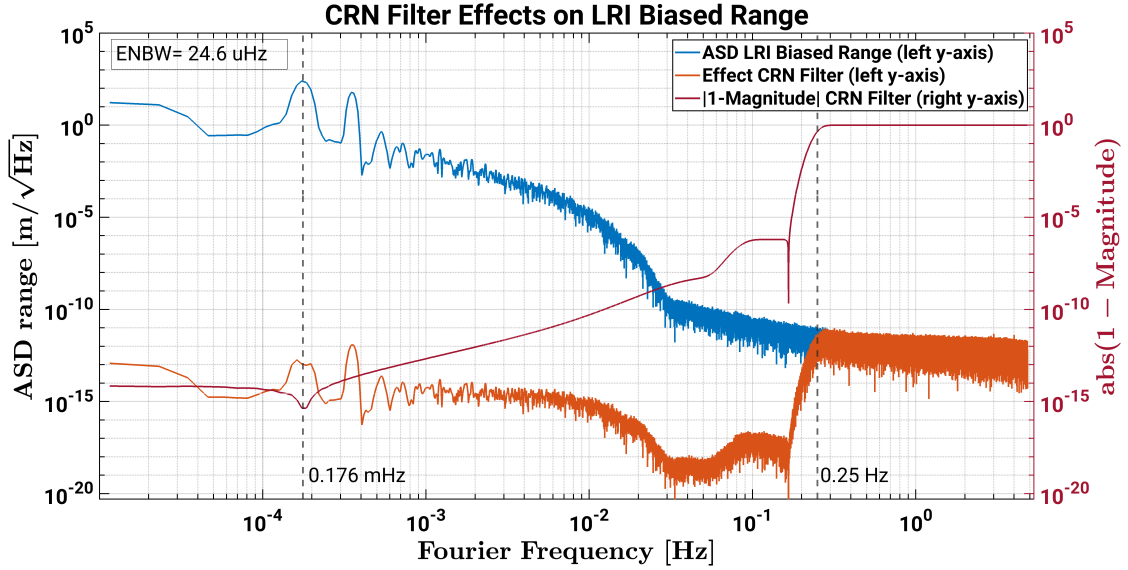


Figure 6.15: CRN filter effect on LRI biased range for January 1st, 2019. The ASD of the LRI biased range in blue, belongs to the left y-axis. The dark red curve shows the effect of $|1 - M|$ of the CRN filter (y-axis right). The light red curve illustrates the product from the dark red and blue curve, which is the undesired distortion of the signal at low frequencies.

6.11 Preparation of Different Data Streams for LRI1B

The LRI phase data is divided into segments due to LRP reboots. The corresponding absolute laser frequency, the time offsets $\Delta t_{\text{LRI-KBR}}$ and Δt_{CRN} are used for these data segments in order to derive the corrected LRI time-tags and the CRN filtered LRI biased range as 10 Hz data. Due to the CRN filter warm-up, it is necessary to cut out a few samples at the beginning of each segment. Here, a number of 400 samples is chosen, which correspond to ≈ 40 s. In addition to the 10 Hz data (biased range, conversion factor $\lambda/2$ and the time shift $\Delta t_{\text{LRI-KBR}}$), the LRI1B data contains the light time correction $c_0 \mathcal{T}_{\text{TWR}}$ introduced in section 4.3. The GNI1B v04 orbit product is used to derive it. The resulting data has a rate of 0.2 Hz. Furthermore, the enhanced CNR with a sampling rate of 0.1 Hz is computed from `LriHealthMonitor` data with eq. (4.31).

Afterwards, all these different data streams are interpolated onto a 0.5 Hz time-grid, which is the usual rate of the LRI1B format. Therefore, it is necessary to determine a data point every 2 seconds, using the even seconds of one day. The interpolation is performed with the function `interp1_highprecision`, which was mentioned in section 6.5, such that the integer and fractional time-tags can be used as two doubles. The chosen interpolation method is ‘spline’. Another peculiarity concerns the quality flag that has to be taken into account in this down-sampling process. All events that are indicated on the 10 Hz data, but are shorter than 2 seconds in time, needs to be enlarged to at least 20 samples, so that each event is still marked on the 0.5 Hz data.

It should be noted that gaps in the LTC are also considered. If a gap is larger than 300 s, all data streams are also divided into segments for LTC breaks. That means, when no LTC data is available, the other data is also not included for LRI1B. In case of smaller gaps, the LTC is interpolated for this period.

6.12 Time Derivatives and Removal of Instabilities

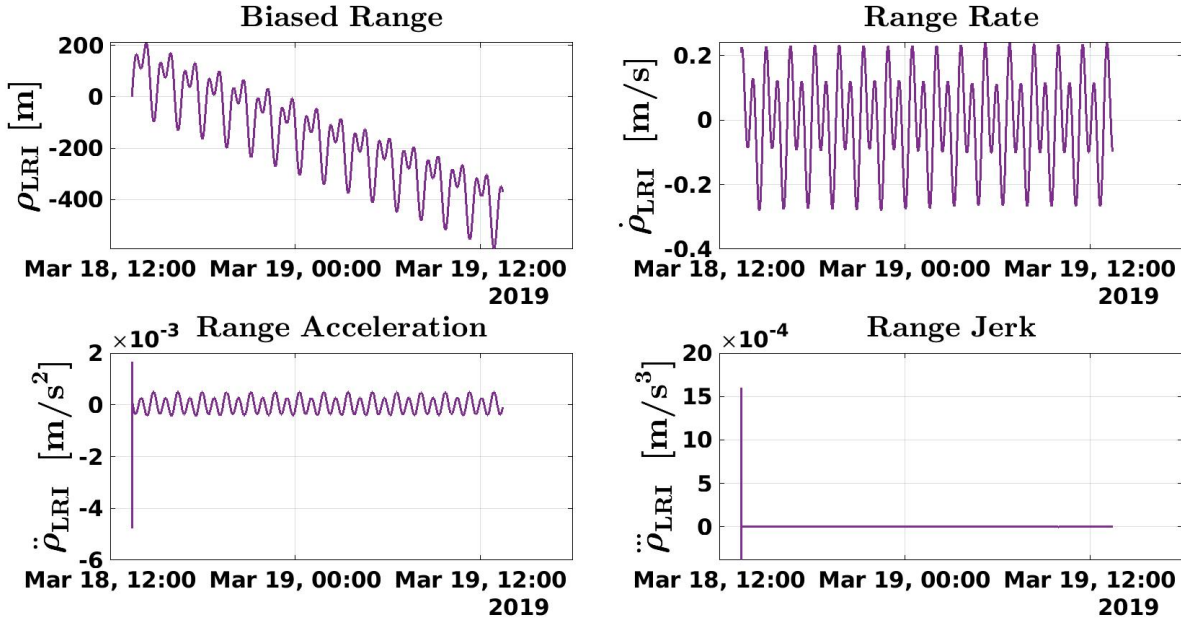


Figure 6.16: Calendar week 12 in 2019 shows an unstable phase behaviour after the LRI was turned on again on March, 18. The link was lost again on the next day. A few samples in the beginning of this segment have to be cropped out, because the range jerk $\ddot{\rho}_{\text{LRI}}$ exceeds the threshold of $5 \cdot 10^{-6} \text{ m/s}^3$.

Further on the first and second time derivatives of the biased range and of the corresponding light time correction are computed for each generated segment with a central 5-point numerical differentiation method. This yields the so-called range rate, range acceleration, light time rate and light time acceleration. The method is introduced in appendix A.2.

The formulas in eq. (A.25) and eq. (A.26) are implemented in our processing for computing the derivatives. The function is called

$$\text{numdiff}(\rho_{\text{LRI}}, f_s = 0.5 \text{ Hz}, 5, \text{order}) \quad (6.53)$$

and needs the time series which should be differentiated. Furthermore, the sampling rate $f_s = 1/h$ for determining the sample spacing h in time and the method number 3 or 5 is needed. Here, the latter one for the centered 5-point numerical differentiation method is chosen. Finally, the order of 1 or 2 for computing the first or second time derivative is entered to the function. Appendix A.2 points out that the first and last two samples need a different calculation, which is why one should use a little bit larger time series as necessary, to avoid jumps at the segment boundaries (cf. fig. A.6). However, sometimes it is not possible to choose a larger time span, because the data is interrupted by lost locks or LRP restarts. These jumps are usually small and will be removed when they exceed a certain threshold. This will become clear in the following example, where an unusual phase oscillation was observed and removed.

In calendar week 12 in 2019 (March, 18-24), the LRI was turned on again on March, 18 around 12:00 p.m. and the lock was lost again on March, 19 at approx. 13:30.

The derivatives of the biased range for this data segment are depicted in fig. 6.16 and show a few more instabilities in the beginning. However, these are not related to the calculation method of the derivatives. Sometimes the cleaning step (cf. section 6.1) in our processing is not sufficient and a few instabilities (phase oscillations) remain.

To remove unstable behaviour like this, the third derivative is calculated additionally, which is called range jerk in the following. Our processing removes a few more samples in the beginning or ending, where the difference between two samples of $\ddot{\rho}_{\text{LRI}}$ is larger than $5 \cdot 10^{-6} \text{ m/s}^3$ plus five more samples. Usually the range jerk is about $\pm 2 \cdot 10^{-6} \text{ m/s}^3$ and shows a difference between consecutive samples of $< 10^{-7} \text{ m/s}^3$ at 0.5 Hz rate.

6.13 Post-Processing Steps for Quality Flag of LRI1B

Phase Breaks The AEI decided to reset the biased range to zero meter at the beginning of a new month and whenever the phase measurement was interrupted, e.g. due to a LRP reboot. This should prevent extremely large numerical values for the biased range, which could reduce the precision due to double floating-point representation. These phase breaks are marked as bit 0 in the quality flag of v50 data to indicate the beginning of a new phase segment (cf. table 6.3).

Sun-Blinding Sun-blinding periods are data quality reducing events. In this special time span, which repeats approx. every six months, the orbital plane of the satellites is aligned with the sun in such a way, that the sun-light falls into the aperture and saturates the DC measurement of the QPDs. The phase measurement might be falsified during the events and an increased occurrence of PJs and cycle slips can be expected. The last LRI1B processing step scans through the QPD DC values of each satellite, which are available in the `LaserTlm` packets, and identifies such events based on the four QPD channels

$$\frac{\text{DC}_1 + \text{DC}_2 + \text{DC}_3 + \text{DC}_4}{4} \geq 3500 \text{ counts} , \quad (6.54)$$

where DC_i is the i th QPD DC value. This sun-blinding condition is marked with bit 4 in the quality flag (cf. table 6.3). In periods of sun-blinding each satellite is affected by approx. 30 s per orbit.

Momentum Transfer Events Bit 6 of the v50 quality flag shows Momentum Transfer Events (MTEs), which could result from e.g. micro-meteorites from space dust and hit one of the satellites. This events are stored in a separate data bank at AEI, and result from an analysis of accelerometer and LRI phase data. The corresponding GPS time for each event are used to mark the MTEs in the 0.5 Hz quality flag.

6.14 Summary of the Generated LRI1B v50 Product

Usually, the LRI1B v50 is computed on a calendar week basis (with overlap) and is stacked together to monthly solutions. These monthly solutions are divided at the day bounds and are written in a text file for the daily LRI1B, which has a compatible format to the official LRI1B v04 files. This space-separated table, which includes all the time-tags and computed data streams in a time sorted order, is shown in table 6.3. Additionally, the text file contains a YAML-formated header with information about the creator and a description of content for the columns of LRI1B v50. One month of such LRI1B v50 files is compressed to the *.tgz format and needs ≈ 85 MB in storage.

Column	Parameter	Unit	Type	Information
1	GPS time-tag	s	[uint32]	Seconds past 2000-01-01 12:00:00.
2	biased_range	m	[double]	Inter-satellite distance.
3	range_rate	m/s	[double]	First derivative of biased_range.
4	range_accl	m/s ²	[double]	Second derivative of biased_range.
5	scale factor	m	[double]	Factor to convert phase to range: $\lambda/2$.
6	lighttime_corr	m	[double]	Light time correction for biased_range.
7	lighttime_rate	m/s	[double]	Light time correction for biased_rate.
8	lighttime_accl	m/s ²	[double]	Light time correction for biased_accl.
9	ant_centr_corr			Not defined. In future TTL coupling.
10	ant_centr_rate			Not defined. In future TTL coupling.
11	ant_centr_accl			Not defined. In future TTL coupling.
12	CNR GF1	dB-Hz	[uint32]	Carrier to noise density ratio for GF1.
13	Ka_A_SNR			Not defined.
14	CNR GF2	dB-Hz	[uint32]	Carrier to noise density ratio for GF2.
15	time shift	ns	[int32]	Time offset between KBR and LRI. LRI time was corrected by $-\Delta t_{\text{LRI-KBR}}$.
16	qualflg		[string]	Quality of the data is indicated with bit 0-7. Bit 0 starts rightmost. Bit 0: Phase breaks. Bit 1: Phase data was smoothed. Bit 2: Phase Jumps removed. Bit 3: Mega Phase Jumps removed. Bit 4: Sun-blinding period. Bit 5: Other phase disturbances. Bit 6: Momentum transfer event. Bit 7: not defined.

Table 6.3: Summarised information of LRI1B v50 format.

It should be noted that the format of LRI1B is also used for KBR1B within the SDS processing. Therefore, a few columns are not defined for the LRI1B data, and the AEI team decided to use them for other important parameters while maintaining the format of SDS LRI1B v04. For instance, column 15 includes usually the SNR values for the Ka-Band of GF2 (or nothing for LRI), however, LRI1B v50 provides the applied time offset $\Delta t_{\text{LRI-KBR}}$ between the KBR and LRI data sets in units of nanoseconds. Furthermore, in future releases of AEI, it is planned to insert a correction for the tilt-to-length coupling in the columns for the antenna offset correc-

tions of KBR, which are also not defined for LRI.

Another difference to the SDS LRI1B v04 product is the specification of the scale factor ϵ . In case of v04, ϵ is provided in column five of LRI1B v04. The factor $(1 + \epsilon)$, which is equivalent to our scale factor s , can be multiplied with the nominal laser wavelength λ_0 for deriving the absolute wavelength of the master laser. This procedure is equivalent to multiplying with the speed of light c and divide with the nominal frequencies, i.e. [Wen, 2019]

$$\lambda_{\text{GF1}} = \frac{(1 + \epsilon) \cdot c}{2.81616393 \cdot 10^{14} \text{ Hz}}, \quad \lambda_{\text{GF2}} = \frac{(1 + \epsilon) \cdot c}{2.81615684 \cdot 10^{14} \text{ Hz}}. \quad (6.55)$$

In contrast to that, v50 data provides directly the factor $\lambda/2$, which can be applied immediately to the LRI biased range, if one wants to re-scale the biased range into a phase. Important differences for the data of LRI1B v04 and v50 will be presented in chapter 7.

All other columns are similar to the v04 data product. However, we indicate a lot of different events within the v50 quality flag, where all different meanings are summarised in the last row of table 6.3. Additionally, all quality flag events, which has been occurred between June 2018 and July 2021 are illustrated in fig. 6.18. This plot serves also as a calendar, where the ranging data availability can easily be seen from.

To provide an overview, the flowchart in fig. 6.17 summarises all the processing steps of the LRI1B v50 generation. The light blue boxes indicate the single processing steps, which are explained in detail in the sections of chapter 6. The white boxes show which data streams go into the next (light blue) processing step. In the beginning, each quadrant of the photodiodes of master (M) and transponder (T) get a different colored arrow. After the first processing step, one mean clean phase for each spacecraft results. These are indicated in pink and purple arrows. In the end of the processing step of computing the phase difference between master and transponder, only one dark blue array for the LRI ranging phase remains. Obviously, these data is processed to the biased range, range rate and range acceleration on a 0.5 Hz rate and ends in the LRI1B product. Furthermore, the dark red data visualises the included time offset and scale factor from the applied frequency model, the orange data gives the computation of the light time correction, and the green arrow describes the inserted CNR.

Additionally, it is possible to summarise all the applied time corrections and time shifts for a LRI time-tag, i.e.

$$t_{\text{LRI1B}}^{\text{GrGPS}} = \tau_M^{\text{USO}} + t_{\text{total_corr}} - \Delta t_{\text{CRN}} - \Delta t_{\text{LRI-KBR}} - 630763200 \text{ s}. \quad (6.56)$$

With the initial LRP time-tag τ_M^{USO} , the smoothed time-tag correction $t_{\text{total_corr},M}$ from DTRs, TIM1B, CLK1B (cf. section 6.4) and an included correction for the decimation filter delay (cf. eq. (3.10)), the phase delay Δt_{CRN} due to the CRN filter (cf. section 6.10), and the time offset $\Delta t_{\text{LRI-KBR}}$ between KRB and LRI data (cf. section 6.9).

Summary LRI1B v50 Processing Steps

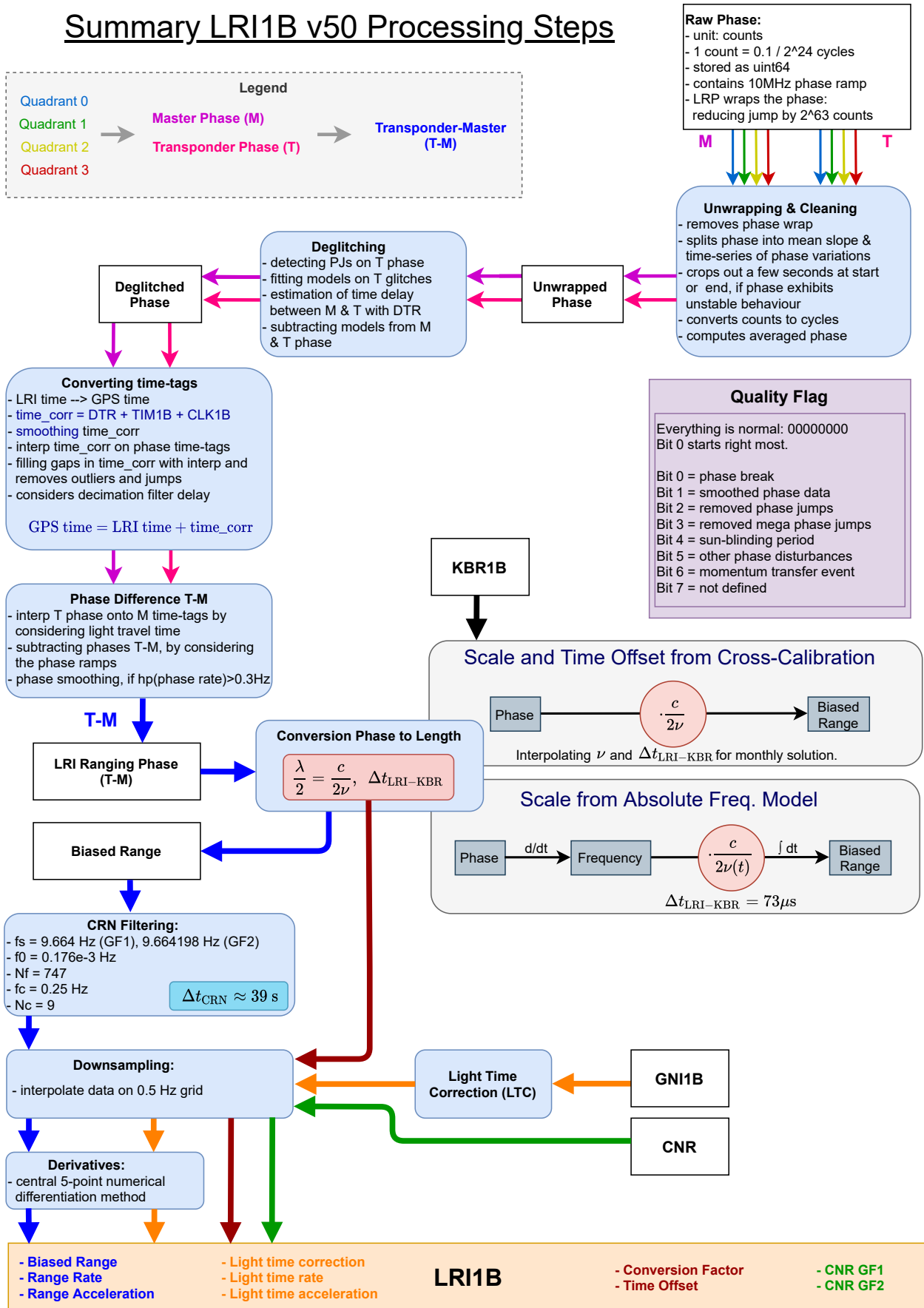


Figure 6.17: Overview of AEI processing steps for the LRI1B data product. All steps are explained in detail in the subsections of chapter 6.

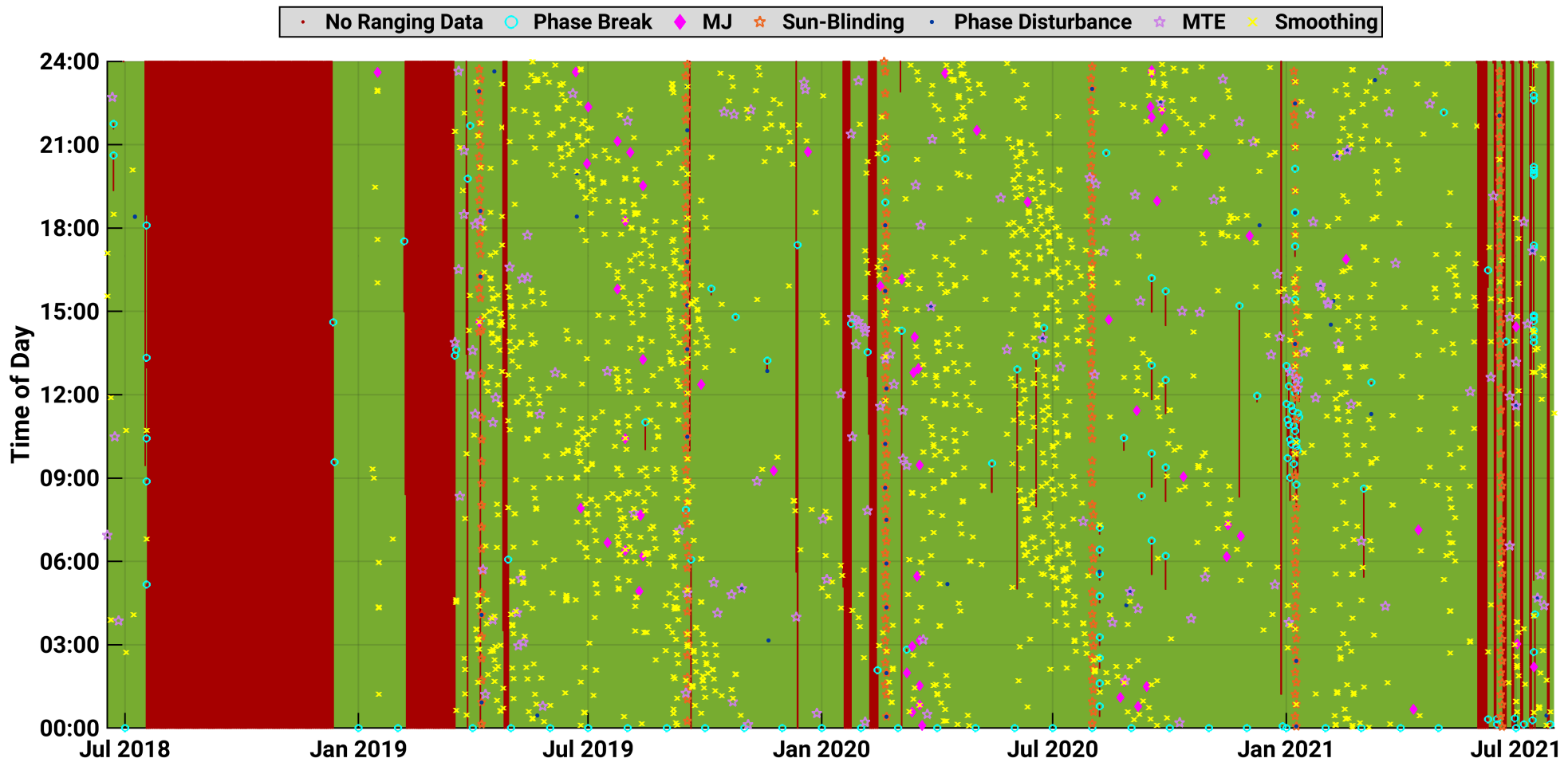


Figure 6.18: Availability of LRI1B v50 data and occurring events from v50 quality flag. Whenever ranging information is available, the background color is shown in green. Normal phase jump events are also assigned to this green data. All other events which might affect the LRI phase measurement are illustrated with different markers. It should be noted that the smoothing event refers to the second smoothing step from section 6.6.

7

Verifying the Official LRI Level 1B Product

In chapter 6, the derivation of the LRI1B v50 product was explained in detail. Now, the differences and commonalities between the publicly available LRI1B v04 and the alternative AEI v50 data is presented. The following comparison could only be done for a few different months that can serve as examples. However, every month from June 2018 to July 2021 were processed at AEI. An overview of the availability of the LRI1B v50 data product is shown in a calendar-like illustration in fig. 6.18.

Here, special attention is paid to the different scale factor estimations in section 7.1, to the effects from different deglitching algorithms in section 7.2 and section 7.3, to the light time corrections of each product in section 7.4, and to the deviation of the first and second time derivatives in section 7.5.

7.1 Comparison of Scale Factor and Time Shift

Scale Factor / Absolute Laser Frequency: The scale factor ϵ for scaling the nominal laser frequency of the master laser to the absolute values is reported in column five of v04. The relation was introduced with eq. (6.55). ϵ is derived on a daily basis by minimizing the difference between LRI and KBR [Wen, 2019], which is similar to the presented cross-calibration method in section 6.9.1. The relation between our cross-calibration scale factor s and the scale factor ϵ of v04 is $s = (\epsilon + 1)$. It should be noted that our scale factor $s = (\epsilon + 1)$. However, the AEI provides a conversion factor of $\lambda_{\text{corr}}/2$, which is the absolute value for re-scaling the one-way biased range back into the two-way phase measurement. The reader is reminded that the conversion factor of AEI can be computed with two different models, where both results become a continues time-dependent series. Therefore, column five has to be applied in the range rate domain and afterwards one has to integrate the derived phase rate (cf. section 6.9). It is possible to convert the conversion factor of AEI to the SDS scale factor ϵ by using the approach

$$\epsilon = \frac{\lambda_{\text{corr}}}{\lambda_0} - 1 = \frac{\nu_0}{\nu_{\text{corr}}} - 1 \quad (7.1)$$

with $\nu_{0,\text{GF1}} = 2.81616393 \cdot 10^{14}$ Hz and $\nu_{0,\text{GF2}} = 2.81615684 \cdot 10^{14}$ Hz.

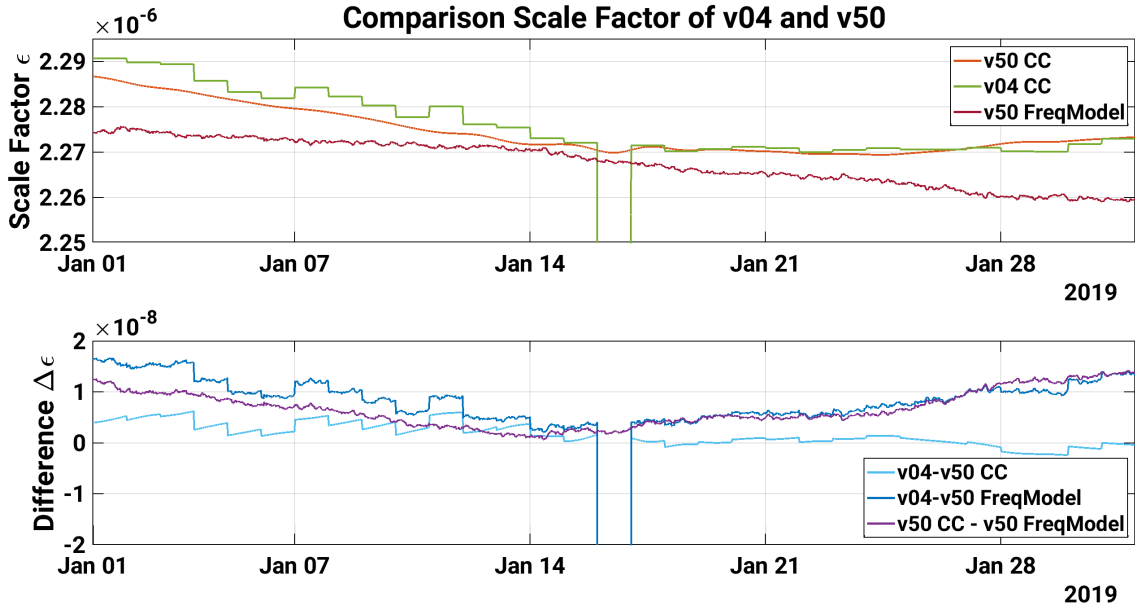


Figure 7.1: Comparison of the estimated scale factors for v04 and v50 models for January 2019. The upper plot shows the results for ϵ , while the lower plot is illustrating the differences between each model. The cross-calibration approach is abbreviated with CC and the calibrated frequency model with FreqModel. The outlier on the 16th in the v04 scale factor is related to a mega phase jump, which has not been sufficiently removed.

A comparison of ϵ from the two AEI methods, the cross-calibration (CC) approach and the calibrated frequency model (FreqModel), w.r.t. the SDS v04 cross-calibration is plotted in fig. 7.1. In the upper subplot, the resulting ϵ values are shown with a light and dark red curve for v50 models and with a green curve for the scale factor of v04. The period of January 2019 was chosen.

The differences between the models are illustrated in the lower subplot. The light and dark blue curves presenting the residuals between v04 and v50 solutions and the purple one shows the difference between the two AEI models.

The observed behaviour of the green v04 curve is a step wise change at every day bound, due to the daily ϵ generation. In contrast to that, both AEI models show a continuous course, which obviously does not evoke jumps at day bounds. Both models are close to the results of v04. Only one larger difference can be found on January 16th. Here, the scale factor of v04 contains a large jump, which does not fit into the other data points. Most likely, the estimation of the scale factor was falsified by a mega phase jump in the LRI phase. The AEI deglitching step was able to remove that mega phase jump, thus, the scale factor is more meaningful.

The maximal scale factor differences in January 2019 between v50 and v04 cross-calibration show values up to $|\Delta\epsilon| \approx 7 \cdot 10^{-9}$, and for v04 CC and v50 FreqModel $|\Delta\epsilon| \approx 1.6 \cdot 10^{-8}$, which is comparable to a difference of the absolute laser frequency of $|\Delta\nu| \approx 1.8$ MHz and $|\Delta\nu| \approx 4.5$ MHz (except for January 16th). The largest difference between CC v50 and FreqModel v50 correspond to a frequency offset of $|\Delta\nu| \approx 4$ MHz.

Misfeldt et al. [2020] shows residuals between v04 CC and v50 FreqModel for the period of December 2018 until July 2020 with magnitudes of $\Delta\epsilon < \pm 7 \cdot 10^{-8}$, which corresponds to ± 20 MHz in the absolute laser frequency.

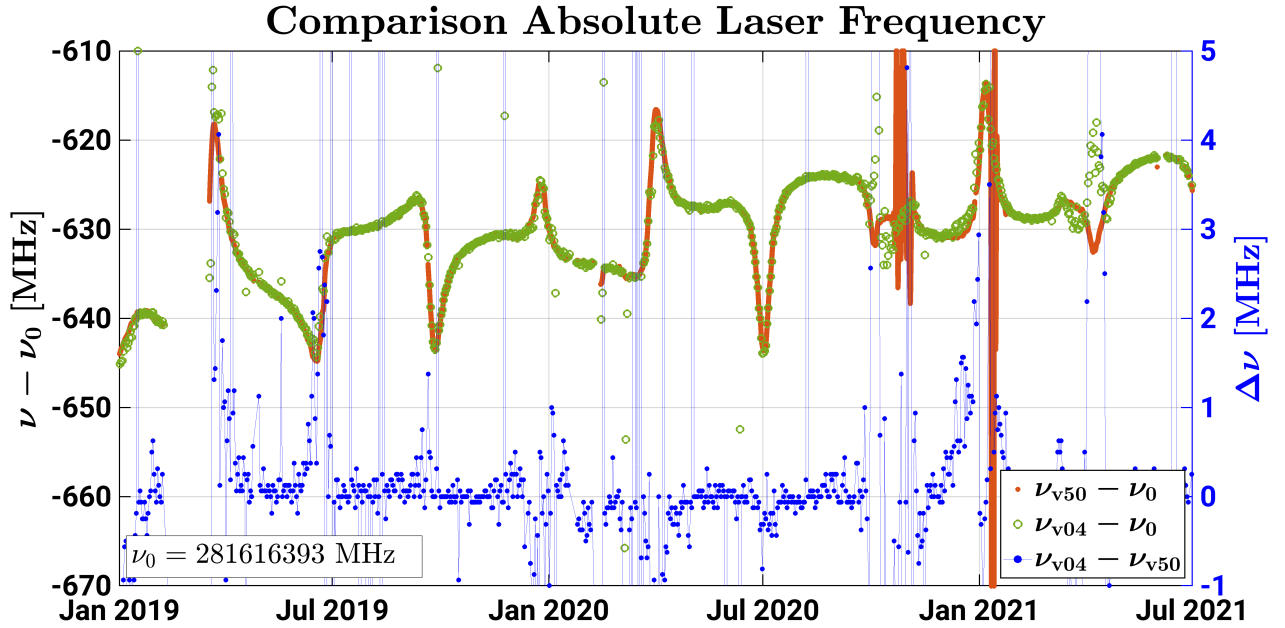


Figure 7.2: Comparison of the absolute laser frequency of v04 (green, 2019 until d161 2021) and v50 (red, 2019 until d181 2021) determined from LRI-KBR cross-calibration. The blue curve is described by the right y-axis, and shows the differences between v04 and v50. The results of both models match up to ± 1 MHz when some outliers are neglected.

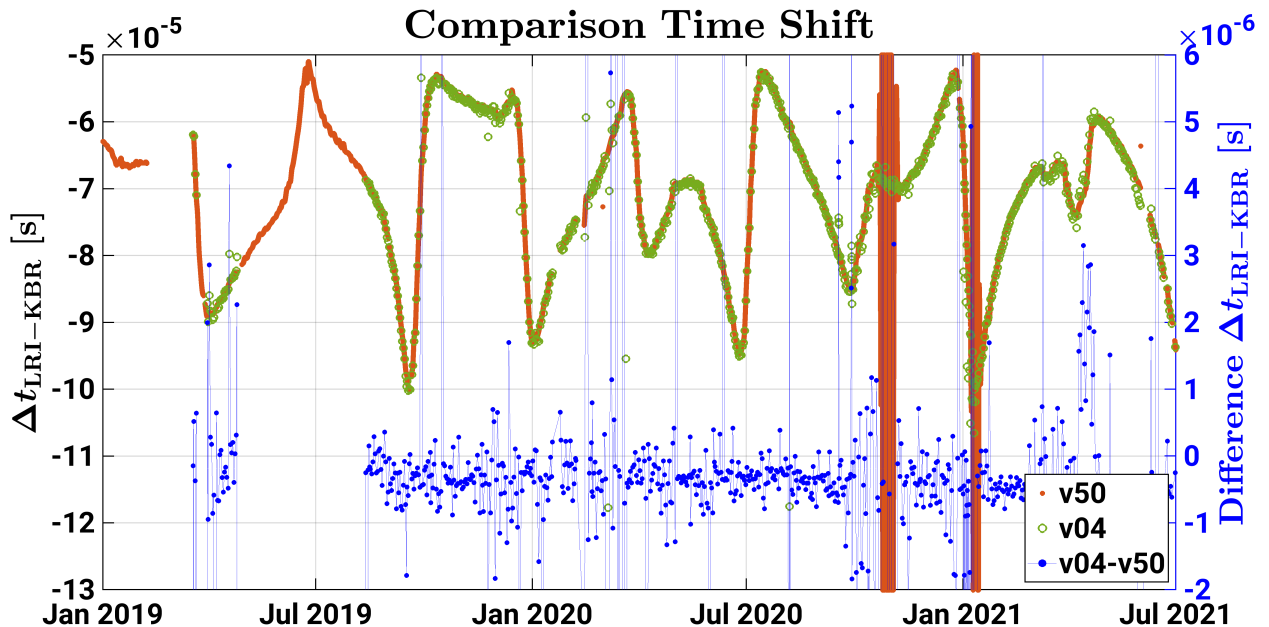


Figure 7.3: Comparison of the time offset $\Delta t_{\text{LRI-KBR}}$ between LRI and KBR data, which is generated during the LRI-KBR cross-calibration process of v04 and v50. The corresponding results are shown in green (2019 until d161 2021) and red (2019 until d181 2021). The blue curve is described by the right y-axis and shows the difference. For the majority of the days there is a difference of $\pm 1 \mu\text{s}$.

For the cross-calibration method, a plot was generated to show the estimated absolute laser frequency values of v04 and v50 for a longer period between January 2019 until June 2021. The deviations from the nominal laser frequency $\nu_0 = 281616393$ MHz, which was selected by SDS based on some early and rather inaccurate assessment, for v04 and for v50 are illustrated in green and red in fig. 7.2. The blue trace shows the difference between the derived frequencies of v04 and v50, and it belongs to the right y-axis. Neglecting some outliers, the differences between the data sets is about ± 1 MHz on average.

Some outliers in the v50 frequency estimation are observed in October 2020 (calendar week 43-45) and January 2021 (calendar week 12). At this time, our processing has some problems with the smoothed time-tag correction, due to incorrect CLK1B data for the transponder. We had already removed unusual CLK1B data manually and smooth the data using interpolation for some days in 2019 and 2020. This manual data screening and cleaning was not performed for October 2020 and January 2021, but will be performed as soon as possible. In table 7.1 are shown affected days, which are already considered for the v50 processing and also the mentioned time spans, which needs to be adjusted soon.

Also some of the green data points in fig. 7.2 can be identified as outliers. A few of them do not fit into the pattern. Due to the scaling of the y-axis not all green outliers are visible. However, they can still be identified from the blue vertical lines. As mentioned before one reason for the outliers in v04 scale factor estimations results from not fully removed phase jumps or mega phase jumps.

It can be concluded that the fitted scale factor, i.e. the fitted absolute laser frequency of v04 and v50, show similar results for most days in the time span of January 2019 to June 2021. The observed pattern in fig. 7.2 is probably not related to actual frequency variations. We assume that other effects like thermal variations on the satellites or tone errors could cause this pattern. Therefore, the AEI is still working on the FreqModel, to consider effects of this kind. Additionally, parts of the pattern could also result from errors in the KBR system, which might couple into the LRI measurement by cross-calibrating the two data sets.

Time Shift between LRI and KBR: During the cross-calibration process, one can also derive a daily time shift between the data sets of KBR and LRI (cf. section 6.9). The derived time offset of SDS is reported as the sum of CLK1B and $\Delta t_{\text{LRI-KBR}}$ in the LLK1B product [Wen, 2019]. Therefore, one can subtract the columns of `eps_time` from LLK1B v04 and CLK1B v04, to get the estimated time shift of v04, which is illustrated by the green circles in fig. 7.3. In contrast to that, the AEI provides its $\Delta t_{\text{LRI-KBR}}$ in the unused column 15 of LRI1B v50. This data is marked by red dots. Again, the blue curve shows the differences between the two time offsets on the right y-axis.

In the time spans for January to March and for May to August in 2019, one can observe larger time offsets for the v04 data, which are not visible in fig. 7.3, due to the smaller range of the y-axes. The largest time offsets in v04 data were estimated in the beginning of August 2019 with magnitudes of ≈ 0.1 s. At this time, SDS estimates the datation bias and the $\Delta t_{\text{LRI-KBR}}$ in the LRI/KBR cross-calibration, which seems to result in large offsets for $\Delta t_{\text{LRI-KBR}}$. However, SDS adjusted their computation for data since 2019-08-10. Since then, SDS is using the Datation Reports from the `gis1` files, instead of estimating the datation bias and the $\Delta t_{\text{LRI-KBR}}$ together in the cross-calibration process [Wen et al., 2020]. This yields the well-behaving time offsets in v04 for the period between August 2019 to June 2021. These time shifts are similar to the results of v50. Their differences are only between $\pm 1\mu\text{s}$, when

previously mentioned outliers are omitted. Here, the observed pattern is also not related to real variations in the time delay between the KBR and LRI. Usually the time shift should be constant as long as there are no instrument reboots, because both measurements are taken with the time information from the same USO.

Period Start	Period End	S/C	Period Start	Period End	S/C
2019-11-06 19:36	2019-11-07 07:42	D	2020-11-13 11:45	2020-11-13 16:35	D
2020-03-14 13:08	2020-03-14 21:43	D	2020-11-17 06:18	2020-11-17 09:40	C
2020-06-02 16:26	2020-06-03 00:55	C	2020-11-20 21:44	2020-11-21 03:26	C
2020-07-14 20:44	2020-07-15 11:46	C	2020-11-24 05:05	2020-11-24 14:59	C
2020-08-09 20:32	2020-08-10 11:47	C	2020-12-02 13:03	2020-12-02 22:32	D
2020-10-03 18:30	2020-10-04 12:05	D	Not considered yet:		
2020-10-02 03:55	2020-10-03 20:43	C	2020-10-22 20:18	2020-10-23 13:50	D
2020-10-08 21:01	2020-10-08 21:06	C	2020-10-26 21:50	2020-10-27 08:15	D
2020-10-12 02:06	2020-10-12 04:39	D	2020-10-28 19:30	2020-10-29 07:45	D
2020-11-09 18:27	2020-11-10 04:36	D	2020-11-02 19:52	2020-11-03 07:00	D
2020-11-11 02:15	2020-11-11 16:35	D	2021-01-11 12:00	2021-01-12 12:15	D
2020-11-11 02:01	2020-11-12 03:30	C	Dates in 2018		

Table 7.1: Sometimes CLK1B v04 shows an unusual behaviour. Therefore, AEI corrects the listed CLK1B regions manually for achieving a correct mapping between LRP rcv time and GPS time. There exist a few more days, where AEI identified that a cleaning needs to be performed. This time spans are listed below the pink row.

7.2 Comparison of Biased Range for January 2019

Using the discussed scaling to convert the phase from cycles to a range in meter, as it is described in section 6.9, yields the biased range of v04 and v50 as shown in fig. 7.4 a) for January 2019. The biased range of v04 is colored in green and v50 in red, and their residuum in blue is shown with the right y-axis. Having a closer look at the blue trace, smaller jumps at every day bound are noticeable. These jumps in the residuum are related to the daily scale factor estimation of v04. To avoid these jumps in the biased range of v50, the scale factor from the cross-calibration method at AEI is interpolated from daily sampling to 10 Hz sampling for the monthly solutions. Additionally, the biased range will start at zero meter at the beginning of a new month, and whenever a LRP reboot was performed or the link was lost. This ensures that the numerical values of the range are not getting too large and numerical precision is guaranteed.

Some other important effects in fig. 7.4 a) can be observed in the difference. At January 12th and 26th IPU reboots occurred, which are related to the KBR data. As we will see later, these events can couple into the LRI data of v04 and can be identified by larger jumps at the beginning of each day, where the IPU has rebooted. Also, the mega phase jump on January 16 appears in that data, which is caused by the different deglitching algorithms. That mega phase jump leads to the additional 1/rev and 2/rev oscillations in v04.

For further analysis, the range offsets at day bounds arising from daily scale factor estimations and IPU reboots were removed from v04 data. Without these offsets, the difference between v04 and v50 biased range yields the plot in fig. 7.4 b). The remaining differences are in the magnitude of a few micrometer (except January 16th), which are possibly resulting from the

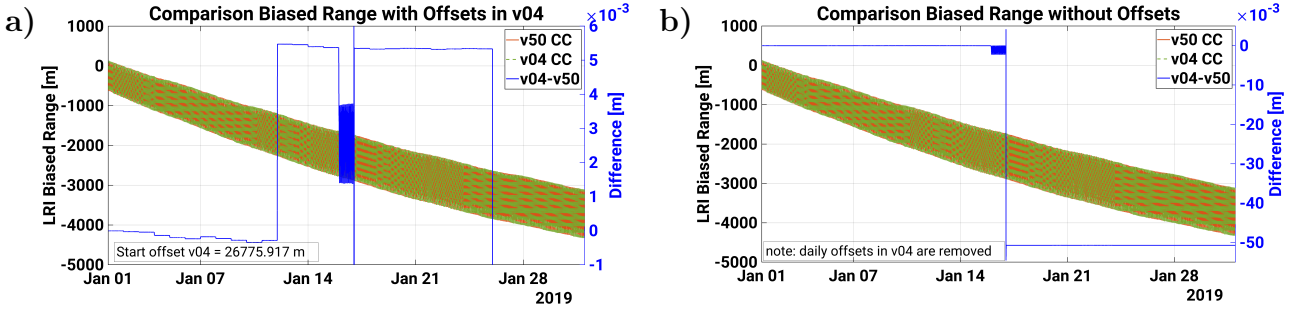


Figure 7.4: Time series of biased range for cross-calibration. **a)** With offsets at day-bounds in v04 data, and **b)** with manually removed offsets at day bounds in v04. The oscillations in the difference of v04 and v50 for January 16th, result from a not fully removed mega phase jump in v04 data.

different algorithms for removing phase jumps. This day bound offset correction allows creating more meaningful spectra for comparing the quality of the two data sets.

In fig. 7.5, the amplitude spectral density of the biased range of v04 and the two models of v50 are shown with the same color coding as before, for the whole January 2019. The light and dark red curve, for the v50 cross-calibration and the (latest) calibrated frequency model, respectively, show the same signal level for the biased range. The corresponding signal of the LRI biased range shows at $1/\text{rev}$ a value of approx. $154 \text{ km}/\sqrt{\text{Hz}}$. However, since $1/\text{rev}$ contains mainly a sinusoidal variation, the ASD value is not meaningful and can be related to a value of 365 m rms in the amplitude using the ENBW. The noise floor decreases from 10 to $1 \text{ nm}/\sqrt{\text{Hz}}$ for Fourier frequencies above 30 mHz.

The purple curve illustrates the difference of the two v50 models, which shows a rms amplitude at $1/\text{rev}$ of $\approx 2 \mu\text{m rms}$, and the noise level of $\approx 3 \text{ pm}/\sqrt{\text{Hz}}$ in the frequencies between 30-250 mHz.

A detailed discussion on the difference between CC and FreqModel is beyond the scope of this thesis. A publication on this topic is in preparation. The interested reader is referred to [Misfeldt et al., 2020].

Comparing the green (v04) and the light red (v50) curve, a higher noise level for v04 data can be found at Fourier frequencies larger than 20 mHz. The ASD of the biased range of v04, in case of January, has this higher noise level, due to the not fully removed mega phase jump on 2019-01-16. For single days or months without comparable MJs, v04 performs more similar to v50 data, as long as daily offsets are removed. This is apparent in fig. 7.9, where also the LRI biased range of v04 (green) is shown for January 1st, 2019.

The magenta curve is a noise estimation for an offset in the estimated absolute laser frequency. For this calculation the actual absolute laser frequency ν_{true} and the estimated absolute laser frequency ν_{est} are assumed to be differing in an offset of

$$\Delta\nu = \nu_{\text{true}} - \nu_{\text{est}} = 10\text{MHz} . \quad (7.2)$$

Here, the biased range computed from the LRI phase in cycles and ν_{est} , i.e.

$$\rho_{\text{LRI}}(\nu_{\text{est}}) = \varphi_{\text{LRI}} \cdot \frac{c_0}{2\nu_{\text{est}}} . \quad (7.3)$$

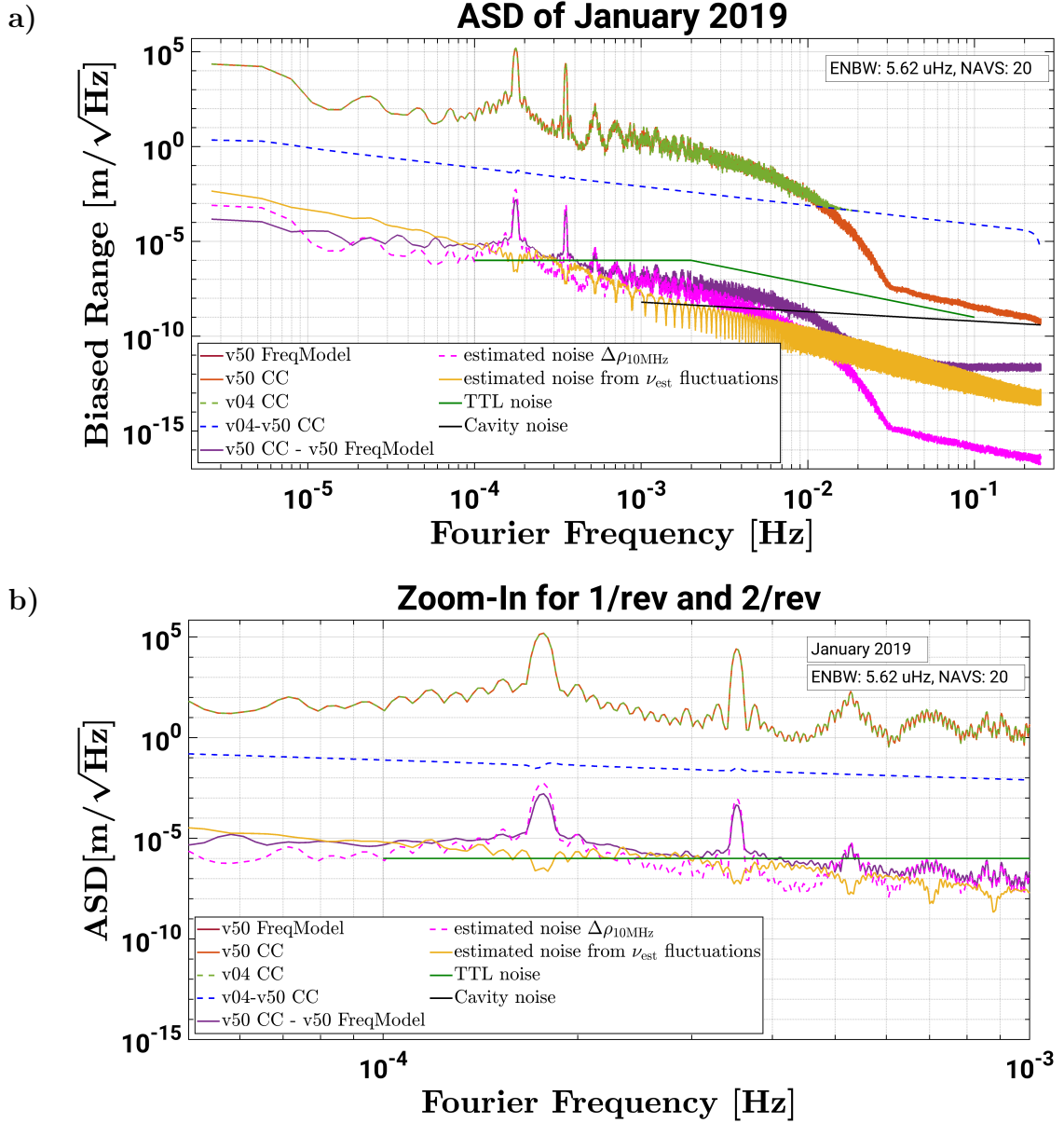


Figure 7.5: ASD of biased range for v04 and both models of v50 in January 2019. The whole ASD is shown in a) and a zoom-in for the frequencies of 1/rev and 2/rev in b).

Therefore, the true inter-S/C distance or the true biased range is defined as

$$\rho_{\text{LRI}}(\nu_{\text{true}}) = \rho_{\text{LRI}}(\nu_{\text{est}} + \Delta\nu) = \rho_{\text{LRI}}(\nu_{\text{est}}) + \Delta\rho, \quad (7.4)$$

where $\Delta\rho$ describes the resulting error for the biased range by using a 10 MHz incorrectly estimated absolute laser frequency. It can be calculated with the Gaussian error propagation (GEP) until the first order of the Taylor expansion, such that

$$\rho_{\text{LRI}}(\nu_{\text{est}} + \Delta\nu) = \rho_{\text{LRI}}(\nu_{\text{est}}) + \frac{1}{1!} \frac{d\rho(\nu_{\text{est}})}{d\nu_{\text{est}}} \cdot \Delta\nu + \dots \quad (7.5)$$

$$\Delta\rho = \rho_{\text{LRI}}(\nu_{\text{est}} + \Delta\nu) - \rho_{\text{LRI}}(\nu_{\text{est}}) = \varphi_{\text{LRI}} \left(-\frac{c_0}{2\nu_{\text{est}}} \cdot \frac{\Delta\nu}{\nu_{\text{est}}} \right) \quad (7.6)$$

$$\Delta\rho = -\rho_{\text{LRI}}(\nu_{\text{est}}) \cdot \frac{\Delta\nu}{\nu_{\text{est}}}. \quad (7.7)$$

This yields the error term for the biased range $\Delta\rho_{10\text{ MHz}}$ by assuming an frequency offset of $\Delta\nu = 10\text{ MHz}$, i.e.

$$\Delta\rho_{10\text{MHz}} = -\rho_{\text{LRI}}(\nu_{\text{est}}) \cdot \frac{10\text{MHz}}{\nu_{\text{est}}} . \quad (7.8)$$

The ASD of this modelled error is shown by the magenta trace. It has an rms amplitude of $\approx 10\mu\text{m}$ at 1/rev. That means the resulting error, due to a static $\Delta\nu = 10\text{ MHz}$ incorrectly estimated scale factor is larger in comparison to the purple curve at 1/rev. This is in agreement with section 7.1, where it was shown that the largest difference of $\nu_{\text{CC}} - \nu_{\text{FreqModel}} \approx 4\text{ MHz}$ in January 2019.

In order to estimate the effect of fluctuations in $\Delta\nu = \nu_{\text{true}} - \nu_{\text{est}}$, we investigate the fluctuations in ν_{true} and ν_{est} separately. The black curve is showing the level of a noise estimate for ν_{true} , i.e. for the laser frequency noise (LFN) due to imperfections in cavity stabilisation. This model approximates the induced ranging error by ([Spero, 2021] and [Abich et al., 2019])

$$\text{ASD}[\Delta\rho_{\nu_{\text{true}}}] = \frac{10^{-15} \cdot 200\text{km}}{\sqrt{f_{\text{Fourier}}}}, \quad 1\text{ mHz} < f_{\text{Fourier}} < 5\text{ Hz} . \quad (7.9)$$

The yellow curve is a noise estimate for the effect of fluctuations of the estimated absolute laser frequency ν_{est} into the biased range when the scale factor is applied. Assuming a relative velocity between the two spacecraft of 1 m/s and a mean value for the absolute laser frequency of 281 THz results in the following expression

$$\text{ASD}[\Delta\rho_{\nu_{\text{est}}}] = \frac{\text{ASD}[\nu_{\text{est}}]}{2 \cdot 281\text{ THz}} \cdot \frac{1\text{ m/s}}{2\pi f_{\text{Fourier}}} \quad (7.10)$$

with the factor 1/2 to achieve the noise for the one-way ranging error. Finally, it can be said that eq. (7.10) is an upper limit for the noise, induced by fluctuations of the modelled or estimated laser frequency ν_{est} . Due to the stability of the cavity we are expecting no actual signal for frequencies $> 1/\text{day}$, hence we use a moving mean filter with a length of the orbit period to suppress n/rev tones in our model and other frequency content at higher frequencies (cf. section 6.9.2). Therefore, one can observe these dips at n/rev in the yellow curve. For the remaining noise at frequencies $< 1/\text{day}$ it is not clear if that is related to a real signal or to some artifacts in ν_{est} . Therefore, the calibrated frequency model is still under investigation, where we try to achieve a model without all these variations, i.e. the yellow curve should possibly shift downwards for the lower frequencies.

Consequently, one must be aware that the real error from the absolute laser frequency is actually $\text{ASD}[\nu_{\text{true}} - \nu_{\text{est}}]$, however, it is unknown and can not be computed. Therefore, the yellow and black curve can only provide a first estimation for the induced ranging error.

7.3 Comparison of Biased Range September 2020

SDS improved the deglitching algorithm for data since July 2020 [Wen et al., 2020]. Here, September 2020 of v04 and v50 data is compared, because many events like several PJs, some MJs and other phase disturbances were observed in this month. Another reason is that we are interested to show the differences between v04 and v50 data, and the month of September shows a few days where the data quality of v04 shows more glitches than in other months.

An overview of the events in September 2020 is shown in fig. 7.6 in terms of the quality flag of v50 data. The phase break parameter in fig. 7.6 indicates gaps in the LRI data, due to a

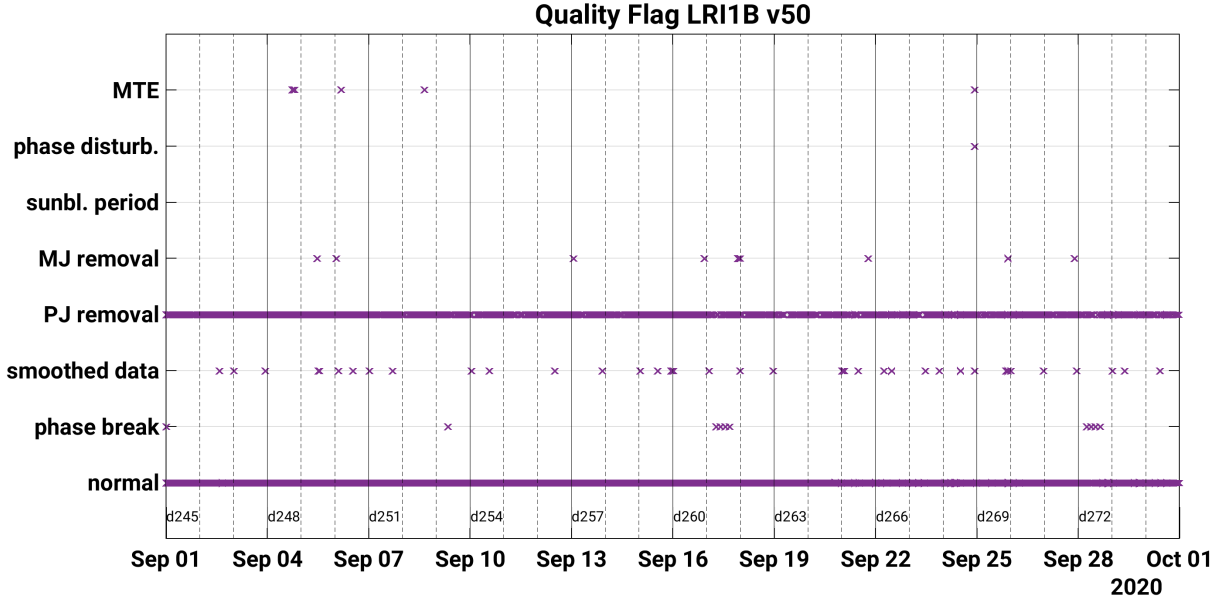


Figure 7.6: The quality flag of September 2020 shows several PJ events, a few MJs on September 5th, 6th, 13th, 16th, 17th, 21st, 25th and 27th, a mass transfer event on September 24th and some smoothing events for v50 data.

lost lock event on the 2020-09-09, and due to MWI calibration maneuvers on 2020-09-17 and 2020-09-28. For the first two continuous data segments, the ASD of the LRI biased range is illustrated in fig. 7.7 for Fourier frequencies above 10 mHz. The left plot contains the data segment of September 1st to 9th and the right one for September 9th to 17th. Both ASDs for the red curve of v50 data show a decreasing noise floor of approx. $10 \text{ nm}/\sqrt{\text{Hz}}$ to values $< 1 \text{ nm}/\sqrt{\text{Hz}}$ for Fourier frequencies of 0.04 Hz to 0.25 Hz. In contrast to that the ASD level of the green curve for v04 ends up at 0.25 Hz with values of approx. 1 order of magnitude larger in fig. 7.7 a), and approx. 0.5 orders of magnitude larger in fig. 7.7 b). This higher values are related to glitches or steps in the ranging measurement, which will be analysed in the following.

From the quality flag of v50 in fig. 7.6, one can observe different events for the data segments of 1st to 9th and 9th to 17th of September 2020. In table 7.2 the events within different time spans were computed to events per day. As a comparison, also the events per day for January 2019 are shown, which shows a more usual occurrence of events. For example, in both time spans of September are observed two MJs, which can be converted to MJs per day, by using

$$\text{First Segment: } \frac{2 \text{ MJ}}{8.34 \text{ days}} = 0.24 \text{ MJ/day} \quad (7.11)$$

$$\text{Second Segment: } \frac{2 \text{ MJ}}{7.88 \text{ days}} = 0.25 \text{ MJ/day} . \quad (7.12)$$

However, the slightly increased amount of MJs, in comparison to January 2019, might not be related to the higher ASD level of v04 in fig. 7.7. This can be clarified with fig. 7.8 a). Here, the ASD of the single day of 2021-09-05 is shown, where a MJ was observed at 11:25:32 in GPS time. The green curve of v04 reaches a ASD level of $\approx 1 \text{ nm}/\sqrt{\text{Hz}}$ at 0.25 Hz, while v50 data ends at $\approx 400 \text{ pm}/\sqrt{\text{Hz}}$. Thus, v04 and v50 data are similar and they only differ for the very high frequencies.

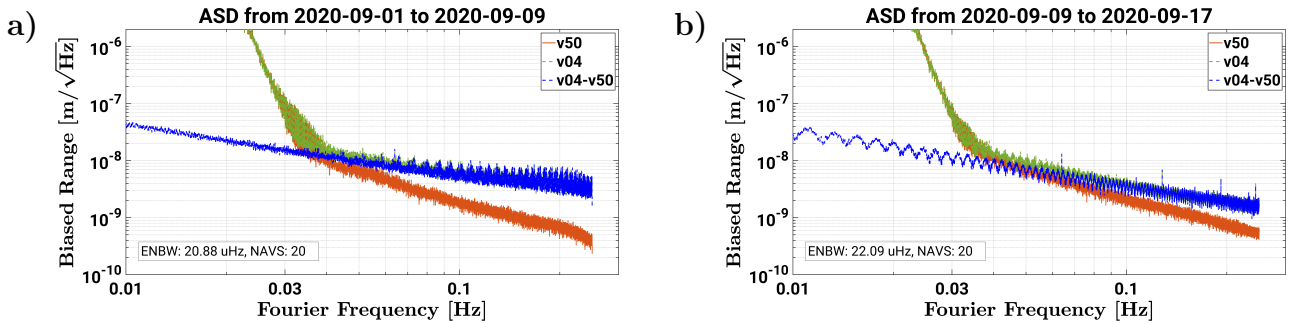


Figure 7.7: ASD of biased range of v04 (without daily offsets) and v50 for the period of 2020-09-01 to 2020-09-09 in the left plot **a)**, and for 2020-09-09 to 2020-09-17 in the right plot **b)**.

Furthermore, the v04 ASD level is also lower in comparison to January 2019 (cf. fig. 7.5), where a MJ has led to a high ASD level for frequencies larger than 20 mHz. Consequently, the new SDS deglitching has improved the data quality for LRI1B for most of the days. Therefore, we assume that the new SDS deglitching for v04 data is able to remove the MJs sufficiently, and there must be another reasons for the higher difference between v04 and v50 data in fig. 7.7. The day which might have the biggest effect on the first data segment of v04 data is the 8th of September. Its ASD is plotted within fig. 7.8 b) and shows an increased ASD level in comparison to a). On this day the IPU performed a reboot around 02:30 in GPS time. Computing just the spectra for the time span of 03:00 a.m. to 23:59 p.m. again, yields a similar ASD level as the v04 level on 5th of September.

Further IPU reboots on the 10th, 18th and 23rd of September might cause the same issue. Additionally, the 15th and 27th are also affected by IPU reboots, but might not be visible in the daily spectrum, since the reboots occurred in the very beginning or ending of these two days, and the Nuttall4a-Window drops to zero at the boundaries. For more details about window functions and spectral densities, please refer to appendix A.1.

Another example for an unusual ASD level of v04 is given by fig. 7.8 c). Here, one can see that the ASD level increases again for higher frequencies of 0.1 Hz and finally decreases again. The caption of fig. 7.8 lists some more days, where the resulting spectra look similar to the shown ones. All listed days, which are not considered yet, might have a higher ASD level due to the v04 phase jump removal. The v04 deglitching seems to have difficulties to remove a few PJs. For example, the AEI also needed to apply the additional smoothing step for events on the 7th at 00:30:12 and 16:59:20 in GPS time. Furthermore, a *volatile* event on the transponder phase, which has transferred into the master phase was removed around 01:47:43 in GPS time (cf. table 7.3).

One last remark for the data quality of the v04 ranging measurement in general is related to the mentioned CLK1B issue in section 7.1. It was explained that AEI needs a manual data screening and cleaning for some unusual CLK1B segments, which could lead to wrong estimates for the scale and time shift and also the ASD levels will increase for frequencies > 30 mHz. The v04 data seems to be affected as well. In table 7.3 are listed a few data segments for 2020, where the ASD level of v04 is also increased. In addition to incorrect CLK1B regions, there can also be some other causes like IPU reboots and critical phase jump events, which are removed by the second smoothing step at AEI. The suspected reasons for the increased ASD level are listed in the last column of table 7.3.

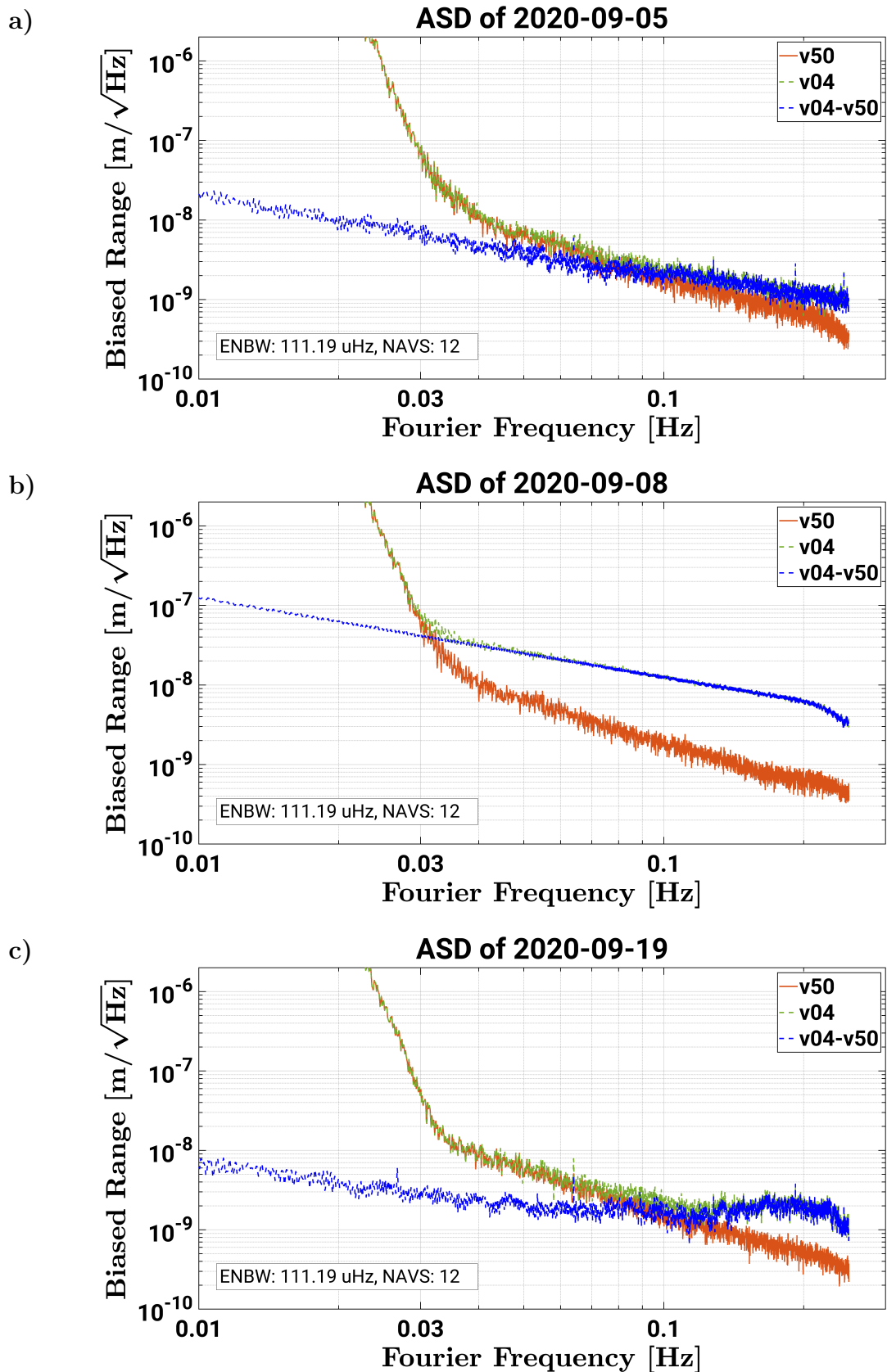


Figure 7.8: ASD of biased range of v04 and v50 for **a)** 2020-09-05, **b)** 2020-09-08, and **c)** 2020-09-19. Days in September 2020 with similar spectra as **b)**: September 7th, 10th, 16th, 23rd and 28th (last segment), and as **c)**: September 18th, 19th and 20th. **a)** shows the data quality of v04 and v50 for most of the days since July 2020.

Time Span	Number of Days	Smoothing per Day	PJ per Day	MJ per Day	PD per Day	MTE per Day
Jan 2019	31	0.5	27.7	0.03	0	0
01. - 09. Sep 2020	8.34	1.3	190.3	0.24	0	0.6
09. - 17. Sep 2020	7.88	1.5	122.6	0.25	0	0

Table 7.2: Quality reducing observations per day in the ranging data, which are computed from the given time span. As an example for less events January 2019 is shown. The two data segments for September 2020 contains several PJ events. Additionally, for v50 data the second phase smoothing step was used more often.

Segment Start	Segment End	ASD level v04 for $f > 30$ mHz	Possible Reason
2020-08-09	2020-08-12	$\approx 10^{-8}$ m/ $\sqrt{\text{Hz}}$	- unusual CLK1B data
2020-09-01	2020-09-09	$\approx 10^{-8}$ m/ $\sqrt{\text{Hz}}$	- Volatile in transponder phase on 7th at 01:47 a.m. - several smaller PJs on 7th between 04:55 - 05:00 p.m. and between 06:30 - 06:35 p.m. - critical PJ on 7th at 04:59 p.m. - IPU reboot on 8th
2020-10-04	2020-10-10	$> 10^{-5}$ m/ $\sqrt{\text{Hz}}$	- unusual CLK1B data - IPU reboot on 8th
2020-10-18	2020-10-23	$> 10^{-5}$ m/ $\sqrt{\text{Hz}}$	- unusual CLK1B data - COM calibration on 20th and 21th (several interruptions in KBR data)
2020-11-08	2020-11-14	$> 10^{-7}$ m/ $\sqrt{\text{Hz}}$	- unusual CLK1B data - IPU reboot on 9th and 10th
2020-11-15	2020-11-21	$> 10^{-7}$ m/ $\sqrt{\text{Hz}}$	- unusual CLK1B data - IPU reboot on 20th - critical PJ on 15th at 07:42 a.m. and on 17th at 07:44 and 08:43 a.m.
2020-11-29	2020-12-05	$> 10^{-7}$ m/ $\sqrt{\text{Hz}}$	- unusual CLK1B data - IPU reboot on 2nd
2020-12-09	2020-12-12	$\approx 10^{-7}$ m/ $\sqrt{\text{Hz}}$	- Volatile in transponder phase on 11th at 06:06 p.m. - CCS in master phase on 11th at 08:03 p.m.
2020-12-13	2020-12-19	$\approx 10^{-7}$ m/ $\sqrt{\text{Hz}}$	- Volatile in transponder phase on 19th at 04:44 a.m.

Table 7.3: v04 data segments in 2020 for new deglitching algorithm, where the ASD level is increased in comparison to normal days like September 5th, 2020 (cf. fig. 7.8 a)). Possible reasons are listed in the last column. For the unusual CLK1B data, please refer to table 7.1. The critical phase jump events can be identified by bit 1 of the v50 quality flag (cf. table 6.3).

7.4 Comparison of Light Time Correction

For gravity field recovery the instantaneous range has to be computed from the biased range and the light time correction (cf. section 4.3). Therefore, it is necessary that the LTC has a lower noise level than the ranging measurement to not deteriorates the signal quality.

Figure 7.9 shows the ASD for the biased range and light time correction on the left side for January 1st, 2019, and on the right side for August 27th, 2020. It is used a number of averages of 10, in order to have a clearer view on the noise floor at high frequencies. The green and light red curve show the biased range of v04 and v50 and the dark blue curve their difference as described in the previous figures like fig. 7.5. The additional yellow and dark red curve show the ASD of the v04 and v50 LTC. Their difference is pointed out by the light blue one.

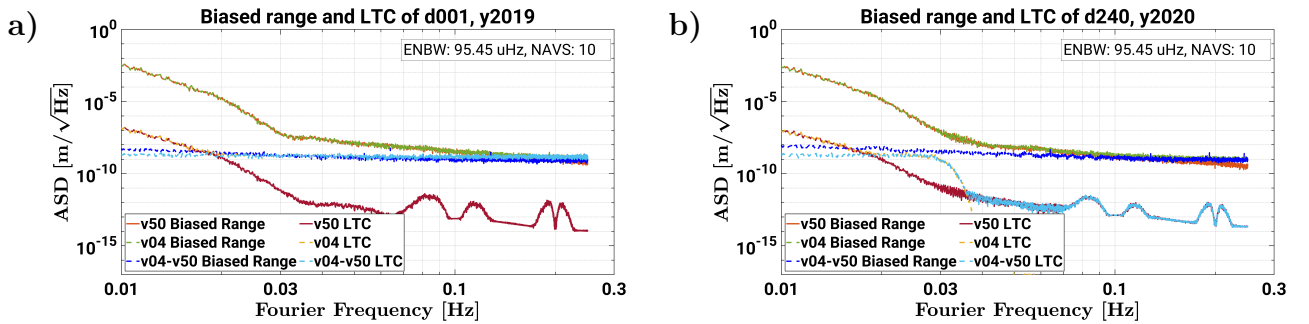


Figure 7.9: ASD for biased range and ltc with cross-correlation model. **a)** On the left side the data is shown for January 1st, 2019 and **b)** on the right side for August 27th, 2020.

At January 1, 2019, a noise level well below $10\text{pm}/\sqrt{\text{Hz}}$ is observed for v50 data at Fourier frequencies above 30 mHz. That means the dark red curve does not affect the light red one, when biased range and LTC are added. In contrast to that, the v04 LTC data shows a noise level $> 1\text{nm}/\sqrt{\text{Hz}}$, which will induce noise in the sum of biased range and LTC at Fourier frequencies larger than 0.1Hz.

For that reason SDS adjusted the LTC calculation for v04 data since 2020-06-27 by using a cut-off frequency of 30mHz instead of 250mHz in the CRN-filter [Wen et al., 2020]. This adjustment can be noticed by the much lower noise level of the yellow trace in fig. 7.9 b).

Another odd behaviour of the LTC in January 2019 is observable by looking at its time series in fig. 7.10. The difference of v04 and v50 is shown as light blue trace. On most of the days, the difference between these two data sets is at the nanometer level. However, the data contains jumps approximately at every fourth day bound, i.e. in the very beginning of affected days but not exactly at the day bound. These disturbances can be identified in v04 data by computing its ASD for the whole month (fig. 7.10 b)) . Due to the jumps, the ASD level of the v04 LTC is elevated for Fourier frequencies above 30mHz.

This peculiar behaviour was only observed in in December 2018 and January 2019. No remark is present on this issue in the release notes of v04 ([Wen et al., 2020]).

However, we found a few single days, where the difference of v04 and v50 LTC show a jump in the beginning of a day. All affected dates, including December 2018 and January 2019, are listed in table 7.4.

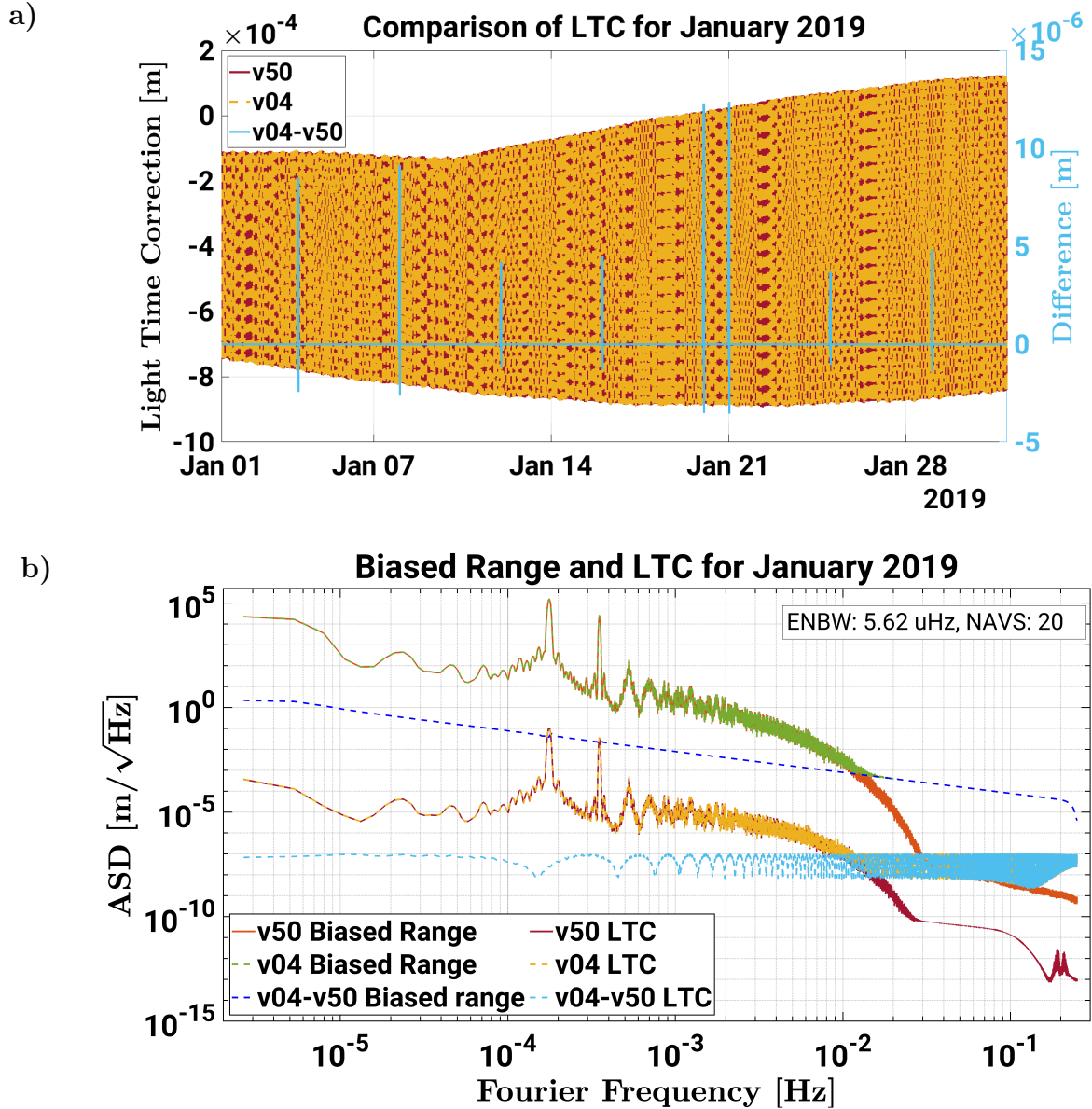


Figure 7.10: a) Light time correction time series for January 2019 and b) ASD of LTC and biased range (with corrected offsets at v04 day-bounds (cf.section 7.2)) for the same period.

Date	Magnitude in v04-v50 [m]	Date	Magnitude in v04-v50 [m]
2018-06-22	$\approx 1 \cdot 10^{-6}$	2019-01-20	$\approx 1 \cdot 10^{-5}$
2018-07-05	$\approx 5 \cdot 10^{-6}$	2019-01-21	$\approx 1 \cdot 10^{-5}$
2018-07-14	$\approx 1 \cdot 10^{-5}$	2019-01-25	$\approx 5 \cdot 10^{-6}$
2018-12-13	$\approx 5 \cdot 10^{-6}$	2019-01-29	$\approx 5 \cdot 10^{-6}$
2018-12-22	$\approx 1 \cdot 10^{-5}$	2019-02-07	$\approx 5 \cdot 10^{-6}$
2018-12-26	$\approx 1 \cdot 10^{-5}$	2019-03-27	$\approx 5 \cdot 10^{-6}$
2019-01-04	$\approx 1 \cdot 10^{-5}$	2019-04-09	$\approx 5 \cdot 10^{-6}$
2019-01-08	$\approx 1 \cdot 10^{-5}$	2019-04-22	$\approx 5 \cdot 10^{-6}$
2019-01-12	$\approx 5 \cdot 10^{-6}$	2020-05-01	$\approx 1 \cdot 10^{-7}$
2019-01-16	$\approx 5 \cdot 10^{-6}$		

Table 7.4: Observed LTC jumps in difference of v04 and v50 data for June 2018 until July 2021.

7.5 Time Derivatives of Biased Range and Light Time Correction

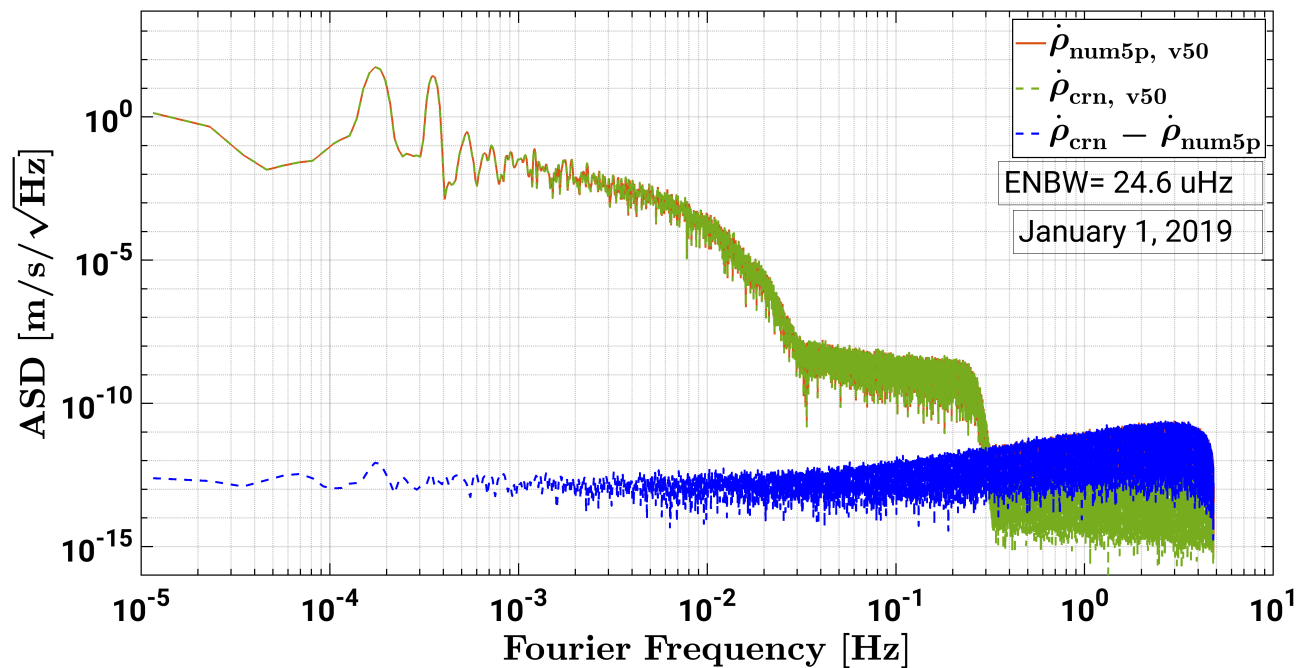


Figure 7.11: Derivative of LRI biased range (range rate) with numdiff and CRN-filter method for January 1st, 2019.

The calculation of the time derivatives of the biased range is another difference between the v04 and v50 data. At AEI the range rate and range acceleration are computed with a central 5-point numerical differentiation method. The exact formulas are introduced in appendix A.2. Another possibility is to derive them with the CRN-filter from section 6.10. To our knowledge the second option is used at the SDS processing for LRI1B v04.

For comparing the two methods, the range rate $\dot{\rho}$ is computed from the 10 Hz and CRN-filtered biased range ρ of v50 data with both methods. For the centered 5-point numerical derivative, the function `numdiff` from section 6.12 is used, i.e.

$$\dot{\rho}_{\text{num5p}} = \text{numdiff}(\rho, 9.664 \text{ Hz}, 5, 1) . \quad (7.13)$$

The differentiated normalized CRN-filter coefficients \dot{F}_n , can be used for filtering the signal (cf. Thomas [2000]), such that

$$\dot{\rho}_{\text{CRN}} = \text{filter}(\dot{F}_n, 1, \rho) , \quad (7.14)$$

where the MATLAB ‘filter’ command is used. It is necessary to cut out a few samples in the beginning of the CRN derived range rate, due to the filter warm-up. Additionally, a few samples of the `numdiff` derived range rate need to be removed in the beginning and end, because the first and last centerable points for the 5-point method are the third and third last sample (cf. appendix A.2). However, to have the same amount of samples for comparing both results, we remove 800 samples in the beginning and 2 samples in the end of each data set.

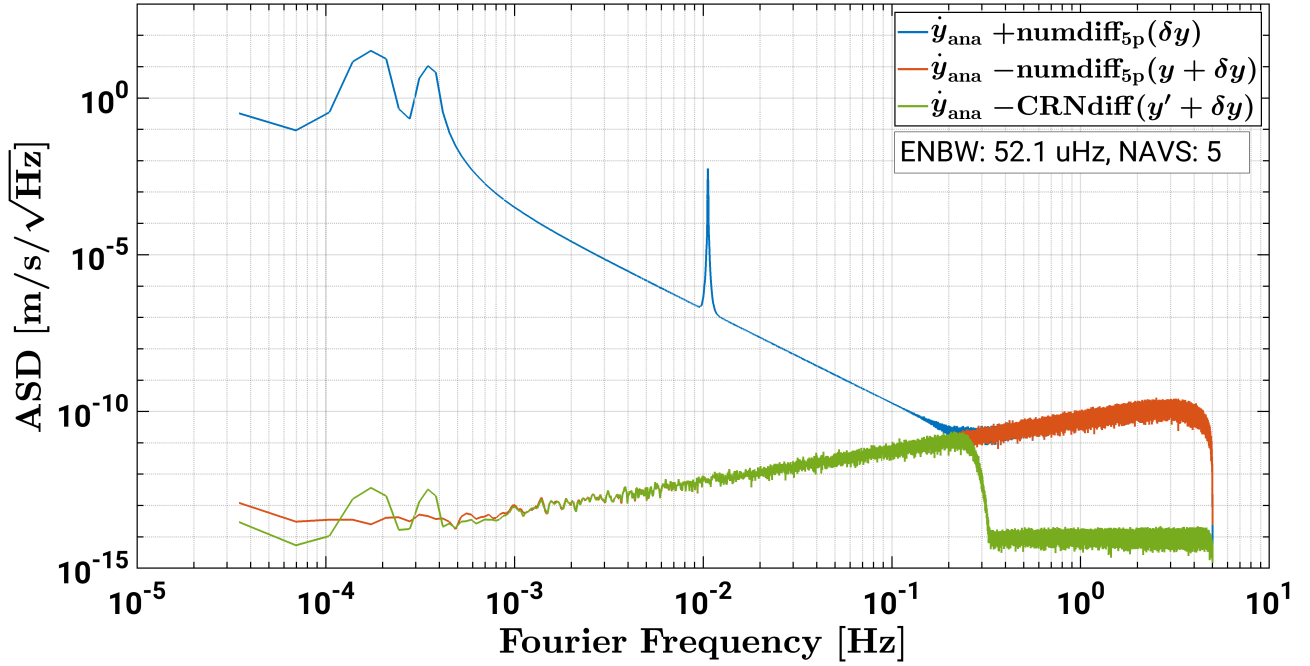


Figure 7.12: Comparing `numdiff` and CRN-filter derivatives with analytical solution. The used window function is the Hanning-Window.

The final results for the range rates and the difference of both methods are shown in fig. 7.11 as ASD for the v50 data of January 1, 2019. One can clearly see the CRN cut-off frequency at 0.25 Hz. However, due to the smaller sampling rate of LRI1B of 0.5 Hz, we are only interested in the frequencies below 0.25 Hz. Obviously, the difference between the two models is small, because the blue curve does not exceed values above $3 \text{ pm/s}/\sqrt{\text{Hz}}$. The rms amplitude at $1/\text{rev}$ is $\approx 4 \cdot 10^{-15} \text{ m/s}$.

In conclusion the impact of both calculations in the ranging measurement is insignificant due to other noise sources, such as a slightly incorrect scale factor or the noise of the laser frequency.

For v50 data the `numdiff` method is used, because it provides slightly lower errors at $1/\text{rev}$ and $2/\text{rev}$ in our analysis. The analysis uses a well-defined analytical signal y given by the sum of three sinusoidal oscillations (cf. appendix A.2, eq. (A.29)). An additional white noise δy of $10 \text{ pm}/\sqrt{\text{Hz}}$ is added to y . The centered 5-point numerical derivative for that signal is computed with

$$\dot{y}_{\text{num5p}} = \text{numdiff}(y + \delta y, f_s, 5, 1). \quad (7.15)$$

For the CRN technique a phase delay of the CRN-filter has to be considered, which shifts the signal y by $-\Delta t_{\text{CRN}}$. The delay was accounted for by using a time-shifted signal y' as input. The derivative is computed by

$$\dot{y}_{\text{CRN}} = \text{filter}(\dot{F}_n, 1, y' + \delta y). \quad (7.16)$$

The plot in fig. 7.12 shows the analytical derivative with noise δy in blue, and the difference between the analytical derivative and the `numdiff` method in red. The green curve is the difference between \dot{y}_{ana} and \dot{y}_{CRN} . For frequencies between 0.5mHz and 0.25Hz the red and green curve are very similar, which is expected. However, at $1/\text{rev}$ and $2/\text{rev}$, the `numdiff` derivative is slightly closer to the analytical solution than the CRN derivative. Such a small difference is insignificant for the LRI1B calculation, but more of academic interest.

Finally, another month of data was chosen, to give an overview about the resulting range rate and range acceleration, and the corresponding correction terms from LTC of v04 and v50. The continuous LRI measurement for July 2020 contains only a few larger events, like the beginning of a sun-blinding period on July 31. The ASD of the biased range in fig. 7.13, is very similar for v50 and v04 (offsets at day-bounds are removed (cf. section 7.2)). The noise level for both data sets reaches values below $10 \text{ nm}/\sqrt{\text{Hz}}$ for Fourier frequencies above 70 mHz. The rms amplitude at $1/\text{rev}$ is $\approx 207 \text{ m}$. The LTC of v04 and v50 shows a noise level well below $0.1 \text{ nm}/\sqrt{\text{Hz}}$, which does not affect the range significantly. The rms amplitude at $1/\text{rev}$ is $\approx 132 \mu\text{m}$.

Computing the first time derivative of that data yields the range rate and light time rate. The results are illustrated as ASD in fig. 7.14. The range rate noise for frequencies above 70 mHz is smaller than $10 \text{ nm/s}/\sqrt{\text{Hz}}$ for v04 and v50, and shows a rms amplitude of $\approx 0.23 \text{ m/s}$ at $1/\text{rev}$. For the LTC rate a rms amplitude at $1/\text{rev}$ of $\approx 140 \text{ nm/s}$ is observed.

The second time derivative yields the range acceleration and light time acceleration and is plotted at fig. 7.15. The noise level of the range acceleration increases slightly for frequencies above 70 mHz. In case of v04 the level reaches $\approx 7 \text{ nm/s}^2/\sqrt{\text{Hz}}$ at 0.25 Hz, while the v50 curve decreases again between 0.2 Hz and 0.25 Hz from $\approx 3 \text{ nm/s}^2/\sqrt{\text{Hz}}$ to $\approx 0.8 \text{ nm/s}^2/\sqrt{\text{Hz}}$. The rms amplitude at $1/\text{rev}$ is $\approx 255 \mu\text{m/s}^2$ for the range acceleration and $\approx 16 \text{ nm/s}^2$ for the light time acceleration.

Finally, it should be noted that the small differences in range rate and range acceleration between v04 and v50 are not related to the computation method of the derivative. The resulting differences are already observed in the biased range or LTC. Reasons for that were already presented in section 7.1 and section 7.3.

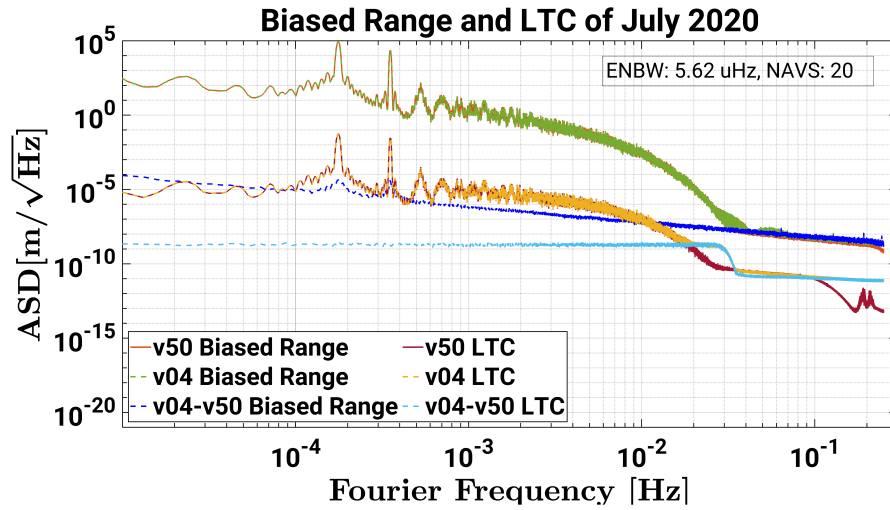


Figure 7.13: Biased Range and LTC of v04 and v50 for July 2020.

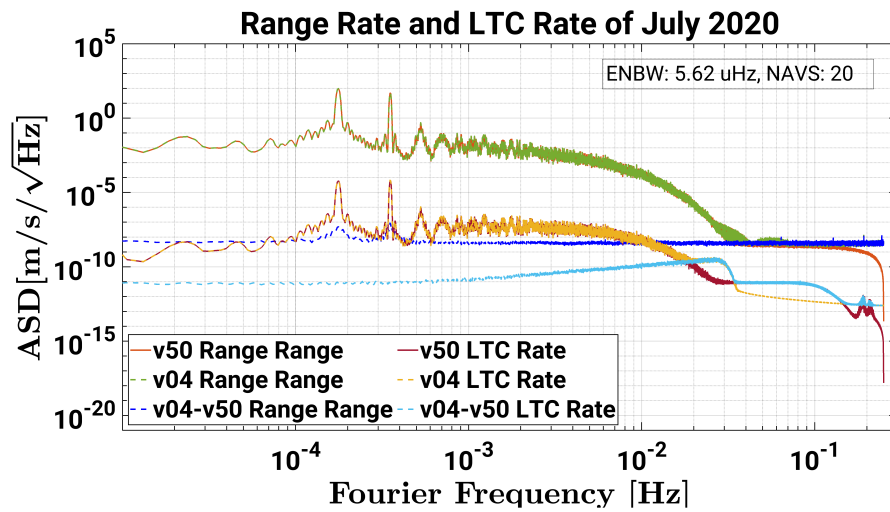


Figure 7.14: Range Rate and Light Time Rate of v04 and v50 for July 2020.

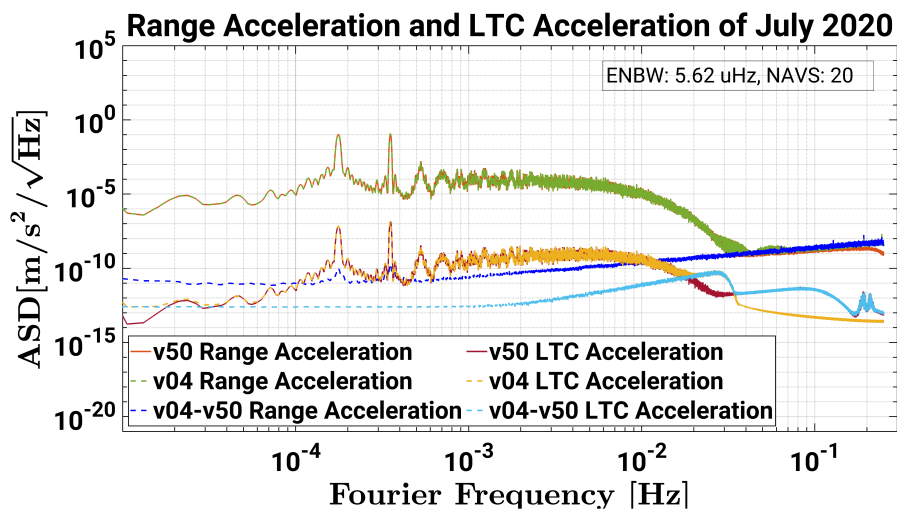


Figure 7.15: Range Acceleration and Light Time Acceleration of v04 and v50 for July 2020.

7.6 Conclusion of Verification

This chapter has presented the verification and validation of the publicly available LRI1B v04 data of SDS, by comparing different aspects with the alternative LRI1B v50 product of AEI. Data sets of a few months were selected to demonstrate the differences between v04 and v50, whereby periods before and after the v04 processing adjustments were taken into account.

The v04 deglitching algorithm was improved by SDS for data since July 2020. In the previous time span, mega phase jumps were not removed completely, meaning that scale factor estimates show some outliers in comparison to other days without mega phase jumps (cf. fig. 7.1). This incorrect scale factor propagates into the ranging measurement, which is the reason for high ASD levels for the v04 biased range (cf. fig. 7.5 a)). This issue was resolved by the new phase jump removal of SDS, which was presented for the date of September 5th, 2020 (cf. fig. 7.8 a)). For most of the days, this adjustment improved the LRI1B v04 data quality and is similar to v50 (except for frequencies > 0.1 Hz).

However, for days with IPU reboots or incorrect CLK1B v04 data, a few issues are observed for v04. In case of unusual CLK1B data, AEI does a manual data screening and cleaning by using an interpolation approach. The currently considered dates as well as other identified days, but which are not corrected in v50 yet, are listed in table 7.1.

Furthermore, the v04 deglitching seems to have difficulties to remove some phase jumps. As explained in section 7.3, the v50 processing uses an additional phase smoothing step when the deglitching was not able to sufficiently remove a glitch. Events like this are marked in the quality flag of v50, as well as other occurrences which might affect the data quality. In addition, AEI directly removes some unusual phase disturbances like *volatile* events, which might have a larger impact on the LRI phase than the typical phase jumps.

It should also be noted that the scale factor of SDS is a constant value per day, which also leads to jumps in the biased range at every day transition. To get around this, AEI uses a time dependent scale factor, i.e. the daily generated scale factor is interpolated onto the 10 Hz time series before it is applied on the LRI phase. To compute meaningful spectra for our comparison, it was necessary to remove all those daily offsets from v04 data. After a LRP reboot or at the beginning of each new month, the biased range of v50 starts at zero meter to ensure numerical precision. As a result, there are no offsets for continuous data segments within one month of v50 data.

The light time correction of v04 shows a noise level which is affecting the sum of biased range and LTC for the computation of the instantaneous range until June 27, 2020. Afterwards, SDS implemented a cut-off frequency of 30 mHz for low-pass filtering the LTC with the CRN filter. This leads to a noise level below $10 \text{ pm}/\sqrt{\text{Hz}}$, as is the case for v50 data (cf. section 7.4).

Additionally, at the beginning of some days a few jumps in the LTC of v04 are observed. In December 2018 and January 2019, they occur more frequent, approximately every four days. All affected dates between 2018 and July 2021 are listed in table 7.4.

The last aspect of the v04 and v50 comparison contains different computations for the time derivatives of biased range and LTC, i.e. range rate, light time rate, range acceleration and light time acceleration. These parameters are computed with the CRN filter in v04 and with a centered 5-point numerical differentiation method in v50. By deriving the range rate with both methods from the biased range of v50, it becomes clear that both methods are sufficient and differ only in magnitudes smaller than $\text{pm}/\text{s}/\sqrt{\text{Hz}}$ (cf. fig. 7.11). In conclusion, the differences

between the time derivatives of v_{04} and v_{50} are not related to this computation, but rather to already mentioned points above.

8

Summary and Outlook

The first Laser Ranging Interferometer in space provides valuable data for determining the gravitational field of the Earth. The raw data from the GRACE Follow-On mission needs some processing steps before the gravity recovery can start. This thesis showed an alternative data processing for most of GRACE Follow-On LRI Level 1 data products.

In chapter 2 the heterodyne measurement principle was presented and effects of relativity for clocks in low Earth orbiters and for the flight time of a photon inside an interferometer like the LRI. Afterwards, the GRACE Follow-On mission with its different processing units and time frames was introduced in chapter 3. In chapter 4, the LRI setup and the resulting information at the phase readout was explained.

The following chapter 5 has dealt with the data processing of LRI data. Furthermore, the assignment of timing information to LRI data streams on the spacecraft, and how the AEI team integrates the data within the so-called `gislparsr`, are discussed.

With this knowledge, the different LRI Level 1A products can be derived. Their processing is presented in appendix B. In general, the AEI team wanted to verify and validate the official LRI Level 1 v04 products of SDS, to ensure that the provided LRI data is useful for gravity field recovery. Therefore, the resulting Level 1A products of AEI (v50) were compared with SDS (v04) products in appendix C. It can be summarised that the data products are very similar, but a few minor mistakes in v04 products were found. An example are missing data streams or log messages in LHK1A, LLG1A and LRI1A of v04. AEI has already compiled a document for SDS/JPL containing all discrepancies and other recommendations by AEI.

The data generation of LRI1B by AEI was presented in chapter 6. Especially the deglitching algorithm for removing jumps in the phase measurement and applying a smoothing, if there are large residuals left, are important steps within the LRI1B processing. Furthermore, the derivation of a conversion factor to convert the LRI phase into a range and computing the time derivatives for the range rate and range acceleration were presented. Additionally, one needs the time-tag conversion for transforming LRP times into GPS times and a so-called CRN filter. The processing for the Light Time Correction (LTC) was discussed in section 4.3 and the computation for the enhanced Carrier to Noise Ratio (CNR) in section 4.4. Some of

these mentioned steps differ from the v04 data processing, therefore a comparison between the resulting v50 and the official v04 product was done in chapter 7. The following bullet points summarise the most important differences.

- It turns out, that the daily piecewise-constant scale factor of v04 shows offsets at day-bounds and slope changes, which leads to jumps in the LRI biased range with the beginning of a new day. Our v50 version uses a time-dependent scale factor, because this ensures continuous ranging data over long time-spans.
- The phase jump removal of SDS was not optimal for v04 in the period before July 2020. Due to the remaining glitches in the LRI phase, the scale factor estimation was incorrect for several days, especially for days with mega phase jumps. Therefore, SDS adjusted the v04 deglitching algorithm for data since July 2020. The new deglitching has improved the data quality for the majority of the days. Only a few days, for example 2020-09-08, seem to have some glitches in the ranging data in comparison to v50, which might be related to IPU reboots, incorrect clock data (CLK1B) and phase jump events, where the v04 removal was not completely successful.
- Another difference was found in the Light Time Correction of v04 and v50. Between June 2018 and June 2020, the LRI instantaneous range of v04 could be limited at higher frequencies by the noise of the LTC. In general, the noise of the LRI biased range decreases from $100 \text{ nm}/\sqrt{\text{Hz}}$ to $1 \text{ nm}/\sqrt{\text{Hz}}$ for Fourier frequencies between 30 mHz and 0.25 Hz, while the LTC of v04 had a noise level of a few nanometer/ $\sqrt{\text{Hz}}$. SDS adjusted the computation by using a different CRN filter with a cut-off frequency of 30 mHz. This ensures a noise level well below $0.1 \text{ nm}/\sqrt{\text{Hz}}$ for data since July 2020, as it is the case at v50 LTC data.

Finally, it can be said that AEI's alternative processing strategies were used to optimize the LRI Level 1 data products by verifying and validating the SDS v04 data products. This also shows that collaboration between different institutions is often helpful and that data quality can be further improved through collaboration.

SDS/JPL already started to work on the corrections for the mentioned Level 1A data products, but some issues can only be fixed for the next release v05. It should be noted that the found discrepancies in Level 1A are only minor issues, because the important phase measurements for the LRI1B (and further data products) were provided correctly.

SDS has also changed some algorithms for the LRI1B processing, such that v04 is generally comparable with v50 data quality for data since July 2020.

For the future, there are still some aspects that could further improve the data quality. These include, for example, the adjustment of the AEI time-tag conversion for single days of unusual CLK1B data, to accomplish a more meaningful scale factor and time shift between KBR and LRI data for the affected days. Additionally, the missing quality flags could be integrated into the Level 1A products, and a processing for the LLT1A product (cf. appendix B.5), which was not generated yet, could be implemented too. Furthermore, investigations about the absolute laser frequency and the determination of the tilt-to-length coupling for the LRI might improve the LRI1B product. It is also planned to provide all generated months of LRI1B v50, such that other institutions could compare gravity field solutions of v50 and v04 data.

Finally, it should be noted that all these improvements and the knowledge of most suitable algorithms might help for the design and future data analysis of laser interferometers in next generation gravity missions as well as for the Laser Interferometer Space Antenna.



Theoretical Basics

The principles for the analysis of digital signals in the frequency domain, by using discrete Fourier transformations and window functions, are discussed in appendix [A.1](#). Afterwards, the centered 5-point (and 3-point) numerical differentiation method is demonstrated in appendix [A.2](#). Finally, two different methods for deriving a scale factor and a time shift between two slightly different time-series are presented in appendix [A.3](#).

A.1 Spectral Analysis of Signals

Sometimes it is helpful to analyse digital signals in the frequency domain e.g. to get information about the present frequency components. The principles of deriving estimations of spectra or spectral densities are described in the next sections.

A.1.1 Discrete Fourier Transformation

Let us consider a sinusoidal signal x with an amplitude of $A = 400$ m and an oscillation frequency of $f_{\text{sin}} = 1/5670$ Hz. Now this signal is sampled equidistantly with $f_s = 10$ Hz. The time-tags $t = [0, 0.1, 0.2, \dots, 85049.9]$ seconds yields $N = 850\,500$ elements of the time series

$$x_k = A \cdot \sin(2\pi f_{\text{sin}} t_k), \quad k = 0 \dots N - 1 \quad (\text{A.1})$$

$$x_k = 400 \cdot \sin\left(2\pi \frac{t_k}{5670}\right). \quad (\text{A.2})$$

This digital signal can be transformed from its time series into the frequency domain by computing the Discrete Fourier Transformation (DFT). This real-to-complex DFT can be defined with different normalizations, however, for calculating spectral densities the following approach is used [[Heinzel et al., 2002](#)]

$$y_m = \sum_{k=0}^{N-1} x_k \exp\left(-2\pi i \frac{mk}{N}\right), \quad k, m = 0 \dots N - 1. \quad (\text{A.3})$$

Here, y_m is a vector with N complex elements and expresses x_k in the frequency domain. However, this transformation assumes that the input time series x_k is a periodic signal and

repeats it continually in a cyclic process. Consequently, at the boundaries of these repetitions some discontinuities occur, when the input signal is not periodic. In this case the resulting spectrum will be falsified by the effect of spectral leakage, which will be explained soon.

For avoiding this inconsistency between the original signal and the periodic continuation of the DFT, the frequency f_{sin} of the input signal x_k has to be a multiple of the frequency resolution [Heinzel et al., 2002]

$$f_{\text{res}} = \frac{f_s}{N} . \quad (\text{A.4})$$

Computing this condition for our example yields

$$\frac{f_{\text{sin}}}{f_{\text{res}}} = \frac{1/5670 \text{ Hz}}{10 \text{ Hz}/850500} = 15 . \quad (\text{A.5})$$

Obviously, the signal is periodic, which means that an exact multiple of signal oscillations is included within the chosen time-span. An amplitude spectrum of this signal is shown in blue in the fig. A.1. The computation of such spectra and spectral densities will be discussed in appendix A.1.3. The peak at $f_{\text{sin}} \approx 0.176 \cdot 10^{-3} \text{ Hz}$ is clearly identifiable. Also the rms amplitude with 282 m can be read out. All values for other frequency bins are close to zero.

In reality it is not always possible to choose the correct number of samples N , due to unknown and several different frequency components. Now, the same signal but with a longer time span of 86 467.4 s, and $N = 864 675$ elements is assumed. It contains one additional quarter period and yields in this example the largest mismatch between every first and last sample in the cyclic continuation, i.e.

$$\frac{f_{\text{sin}}}{f_{\text{res}}} = \frac{1/5670 \text{ Hz}}{10 \text{ Hz}/864675} = 15.25 . \quad (\text{A.6})$$

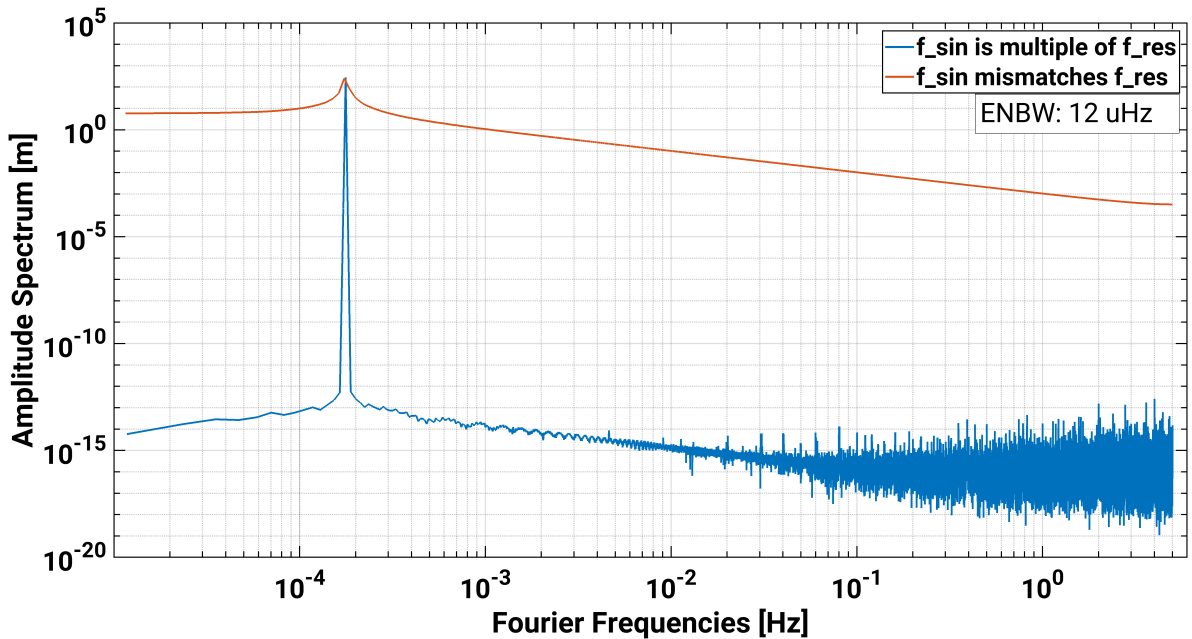


Figure A.1: Amplitude spectrum of a sinusoidal signal with Rectangular window. The blue curve shows the result for a signal time series, where the oscillation frequency is a multiple of the frequency resolution. The orange curve includes one additional quarter period, such that $f_{\text{sin}}/f_{\text{res}}$ is not an integer number. It illustrates the effect of spectral leakage.

The orange curve in fig. A.1 shows the amplitude spectrum for this signal. Undoubtedly, the main peak can be seen, but also all the other frequency bins are present in the spectrum now. This effect, where the power of the main peak spreads over other frequency bins is known as spectral leakage and is undesirable [Heinzel et al., 2002]. This effect will be explained within the next sub-section.

A.1.2 Window Functions

For removing the discontinuity (cf. appendix A.1.1), a so called window function is multiplied with the time series of the signal before the DFT is computed. The window functions ensure a smooth transition between the last and first sample in the periodic continuation of the signal. There exist many window functions with different properties, however, a compromise has to be made between three different effects on the signal. These effects are the spectral leakage, the accuracy of the amplitude representation and the width of the peak [Heinzel et al., 2002]. They will be explained in the following for the Nuttall4a window. Afterwards it will be compared to the Rectangular and the HFT116D window, which will also be applied on a range measurement of the LRI as an example, because we want to show the most suitable window for the computations of spectra and spectral densities inside this thesis.

The previously discussed amplitude spectrum in fig. A.1 was computed with the Rectangular window. Using the Rectangular window means the same as applying no window function at all. Therefore, we want to show some important quantities of window functions for the Nuttall4a window, which was derived by Nuttall [1981].

Nuttall [1981] presented one special set of window functions, whose values can be generally expressed in the form of [Heinzel et al., 2002]

$$w_j = \sum_{k=0}^m c_k \cdot \cos\left(\frac{2\pi \cdot j}{N} k\right), \quad j = 0 \dots N - 1. \quad (\text{A.7})$$

Each of these window functions are described with different values for the coefficients $\{c_k\}$. In this section, we are using the set of

c_0	c_1	c_2	c_3
0.338946	-0.481973	0.161054	-0.018027

for the so called Nuttall4a window [Heinzel et al., 2002, C.7]. The transfer function of Nuttall4a is illustrated in fig. A.2. One can zoom into the frequency offset interval of $[-0.5, 0.5]$ bins, where the maximum of the main peak is achieved at 0 dB at 0 bins. This maximum refers to the highest peak in a spectrum of a sinusoidal signal, which means that the amplitude of the main frequency peak of a sinusoidal signal is represented correctly, if there is an offset of 0 bins. At ± 0.5 frequency bins the transfer function drops to a value of -0.7321 dB, which is called maximum amplitude error e_{\max} . It shows how much the amplitude of the highest peak could be misrepresented.

Next to the centered main peak in fig. A.2 are many other smaller peaks, which are known as sidelobes. The maximum of the highest sidelobe, called Peak Sidelobe Level (PSLL), and also the decreasing height of all sidelobes towards higher frequency offsets are characteristic parameters of a window function. Since the faster the sidelobes drop, the less is the spreading of the power of the main peak into other frequency bins. By designing window functions, one

tries to lower the levels of these two parameters as much as possible. However, a compromise has to be found between these two properties.

This decreasing leakage into neighboring frequency bins is described by the Sidelobe Dropping Rate (SLDR) and is expressed with f^{-n} . In case of Nuttall4a $n = 5$ [Heinzel et al., 2002].

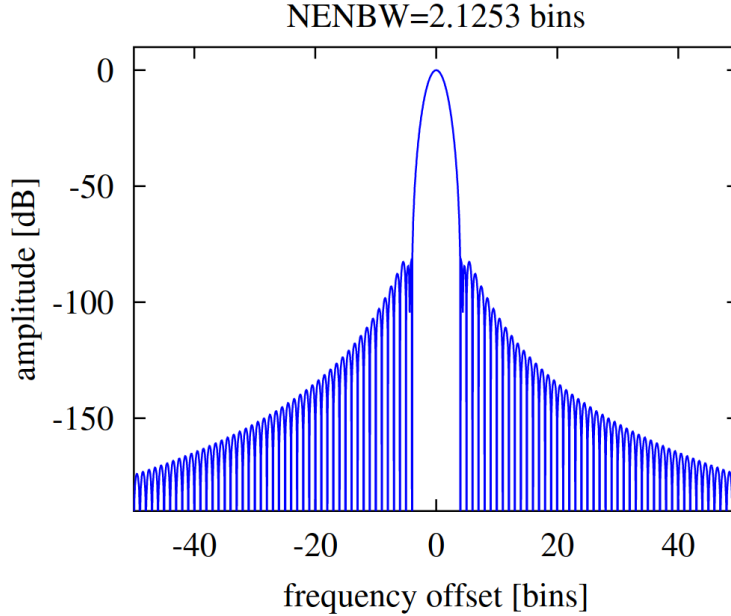


Figure A.2: Transfer function of the Nuttall4a-Window. The first sidelobes, next to the main peak in the center, have an amplitude of -82.6 dB. The Normalized Equivalent Noise Bandwidth for Nuttall4a is 2.1253 bins. The plot is taken from Heinzel et al. [2002], for more information about Nuttall4a or other window functions please refer to this publication.

One might think that a window with a high accuracy in the amplitude and only with a small leakage effect is always a good choice. However, the faster the sidelobes drop, the larger is the so called 3 dB bandwidth [Heinzel et al., 2002]. This is the width after which the transfer function reaches -3 dB. The consequence of this greater bandwidth (and flattened top) is that the resulting peaks in the spectrum are more widened. Depending on the signal, it could be unclear to which frequency bin the peak actually belongs, and also closely adjacent peaks cannot be distinguished anymore.

Table A.1 summarises all the mentioned properties for the Nuttall4a window and additionally for the Rectangular window and the HFT116D flat-top window.

Window	e_{\max} [dB]	$W_{3\text{dB}}$ [bins]	SLDR	A_{PSLL} [dB]	W_{PSLL} [bins]
Nuttall4a	-0.7321	2.0123	f^{-5}	-82.6	5.452
Rectangular	-3.9224	0.8845	f^{-1}	-13.3	1.430
HFT116D	-0.0028	4.1579	f^{-3}	-116.8	7.523

Table A.1: Properties of different window functions from Heinzel et al. [2002].

The PSLL has an amplitude value A_{PSLL} and the corresponding frequency offset W_{PSLL} , which can be read from the position of the maximum of the highest sidelobe in the transfer function.

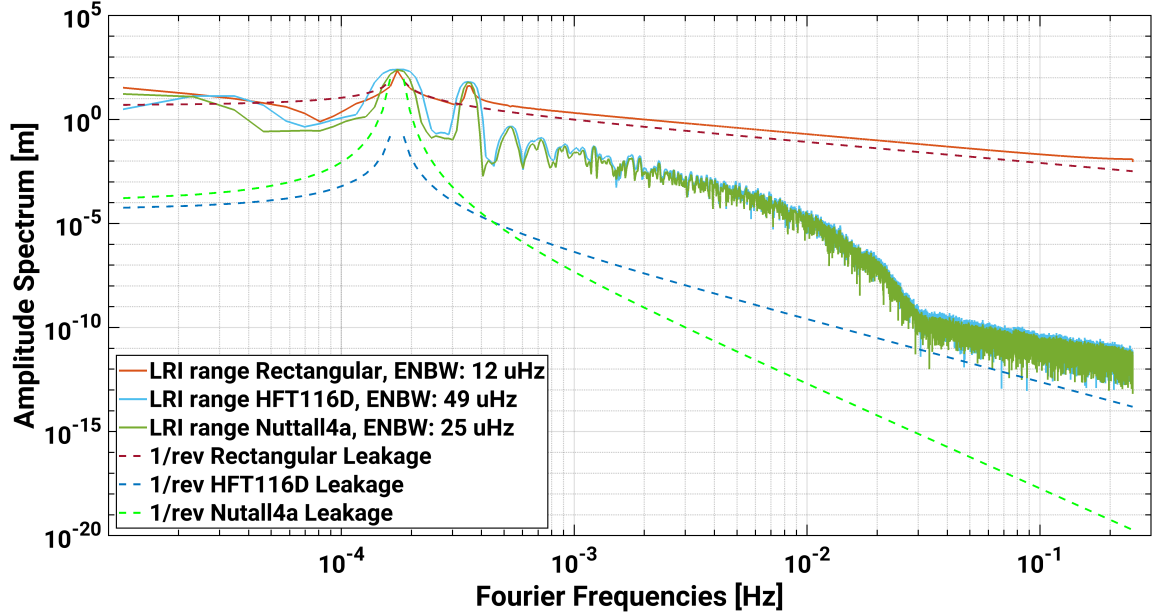


Figure A.3: Amplitude spectrum of LRI range and leakage models at 1/rev for different window functions.

These values can be used for computing an estimation of the maximal spectral leakage as

$$y_{\text{leakage}} = a \cdot \left(|(f - f_{\text{sin}})|^2 \right)^{-n} \quad (\text{A.8})$$

$$\text{with } a = 10^{(A_{\text{PSLL}}/20)} \cdot (W_{\text{PSLL}} \cdot f_{\text{res}})^n \cdot A_{\text{peak}} \quad (\text{A.9})$$

which holds for larger frequency offsets, i.e. $> 10^1$ bins. Here, A_{peak} is the amplitude of the highest peak in the spectrum of the sinusoidal signal, and n denotes the order of the SLDR.

Figure A.3 illustrates the amplitude spectrum of a ranging measurement of the LRI for January 1st, 2019. For the orange curve a Rectangular window was applied. The corresponding leakage model for the orbital frequency (1/rev) is shown in dark red. We know that the LRI noise is well below 1 nm for Fourier frequencies above 30 mHz. The dark red curve shows a high leakage effect, therefore the LRI performance cannot be resolved in all its details. In contrast to that, the light green curve for the Nuttall4a window reveal the behavior for all frequency bins. The estimated leakage of the 1/rev oscillation is approx. four orders of magnitude smaller than the actual spectrum at 30 mHz. Also the peaks at 1/rev and 2/rev are easy to identify and have a smaller error in the peak amplitude, compared to the Rectangular window. However, the peaks are more widened. The light blue spectrum of HFT116D looks very similar to the green one, especially for the noise floor. That means the leakage effect is not limiting. Additionally, the peak amplitude is a little more accurate than the Nuttall4a. This is related to the properties of a flat-top-window, because they are optimised for a small error in the peak amplitude representation. The name for these functions refers to the flat-top of the centered peak of the transfer function. The value of e_{max} for the HFT116D is the smallest in comparison to the other two windows.

However, the peak width is even wider compared to Nuttall4a or Rectangular.

Finally it becomes clear that one has to find the best parameters for the application and that it is always a trade-off between various optimizations. To display the spectra for LRI data the Nuttall4a is our preferred choice, because it allows to observe the amplitude at 1/rev with a

few hundred meter, and also the noise level of a few hundred picometer/ $\sqrt{\text{Hz}}$ (in case of ASD) at higher frequencies. The peaks are not widened too much, so that neighboring frequency bins can still be resolved.

A.1.3 Spectra and Spectral Densities

The resulting DFT, computed with eq. (A.3) for the product of time series and window function ($x'_j = x_j \cdot w_j$), needs to be normalized by the sum of the window values to get the power spectrum (PS) [Heinzel et al., 2002]

$$\text{PS}_{\text{rms}}(f_m = m f_{\text{res}}) = \frac{2|y_m|^2}{\left(\sum_{j=0}^{N-1} w_j\right)^2}, \quad m = 0 \dots N/2. \quad (\text{A.10})$$

For converting between Power Spectrum (PS), Power Spectral Density (PSD), Amplitude Spectrum (AS), and Amplitude Spectral Density (ASD) as [Heinzel et al., 2002]

$$\text{AS} = \sqrt{\text{PS}} = \text{ASD} \cdot \sqrt{\text{ENBW}} \quad (\text{A.11})$$

$$\text{ASD} = \sqrt{\text{PSD}} \quad (\text{A.12})$$

$$\text{PSD} = \text{PS}/\text{ENBW} \quad (\text{A.13})$$

the Equivalent Noise Bandwidth (ENBW) is needed. It results from the so called Normalized Equivalent Noise Bandwidth (NENBW). Each window function has a NENBW, which can be derived from the window values w_j . The NENBW for the Nuttall4a reads [Heinzel et al., 2002]

$$\text{NENBW}(\text{Nuttall4a}) = N \frac{\sum_{j=0}^{N-1} w_j^2}{\left(\sum_{j=0}^{N-1} w_j\right)^2} = 2.1253 \text{ bins}. \quad (\text{A.14})$$

For the ENBW, the sampling frequency f_s and the number of samples N are used as follows [Heinzel et al., 2002]

$$\text{ENBW} = \text{NENBW} \cdot \frac{f_s}{N} = \text{NENBW} \cdot f_{\text{res}}. \quad (\text{A.15})$$

As a consequence the PS and AS are useful for analysing sharp peaks of sinusoidal signals, but they should not be used for characterising continuously distributed noise power. With a larger time series (increasing values for N) the ENBW decreases and the resolution of one frequency bin is finer. That means in every frequency bin is less noise power, which is picked up. In the case of PSD and ASD it is the other way round. The peak height of sinusoidal signals depends on the width of the frequency bins, but the noise power remains constant [Heinzel et al., 2002].

Nevertheless the resulting spectra are often a little bit noisy towards higher frequencies. To compute a smoother trace it can be helpful to use averaging, where the time series is divided into M smaller overlapping segments. Performing the same calculation for the smaller segments and averaging in the frequency domain, reduces the standard deviation of the resulting trace by a factor of $1/\sqrt{M}$ [Heinzel et al., 2002]. If a Number of Averages (NAVS) larger than one is used, then it is written to the corresponding plot in this thesis.

For more details on the topics of window functions and spectral densities please refer to [Heinzel et al., 2002].

A.2 Central 5-Point Numerical Differentiation Method

The data processing in section 6.12 needs the time derivatives of the LRI biased range. These LRI range rate and range acceleration has to be computed numerically. This section presents the derivation of a central 5-point numerical differentiation method (or also known as 5-point-stencil in one dimension) for computing approximations of finite differences. In the end follows a comparison with the 3-point numerical differentiation method, by comparing their differences with a defined signal with known analytical derivative.

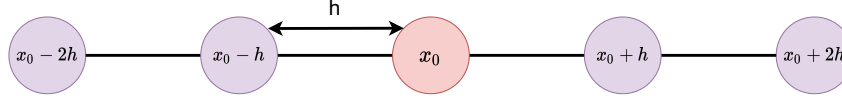


Figure A.4: 5-Point stencil in one dimension. Computing the derivative of $f(x_0)$ in x_0 , with a central 5-point numerical differentiation method, needs the nearest four neighbors. The data points have an equidistant spacing of h .

Figure A.4 shows the idea of a centered numerical differentiation. The red point indicates the value pair $(x_0, f(x_0))$. The computation of the derivative $f'(x_0)$ in the point x_0 uses the nearest four neighbours, which are colored in purple. These data points have an equidistant sampling and the distance in time between each sample should be finite and small [Lambers, 2009]. It is denoted by the value of h . For computing the derivative of $f(x_0)$ in x_0 , the elements of

$$(x_{-2}, y_{-2}), (x_{-1}, y_{-1}), (x_0, y_0), (x_1, y_1), (x_2, y_2) \quad (\text{A.16})$$

are needed, where $x_{\pm 2} = x_0 \pm 2h$, $y_{\pm 2} = f(x_0 \pm 2h)$ and $x_{\pm 1} = x_0 \pm h$, $y_{\pm 1} = f(x_0 \pm h)$.

A polynomial of order $n = 4$ is used as an interpolation approach to fit the data of $f(x)$ in the desired points. Inserting the values into the polynomial yields the following equations [Holoborodko, 2008]

$$f(x_{\pm 2}) = P_4(x_{\pm 2}) = a_0 + a_1(x_0 \pm 2h) + a_2(x_0 \pm 2h)^2 + a_3(x_0 \pm 2h)^3 + a_4(x_0 \pm 2h)^4 \quad (\text{A.17})$$

$$f(x_{\pm 1}) = P_4(x_{\pm 1}) = a_0 + a_1(x_0 \pm h) + a_2(x_0 \pm h)^2 + a_3(x_0 \pm h)^3 + a_4(x_0 \pm h)^4 \quad (\text{A.18})$$

$$f(x_0) = P_4(x_0) = a_0 + a_1x_0 + a_2x_0^2 + a_3x_0^3 + a_4x_0^4 \quad (\text{A.19})$$

For deriving the first derivative $f'(x) \approx P'_4(x)$ one can assume that the centered point $x_0 = 0$, to simplify the expressions [Holoborodko, 2008]. With the system of eq. (A.17) to eq. (A.19) one obtains the relation

$$f'(x_0 = 0) \approx P'_4(x_0 = 0) = a_1 = \frac{P_4(x_{-2}) - 8P_4(x_{-1}) + 8P_4(x_1) - P_4(x_2)}{12h}, \quad (\text{A.20})$$

because the polynomials in the points of $x_{\pm 2} = \pm 2h$ and $x_{\pm 1} = \pm h$ yields the same result as the derivative of eq. (A.19), i.e.

$$\frac{P_4(x_{-2}) - 8P_4(x_{-1}) + 8P_4(x_1) - P_4(x_2)}{12h} = \frac{8}{12h} \left(P_4(x_1) - P_4(x_{-1}) \right) + \quad (\text{A.21})$$

$$\frac{1}{12h} \left(P_4(x_{-2}) - P_4(x_2) \right) \\ = \frac{16}{12h} a_1 h - \frac{4}{12h} a_1 h + \frac{16}{12h} a_3 h - \frac{16}{12} a_3 h \quad (\text{A.22})$$

$$= a_1. \quad (\text{A.23})$$

The second derivative is derived analogously to the first derivative, such that

$$f''(0) \approx P_4''(0) = 2a_2 = \frac{-P_4(x_{-2}) + 16P_4(x_{-1}) - 30P_4(x_0) + 16P_4(x_1) - P_4(x_2)}{12h^2}, \quad (\text{A.24})$$

is valid. Replacing P_4 by $f(x)$ and using the expression of x_0 again, yields the formula for the computation of first and second derivative for a central 5-point numerical differentiation:

$$f'(x_0)_{5p} \approx \frac{f(x_0 - 2h) - 8f(x_0 - h) + 8f(x_0 + h) - f(x_0 + 2h)}{12h} \quad (\text{A.25})$$

$$f''(x_0)_{5p} \approx \frac{-f(x_0 - 2h) + 16f(x_0 - h) - 30f(x_0) + 16f(x_0 + h) - f(x_0 + 2h)}{12h^2}. \quad (\text{A.26})$$

Estimated errors for these equations are in the order of $\mathcal{O}(h^4)$ [Lambers, 2009], [Abramowitz and Stegun, 1972]. In the same way, the formulas for the first and second derivative for a central 3-point numerical differentiation method can be derived, i.e. [Holoborodko, 2008]

$$f'(x_0)_{3p} \approx \frac{f(x_0 + h) - f(x_0 - h)}{2h}, \quad (\text{A.27})$$

$$f''(x_0)_{3p} \approx \frac{f(x_0 - h) - 2f(x_0) + f(x_0 + h)}{h^2}. \quad (\text{A.28})$$

Now a signal $y = [y_1, y_2, \dots, y_m]$ with oscillations at $1/T$, $2/T$ and $60/T$ with the period $T = 5670$ s and amplitudes of $A_1 = 300$ m, $A_2 = 50$ m and $A_3 = 1$ mm is defined, such that

$$y = A_1 \sin\left(\frac{2\pi t}{T} \cdot 1\right) + A_2 \sin\left(\frac{2\pi t}{T} \cdot 2\right) + A_3 \sin\left(\frac{2\pi t}{T} \cdot 60\right). \quad (\text{A.29})$$

The analytical time derivative of the signal y is

$$\dot{y}_{\text{ana}} = \frac{2\pi}{T} \cdot A_1 \cos\left(\frac{2\pi t}{T}\right) + \frac{4\pi}{T} \cdot A_2 \cos\left(\frac{4\pi t}{T}\right) + \frac{120\pi}{T} \cdot A_3 \cos\left(\frac{120\pi t}{T}\right). \quad (\text{A.30})$$

The time-tags $t = [t_1, t_2, \dots, t_m]$ are in the interval of 0 and 86400 s and are sampled equidistantly with $f_s = 10$ Hz. However, it is necessary to generate a very precise signal for this analysis. Therefore the argument of sine has to be computed a little bit different, to preserve numerical precision. To ensure that the numbers do not get too large, it is suggested to use integer arithmetic. In this case the new samples s are defined in integer resolution and the modulo command of MATLAB is used for obtaining the argument α in double precision, i.e.

$$s = \text{int32}(0 : m - 1), \quad (\text{A.31})$$

$$\frac{2\pi t}{T} \equiv \frac{2\pi}{T \cdot f_s} \cdot \text{double}(\text{mod}(s, T \cdot f_s)) = \alpha. \quad (\text{A.32})$$

Computing the signal y and its analytical time derivative \dot{y} can be done by inserting eq. (A.32) into the sine and cosine arguments in eq. (A.29) and eq. (A.30).

For computing now the numerical derivative, an additional noise of $10 \text{ pm}/\sqrt{\text{Hz}}$ is considered for the signal y as

$$\delta y = \text{randn}(m) \cdot \sqrt{\frac{f_s}{2}} \cdot 1 \cdot 10^{-11}, \quad (\text{A.33})$$

where the MATLAB command ‘randn’ generates random numbers in the length (m) of y . This numbers are normally distributed. Using $x = y + \delta y$ and $h = 1/f_s$ allows to compute the first

derivative with a 3-point and 5-point numerical differentiation method described by eq. (A.27) and eq. (A.25).

In fig. A.5, the blue line is the ASD of the analytical derivative \dot{y}_{ana} with a noise assumption of δy_{ana} , which was computed via the centered 5-point numerical differentiation method for δy . The yellow curve is the difference between the 3-point differentiation and the analytical solution. It is visible that the difference at $1/T$, $2/T$ and $60/T$ is about 5-6 magnitudes larger in comparison to the red curve. The red curve is the difference between the 5-point method and the analytical solution. It should be noted that the blue and red curve are the same as shown in fig. 7.12. For the red curve, no special features at the oscillation frequencies are observed. For example at $1/T$ the rms amplitude at the red curve is only $\approx 2 \cdot 10^{-16}$ m/s, while the yellow curve shows a rms amplitude of $\approx 5 \cdot 10^{-10}$ m/s. Therefore, the 5-point method will be the preferred choice for computing numerical time derivatives for the LRI range data in section 6.12, because it ensures a more precise representation of the derivative and therefore the induced errors are small. Furthermore, a comparison with a third method for computing time derivatives with a CRN filter (cf. section 6.10) was presented in section 7.5.

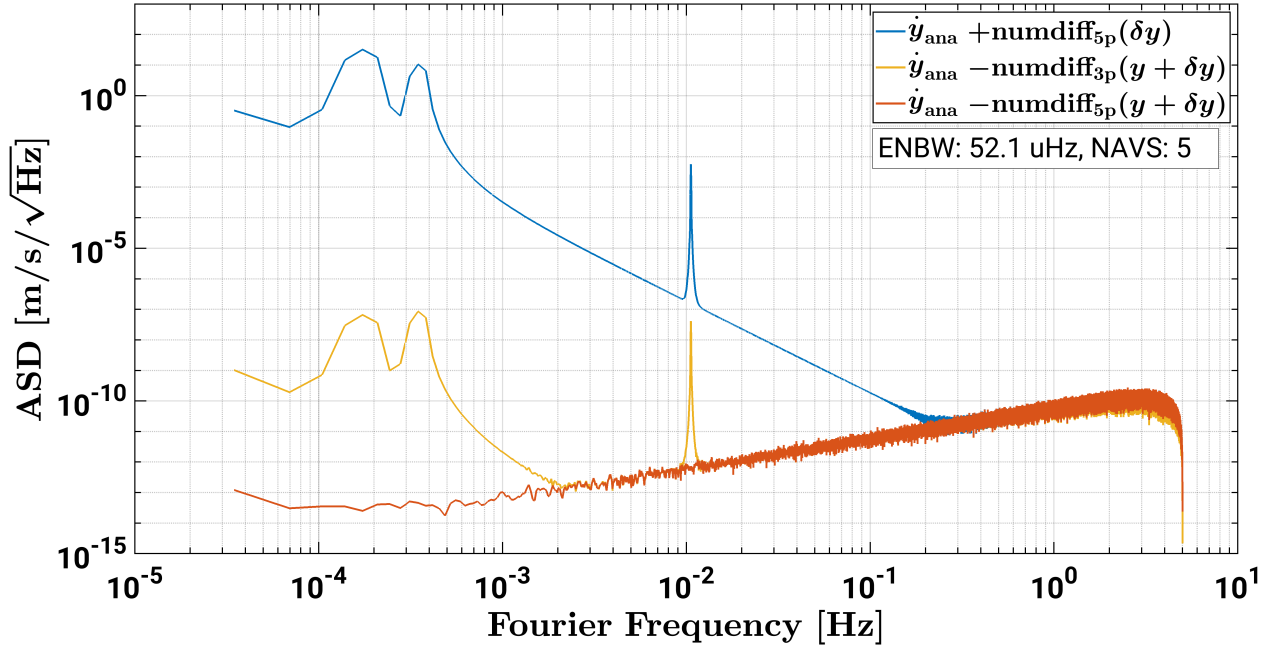


Figure A.5: ASD of comparison of analytical and numerical derivative for central 3-point and 5-point numerical differentiation methods. It is used the Hanning-Window function.

It should be noted that the calculation for the 5-point method has to use a different computation for the first and last two elements of a time series y , because the first and last centerable points are element 3 and $m - 2$, when y consists of m elements. The first two elements can be derived using¹

$$\dot{y}_{\text{num5p}}(1) = \frac{y(2) - y(1)}{h} \quad (\text{A.34})$$

$$\dot{y}_{\text{num5p}}(2) = \frac{y(3) - y(1)}{2 \cdot h} . \quad (\text{A.35})$$

¹Here the formulas for forward/backward difference of first order are used to be consistent with the LTPDA ‘diff’ function. In the future, one might want to use a higher order formula.

An extrapolation approach for the last two samples is applied as

$$\dot{y}_{\text{num5p}}(m-1) = 2 \cdot \dot{y}(m-2) - \dot{y}(m-3) \quad (\text{A.36})$$

$$\dot{y}_{\text{num5p}}(m) = 2 \cdot \dot{y}(m-1) - \dot{y}(m-2) . \quad (\text{A.37})$$

These samples were also removed for fig. A.5, because they lead to jumps in the beginning and ending of the time series. This issue is presented with fig. A.6. In the upper plot the derivatives of \dot{y}_{ana} and \dot{y}_{num5p} can be seen on the right y-axis. The left y-axis illustrates their differences.

The lower plot shows the same difference for $\dot{y}_{\text{ana}} - \dot{y}_{\text{num5p}}$, but in the beginning and ending two samples are removed. The variations in the difference of $\approx 10^{-12}$ m/s were already expected from the noise level at higher frequencies in fig. A.5. At approx. 3 Hz a rms amplitude of $2 \cdot 10^{-10}$ m/s/ $\sqrt{\text{Hz}} \cdot \sqrt{52.1 \mu\text{Hz}} \approx 1.5 \cdot 10^{-12}$ m/s is present.

Due to that mentioned jumps, it is recommended to use a little longer time series as it is desired for further calculations, such that the first and last samples can be cut out.

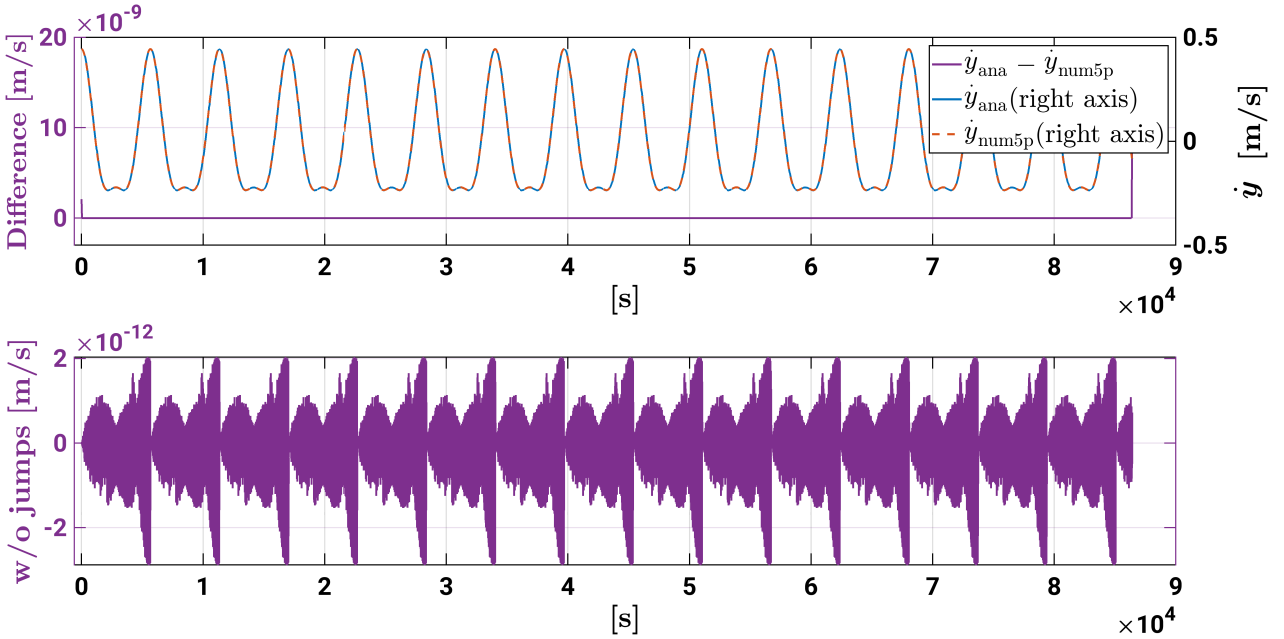


Figure A.6: Comparison of analytical and central 5-point numerical differentiation method in the time domain. The upper plot shows the resulting derivatives for both cases on the right y-axis, and their difference on the left. For the lower plot the first and last two samples are cropped out, which needs another computation, because they are not centerable inside the 5-point method.

A.3 Scale Factor and Time Shift between Two Similar Time Series

It is assumed that two equally sampled time series \vec{x} and \vec{y} are very similar, except for a scale s and a small time shift Δt . Two different methods for deriving a scale and time shift between \vec{x} and \vec{y} were investigated. A function called `computeScaleTimeshift` was implemented to minimize the figure of merit

$$\text{rms}(\vec{x}(t + \Delta t) \cdot s - \vec{y}(t)) \quad (\text{A.38})$$

where the rms is the root mean square.

The function of `computeScaleTimeshift` supports the following two methods:

xcorr: This method in `computeScaleTimeshift` uses the `xcorr`-function of MATLAB. It based on a cross-correlation, where the time series \vec{x} is shifted for certain samples to compute the similarity between $\vec{x} = x_1, \dots, x_n$ and $\vec{y} = y_1, \dots, y_n$. The function call

$$[\vec{\text{corr}}, \vec{\text{lag}}] = \text{xcorr}(\vec{x}, \vec{y}) \quad (\text{A.39})$$

will compute a vector of correlation values (`corr`) for the corresponding integer lag of the time series \vec{x} . We detrend both time series \vec{x} and \vec{y} in order to remove potential offsets, since a offset between both time series is not estimated and it would disturb the subsequent calculation of scale and time shift.

A higher `corr`-value indicates a higher similarity between \vec{x} and \vec{y} . Thus, the maximum of $\vec{\text{corr}}$ and the corresponding `lag` is selected, which are called corr_{max} and lag_{max} .

The MATLAB-function `xcorr` shows an accuracy of one sample.

For that reason, the `computeScaleTimeshift` function fits a polynomial of degree 2 to corr_{max} and its two neighbouring values. The maximum of this parabola estimates a correlation with sub-sample resolution. The new maximum lag can be derived from the previous integer position, and from the fractional part by setting the first derivative of the fitted polynomial ($p = C_1 x^2 + C_2 x + C_3$) to zero. This yields the position of the maximum

$$\text{lag}'_{\text{max}} = \frac{-C_2}{2 \cdot C_1} + \text{lag}_{\text{max}} \quad (\text{A.40})$$

The maximum value of correlation is found by evaluating the polynomial at its maximum, with the MATLAB function ‘`polyval`’, i.e.

$$V_{\text{max}} = \text{polyval}\left(p, -\frac{C_2}{2 \cdot C_1}\right) \quad (\text{A.41})$$

Using the rms-amplitude (A_{rms}) of \vec{x} and the number of samples N of \vec{x}

$$A_{\text{rms}} = \sqrt{\frac{\sum_{n=1}^N x_n^2}{N-1}} \quad (\text{A.42})$$

one can obtain the scale from

$$s = \frac{V_{\text{max}}}{(A_{\text{rms}} \cdot \sqrt{(N-1)})^2} \quad (\text{A.43})$$

and the time shift from

$$\Delta t = \frac{\text{lag}'_{\max}}{f_s}, \quad (\text{A.44})$$

where f_s denotes the sampling frequency of \vec{x} and \vec{y} .

numdiff: This method for deriving the scale and time shift minimizes the figure of merit

$$\|\vec{y} - s \cdot \vec{x} - s \cdot \Delta t \cdot \dot{\vec{x}}\|^2 \quad (\text{A.45})$$

with $\dot{\vec{x}}$ being the first time derivative of \vec{x} . This derivative is computed with a central 5-point numerical differentiation method, as described in appendix A.2.

For solving eq. (A.45) the MATLAB command ‘mldivide’ is used, i.e.

$$\vec{p} = \text{mldivide}([\vec{x}, \dot{\vec{x}}], \vec{y}). \quad (\text{A.46})$$

The two components of $\vec{p} = [p_1, p_2]$ can be converted to the scale factor s and time shift Δt with

$$s = p_1, \quad \Delta t = \frac{p_2}{p_1}. \quad (\text{A.47})$$

The **xcorr** and **numdiff** method of the function `computeScaleTimeshift` will be compared in the following. The two time series in table A.2 are cross-correlated with our function `computeScaleTimeshift`.

sampling frequency	time	data
$f_s = 0.2$ Hz	$t_x = [0 : 1/f_s : 86400]$	$x = 0.5 \sin\left(\frac{2\pi}{5674} \cdot (t_x + 0.25)\right)$
	$t_y = [0 : 1/f_s : 86400]$	$y = \sin\left(\frac{2\pi}{5674} \cdot t_y\right)$

Table A.2: Definition of two simulated signals x and y , where x differs in comparison to y in a scale of $s_{\text{true}} = 2$ and a shift in time of $\Delta t_{\text{true}} = 0.25$ s.

For the **xcorr** method results

$$[s, \Delta t] = \text{computeScaleTimeshift}(f_s, x, y, \text{'xcorr'}) \quad (\text{A.48})$$

$$s_{\text{true}} - s = 56 \cdot 10^{-6} \quad (\text{A.49})$$

$$\Delta t_{\text{true}} - (-\Delta t) = 0.196 \text{ s} . \quad (\text{A.50})$$

The scale factor difference is very close to zero which is expected. But the estimation for the time shift dt is not close to 0.25 seconds. The calculated value differs from the expected value by approx 0.2 s. Even if more iterations are used, the time offset is not estimated very well. After five iterations the difference of expected and computed value is 0.074 s.

Using the **numdiff** method yields

$$[s, \Delta t] = \text{computeScaleTimeshift}(f_s, x, y, \text{'numdiff'}) \quad (\text{A.51})$$

$$s_{\text{true}} - s = 78 \cdot 10^{-9} \quad (\text{A.52})$$

$$\Delta t_{\text{true}} - (-\Delta t) = 53 \cdot 10^{-6} \text{ s} . \quad (\text{A.53})$$

The computed scale factor is very close to the true scale factor. Also the estimation for the time shift matches better with the expected value. The differences is about $50\mu\text{s}$.

After a few more iterations one can achieve an even higher agreement. After five iterations

$$s_{\text{true}} - s = -2 \cdot 10^{-13} \tag{A.54}$$

$$\Delta t_{\text{true}} - (-\Delta t) = -2 \cdot 10^{-12} \text{ s} . \tag{A.55}$$

The results suggest that the `numdiff` method is more precise for our use-case, which is why we use this method for the computation of LRI1B v50 (cf. section [6.9.1](#)).

B

The LRI Level 1A v50 Processing at AEI

This chapter will present the AEI data processing for the Level 1A data products of the LRI. This data products can also be identified by the abbreviation of v50. Each product contains a YAML-formated header with information about the creator and a description of content for the listed data, followed by a large space-separated table, which includes all the time-tags and measurements or sensor values in a time sorted order (similar to LRI1B, cf. section 6.14).

The generated products are aligned to day bounds, however, our processing accumulates the data of more days. The reason for that is, that not always all the Pus-Packets are downlinked before the new day starts. It is possible that a few packets only arrive the next day. The same problem could appear, when the normal operating mode of the LRI, the Science Mode, gets lost. The `QuadPhotoreceiverTlm`, `SteeringMirrorTlm` and `LaserTlm` are only reported in Science Mode. Consequently, if the recording of such a Pus-Packet was not finished, it will be completed and downlinked when entering the Science Mode again. In the end only the data with the time-tags of each single day are saved in a *.txt-file to achieve the daily solutions. All Level 1A products of one day (≈ 500 MB/day) are compressed to the *.tgz format (≈ 105 MB/day). Each of the following Level 1A products are generated for both satellites.

In the end of this section an overview is given about all the derived time-tags inside each product and how the data is sorted. Every detail from the following sub-sections are illustrated in fig. B.1.

B.1 LRI Data Product - LRI1A

LRI1A is the main scientific data product, because it contains the LRI phase measurements. This data will be needed for further processing steps to finally derive the gravity field solutions. All the data listed in LRI1A is summarised in table B.1. LRI1A contains the phase measurements and values for computing the Carrier to Noise Ratio (CNR) from the

- `QuadPhotoreceiverTlm` (VC4)
- `LriHealthMonitor` (VC2)

packets. As shown in fig. 5.1, the `QuadPhotoreceiverTlm` is defined as science data (VC4) and the `LriHealthMonitor` as housekeeping data (VC2). The two packets have a high accuracy in their timing information in contrast to the other packets.

The time-tags in Level 0 are stored as `TimeUp` and `TimeLow`, as introduced in section 5.2. For the LRI1A format, the `TimeUp` is converted from GPS seconds into GRACE GPS seconds using eq. (3.1). `TimeLow` is converted by dividing the `clock_rate` of the corresponding satellite and multiplying with 10^9 to transform it into nanoseconds with 16 significant digits (cf. appendix C.1, second bullet point). These integer and fractional time values are the first and second column in the LRI1A product. The third column of table B.1 shows the S/C identifier (ID) of the corresponding satellite.

Column	Parameter	Unit	Type	Information
1	LRP time-tag	s	[uint32]	Seconds past 2000-01-01 12:00:00.
2	LRP time-tag	ns	[double]	Fractional part of time in ns with decimal digits (16 significant digits).
3	S/C ID		[char]	Data recording from GF1 = C, GF2 = D
4	product flag		[string]	Bit-wise meaning for data availability.
5	quality flag		[string]	Currently not used in v50, i.e '00000000'.
6	piston phase	cycles	[double]	Averaged phase from all segments.
7	Quadrant 0 Up	counts	[uint32]	Upper part of measurement from QPD segment 0.
8	Quadrant 0 Low	counts	[uint32]	Lower part of measurement from QPD segment 0.
9	Quadrant 1 Up	counts	[uint32]	Upper part of measurement from QPD segment 1.
10	Quadrant 1 Low	counts	[uint32]	Lower part of measurement from QPD segment 1.
11	Quadrant 2 Up	counts	[uint32]	Upper part of measurement from QPD segment 2.
12	Quadrant 2 Low	counts	[uint32]	Lower part of measurement from QPD segment 2.
13	Quadrant 3 Up	counts	[uint32]	Upper part of measurement from QPD segment 3.
14	Quadrant 3 Low	counts	[uint32]	Lower part of measurement from QPD segment 3.
15	fftSNR	counts	[uint32]	Amplitude of the highest peak in FFT spectrum.
16	noise8_9	counts	[uint32]	RMS noise in frequency band 8...9 MHz from FFT
17	noise11_12	counts	[uint32]	RMS noise in frequency band 11...12 MHz from FFT

Table B.1: Description of LRI1A format.

The downlinked LRI data contains integer values with not more than 32 bit depth, probably to ensure downward compatibility with older computer systems. The measurements from the QPD segments have internally 64 bit, but are split into two 32 bit integers, where an upper and a lower value for each segment is stored. This fact causes eight columns in the LRI1A product for the data of four QPD segments in units of counts.

For LRI1A the so-called piston phase is computed, which is an averaged phase from all four QPD channels. To convert the counts into cycles the calculation of

$$\varphi_{\text{piston}}[\text{cycles}] = \frac{1}{4} \sum_{i=1}^4 \frac{2^{32} \cdot \varphi_{i,\text{up}} + \varphi_{i,\text{low}}}{10 \cdot 2^{24}}, \quad (\text{B.1})$$

is applied. The result is written with 16 significant numbers in column six of LRI1A. It is not recommended to make further calculations with this piston phase, because it leads to a loss of precision. The derivation of a more exact mean phase was explained in section 6.1 (see also eq. (6.3) and eq. (6.4)).

The last three columns are filled with measurements of `fftSNR`, `noise8.9` and `noise11.12` which were mentioned in section 4.4. They are needed for computing the Carrier to Noise Ratio (CNR) for the LRI1B product. However, these measurements need to be interpolated onto the QPD time-tags, because the `LRIHealthMonitor` data has a smaller sampling rate of 0.1 Hz. The QPD measurements are taken with a sampling rate of approx. 10 Hz. For that interpolation the MATLAB method ‘previous’ is used.

Column four contains a so-called product flag. It is a sequence of 16 bits. This bit-wise meaning indicates, when data in the individual columns is available or not. Here, bit 0 starts right most. An example could be a product flag of: ‘0000000111111111’. Bit 0 to bit 9 are equal to one, which means that the data streams from column six to fourteen (i.e. the phase measurements) are available in LRI1A. Bit 10 to bit 12 indicates the data columns of the `LRIHealthMonitor`, which seems to be missing in this example, because the product flag is set to zero. The last four bits are not defined, hence they are always zero.

Column five contains a quality flag, which gives information about the quality of the data. It is also defined by a bit-wise meaning. For example it could indicate a phase break in the QPD measurements, by setting the first bit to one. When no special events occur the eight bits of column five are zero. Currently, the LRI1A v50 product does not use the quality flag. All eight bits are always zero.

B.2 LRI Steering Mirror Data Product - LSM1A

The measured and commanded (angular-) positions of the Fast Steering Mirror can be found in the LRI Steering Mirror (LSM1A) product. The Fast Steering Mirror was presented in more detail in section 4.1.2. The generation of the LSM1A product requires the

- `SteeringMirrorTlm` (VC4)

packet. It also belongs to the science data (VC4) but has less precise time-tags compared to the packets in LRI1A (cf. fig. 5.1). The time-tags for each value in a tuple of 30 are computed as it was described in section 5.2.

The formatting of the LSM1A product is shown in table B.2. One new parameter is given by column three, which indicates the time reference frame. For the LSM1A it is always ‘S’ and

describes that the data was time-tagged after the LRP FPGA has received a timing information from the OBC. For more details about the time reference system, please refer to appendix B.3. The positions of the steering mirror are given as data types of [uint12] (cf. table B.2).

Column	Parameter	Unit	Type	Information
1	LRP time-tag	s	[uint32]	Seconds past 2000-01-01 12:00:00.
2	LRP time-tag	ns	[uint32]	Fractional part of time.
3	time reference frame		[char]	S = After the Science FPGA loads in Receiver Time
4	S/C ID		[char]	Data recording from GF1 = C, GF2 = D
5	internalSensor 0	[counts]	[uint12]	measured position axis 0.
6	internalSensor 1	[counts]	[uint12]	measured position axis 1.
7	commanded 0		[uint12]	commanded position axis 0.
8	commanded 1		[uint12]	commanded position axis 1.
9	quality flag		[string]	Bit 0-7 not defined: '0000000'

Table B.2: Format and content of of LSM1A product.

B.3 LRI Housekeeping Data Product - LHK1A

The LRI Housekeeping (LHK1A) product contains information about the status of the instrument and many different sensor observations. It needs the following packets:

- ADCSamples (VC4)
- Datation Reports (VC2)
- LaserTlm (VC4)
- LriHealthMonitor (VC2)
- LriHousekeepingTlm (VC2)
- LriStateTlm (VC2)

The packets of LHK1A are written into a large table with characteristics as shown in table B.3. The data is sorted in ascending order by time-tags, sensor types and sensor names.

It should be noted that LHK1A v50 also includes the `fftSNR`, `noise8_9` and `noise11_12` from the `LriHealthMonitor`, because only interpolated values are provided in LRI1A.

Additionally, different sensor values are processed as different data types. For the used data types please refer to table B.5.

It should be noted that the quality flag in LHK1A v50 is not used yet.

Time Reference Frame S or B: LHK1A contains a time reference specification in its fifth column. Usually the marker “S” is used in the AEI processing. It describes the typical time-tags, which are given “after the FPGA loads in receiver time” [Wen, 2019]. The case “B” means “before the science FPGA loads in receiver time” [Wen, 2019]. AEI only uses it, if the LRP has rebooted and has not received timing information from the OBC yet. For the processing of Level 1A, we distinguish the two cases as follows:

$$\text{time reference frame S, if LRP rcv time_tag} > 9 \cdot 10^8 \text{ s} \quad (\text{B.2})$$

$$\text{time ref. frame B, directly after LRP reboot if LRP rcv time_tag} \leq 9 \cdot 10^8 \text{ s} . \quad (\text{B.3})$$

Column	Parameter	Unit	Type	Information
1	LRP time-tag	s	[uint32]	Seconds past 2000-01-01 12:00:00.
2	LRP time-tag	ns	[uint32]	Fractional part of time.
3	time reference frame		[char]	B = Before the Science FPGA loads in Receiver Time S = After the Science FPGA loads in Receiver Time
4	S/C ID		[char]	Data recording from GF1 = C, GF2 = D
5	quality flag		[string]	Currently '0000000' in v50.
6	sensor type		[char]	? = no unit, A=Current [Ampere], T=Temperature [deg C], V=Voltage [Volts]
7	sensor value	cf. column 6	cf. table B.5	measured value, or number (cf. table B.4)
8	sensor name		[string]	name of measuring sensor

Table B.3: Summarised information of LHK1A format.

A time-tag of $9 \cdot 10^8$ s correspond to a date in 2008, thus, it is much smaller than the actual time-tags after 2018. This issue was discussed in more detail in section 5.2, where the computation of `lriobctime_gisl` was presented.

The internal ‘incorrect’ LRP receiver time-tags are replaced by the `PusTime` for deriving the LRP integer time-tag in column one, to maintain the chronological order. The fractional part of time in column two remains as it is. This approach is used for all the packets in LHK1A except for the `LriStateTlm` and `Datation Reports`. The `Datation Reports` are inserted in LHK1A only with their `PusTime` and a fractional part of 0 clock ticks. The `Datation Reports` contain two additional sensor values (`lriTimeUpper` in GPS seconds and `lriTimeLower` in clock ticks), which show the exact time-tags of the LRP rcv time, when the time offset between OBC and LRP was measured.

The `LriStateTlm` has only an integer `Pus-Packet` GPS time-tag, while the fractional part of time is also set to 0. Consequently, this data is always assigned to the time reference system S, because the `PusTime` is not affected by a potentially uninitialized LRP time directly after reboot.

In case of nominal time frame S, the `ADCSamples`, `LaserTlm`, `LriHealthMonitor` and the `LriHousekeepingTlm` packets can keep their LRP assigned time-tags. In the very end all the mentioned time-tags are now converted to the GRACE GPS time and the clock ticks to nanoseconds (in integer resolution). All these special details are also summarised in fig. B.1.

Some states of the instruments, e.g. of the laser, FPGA or USO, are also listed inside the LHK1A. This information is expressed by a string of the sensor name and a number for the sensor value. This number-string assignments are listed in table B.4.

Furthermore, the table B.5 shows the used data types for all different sensor values from different data streams (different `Pus-Packets`).

Status	String	Number
role	transponder	0
	master	1
usoState	usoA	1
	usoB	2
Mode states	INVALID_VALUE	1
	standby	2
	instrumentSetup	3
	reacquisition	4
	initialAcquisition	5
	science	6
	diagnostic	7
Laser states	INVALID_VALUE	-1
	enabled	1
	notEnabled	0
FPGA states	INVALID_VALUE	65535
	SCIENCE_STATE	45
	PERSIST	51
	PL_LOCK	52
	PM_RESET	75
	DWSC_TURN_ON	76
	PM_LOCK	82
	REACQ_GO_TO_FLASH	385
	REACQ_SCAN	127
	REACQ_SETUP	120
	REACQ_PDH_WAIT	102
	REACQ_PDH_SETUP	97
	REACQ_PDH_RESET	85
	IDLE	0
	LASER	7
	INITIAL_WAITING	25
	INITIAL_SETUP	30
INITIAL_SCAN	42	

Table B.4: String and corresponding numerical values in LHK1A product.

ADCSamples Type	Sensor names of sensor values, to which Type refers.
[uint12]	TMA_PMH_CURRENT, TMA_LASER_POWER, TMA_PMH_TEMP, TM_RLU_TEMP, TEMPERATURE_READOUT_0, CAVITY_RX_DC, CAVITY_TX_DC, QUAD_DC_0, QUAD_DC_1, QUAD_DC_2, QUAD_DC_3, MIR_POS1_P, MIR_POS0_P, COIL_CURRENT_1, COIL_CURRENT_0, TEMP_SCI_FPGA, TEMP_POL, TEMP_PROC, TEMP_REG_2V5, TEMP_REG_2V5A, 3V3_SW_I_TEL, 2V5_TEL, 1V0_TEL, 3V3, 5V0, 12V0P_CAV 12V0N_CAV, 15V0P_LAS, 15V0N_LAS, 15V0P_MON, 3V3_ISENSE, 15V0P_LAS_ISENSE, DCDC_TEMP_3V3, DCDC_TEMP_5V, DCDC_TEMP_15V, DCDC_TEMP_15V0P_LAS, DCDC_TEMP_15V0N_LAS PDH_ERROR_MAX, PM_FMODEL, NOISE8_9, NOISE11_12
[uint16]	PZT_IN_LOOP_STATUS, PZT_OUT_OF_LOOP_STATUS, THERM_IN_LOOP_STATUS, THERM_OUT_OF_LOOP_STATUS
LaserTlm Type	Sensor names of sensor values, to which Type refers.
[uint32]	pztInLoopStatus, pztOutOfLoopStatus, thermInLoopStatus, thermOutOfLoopStatus
[uint12]	TMA_PMH_CURRENT, TMA_PMH_TEMP, TMA_LASER_POWER, TM_RLU_TEMP, quadDc0, quadDc1, quadDc2, quadDc3
LriHealthMonitor Type	Sensor names of sensor values, to which Type refers.
[uint32]	fftSnr, i_0, q_0, i_1, q_1, i_2, q_2, i_3, q_3, noies8_9, noise11_12, pm_fmodel, pdh_error_max
HousekeepingTlm Type	Sensor names of sensor values, to which Type refers.
[uint12]	scienceTemp, pmHeadTemp, laserTemp, 2V5_TEL, 1V0_TEL, 3V3_I_TEL, TEMP_REG_2V5A, procTemp, DCDC_TEMP_15V0P_LAS
[int]	mode, laserEnabled, fpga_state (cf. table B.4)
LriStateTlm Type	Sensor names of sensor values, to which Type refers.
[int]	lriMode, command_sc, aaModeState, laserState, standbyState, testState, fswInternalState, usoSelect, fpga_state, reserved2, role (cf. table B.4)
Datation Report Type	Sensor names of sensor values, to which Type refers.
[uint32]	dayFsw, millisecFsw, nanosecFsw, dayRcvd, millisecRcvd, nanosecRcvd, lriTimeLower, lriTimeUpper

Table B.5: Types of LHK1A sensor measurements.

B.4 LRI Log Messages - LLG1A

The LRI Log Messages (LLG1A) product contains the packets

- BootMessages (VC4)
- EventReports (VC4) (remark: no RealTime-EventReports)
- DirectoryListings (VC4)

in a format as shown in table B.6. In general, the messages and `DirectoryListings` get their `PusTime` for the first column in LLG1A with LRP rcv time-tags in GRACE GPS time. There are some particularities for a few messages, which are explained below. To restore the correct order of the messages the `lriobctime_gisl(:,4)` from section 5.2 is used.

BootMessages: The `BootMessages` occur after every LRP restart. To bring these time-tag free messages in the correct order, the `lriobctime_gisl(:,4)` value is rounded to the next integer time-tag. This yields an estimated `PusTime` for the LLG1A time-tag. Consequently, many consecutive `BootMessages` have the same time-tag in LLG1A and are further numbered with the `pkt_count` (see explanation below).

EventReports: All `EventReports` are inserted with the `PusTime`. The only exception is the `EventReport` “Rmgr::FsMgr: malloc gave...”, which is called `defaultBootMsg` in our processing. Because of its invalid `PusTime` (cf. fig. 5.2, last column) the rounded `lriobctime_gisl(:,4)` is used in LLG1A.

DirectoryListings: The messages of the `DirectoryListings` indicate the content of specific directories in the file system. These messages start with “Listing of directory xxx”, where xxx can be replaced by the actual file directory. Afterwards, all the files inside the directory are listed. Each file has some additional information in Level 0, which is converted to one message for the LLG1A. One example is shown below.

Column	Parameter	Unit	Type	Information
1	LRP time-tag	s	[uint32]	Seconds past 2000-01-01 12:00:00.
2	pkt_count		[int]	Counter for messages at same integer time: - Boot Messages have a negativ counter e.g. (-3, -2, -1). - First counter after Boot Messages is 0. - Other messages have a positiv counter e.g. (1, 2, 3).
3	S/C ID		[char]	Data recording from GF1 = C, GF2 = D
4	logpacket		[string]	Message

Table B.6: Summarised information of LLG1A format.

File listing in the AEI LriToolbox for directory: /ect1:

File name	Quality flag	Size of file [bytes]	File CRC	position in memory start	position in memory end
diagDataType1.bin	1	4000000	1959540988	570177039	5589500

Output in LLG1A:

```
">Listing of directory /etc1"
">diagDataType1.bin, 0x1, 0x3d0900, 0x74cc38fc, 0x21fc360f:0x354e3d8"
```

One can see that the resulting LLG1A message on a file contains hexadecimal information on quality flag, file size, a CRC checksum and other parameters. If one directory contains more than 21 messages, it is divided into more parts (in our processing we can identify it by the value `isLast = F` (false) instead of `T` (true)).

Additionally, every `DirectoryListing` message, `BootMessage` and `EventReport` have the symbol '>' in the beginning of each message.

Sorting LLG1A data: All messages of LLG1A are sorted by their (corrected) `PusTimes` and their computed times of `lriobctime_gisl(:,4)` for keeping the chronological order. `lriobctime_gisl(:,4)` is not included in the LLG1A file, it is only used for restoring the correct message order (cf. fig. B.1).

Message Counter: Another feature of LLG1A is the message counter (or packet counter (`pkt_count`) in table B.6). It counts the messages, which were recorded within one second. The `BootMessages` have a negative counter. For example, when 30 `BootMessages` occur the first one has a `pkt_count = -30`, and the last one `pkt_count = -1`. `EventReports` and `DirectoryListings` have a positive counter. For instance, two `EventReports` with the same LLG1A time-tag, get the counter numbers: `pkt_count = +1` and `pkt_count = +2`. One exception is the `defaultBootMsg`, which marks the transition between normal events and `BootMessages`. This message has the `pkt_count = 0`.

B.5 LRI Light Time Product - LLT1A

The LRI Light Time (LLT1A) product is not generated at the AEI yet, but for the sake of completeness, a few general things about this product are mentioned here. LLT1A contains information about the signal travel time \mathcal{L} between the master and transponder S/C. This product contains the information for GF1 and GF2 and is computed once per day, while the other Level 1A data products of the LRI are computed for each spacecraft.

Table B.7 gives an overview of the included data as it is used in the official available SDS v04.

Section 4.2 addressed how the signals in the LRI are received and transmitted between the master and transponder S/C. The reader should be reminded that each S/C works as receiver and transmitter, hence a signal travel time \mathcal{L} (cf. section 2.2.3) can be computed for the path of

$$\text{master} \rightarrow \text{transponder} =: \mathcal{L}_{\text{MT}} \quad (\text{B.4})$$

and for

$$\text{transponder} \rightarrow \text{master} =: \mathcal{L}_{\text{TM}} . \quad (\text{B.5})$$

Example for two rows in LLT1A with GF2 (transponder) and GF1 (master):

time-tag	rcv S/C	tran S/C	\mathcal{L}	position	velocity	qualflag
t_0	C	D	\mathcal{L}_{TM}	$x_C y_C z_C$	$vx_C vy_C vz_C$	00000000
t_0	D	C	\mathcal{L}_{MT}	$x_D y_D z_D$	$vx_D vy_D vz_D$	00000001

The first row is showing the direction of signal traveling from GF2 to GF1. GF1 receives a signal at t_0 , which was previously transmitted from GF2 at $t_0 - \mathcal{L}_{\text{TM}}$. The S/C ID of the receiving satellite, here C, is inserted in column two. The time-tag of the signal receiving is shown in column one in GrGPS seconds. The S/C ID of the transmitting satellite, here D, is inserted in column three. The signal travel time \mathcal{L}_{TM} from transponder to master is inserted in column four, which is negative by definition [Wen \[2019\]](#).

In the next row would be shown the other direction. GF2 receives (column two: D) a signal from GF1 (column three: C) at $t_0 - \mathcal{L}_{\text{TM}}$, which was sent at $t_0 - \mathcal{L}_{\text{TM}} - \mathcal{L}_{\text{MT}}$. Therefore, \mathcal{L}_{MT} is inserted in column four. In the columns of five to ten, the position and velocity of the receiving S/C are shown. These values are computed from the Precision Orbit Determination [[Wen, 2019](#)].

Usually the LLT1A product is used to derive the LRI1B product. So far, we have not derived a LLT1A product, though all information is available and is used in the generation of LRI1B.

Column	Parameter	Unit	Type	Information
1	GPS time-tag	s	[unit32]	Time of signal receiving at receiving S/C at GrGPS time.
2	S/C ID		[char]	Receiving S/C to which \mathcal{L} refers.
3	S/C ID		[char]	Transmitting S/C to which \mathcal{L} refers.
4	\mathcal{L}	s	[double]	Light travel time between receiving and transmitting S/C.
5	xpos	m	[double]	Position along x axis of receiving S/C.
6	ypos	m	[double]	Position along y axis of receiving S/C.
7	zpos	m	[double]	Position along z axis of receiving S/C.
8	xvel	m/s	[double]	Velocity along x axis of receiving S/C.
9	yvel	m/s	[double]	Velocity along y axis of receiving S/C.
10	zvel	m/s	[double]	Velocity along z axis of receiving S/C.
11	qualflag not used in v04 yet		[string]	Bit 0 = 0 if receiving S/C is master, = 1 if receiving S/C is transponder. Bits 1-7: Not defined.

Table B.7: LLT1A format as it is used in v04 of SDS [[Wen, 2019](#)].

B.6 Summary of Time-tags and Sorting for Level 1A Products

The used timing information for the different products of Level 1A and how the data was sorted is illustrated in fig. B.1. The figure summarises all the important explanations from appendix B.

The time conversion for each LRI data stream from TimeUp and TimeLow or PusTime into the GRACE GPS time-tags for the Level 1A format are shown by the white boxes. The yellow boxes summarise how the data is sorted, while the purple boxes provide a few more details for special cases.

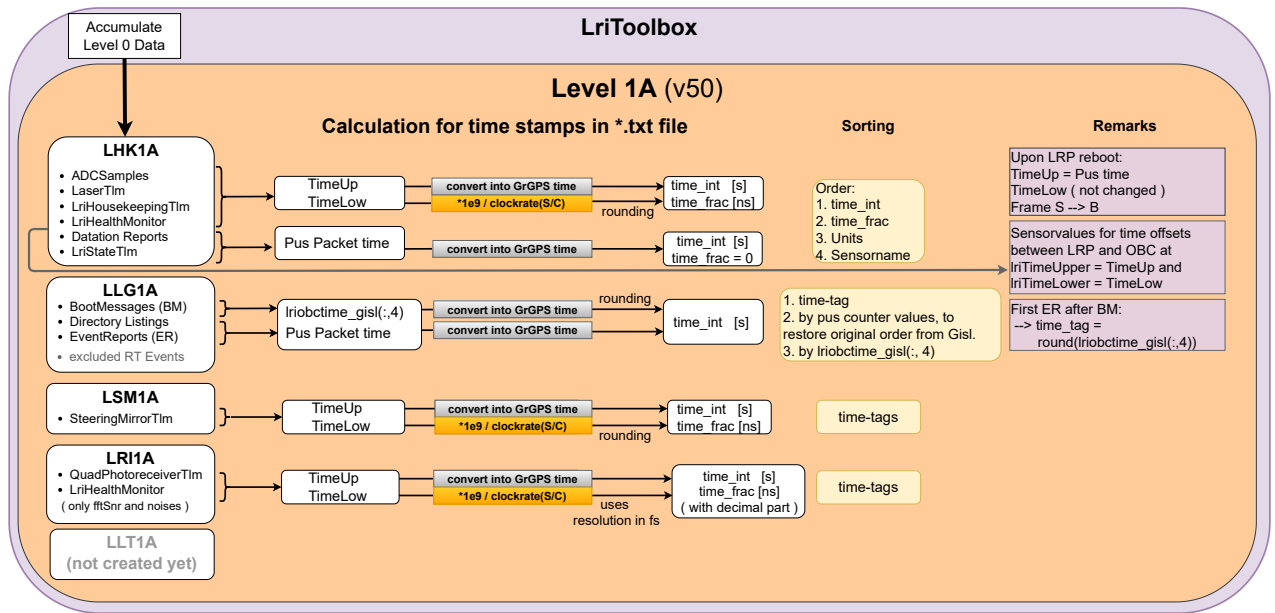


Figure B.1: Summary of used timing information and sorting for LRI Level 1A data products. Each data product shows the included Pus-Packets and which of the original or corrected time-tags are converted from GPS to GRACE GPS time. All products, except the LLG1A, have two columns for an integer time-tag (time_int) and a fractional one (time_frac). The sorting inside each packet is given by the yellow boxes. Some special remarks are shown in the purple boxes. For a better understanding of TimeUp, TimeLow, PusTime and lriobctime_gisl(:,4) it is referred to section 5.2.



Validation of SDS LRI Level 1A v04 data

To verify and validate the correctness of the official available LRI Level 1 data products of SDS v04, they are compared with the alternative AEI v50 products. The v04 data of SDS is publicly available and can be downloaded from [FTP server of GFZ](#).

The most important discrepancies between v04 and v50 Level 1A has already been forwarded to JPL [[Müller et al., 2020](#)], because JPL is responsible for the Level 1A v04 processing. The following comparison was performed for the period between 2018-06-11 to 2020-04-01.

One advantage of the alternative processing of Level 1A data products is that v04 and v50 can be compared in a text editor due to their same format. Therefore, a few extractions (screenshots) will be used in the following sections for highlighting differences.

C.1 Comparison of LRI1A v04 and v50

The processing of LRI1A v50 was introduced in appendix [B.1](#). One example for the data sets of v04 and v50 is shown in [fig. C.5](#). The red box marks missing data in v04 and the green boxes the suggestions for an alternative data providing. The discrepancies between v04 and v50 are shown in the following:

- Missing Health Monitor values:
Occasionally, the `fftSNR`, `noise8_9` and `noiese11_12` measurements are not present in v04 data, which can be recognized at the product flag, where bit 10 to 12 are set to zero to indicate unavailability. However, the last three columns in LRI1A v50 contain the LriHealthMonitor data. All affected days are shown in [table C.1](#).
- Time-tags with a higher resolution (nanoseconds with a decimal part) are used in v50, because the phase measurements are sampled equally in a separation of 4000000 clock ticks. That means the sampling rate is an irrational number with 103476821.192053... nanoseconds for GF1 and 103474701.159889... nanoseconds for GF2. Using a resolution of 1 ns yields a time-tag jitter with steps of 1 ns, which is equivalent to a ranging error of 10 nm, due to the 10 MHz offset. For that reason the AEI team recommends to use a higher resolution to maintain the accuracy for LRI1A. In order to preserve full double

precision in the text files, we print out 16 significant digits for the fractional time-tags corresponding to 1 fs resolution. The resulting time-tag jitter shows steps of 1-2 fs. This is equivalent to a ranging error of ≈ 21 fm.

- So far, neither the AEI nor SDS has implemented a quality flag in LRI1A.

year	S/C	day of year
2018	GF1/GF2	d165-d200, d346-d365
2019	GF1/GF2	d001-d038, d077-d115, d119-d181, d263
	GF1	d249, d359, d364
	GF2	d347, d352, d354, d355, d360, d363
2020	GF1	d002, d004, d007, d009, d014, d017, d030, d045, d064
	GF2	d003, d005, d008, d010, d013, d015, d024, d025, d045

Table C.1: Affected days of missing HealthMonitor data in LRI1A v04.

C.2 Comparison of LSM1A v04 and v50

Details for the LSM1A v50 processing can be found in appendix B.2.

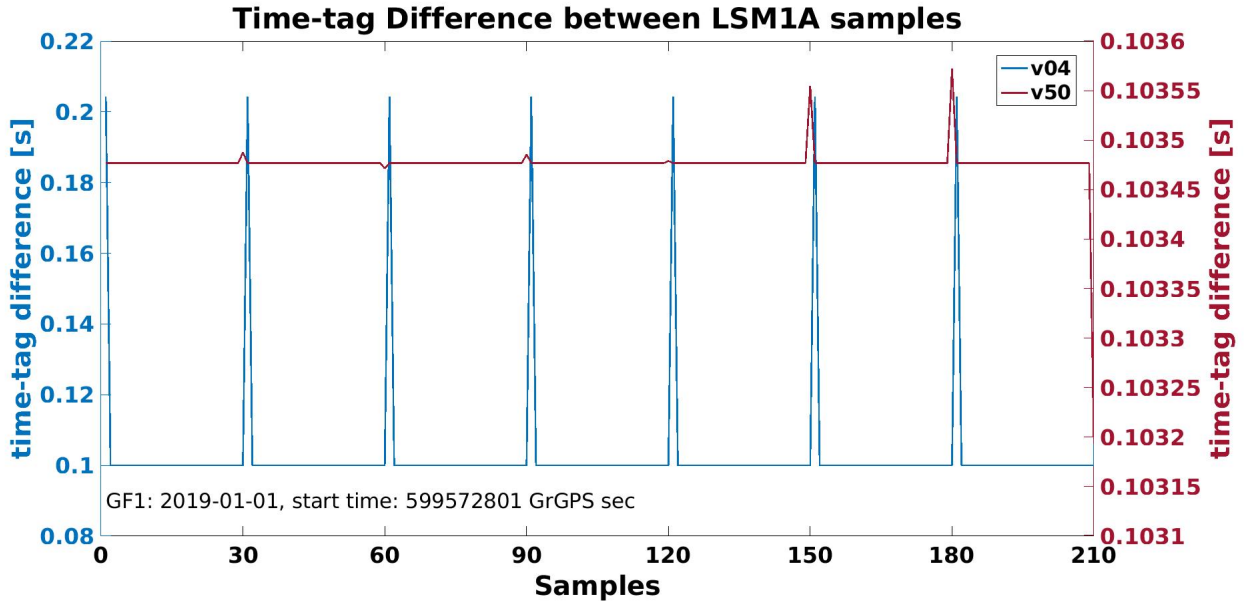


Figure C.1: Comparison of LSM1A time-tag differences for v04 and v50. In the v04 product jumps with a magnitude of 0.2 s are observed, with the beginning of each new Pus-Packet, while v50 shows a time-tag jitter of a few microseconds.

- The Steering Mirror Telemetry comes in packets with 30 tuples, where only the last one gets a time-tag (cf. section 5.1). For the other 29 tuples the time-tags are computed by interpolating with the sampling rate of GF1 and GF2 for v50 data. In contrast to that, v04 uses a sampling rate of 0.1 s between each tuple. This leads to a larger spacing of approx. 0.2 s after every packet.

The blue curve in fig. C.1 shows the time-tag difference of v04 for the first samples at the beginning of January 1st, 2019. After every 30th sample the mentioned behaviour can be observed. The right y-axis shows the difference for v50 time-tags in dark red. There occurs only a jitter in a magnitude of some microseconds, which might be related to the less precise time-tag assignment of the LRP (cf. fig. 5.1).

C.3 Comparison of LHK1A v04 and v50

All information about the processing for LHK1A v50 are summarised in appendix B.3.

More general issues and differences:

- The `ADCSamples` in LHK1A v04 are reported with a fractional part of time in clock ticks. However, the product description demands the time-tags in nanoseconds, which is the reason why LHK1A v50 uses this unit.
- The `LriHousekeepingTlm` contains the I&Q values, `pdh_error_max` and `pm_fmodel`. For the time-tags of the I&Q values in v04, the filter delay from eq. (3.11) is used. v50 refrains from correcting the time-tags in Level 1A, because the data from one `LriHousekeepingTlm` packet would not stay together after the sorting process. Furthermore, the filter delay for the phase measurements will also be applied in the Level 1B processing and not for LRI1A (cf. chapter 6). To make it uniform, I&Q time-tags are not corrected for Level 1A of v50 data.
- The v04 time frame markers “S” and “B” are not used as it is defined in the product description. The telemetry packets of `ADCSamples`, `Datation Reports` and `LriStateTlm` are always using the time frame identifier “B”. On the contrary the `LaserTlm` and the `LriHealthMonitor` use always “S”. Only the `LriHousekeepingTlm` shows a change from “S” to “B”, whenever the mode state changes to `mode:diagnostic` or to the state `mode:instrumentSetup`. In appendix B.3 was explained that “B” should only be used, if the LRP does not receive a time information from the OBC directly after a LRP reboot. Otherwise it should be used “S”.
- Furthermore, `fftSNR`, `noise8_9` and `noiese11_12` of the `LriHealthMonitor` data are included in v50 (cf. appendix B.3), because they are reported in LRI1A with interpolated time-tags. One additional reason is that the entire packet should be available in LHK1A v50.

Issues on different days:

- A problem with wrong assigned data for GF2, caused by the ground station NSG, exists in 2018. The data of GF1 was downlinked to two ground stations by a double pass, and than correctly assigned to GF1 (from one station) and wrongly assigned to GF2 from NSG. V. Müller (AEI, 2020) has already been forwarded this information to DLR in a mail from February 11th, 2020. Due to that, a few packets of identical VC2 data in GF1 and GF2 were included in v04. One example is illustrated in fig. C.2 for doy 231 in year 2018. On the left side a screenshot of the GF1 LHK1A v04 file, and on the right side of GF2 is shown. The yellow marked time-tags indicate the duplicates. All affected days are listed in table C.2.

To determine the affected files, one could compare the bit-sizes of GF1 and GF2 files or their Pus-Headers, because most of them are exactly the same. Additionally, reading all GF2 Pus-Headers also identifies the affected files, because the Pus-Headers from NSG do not match in the order of normal GF2 Pus-Headers ([priv. comm. V. Müller, AEI, 2020](#)).

year	S/C	day of year
2018	GF2	d226, d228, d229, d230, d231, d233, d235, d238, d242, d245

Table C.2: Affected days of wrong assigned data caused by ground station NSG.

LRI1Av04 - GF1				LRI1Av04 - GF2			
587955960	6835906	B C	00000000 V 2031 5v0	587955918	27191294	B D	00000000 V 82 1V0_TEL
587955960	6835906	B C	00000000 V 1910 TMA_LASER_POWER	587955918	27191294	B D	00000000 V 195 2V5_TEL
587955969	25499836	B C	00000000 ? 0 fpga_state: idle	587955969	25499836	B D	00000000 ? 0 fpga_state: idle
587955969	25499836	B C	00000000 ? 1 laserEnabled	587955969	25499836	B D	00000000 ? 1 laserEnabled
587955969	25499836	B C	00000000 ? 7 mode: diagnostic	587955969	25499836	B D	00000000 ? 7 mode: diagnostic
587955969	25499836	B C	00000000 A 27 3V3_I_TEL	587955969	25499836	B D	00000000 A 27 3V3_I_TEL
587955969	25499836	B C	00000000 T 1606 DCDC_TEMP_15V0P_LAS	587955969	25499836	B D	00000000 T 1606 DCDC_TEMP_15V0P_LAS
587955969	25499836	B C	00000000 T 81 TEMP_REG_2V5A	587955969	25499836	B D	00000000 T 81 TEMP_REG_2V5A
587955969	25499836	B C	00000000 T 509 laserTemp	587955969	25499836	B D	00000000 T 509 laserTemp
587955969	25499836	B C	00000000 T 3029 pmHeadTemp	587955969	25499836	B D	00000000 T 3029 pmHeadTemp
587955969	25499836	B C	00000000 T 1371 procTemp	587955969	25499836	B D	00000000 T 1371 procTemp
587955969	25499836	B C	00000000 T 1382 scienceTemp	587955969	25499836	B D	00000000 T 1382 scienceTemp
587955969	25499836	B C	00000000 V 82 1V0_TEL	587955969	25499836	B D	00000000 V 82 1V0_TEL
587955969	25499836	B C	00000000 V 196 2V5_TEL	587955969	25499836	B D	00000000 V 196 2V5_TEL
587956029	25513361	B C	00000000 ? 0 fpga_state: idle	587955978	27205405	B D	00000000 ? 0 fpga_state: idle
587956029	25513361	B C	00000000 ? 1 laserEnabled	587955978	27205405	B D	00000000 ? 1 laserEnabled

Figure C.2: LHK1A example for wrong assigned data in v04. GF1 data of d231 y2018 is also inserted in GF2. One duplicated Pus-Packet is highlighted in yellow.

- Not all the packets are included in v04 for several days. In table C.3 are listed all the days, where `LriHealthMonitor` and `LriHousekeepingTlm` packets are missing. Table C.4 contains all the days, where the `ADCSamples` and `LaserTlm` are not completely inserted. In addition, there were found a few other days in 2018, where it was not easy to find out which packets are missing. These affected days are listed in table C.5.

year	S/C	day of year
2019	GF1	d354, d359, d364
	GF2	d352, d355, d360, d363, d365
2020	GF1	d002, d004, d007, d009, d014, d021, d024, d029, d030
	GF2	d003, d005, d008, d010, d013, d015, d025, d030, d040, d041

Table C.3: Affected days of missing `LriHealthMonitor` and `LriHousekeepingTlm` in LHK1A v04.

year	S/C	day of year
2019	GF1	d203, d209, d215, d218, d226, d227, d236, d240, d249, d257, d259, d269, d284, d297, d305, d308, d310, d311, d313, d318, d323, d325, d326, d328, d330, d336, d338, d348, d349, d360
	GF2	d205, d207, d215, d231, d248, d249, d252, d255, d257, d261, d262, d271, d275, d285, d299, d311, d312, d314, d317, d321, d325, d327, d328, d345, d358
2020	GF1	d006, d016, d017, d032, d055, d067, d078, d080, d086
	GF2	d004, d006, d012, d048, d067, d076, d086, d089

Table C.4: Affected days of missing `ADCSamples` and `LaserTlm` in LHK1A v04.

year	S/C	day of year
2018	GF1	d162, d163, d164, d364
	GF2	d163, d164, d346

Table C.5: Affected days of other missing data in LHK1A v04.

- On doy 334 in 2019, a wrong time-tag sorting for the GF2 LHK1A v04 product was observed. The affected time-tags are 628403116 s (GrGPS time) and 26057361 nanoseconds (cf. fig. C.3).

```

628403116 26057363 S D 00000000 ? 9643731 i_3
628403116 26057361 S D 00000000 ? 4287140719 pztInLoopStatus
628403116 26057361 S D 00000000 ? 33061986 pztOutOfLoopStatus
628403116 26057363 S D 00000000 ? 63460 q_0
628403116 26057363 S D 00000000 ? 63420 q_1
628403116 26057363 S D 00000000 ? 63244 q_2
628403116 26057363 S D 00000000 ? 63420 q_3
628403116 26057361 S D 00000000 ? 2227 quadDc0
628403116 26057361 S D 00000000 ? 2207 quadDc1
628403116 26057361 S D 00000000 ? 2309 quadDc2
628403116 26057361 S D 00000000 ? 2246 quadDc3
628403116 26057361 S D 00000000 ? 4294494032 thermInLoopStatus
628403116 26057361 S D 00000000 ? 572865494 thermOutOfLoopStatus
628403116 26057361 S D 00000000 A 1233 TMA_PMH_CURRENT
628403116 26057361 S D 00000000 T 2937 TMA_PMH_TEMP
628403116 26057361 S D 00000000 T 491 TM_RLU_TEMP
628403116 26057361 S D 00000000 V 1908 TMA_LASER_POWER
628403116 129530976 S D 00000000 ? 0 pdh_error_max

```

Figure C.3: LHK1A example for wrong sorting in LHK1A v04 of GF2 on d334, y2019.

- Sometimes the LRP FPGA goes into an “INVALID_VALUE” state, where most of the other values from `LriHousekeepingTlm` are zero. These special packets are not present in v04. This might be related to the missing time information after the LRP has rebooted. In this case the time-tags are invalid (as it was explained in appendix B.3) and the data will be removed, when only the data with time-tags of the specific day is taken. Therefore, LHK1A v50 uses the `PusTime` in these situations.

The affected days in v04 are listed in table C.6. On example is shown in fig. C.4 for GF2 on doy 24 in 2020 . On the left side the v50 data with the INVALID_VALUE packet is shown. Since it is the first available packet at this day, one can see that it is missing in v04 (orange arrow on the right side).

year	S/C	day of year
2018	GF1	d162, d164, d165, d166, d167, d200, d222, d235, d249, d269, d308, d309, d326 ,d346, d347
	GF2	d163, d164, d165, d166, d167, d199, d222, d346, d347
2019	GF1	d038, d039, d089, d263,d346, d347
	GF2	d077, d115, d119, d263, d346, d347
2020	GF1	d045, d064
	GF2	d024, d068

Table C.6: Affected days of missing data, where LRP is in an unusual state.

```

# End of YAML header v50
633147978 474566255 B D 00000000 ? 65535 fpga_state: INVALID_VALUE
633147978 474566255 B D 00000000 ? 1 laserEnabled
633147978 474566255 B D 00000000 ? 3 mode: InstrumentSetup
633147978 474566255 B D 00000000 A 0 3V3_I_TEL
633147978 474566255 B D 00000000 T 0 DCDC_TEMP_15V0P_LAS
633147978 474566255 B D 00000000 T 0 TEMP_REG_2V5A
633147978 474566255 B D 00000000 T 0 laserTemp
633147978 474566255 B D 00000000 T 0 pmHeadTemp
633147978 474566255 B D 00000000 T 0 procTemp
633147978 474566255 B D 00000000 T 0 scienceTemp
633147978 474566255 B D 00000000 V 0 1V0_TEL
633147978 474566255 B D 00000000 V 0 2V5_TEL
633148038 245166619 S D 00000000 ? 127 fpga_state: reacq_scan
633148038 245166619 S D 00000000 ? 1 laserEnabled
633148038 245166619 S D 00000000 ? 4 mode: reacquisition
633148038 245166619 S D 00000000 A 0 3V3_I_TEL
633148038 245166619 S D 00000000 T 0 DCDC_TEMP_15V0P_LAS
633148038 245166619 S D 00000000 T 0 TEMP_REG_2V5A
633148038 245166619 S D 00000000 T 0 laserTemp
633148038 245166619 S D 00000000 T 0 pmHeadTemp
633148038 245166619 S D 00000000 T 0 procTemp
633148038 245166619 S D 00000000 T 0 scienceTemp
633148038 245166619 S D 00000000 V 0 1V0_TEL
633148038 245166619 S D 00000000 V 0 2V5_TEL

# End of YAML header v04
633148038 245166619 S D 00000000 ? 127 fpga_state: reacq_scan
633148038 245166619 S D 00000000 ? 1 laserEnabled
633148038 245166619 S D 00000000 ? 4 mode: reacquisition
633148038 245166619 S D 00000000 A 0 3V3_I_TEL
633148038 245166619 S D 00000000 T 0 DCDC_TEMP_15V0P_LAS
633148038 245166619 S D 00000000 T 0 TEMP_REG_2V5A
633148038 245166619 S D 00000000 T 0 laserTemp
633148038 245166619 S D 00000000 T 0 pmHeadTemp
633148038 245166619 S D 00000000 T 0 procTemp
633148038 245166619 S D 00000000 T 0 scienceTemp
633148038 245166619 S D 00000000 V 0 1V0_TEL
633148038 245166619 S D 00000000 V 0 2V5_TEL
    
```

Missing in v04.

Figure C.4: Example for the unusual state of the LRP for GF2 on d024 in y2020. On the left side is shown the cutout of the v50 text file and on the right side for the LHK1A v04 file.

C.4 Comparison of LLG1A v04 and v50

The LLG1A v50 processing can be found in appendix B.4. Here, the discrepancies between v04 and v50 are summarised for LLG1A.

- Sometimes the `BootMessages` contain a message like “SerialPortInterfaceImpl::openSerialPort; Serial po...”. In case of v04, this message leads to different issues. Sometimes unreadable characters (shown by an example in fig. C.6) occur, parts from the next message will be inserted, or several messages afterwards are missing. It is assumed that this is related to a bug in the Flight Software. All affected days are listed below in table C.7.

year	S/C	day of year
2018	GF1	d164, d165, d166, d167, d200, d222, d308, d309, d346, d347
	GF2	d164, d165, d166, d199, (d249), d326, d346, d347
2019	GF1	d038, d089
	GF2	d115, d119

Table C.7: Affected days with faulty `BootMessage`.

- Messages or data is missing in v04 (also in SDS Quicklook v00 data) at:

year	S/C	day of year
2018	GF1	d162, d163, d337
	GF2	d163, d166

And Messages or data is missing in v04 (but is present in SDS Quicklook v00 data) at:

year	day of year
2019	d196 – d365
2020	d001 – d018, d024 - d039, d045 - d092

LRI1A v04

599572800	684956876	C	0000000111111111	00000000	78568363916.57001	3069076715	2109044725	3069076715	2108751859	3069076715	2108751716	3069076715	2109044873
599572800	788433697	C	0000000111111111	00000000	78569484908.96179	3069120504	1101032145	3069120504	1100739759	3069120504	1100739780	3069120504	1101032229
599572800	891910518	C	0000000111111111	00000000	78570605912.95645	3069164293	2039659136	3069164293	2039365509	3069164293	2039365497	3069164293	2039659176
599572800	995387340	C	0000000111111111	00000000	78571726928.54474	3069208083	628409030	3069208083	628112846	3069208083	628112884	3069208083	628408899
599572801	98864161	C	0000000111111111	00000000	78572847955.72964	3069251873	1162745632	3069251873	1162456511	3069251873	1162456678	3069251873	1162745557

Missing
fftSNR,
noise8_9,
noise11_12

LRI1A v50

599572800	684956876.034768	C	0000111111111111	00000000	78568363916.57001	3069076715	2109044725	3069076715	2108751859	3069076715	2108751716	3069076715	2109044873	4903	18	19
599572800	788433697.2268209	C	0000111111111111	00000000	78569484908.96179	3069120504	1101032145	3069120504	1100739759	3069120504	1100739780	3069120504	1101032229	4903	18	19
599572800	891910518.4188739	C	0000111111111111	00000000	78570605912.95644	3069164293	2039659136	3069164293	2039365509	3069164293	2039365497	3069164293	2039659176	4903	18	19
599572800	995387339.610927	C	0000111111111111	00000000	78571726928.54474	3069208083	628409030	3069208083	628112846	3069208083	628112884	3069208083	628408899	4903	18	19
599572801	98864160.80297999	C	0000111111111111	00000000	78572847955.72964	3069251873	1162745632	3069251873	1162456511	3069251873	1162456678	3069251873	1162745557	4903	18	19

Figure C.5: LRI1A Comparison of v04 and v50 text file on 2019-01-01 of GF1. The red boxes indicate the missing data of the LriHealthMonitor in v04. The green boxes mark the alternative format in v50. Here, the last three columns are available, and the time-tag resolution is at femotsecond-level in v50, while nanosecond in the v04 case.

```
LRI1A v04
582329502 -17 D >TLM:CmdHdlr@0x4110d5b0
582329502 -16 D >SerialPortInterfaceImpl::openSerialPort; Serial
poJ EA C1 83 I EA C0 83 J E9 C0 84 J EA C0 83 J EA C1 83 I
DB c1 9D 97 A4 : c1 9D 97 AD5 FSHNSQ DA cX CE
cX C5 < cX C5 BB cX CE UHNSQ R0 DA d 82 FD7 C0 9A d 82 FD . B6 B2 d 82 FD .
B7S d 82 FD7 C1 MHNSQ 8F9 DA e&u 84 E0 84 e&u 84 E2 ! EF e&u 84 E2"
582341569 1 D >Scm::FlashPacketHandler: number of packets received= 0x121
582341569 2 D >Scm: flash detected; pssX/pssY/fftIndex0= 0xfffffed1 0xfffffe5c 0x4ca

LRI1A v50
582329502 -17 D >TLM:CmdHdlr@0x4110d5b0
582329502 -16 D >SerialPortInterfaceImpl::openSerialPort; Serial po
582329502 -15 D >rt /dev/gfo_uart0 opened at baud rate of 0xe100.
582329502 -14 D >SerialPortInterfaceImpl::openSerialPort; Serial po
582329502 -13 D >rt /dev/gfo_uart1 opened at baud rate of 0xe100.
582329502 -12 D >SYS:connect_ok.
582329502 -11 D >SYS:endChange ok.
582329502 -10 D >SYS:schedInit done.
```

Figure C.6: Comparison of LLG1A v04 and v50 BootMessages of GF2 on d166, y2018. Here, the Bug-Message “SerialPort...” leads to unreadable characters in v04.

Bibliography

- Klaus Abich et al. *In-Orbit Performance of the GRACE Follow-on Laser Ranging Interferometer*. *PhysRevLett*.123, 031101, 2019. doi: 10.1103/PhysRevLett.123.031101. <https://doi.org/10.1103/PhysRevLett.123.031101>.
- Milton Abramowitz and Irene A. Stegun. *Handbook of Mathematical Functions with Formulas, Graphs, and Mathematical Tables*. 1972. Tenth printing, p. 884, https://personal.math.ubc.ca/~cbm/aands/abramowitz_and_stegun.pdf.
- AEI. *Nearly 900 days of laser measurements in Earth orbit*. 2021. Max Planck Institute for Gravitational Physics (Albert Einstein Institute), Published June 14, 2021, [Online; Accessed: 2021-08-10], <https://www.aei.mpg.de/718828/fast-900-tage-lasermessungen-in-der-erdumlaufbahn?page=1>.
- Neil Ashby. *Relativity in the Global Positioning System*. *Living Rev. Relativity*, 6(1), 2003. <https://doi.org/10.12942/lrr-2003-1>.
- Francesco Basile, Terry Moore, and Chris Hill. *Analysis on the Potential Performance of GPS and Galileo Precise Point Positioning using Simulated Real-Time Products*. *The Journal of Navigation*, 2018. p. 24–25, <https://doi.org/10.1017/S0373463318000577>.
- J. L. Chen, C. R. Wilson, D. D. Blankenship, and B. D. Tapley. *Antarctic mass rates from GRACE*. *Geophysical Research Letters*, 33, L11502, 2006. doi: 10.1029/2006GL026369. <https://doi.org/10.1029/2006GL026369>.
- Albert Einstein. *Zur Elektrodynamik bewegter Körper*. adp, pages 894–895+903–904, 1905. <https://doi.org/10.1002/andp.19053221004>.
- ESA. *Transformations between Time Systems*. *Living Rev. Relativity*, 2011. [Online; Modified: 2018; Accessed: 2021-04-14], https://gssc.esa.int/navipedia/index.php/Transformations_between_Time_Systems.
- ESA eoPortal. *GRACE-FO (Gravity Recovery And Climate Experiment - Follow-on)*. Article provided by Herbert J. Kramer, [Online; Accessed: 2021-10-01], <https://earth.esa.int/web/eoportal/satellite-missions/g/grace-fo>.
- Frédéric Frappart and Guillaume Ramillien. *Monitoring Groundwater Storage Changes Using the Gravity Recovery and Climate Experiment (GRACE) Satellite Mission: A Review*. *Remote Sensing*, 10(6):829, 2018. doi: 10.3390/rs10060829. <https://doi.org/10.3390/rs10060829>.
- Andreas Freise and Kenneth Strain. *Interferometer Techniques for Gravitational-Wave Detection*. *Living Rev. Relativity*, 13:14–16, 2010. <https://link.springer.com/article/10.12942/lrr-2010-1>.

- Bjorn Frommknecht. *Integrated Sensor Analysis of the GRACE Mission*. PhD thesis, Institut für Astronomische und Physikalische Geodäsie, 2007. p. 87, <https://mediatum.ub.tum.de/doc/630607/630607.pdf>.
- FTP server of GFZ. *GRACE Follow-On RL04 Data for Level 1A + 1B, processed from JPL*. <ftp://isdctftp.gfz-potsdam.de/grace-fo/>.
- GFZ. *GRACE-FO Science Data System (SDS)*. 2018. [Online; Accessed: 2021-08-17], <https://www.gfz-potsdam.de/en/section/.../>.
- Gerhard Heinzel, A. Rudiger, and R. Schilling. *Spectrum and spectral density estimation by the Discrete Fourier transform (DFT), including a comprehensive list of window functions and some new flat-top windows*. MPG Publication Repository, 2002. https://pure.mpg.de/pubman/faces/ViewItemOverviewPage.jsp?itemId=item_152164.
- Pavel Holoborodko. *Central Differences (Applied mathematics and beyond)*. 2008. [Online; Modified: 2011, Accessed: 2021-04-23], <http://www.holoborodko.com/pavel/numerical-methods/numerical-derivative/central-differences/>.
- IAU. *IAU and IUGG/IAG recommendations on reference systems and on the IERS*. International Earth Rotation and Reference System Service. [Online; Accessed: 2021-04-15], <https://www.iers.org/IERS/EN/Science/Recommendations/recommendations.html>.
- JPL. *GRACE-FO Logo*. [Online; Accessed: 2020-08-01], <https://gracefo.jpl.nasa.gov/resources/15/grace-fo-logo/>.
- JPL. *Microwave Instrument - How it Works*. 2018. [Online; Accessed: 2021-04-29], <https://gracefo.jpl.nasa.gov/microwave-instrument/>.
- J. F. Kaufeler. *The ESA standard for telemetry and telecommand packet utilisation P.U.S.*, 1994. N95-17595, ESA/ESOC Darmstadt, Germany, <https://ntrs.nasa.gov/archive/nasa/casi.ntrs.nasa.gov/19950011180.pdf>.
- Richard P. Kornfeld, Bradford W. Arnold, Michael A. Gross, Neil T. Dahya, and William M. Klipstein. *GRACE-FO: The Gravity Recovery and Climate Experiment Follow-On Mission*. *Journal of Spacecraft and Rockets*, 53(3), 2019. doi: 10.2514/1.A34326. <https://doi.org/10.2514/1.A34326>.
- Jim Lambers. *Lecture 23 Notes-Numerical Differentiation*. 2009. [Online; Accessed: 2021-04-23], <https://www.math.usm.edu/lambers/mat460/fall09/lecture23.pdf>.
- Kristine M Larson, Neil Ashby, Christine Hackman, and Willy Bertiger. *An assessment of relativistic effects for low Earth orbiters: The GRACE satellites*. *Metrologia*, 44:484–490, 2007. doi: 10.1088/0026-1394/44/6/007. <https://doi.org/10.1088/0026-1394/44/6/007>.
- Christoph Mahrtdt. *Laser Link Acquisition for the GRACE Follow-On Laser Ranging Interferometer*. PhD thesis, Leibniz Universität Hannover, 2014. pp. 5–11, <https://doi.org/10.15488/8321>.
- Alex Maloney. *Lecture 21 General Relativity, Gravitational Redshift and Time Dilation*. McGill University, 2017. [Online; Accessed: 2021-01-08], <http://www.physics.mcgill.ca/~maloney/260/>.

- Malte Misfeldt, Vitali Müller, Henry Wegener, Laura Müller, and Gerhard Heinzel. *Scale Factor of the Laser Ranging Interferometer in GRACE Follow-On*. In *GRACE Science Team Meeting*, page 11, 2020. https://presentations.copernicus.org/GSTM2020/GSTM2020-13_presentation.pdf.
- Malte Matthias Misfeldt. *Data Processing and Investigations for the GRACE Follow-On Laser Ranging Interferometer*. Master's thesis, Leibniz Universität Hannover, June 2019. <https://doi.org/10.15488/9639>.
- Theodore D. Moyer. *Transformation from Proper Time on Earth to Coordinate Time in Solar System Barycentric Space-Time Frame of Reference*. *Celestial Mechanics*, 23:33–56, 1979. Jet Propulsion Laboratory, Pasadena, California, <https://link.springer.com/content/pdf/10.1007/BF01228543.pdf>.
- Jürgen Müller, Michael Soffel, and Sergei A. Klioner. *Geodesy and relativity*. *Journal of Geodesy*, 82:133–145, 2008. doi: 10.1007/s00190-007-0168-7. <https://doi.org/10.1007/s00190-007-0168-7>.
- Laura Müller, Vitali Müller, and Malte Misfeldt. *Validation of LRI Level-1A data of v04 (RL04)*. April 2020. AEI Hannover, PDF document for SDS/JPL, Modified on 2020-04-29.
- Laura Müller, Vitali Müller, and Malte Misfeldt. *Technical Notes for Notations and Phase Subtraction, Version 1.0*. 2021.
- Vitali Müller. *Simulations for LISA & GRACE-Follow-On: Satellite constellations at Lagrangian points for LISA-like missions*. Master's thesis, Leibniz Universität Hannover, 2013. pp. 89-91, <https://www.vimu.de/thesis/>.
- Vitali Müller. *Design Considerations for Future Geodesy Missions and for Space Laser Interferometry*. PhD thesis, Leibniz Universität Hannover, 2017. p. 2, 26–30, 125, 175, 257–260 <https://doi.org/10.15488/9029>.
- The Earth Observatory NASA. *GRACE Gravity Anomaly Maps and The Geoid*. 3 2004. [Online; Accessed: 2021-03-12], <https://earthobservatory.nasa.gov/features/GRACE/page3.php>, Permission for re-using images: <https://earthobservatory.nasa.gov/image-use-policy>.
- Albert H. Nuttall. *Some Windows with Very Good Sidelobe Behavior*. *Acoustics, Speech and Signal Processing*, ASSP-29, NO. 1:84–91, 1981. <https://www.semanticscholar.org/paper/Some-windows-with-very-good-sidelobe-behavior-Nuttall/a1fa3f3bdcb92e17b01d982e660841630991e868>.
- Dirk Puetzfeld and Claus Lämmerzahl. *Relativistic Geodesy Foundations and Applications*, volume 196 of *Fundamental Theories of Physics*. Springer, 2019. ISBN 978-3-030-11499-2. p. 36, <https://doi.org/10.1007/978-3-030-11500-5>.
- Thomas S. Schwarze. *Phase extraction for laser interferometry in space: phase readout schemes and optical testing*. PhD thesis, Leibniz Universität Hannover, 2018. pp. 9-12, <https://doi.org/10.15488/4233>.
- Daniel Schütze et al. *Retroreflector for GRACE Follow-On: Vertex vs. point of minimal coupling*. *Opt. Express*, 22(8):9324–9333, April 2014a. <https://doi.org/10.1364/OE.22.009324>.

- Daniel Schütze et al. *Laser beam steering for GRACE Follow-On intersatellite interferometry*. *Opt. Express*, 22(20):24117–24132, October 2014b. doi: 10.1364/OE.22.024117. <https://doi.org/10.1364/OE.22.024117>.
- B. S. Sheard et al. *Intersatellite Laser Ranging Instrument for the GRACE Follow-On Mission*. *Journal of Geodesy*, 86:1083–1095, 2012. doi: 10.1007/s00190-012-0566-3. <https://doi.org/10.1007/s00190-012-0566-3>, Reprinted by permission from Springer Nature Customer Service Centre GmbH, License No.: 5066491233691.
- Robert Spero. *Point-mass sensitivity of gravimetric satellites*. *Advances in Space Research*, 67, March 2021. Issue 5, pp. 1656-1664, <https://doi.org/10.1016/j.asr.2020.12.019>.
- B. D. Tapley, S. Bettadpur, M. Watkins, and Ch. Reigber. *The Gravity Recovery and Climate Experiment: Mission Overview and Early Results*. *Geophysical Research Letters* 31.9., 2004a. doi: 10.1029/2004GL019920. <https://doi.org/10.1029/2004GL019920>.
- Byron D. Tapley, Srinivas Bettadpur, Paul F. Thompson John C. Ries, and Michael M. Watkins. *GRACE Measurements of Mass Variability in the Earth System*. *Science*, 305 (5683):503–505, 2004b. doi: 10.1126/science.1099192. <https://www.doi.org/10.1126/science.1099192>.
- J. B. Thomas. *A Method for Designing Low-Pass FIR Digital Filters*. Tech Briefs, 2000. [Online; Accessed: 2021-02-03], <https://www.techbriefs.com/component/content/article/tb/pub/techbriefs/information-sciences/2242>.
- Gudrun Wanner. *Space-based gravitational wave detection and how LISA Pathfinder successfully paved the way*. *Nature Physics*, 15:200–202, 2019. doi: 10.1038/s41567-019-0462-3. <https://doi.org/10.1038/s41567-019-0462-3>.
- Henry Wegener, Vitali Müller, Gerhard Heinzel, and Malte Misfeldt. *Tilt-to-Length Coupling in the GRACE Follow-On Laser Ranging Interferometer*. *Journal of Spacecraft and Rockets*, 57(6), 2020. doi: 10.2514/1.A34790. <https://doi.org/10.2514/1.A34790>.
- Hui Ying Wen, Gene Fahnestock, and Meegyeong Paik. *GRACE-FO JPL L1 Release Notes 20200710*. 2020. ftp://isdcftp.gfz-potsdam.de/grace-fo/DOCUMENTS/RELEASE_NOTES/.
- Hui Ying et al. Wen. *GRACE-FO Level-1 Data Product User Handbook*. Jet Propulsion Laboratory, NASA, JPL D-56935, September 2019. ftp://isdcftp.gfz-potsdam.de/grace-fo/DOCUMENTS/Level-1/GRACE-FO_L1_Data_Product_User_Handbook_20190911.pdf.
- Sien-Chong Wu, Gerhard Kruizinga, and Willy Bertiger. *Algorithm Theoretical Basis Document for GRACE Level-1B Data Processing V1.2*. pages 39–40, 2006. https://podaac-tools.jpl.nasa.gov/drive/files/allData/grace/docs/ATBD_L1B_v1.2.pdf.
- Yihao Yan, Vitali Müller, Gerhard Heinzel, and Min Zhong. *Revisiting the light time correction in gravimetric missions like GRACE and GRACE follow-on*. *Journal of Geodesy*, Vol. 95, No. 48, 2021. doi: 10.1007/s00190-021-01498-5. <https://doi.org/10.1007/s00190-021-01498-5>.

Eigenständigkeitserklärung

Hiermit versichere ich, dass die vorliegende Arbeit selbständig von mir verfasst und keine anderen als die angegebenen Quellen und Hilfsmittel benutzt wurden. Alle Stellen der Arbeit, die wörtlich oder sinngemäß aus anderen Quellen übernommen wurden, sind als solche kenntlich gemacht. Diese Arbeit hat noch keiner Prüfungsbehörde in gleicher oder ähnlicher Form vorgelegen.

Ort, Datum

Unterschrift

Matrikelnummer